Measurement of the Arterial Input Function from Radial MR Projections

by

Jennifer Moroz

B.Sc., University of Alberta, 2007

M.Sc., University of Alberta, 2010

A THESIS SUBMITTED IN PARTIAL FULFILLMENT
OF THE REQUIREMENTS FOR THE DEGREE OF

Doctor of Philosophy

in

THE FACULTY OF GRADUATE AND POSTDOCTORAL STUDIES

(Physics)

The University of British Columbia

(Vancouver)

October 2019

The following individuals certify that they have read, and recommend to the Faculty of Graduate and Postdoctoral Studies for acceptance, the dissertation entitled:

Measurement of the Arterial Input Function from Radial MR Projections

submitted by Jennifer Moroz in partial fulfillment of the requirements for

the degree of Doctor of Philosophy in Physics

Examining Committee:

Stefan Reinsberg, Physics
Supervisor

Piotr Kozlowski, Physics
Supervisory Committee Member

Carl Michal, Physics
Supervisory Committee Member

San Xiang, Physics
Supervisory Committee Member

Purang Abolmaesumi
University Examiner

Roger Tam
University Examiner

Abstract

Dynamic Contrast-Enhanced MRI (DCE-MRI) data may be used to non-invasively investigate the health status of tissue. The technique requires that the concentration of a contrast agent vs. time curve is known in both the tissue of interest and in a blood vessel feeding the tissue - commonly referred to as the arterial input function (AIF). Physiologically relevant parameters are extracted through Pharmacokinetic modeling, though the accuracy is known to be highly sensitive to the quality of the acquired data. It is difficult to get a good measurement of the AIF in pre-clinical studies in mice due to their small body size and limited number of vessels of a sufficient size. As a result, several groups use a population averaged curve from the literature. This curve does not account for inter or intra-individual differences, and impacts the accuracy of the fit parameters.

We propose a new projection-based measurement that measures the AIF from a single trajectory in k-space, which provides a temporal resolution equal to the repetition time (TR). This AIF is measured in the mouse tail due to the simpler geometry void of highly enhancing organs nearby. The projection-based AIF is advantageous as it allows for the acquisition of DCE data, in the tissue of interest, between measurements without affecting the temporal resolution of either data set. We set up a dual coil experimental platform that acquires AIF data at the mouse tail and DCE data at the tumour. Our technique allows for data optimization at both locations, without restricting the temporal or spatial resolutions of the AIF or DCE data. It may be applied to any pre-clinical study using mice or rats.

Lay Summary

This thesis presents a technique to measure the concentration of a MRI contrast agent within a blood vessel during a Dynamic Contrast-Enhanced (DCE) MRI study in mice. The blood-based concentration (referred to as the arterial input function (AIF)) is measured from a single acquisition, allowing for a higher temporal resolution measurement.

DCE-MRI data is analyzed quantitatively through modeling. This requires that the contrast agent concentration in the tissue of interest (typically a tumour) and in a blood vessel (AIF) that supplies that tissue are known throughout the duration of the scan. It is challenging to accurately measure both concentration-time curves simultaneously in mice with a high temporal resolution, so most groups use an AIF from the literature. We show that our AIF measurement may be performed simultaneously with a DCE-MRI study without compromising the temporal resolutions of either, while also improving the model fits. This technique may be applied to any pre-clinical study performed on mice or rats.

Preface

This dissertation is the original intellectual work of Jennifer Moroz. MRI scans on mice, detailed in chapters 4 and 7, were approved by UBCs animal care committee (certificate numbers A09-0943, A13-0053, A16-0105 and A17-0042).

MRI coils were designed and constructed by Andrew Yang. This includes both the strip-line tail coil used for the arterial input function (AIF) measurement, and the tumour specific surface coil used to acquired the dynamic contrast-enhanced magnetic resonance imaging (DCE-MRI) data, described in Chapters 4 and 7. All animal tail cannulations were performed by Jennifer Baker or Dr. Stefan Reinsberg.

The discussion on contrast agents in Chapter 7 was published as a book chapter in Pre-clinical MRI: Methods and Protocols (Moroz, J, Reinsberg, S A, Dynamic Contrast-Enhanced MRI, García Martín M., López Larrubia P. (eds) Preclinical MRI. Methods in Molecular Biology, vol 1718. Humana Press, New York, NY, p. 71-87, 2018). Permission to reproduce this information was granted by Springer. Sections 1.1, 1.3, 3.5 and 4.1 were written by me, while sections 1.2, 3.6 and the remainder of section 4 were written by Dr. Stefan Reinsberg. Sections 2 and 3 were a completed collaboratively.

The projection-based AIF, presented in Chapter 4, was published in Magnetic Resonance in Medicine (Moroz, J, Wong, C, Yung, A, Kozlowski, P, and Reinsberg, S A, Rapid measurement of arterial input function in mouse tail from projection phases, MRM, Vol 71, p. 238-245, 2014) and modified for a more in-depth discussion. Permission to use the figures in this thesis was granted by John Wiley and Sons through their online Copyright Clearance Center Rightslink service.

Andrew Yung and Dr. Piotr Kozlowski provided the motivation for this work and assissted with the protocol development. Dr. Stefan Reinsberg supervised the

study, assisted with all MRI scanning and made arrangements for the mass spectroscopy experiment. Clayton Wong designed the pump phantom used to acquired colormetric data to validate the projection-based AIF presented in Chapter 4. He performed all analysis of the colormetric data. The results from Clayton's work are shown in Figure 4.5 a) and c). The same phantom was later used in Chapter 6 to test the radial AIF technique.

Work from Chapters 4, 5, 6 and 7 were presented at ISMRM conferences. Published abstracts are found in the Proceedings International Society Magnetic Resonance in Medicine Journal:

- Moroz, J, Yung, A, Kozlowski, P, Reinsberg, S A, Estimation of the Arterial Input Function in a Mouse Tail from the Signal Phase of Projection Profiles, Vol 20, p. 239, 2012
- Moroz, J, Kozlowski, P, Reinsberg, S A, Determination of Local Tissue Enhancement from Radially Reconstructed Images, Vol 21, p. 3074, 2013
- Moroz, J, Yung, A, Kozlowski, P, Reinsberg, S A, Measurement of a high temporal resolution AIF: extenstion to radial acquisition to compensate for Local Tissue Enhancement, Vol. 22, p. 526, 2014
- Moroz, J, Yung, A, Kozlowski, P, Reinsberg, S A, Interleaved Acquisition of a Radial Projection Based AIF with a Multi-slice DCE Experiment, Vol. 23, p. 194, 2015

Contributions for these abstract are the similar to the publication above. Dr. Stefan Reinsberg and Andrew Yung assisted in writing the pulse program for radial data acquisition (second and third abstract) and also for the interleaved AIF-DCE experiment (fourth abstract). Piotr provided feedback on the results and assisted in interpreting the results. Dr. Stefan Reinsberg assisted with MRI experiments for the first and fourth abstracts.

Table of Contents

List of Tables

List of Figures

Glossary

AIF	arterial input function
ASL	arterial spin labeling
CS	compressed sensing
CT	computer-assisted tomography
DCE	dynamic contrast-enhanced
DCE-MRI	dynamic contrast-enhanced magnetic resonance imaging
DFT	discrete Fourier transform
DSC-MRI	dynamic susceptibility contrast magnetic resonance imaging
EES	extravascular extracellular space
EPI	echo planar imaging
FFT	fast Fourier transform (image space to k-space)
FID	free induction decay
FLASH	Fast Low Angle SHot
FOV	field of view
FT	Fourier transform
GE	gradient echo

GRE	gradient echo pulse sequence
GMN	gradient moment nulling
IFT	inverse Fourier transform (k-space to image space)
IDFT	inverse discrete Fourier transform
IFFT	inverse fast Fourier transform (k-space to image space)
ICA	independent component analysis
IR	inversion recovery
MR	magnetic resonance
MRI	magnetic resonance imaging
mSSIM	mean Structural SIMilarity index
NFFT	Non-equidistant Fast Fourier Transform
PK	Pharmaco-kinetic
PVE	partial volume effects
RF	radio-frequency
ROI	region of interest
SR	saturation recovery
SRT	saturation recovery time
SNR	signal-to-noise ratio
SPGRE	spoiled gradient recalled echo
SSIM	Structural SIMilarity index
STCR	Spatial-Temporal Constrained Reconstruction
TE	echo time

TOI	tissue of interest
TR	repetition time
VFA	variable flip angle

Acknowledgments

Thank-you to Stefan Reinsberg and Piort Kozlowksi, my thesis supervisors, for supporting my work for this degree. Without their support and guidance, this would not have been possible.

Thank-you to my family for their support in getting me through this degree. It is no easy feat, but your belief in my ability to achieve my dreams made it manageable. Another thank-you to my boyfriend, Winston, who looked after me through all the highs and lows that come with a PhD. You kept me focused through triathlon and running races so that I could attach my code during the week.

I have been fortunate to have many friends support my academic and athletic dreams over the past 8 years. This includes Tiffany, Brendan, Katherine, Brendan, Shauna, Sarah, as well as everyone at the Fraser street run club and UBC triathlon club.

Chapter 1

Introduction

The ability to image tissue vasculature non-invasively has applications in identifying the presence of a disease (such as cancers), determining the extents/stage of the disease, and monitoring the response to treatment [1, 2]. Positron emission tomography (PET), single photon emission computed tomography (SPECT) and contrast-enhanced computed tomography (CT) have all been used for this purpose [3, 4]; however, these methods expose the patient to ionizing radiation [2, 5]. Magnetic resonance imaging (MRI) uses time varying magnetic fields to produce images, and therefore allows a non-invasive technique for imaging soft tissue [6].

The field of dynamic contrast-enhanced MRI (DCE-MRI) has grown substantially over the last decade to evaluate the health status of tissue non-invasively [7, 8]. With its growing popularity in cancer research [9, 10], requirements for data with concurrent high spatial and temporal resolutions have become apparent [11]. DCE-MRI data is analyzed quantitatively through pharmaco-kinetic (PK) modeling [12]. Most models, however, require that the concentration-time curves are accurately characterized in the tissue of interest, as well as in a vessel feeding the tissue of interest [1] - which is commonly referred to as an arterial input function (AIF) [13].

Individually acquired AIFs are difficult to measure in mice due to their small body size [14, 15], rapid heart rate [13, 16] and the limited number of vessels of a sufficient diameter for accurate characterization. For these reasons, murine-based studies often use a population averaged AIF [17–19] in their analysis. The popula-

tion averaged curve is expected to approximate the true curve, but does not account for inter [13] or intra-individual [5, 8] differences. In addition, the population average AIF may only be accurate for a specific injection protocol, contrast agent dose and strain of animal.

1.1 Goals of this Thesis

Our lab has relied on a mathematical representation of the AIF from Lyng [19] to model dynamic contrast-enhanced magnetic resonance imaging (DCE-MRI) data. The fitted curve does not have a well defined injection time, so there is a degree of interpretation when this occurs. A typical DCE-MRI study will have a temporal resolution of a couple seconds. The temporal resolution of the AIF from Lyng, at 13 s, is not sufficient for accurate modelling.

Limitations in measuring a high temporal resolution AIF in mice have lead groups to use a population AIF from the literature. Though this curve may be appropriate, it does not account for inter or intra-individual differences, nor variations in the injection protocol. Even if the AIF has a high temporal resolution, the results from modelling may not be specific to the individual. For this reason, it is desirable to acquire the AIF and DCE data simultaneously. Such studies have been performed in mice by Pathak et al. [20] and in rats by McIntyre [21]).

The goal of this thesis is to show that a high temporal resolution AIF may be acquired in a mouse tail using a projection-based measurement. Since the AIF would only require one line of k-space per measurement, the temporal resolution equals the repetition time. A second advantage is our ability to acquire DCE data between consecutive AIF measurements. We show that an interleaved AIF-DCE acquisition may be implemented without sacrificing the temporal resolution of either the AIF or DCE data, and may be applied to any mouse or rat experiment.

Chapter 2 will introduce magnetic resonance imaging (MRI) and the theory relevant for this thesis. This includes the creation of MR signal, how images are constructed and the physics behind contrast enhancement with a contrast agent.

The physics and techniques of DCE-MRI is the subject of Chapter 3. The Chapter opens with a brief discussion of angiogensis - the process in which a tumour rapidly develops new blood vessels to supply proliferating cells with nutri-

ents and oxygen. DCE-MRI evaluates the health status of tissue by tracking the distribution of a contrast agent within a tissue of interest temporally. The primary techniques of studying perfusion and permeability with MRI are discussed, with a primary focus on the concepts and methods related to DCE-MRI. The chapter concludes with a summary of semi-quantitative and quantitative analysis techniques.

We introduce a projection-based arterial input function (AIF) measurement in Chapter 4. The measurement is performed with a single line of k-space, and uses the phase of the MR signal to estimate the concentration of a contrast agent within a vessel (both in a phantom and in-vivo). The Chapter outlines three experiments. The first experimentally measured the phase-concentration conversion factor for our scanner and pulse sequence. The second experiment measured a projection-based AIF within a pump phantom, which was cross-validated using colorimetry. The third measures a projection-based AIF in a mouse tail. The late stage concentration was validated with mass spectrometry 20 min post injection in four mice.

The permeable nature of capillary walls means that some contrast agent may diffuse from within the vessel to the surrounding tissue. This could bias the projection-based AIF if the projection is acquired at the same angle for the duration of the experiment. We propose to extend the measurement to include MR data from multiple angles. Chapter 5 studies three radial reconstruction techniques: interpolation of the radial data onto a Cartesian grid using Shepard's method of interpolation, Spatial-Temporal Constrained Reconstruction (STCR) and Non-equidistant Fast Fourier Transform (NFFT). The goal of this chapter is to determine which method would be best suited for our application. Since the projection-based AIF is calculated from the difference of two complex signals, both the magnitude and phase information should be preserved in the reconstructed image.

Chapter 6 summarizes the results from a simulation study involving radial projections and compensating for contrast perfusion into the surrounding tissue. The contrast agent causes an increase in the signal intensity locally, in T_1-weighted magnetic resonance (MR) images, which is referred to as local tissue enhancement. This chapter compares the three radial reconstruction techniques for their ability to reproduce local tissue enhancement within the images. The proposed local tissue enhancement correction uses the projection of these reconstructed images to correct the acquired data. This involves calculating the difference between the pre and

post-injection background signals, and compensating the acquired data with this information. The chapter concludes with the measurement of a projection-based AIF, after correcting the projections for local tissue enhancement.

The interleaved AIF-dynamic contrast-enhanced (DCE) experiment is outlined in Chapter 7. The chapter opens with a brief description of the pulse sequence and set-up used for this study. The interleaved experiment was performed both in phantom as well as in-vivo, to validate the technique and evaluate its application in a pre-clinical studies in mice or rats. Recently, most **AIFDCE!** (**AIFDCE!**) studies have avoided the AIF measurement in favour of improved spatial and temporal resolutions at the tissue of interest. Our method could improve the accuracy of the model fit parameters as the **[!** (**[!**)AIF will is specific to the animals physiology at the time of imaging and the injection protocol used. The use of projections will allow for high temporal resolution measurements for both the **[!**AIF and tissue of interest.

Chapter 2

Magnetic Resonance Imaging Theory

X-ray, computer-assisted tomography (CT) and ultrasound were traditionally used for imaging internal anatomy [6]. However, these techniques use ionizing radiation to produce images, raising concerns for procedures involving repeat imaging sessions [22]. MRI has the advantages that there are no known side-effects from exposure to the external magnetic or gradient fields, it provides excellent tissue contrast [23] and places no restrictions on the image orientation [6, 24]. MR imaging has been used extensively in clinic to diagnose a broad range of disorders [5].

While MRI is based on quantum mechanics, the concepts reduce to classical mechanics at the macroscopic level [25]. As a result, a majority of MRI theory may be understood from a classical perspective.

2.1 Creation of MR Signal

Magnetic resonance is based on the interaction of a proton - possessing a spin and charge - with an external magnetic field [26]. The nuclear spin is an intrinsic property of an atom related to its angular momentum. It can take on integer and half-integer values, depending on its atomic number (number of protons) and the atomic mass of the nucleus (protons and neutrons) [26]. Table 2.1 summarizes the nuclear spin for atoms of odd and even atomic and nuclear weights.

Table 2.1: Nuclear Spin based on atomic weight and nuclear weight

Atomic Number	Nuclear Weight	Spin
even	even	0 - no interaction
odd	even	integer spin
odd	odd	half integer spin

The hydrogen atom is used in most MRI applications due to its high relative abundance (88 M, compared to 80 mM for other atoms like sodium and phosphorous) in the human body and spin 1/2 [26]. Other common atoms for in-vivo imaging are ^{13}C, ^{23}Na and ^{31}P, which have spins of $\frac{1}{2}$, $\frac{3}{2}$ and $\frac{1}{2}$ respectively [27].

When a nucleus with non-zero spin is placed in a static magnetic field, B_o, it precesses around the field at a constant rate, known as the Larmour frequency:

$$\omega_o = \gamma B_o \tag{2.1}$$

Where ω_o is the Larmour frequency (in MHz), γ is the Gyromagnetic ratio (in MHz/T) [28], and B_o is the strength of the external magnetic field. For hydrogen, $\gamma = 42.6$ MHz/T [6, 29].

The spin creates a constant magnetic moment, which in turn induces a local magnetic field along the axis of rotation. In the absence of an external magnetic field, the individual magnetic moments are randomly oriented, resulting in a net magnetization of zero. When placed in an external magnetic field, more magnetic moments will preferentially align with the main magnetic field, providing an observable net magnetization along its axis [25]. This interaction between the proton's magnetic moment and the magnetic field creates magnetic resonance [30]. The Zeeman effect states that coupling between a proton and a magnetic field has quantized values. Since the hydrogen atom has a spin 1/2, there are two unique states; spin-up and spin-down.

The coupling causes a difference in energy between the two states. A majority of protons will align parallel to the field (lower energy), resulting in a net magnetization described by the Boltzman distribution.

$$\frac{N_{down}}{N_{up}} = e^{-\Delta E/K_B T} \tag{2.2}$$

Where N_{down} is the number of protons aligned anti-parallel to the magnetic field, N_{up} is the number of protons aligned parallel to the magnetic field, ΔE is the energy difference between the two states, K_B ($= 1.381x10^{-23}$ J/K) is the Boltzman constant, and T is the temperature in K.

At room temperature, the difference in protons in each orientation is very small (about 45 out of 10 million at 1.5 T) [30]. However, the proton density in tissue is very large, resulting in a measurable net magnetization. The vector summation of all protons provides the net magnetization, denoted as M_o.

The next three sections will discuss how we can manipulate the net magnetization to construct images.

2.2 Concepts and Properties of MR Signal

This section cites information from [30], [27] and [31]. Refer to these references for a more in-depth discussion.

Signal Excitation

By convention, the main magnetic field is set along the $+Z-axis$ and the receiver coil oriented such that it can detect a changing magnetic flux in the sample in the $X-Y$ plane. The net magnetization is tipped into the $X-Y$-plane with an oscillating radio-frequency (RF) pulse, which is referred to as the B_1 pulse. The B_1 pulse is oriented perpendicular to B_o. The protons in the sample absorb energy from the radio-frequency (RF) pulse if the frequency of the RF pulse exactly matches the Larmour frequency [31]. The RF pulse contains a narrow range or bandwidth of frequencies, centered around a central frequency.

Since the frequency of the B_1 pulse matches the Larmour frequency, the precessing protons will see it as stationary in its frame of reference. We refer to this as the rotating frame of reference and define its axes with x, y and z (compared to X, Y and Z for the laboratory frame). Under these conditions, the RF pulse applies a torque on the magnetization, causing it to rotate towards the $x-y$-plane.

By convention, the B_1 pulse is oriented along the $x-axis$ in the rotating reference frame [31]. The duration and magnitude of the pulse affects the flip angle, α, at which the magnetization tips. The flip angle is determined from [30].

$$\alpha = \int_0^{\tau} \gamma B_1 dt \tag{2.3}$$

Where B_1 is the strength of the B_1 pulse and τ is the duration of the pulse. The application of the B_1 pulse forces all individual magnetization vectors to initially have the same phase [32].

Once in the $x-y$-plane, the transverse magnetization (M_{xy}), continues to precess around the main magnetic field, at a rate of ω_o. From Faraday's law of induction, a changing magnetic flux - such as the spinning magnetization - will induce an electromotive force in a nearby wire loop. This induces a current in the wire, which allows the signal to be recorded. The wire loop is referred to as a receiver coil, and may be designed to optimize the signal-to-noise ratio (SNR) of the anatomy of interest.

The acquired signal is commonly referred to as the free induction decay (FID). The initial magnitude is characterized by the strength of the net magnetization immediately following the B_1 pulse, and is a complex summation of all protons within the sample. This means that the signal contains multiple frequencies as a result of variations in the magnetic environment throughout the sample [31]. These frequencies may be extracted using a Fourier transform.

MR signal is continuous in nature, but is sampled at discrete points (digitized) with an analog-to-digital converter (ADC) [31]. Sampling at definitive points allows for post-processing techniques, such as the fast Fourier transform, to be performed. However, sampling by the ADC limits the range of frequencies that may be resolved. If the sampling rate is not sufficient, then higher frequency components will be wrapped to a lower frequency, such that $f_{obs} = mod(f_{actual}, f_{max})$ (where f_{obs} is the observed aliased frequency, f_{actual} is the actual input frequency and f_{max} is the maximum frequency that may be resolved by the ADC). This effect is known as aliasing. To reduce the impacts of aliased signal, the phase-coherent difference signal between the FID and input RF (frequency and phase) is digitized instead.

This digitized signal is now measured relative to the transmitted frequency, ω_{TR}, and is equivalent to collecting signal in the rotating frame of reference [31].

The number of samples taken from the FID and the total sampling time are user defined. These parameters will impact the maximum frequency that may be accurately represented, which is referred to as the Nyquist frequency, ω_{NQ}. The Nyquist frequency is defined as [31]:

$$\omega_{NQ} = \frac{N_{FID}}{2 \cdot T_s} \tag{2.4}$$

Where N_{FID} is the total number of samples taken from the FID and T_s is the total sampling time. Any acquired frequency beyond the Nyquist frequency will be indistinguishable with its mod(ω,2π). As a result, the frequencies will be wrapped to the lower frequency. To avoid ghosting artifacts from wrapping, a low pass filter may be used prior to digitization. This can also improve the SNR of the signal as most of the higher frequencies are due to noise.

Relaxation and the Bloch Equations

The process of relaxation is well documented ([30], [27], [33], [24]) and is fundamental to the observed signal and contrast in MRI images. Two processes are of interest: the creation of a net magnetization in the direction of the external magnetic field, and the loss of precessing signal orthogonal to the field.

When the B_1 pulse is turned off, the protons experience only the main static magnetic field, B_o. This means that the individuals spins will eventually return to their equilibrium state, resulting in a loss of signal in the $x-y$-plane, and rebuilding of the magnetization along the $+z-axis$. The time required for both effects is dependent on the tissue type, thus providing tissue contrast in MRI images.

The time required to rebuild the net magnetization along the $+z-axis$ is known as T_1 relaxation, or the spin-lattice relaxation time. T_1 relaxation is dependent on the proton's interaction with its environment. An excited spin will release energy to its environment and return to a lower energy state (with preferential alignment parallel to the external magnetic field). The governing formula for this process is defined by the Bloch equation, stating that:

$$\frac{dM_z}{dt} = -\frac{M_z - M_o}{T_1} \tag{2.5}$$

Solving this differential equation for M_z, and assuming complete relaxation to regain magnetization M_o (a time interval of $5T_1$ is recommended for the tissue of interest), we get:

$$M_z = M_o(1 - \exp^{-t/T_1}) + M_z(t = 0)\exp^{-t/T_1} \tag{2.6}$$

Special cases for this equation are for saturation recovery, in which $M_z(T = 0) = 0$ due to a 90° RF pulse and an inversion recovery experiment, where $M_z(t = 0) = -M_o$. The T_1 value for free water is approx. 4 s [34]. As the proton's environment gets more structured, a proton-lattice interaction is more probable, resulting in shorter T_1 for tissues.

Signal loss in the $x-y$-plane results form loss of coherence within M_{xy}, and is referred to as T_2 relaxation or spin-spin relaxation.

The Bloch equation describing the overall T_2 relaxation in the rotating frame of reference is:

$$\frac{dM_{xy}}{dt} = -\frac{M_{xy}}{T_2} \tag{2.7}$$

Here, M_{xy} is a 2-dimensional vector representing the transverse magnetization in the $x-y$-plane. Solving the equation for M_{xy} gives us:

$$M_{xy} = M_{xy}(0)\exp^{-t/T_2} \tag{2.8}$$

Where $M_{xy}(0)$ is equal to longitudinal magnetization prior to the RF excitation pulse. In cases where the flip angle is not 90°, the transverse equation will include a $\cos(\alpha)$ term, where α is the flip angle.

There are two processes involved with signal loss in the $x-y$ plane. The first process deals with the energy transfer, ΔE, between neighboring spins in oppos-

ing energy states or from diffusion of the spin to an area with a different B_o. This is a non-reversible process, and is governed by the T_2 relaxation time constant. The second process is due to magnetic field inhomogeneities. Nearby protons may experience a slightly different magnetic environment, and therefore precess at different Larmor frequencies. In effect, phase coherence of the protons is lost, as some protons spin faster than the bulk magnetization and others precess slower. This process is static, reversible, and defined by $T_2^{'}$. The combined relaxation from reversible and non-reversible effects is defined as T_2^*, and follows the relation:

$$\frac{1}{T_2^*} = \frac{1}{T_2} + \frac{1}{T_2^{'}} \tag{2.9}$$

2.3 Gradient Fields

When a radio-frequency (RF) pulse is applied, only the spins that resonate at a frequency within the bandwidth (BW) of the pulse are excited. It is possible to spatially manipulate the magnetic environment experienced by the object, so that only a small band of spins resonate at the correct frequencies. This is achieved with magnetic gradients.

The gradient coils adjust the magnetic field strength spatially along the physical X, Y and Z-axes of the scanner and allow for spatial encoding [33]. They cause a linearly varying magnetic field, originating at the isocenter of the MR scanner (see Figure 2.1). The gradient fields are all oriented in the same direction as B_o, such that the resonant frequency of the protons varies in a known (linear) fashion. This information is encoded within the FID signal. It is important to note that the strength of the gradient fields is much smaller than the external magnetic field, so any field oriented in the X-Y plane is negligible [33]. The gradient fields are measured in units of mT/m.

The gradient vector may be written as:

$$\vec{G} = \frac{\partial B_Z}{\partial X}\hat{X} + \frac{\partial B_Z}{\partial Y}\hat{Y} + \frac{\partial B_Z}{\partial Z}\hat{Z} = G_X\hat{X} + G_Y\hat{Y} + G_Z\hat{Z} \tag{2.10}$$

Where $G_{X,Y,Z}$ are the gradient strengths in the X, Y and Z directions respectively and $\partial B_Z/\partial X,Y,Z$ represents the linear variation in the magnetic field in the

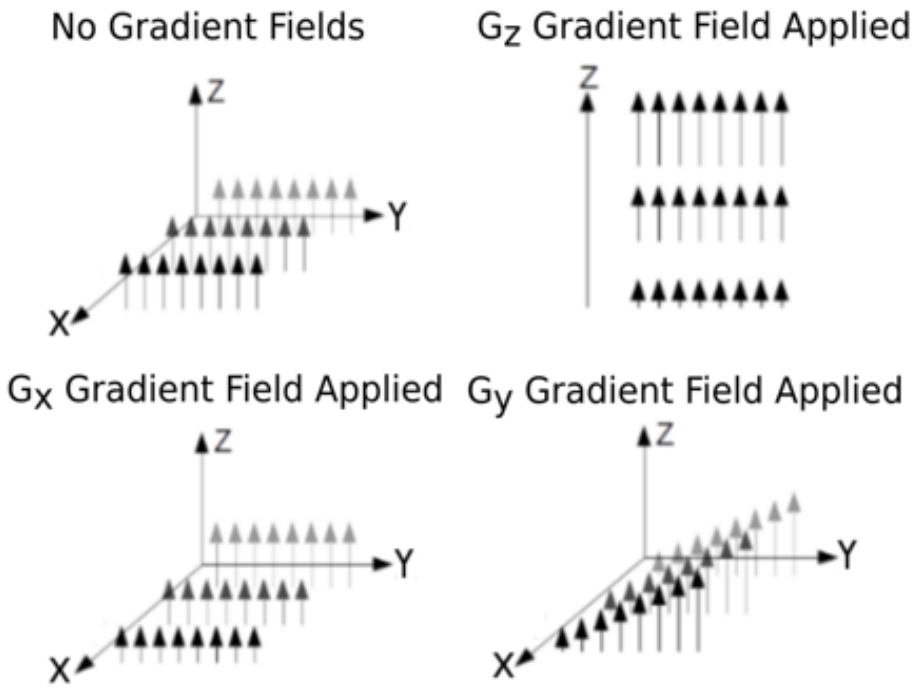

Figure 2.1: Applied gradient fields alter the magnetic field strength linearly along the +Z-axis, to allow for spatial localization (exaggerated to show the effect as $\vec{B_o} \gg G_r\vec{r}$, where $\vec{r}$ is the spatial distance from isocenter). The net magnetic field becomes: $\vec{B_{net}} = \vec{B_o} + G_r\vec{r}$. There are three physical gradients that affect the magnetic field strength in the X, Y and Z directions independently. In doing so, the Larmor frequency, which is dependent on $\vec{B_{net}}$, becomes spatially dependent. The acquired FID contains information about all frequencies present in the sample.

respective direction. These gradients are generated from three separate coils [33].

The gradient fields may be used for slice selection, frequency encoding or phase encoding. This will be the topic of the next section.

Slice Selection

MR slice selection is achieved by applying a gradient field, perpendicular to the desired slice plane, for the duration of the RF excitation pulse. In MRI, the slices may be oriented in any direction, allowing for oblique slices [33]. This requires

that two or more of the physical gradient coils are in use. The magnitude of each is dependent on the angulation of the desired slices relative to the +z-axis [33].

The slice-select gradient can introduce phase dispersion of the magnetization in the slice [33]. This is a combined response of the magnetization to the slice select gradient and the shape of the RF pulse. A slice-refocusing, or rephasing, lobe is applied after excitation to compensate for the phase dispersion. This lobe has the opposite polarity of the slice select lobe, and an area identical to the center of the excitation pulse [33]. For a symmetric RF excitation pulse and slice select gradient, the area of the rephase lobe is half that of the slice select lobe.

The RF excitation pulse has a pre-specified bandwidth (BW). Any spin that precesses with a Larmour frequency in that range will be excited. The slice thickness, Δz and the RF pulse bandwidth, Δf, are related as:

$$\Delta z = \frac{2\pi\Delta f}{\gamma G_z} \tag{2.11}$$

Where γ is the gyromagnetic ratio and G_z is the strength of the slice select gradient. Thinner slices are possible by either increasing the strength of the slice select gradient or reducing the BW (using a longer excitation pulse).

For slices off-set from the magnet isocenter, the RF frequency must be adjusted to match the central Larmor frequency of the slice. The adjustment, δf can be calculated from:

$$\delta f = \frac{\gamma G_z \delta z}{2\pi} \tag{2.12}$$

The excitation pulse is often a sinc or Gaussian pulse, which creates a rectangular or Gaussian slice profile.

Frequency-encoding

Frequency encoding, or the read-out, allows for spatial information to be determined from the sample. This is done by applying a linearly varying magnetic field across the sample, orthogonal to the slice direction, which causes the precessional frequency to vary linearly [33]. The spatial locations of all spins within the sample may be determined from the FT of the acquired time-domain signal. Frequency-

encoding may be applied in any direction, though it is typically oriented perpendicular to the slice for imaging purposes. By convention, frequency-encoding is along the x-axis.

The frequency-encode gradient waveform typically consists of two lobes [33]. The first is a prephasing gradient, and the second is the read-out gradient. The purpose of the pre-phase gradient is to prepare the magnetization to form an echo at a later time. The prephase gradient provides a linearly varying magnetic field, causing some isochromats, defined as a cluster of spins resonating at the same frequency, to precess at a faster rate than others. The net result is a linearly varying phase accumulation across the sample. When the readout gradient is applied, the isochromats will gradually rephase to produce an echo when the gradient areas of the two lobes are equal. The receive coil is on during the readout window so that the echo may be acquired.

The process of refocusing the spins differs between a spin echo and gradient echo. This will be discussed in greater depth in the next section on pulse sequences.

Phase-encoding

Phase-encoding provides spatial information about the sample orthogonal to the frequency-encode direction [33]. This is performed by applying a gradient lobe between the initial excitation pulse and the readout window. Similar to frequency-encoding, a linear gradient field is applied across the sample, causing isochromats at different spatial locations to accumulate phase at different rates. The spatial information may be determined after application of the Fourier transform. By convention, phase-encoding is performed along the y-axis.

Phase-encoding localizes signal in a second (or third) orthogonal dimension through spatially-varying phase accumulation. The phase-encode gradient field can be applied concurrently with other gradients, with the exception of the slice select and acquisition gradients. To maximize signal consistency between phase-encode steps, many pulse sequences will rewind the phase-encode gradient after the readout [33].

The phase-encoding gradient is applied N times, where N is the desired number of samples in this direction. The gradient strength may take on multiple values

from the maximum, G_y, to the minimum, $-G_y$, in equal sized steps ($\Delta y = 2G_y/N$). The equal step size allows for a more uniform coverage of k-space so that techniques, such as the IFFT, may be applied directly to the data. The value of G_y is dependent on the desired field of view.

In 3-D imaging, phase-encoding occurs in two directions; the second of which is along the slice select direction. This form of imaging greatly enhances the spatial resolution in the slice select direction, but also leads to much longer scan times.

Care must be taken to avoid aliasing of the signal into the image. This is not a problem if the Nyquist criterion is satisfied:

$$\Delta k_y \leq \frac{1}{N\Delta y} \tag{2.13}$$

Where Δk_y is the phase encoding step size, Δy is pixel size, and N is the number of phase encode samples. The product $N\Delta y$ is equal to the FOV in the phase-encoding direction.

The Fast Fourier Transform

MR data is acquired in the frequency domain, which is commonly referred to as k-space. The k-space data is converted to an image through application of the inverse Fourier transform (k-space to image space) (IFT). The k-space acquisitions are known as trajectories, and are composed of a linear combination of signals within the slice [6]. Due to the read and phase-encoding gradients, the magnetization at each location will precess at a different frequency. The IFT extracts the frequency information, and maps it to a location in the image.

The Fourier transform (FT), and its corresponding IFT, are defined as [35]:

$$F(\omega) = \int_{\infty}^{\infty} f(x)e^{-i\omega x}dx \tag{2.14}$$

$$f(x) = \frac{1}{2\pi}\int_{\infty}^{\infty} F(\omega)e^{i\omega x}d\omega \tag{2.15}$$

Where ω are the frequencies within the k-space signal, x is the spatial location, and $i = \sqrt{-1}$. These equations are used for continuous signals. MR data, however, is sampled at discrete locations by means of an analog to digital converter [36].

The discrete Fourier transform (DFT) accounts for discrete and periodic signals, mapping the finite set of uniformly spaced sampled onto a uniformly sampled grid in its conjugate space [27]. This is achieved by replacing the integral with a summation at the known sampling positions. The equation for the 1-D DFT and inverse discrete Fourier transform (IDFT) are:

$$A_k = \sum_{j=0}^{N-1} a_j e^{-i2\pi kj/N} \tag{2.16}$$

$$a_j = \sum_{k=0}^{N-1} A_k e^{i2\pi kj/N} \tag{2.17}$$

Where A_k is the discretely sampled (complex) data, a_j is the image-space data, k is the is the discrete frequencies, j (=0, ... N-1) is discrete sampling position, and N is the number of samples acquired. The exponential term may be re-written as W^{jk}, where W $(= e^{2\pi i/N})$ is the Nth root of unity.

The frequency information throughout all of k-space will contribute to each individual pixel in the image. The 1-D inverse fast Fourier transform (k-space to image space) (IFFT) provides the spatial proton density of a projection, while the 2-D IFFT produces an image of the sample with proton density information in both directions. This is a separable function, so the 2-D (or 3-D) IFT may be applied as two (or three) 1-D IFTs; one along each matrix dimension [33].

The DFT computes an order of N^2 iterations per image [35]. A faster technique is the fast Fourier transform (image space to k-space) (FFT) (or IFFT), which calculates the DFT through a sequence of algebraic manipulations [36, 37]. This reduces the number of iterations to $NlogN$, thus allowing for significant improvements in computation time [37]. The FFT/IFFT requires that the number of samples is an even number, though it is most efficient with 2^n samples (n=0,1,2,...). This is a consequence of the discrete FFT operating on signal pairs [35] to reduce the number of computations. Acquisitions with a sampling size that is not 2^n can take advantage of the FFT by zero-filling the matrix to the next power of 2.

A property of the discrete FT states that if the signal is discretely sampled in one domain, then it will be periodic in the other [33]. Since the data in k-space is discretely sampled, the image-space signal will become as a series of replicates

with a period of N samples. If the acquired data does not satisfy the Nyqist criterion, which states that the data sampling rate is at least double the greatest frequency found in the signal, then the image-space replicates overlap. This leads to an aliasing artifact.

2.4 k-Space and Pulse Sequences

The time-varying signals in MRI may be analyzed by tracking the trajectories in a 2-D or 3-D space. This space is the Fourier conjugate of the spatial domain and is referred to as k-space [33]. The k-space domain can improve our understanding of pulse sequences as it shows how the MR signal transverses the Fourier domain.

MR images are constructed from the k-space trajectories [33]. k-Space data is only filled when the acquisition window is active, though it is possible to still transverse k-space without it. The rate at which we transverse k-space is determined from the gradient strength and the gyromagnetic ratio ($|d\vec{k}/dt| = |\gamma G|/(2\pi)$). The total distance covered in k-space is then equal to the area under the gradient waveform. k-Space may be interpreted as the rate at which a stationary spin accumulates phase (measured in cycles/meter) under the influence of a gradient[33].

The magnitude of the acquired signal is dependent on the repetition time (TR) and the echo time (TE) selected for the scan. The repetition time is defined as the time interval between successive excitation pulses. Depending on the pulse sequence, TR may be on the order of 10 ms to several seconds [38]. Setting TR to a larger value will allow for more magnetization to rebuild along the +z-axis, and thus improve the SNR. The echo time is defined as the time interval between the center of the 90° excitation RF pulse and the time at which an echo reaches its maximum [39]. This timing is typically set to a value on the order of 1 ms to 100 ms [38]. The echo may be achieved using a spin echo or gradient echo, both of which are described in greater detail in the next sections.

k-Space has its maximum intensity at the center, and is symmetric about this point. In a majority of applications, the MR signal is acquired as either a spin echo of a gradient echo. This is attractive as data from both sides of k-space is acquired, and the center of k-space can be determined with greater precision. This is a direct result of having a non-zero frequency encode gradient on during the readout

window, which affects the precessional frequency (and hence phase accumulation) spatially.

Spin Echo

Spin echo imaging is popular for T_1-weighted applications or for parallel imaging techniques due to the improved SNR at the echo [33]. The spin echo involves the application of a second, refocusing pulse to rephase the signal. The refocusing pulse may be oriented along either the +x-axis or the +y-axis in the rotating frame [40]. The effect is the same, but the echo will either alternate signs (+y-axis, -y-axis,...) or always be along the +y-axis. The discussion below and in Figure 2.2 uses a refocusing pulse along the +x-axis.

For maximum echo signal, a 180° pulse is played out at a time of TE/2. Prior to the refocusing pulse, the magnetization will dephase due to magnetic field inhomogeneities. In effect, some spins will experience a higher magnetic field and will rotate faster than the Larmor frequency, while others will experience a lower magnetic field and rotate slower than the Larmor frequency. This results in a fan-like pattern in the rotating frame, centered along the +y-axis. The refocusing pulse flips the magnetization across the x-axis, such that the fan-like pattern is now centered along the -y-axis. The spins that were spinning fast continue to spin faster and gradually approach the -y-axis, while the slower precessing spins continue to rotating slower. At the echo time, TE, all spins will be aligned along the -y-axis creating an echo. The image contrast is provided by the factor e^{-TE/T_2}. The spin echo pulse sequence is summarized in Figure 2.2.

The pulse sequence may be designed with the two lobes on either side of the refocusing pulse, or both following the pulse [27]. When the refocusing pulse is positioned between the two lobes, the gradient lobes will have the same polarity. This design allows for a shorter echo time. In the alternative, the gradient lobes have different polarity. Though the echo time is longer, the echo is less sensitive to flow [27]. With a simple spin-echo pulse program, only one echo is acquired within a TR. This could result in very long scan times for T_2-weighted images due to the requirement to rebuild M_o. Multiple spin echos may be achieved with multiple refocusing 180° pulses.

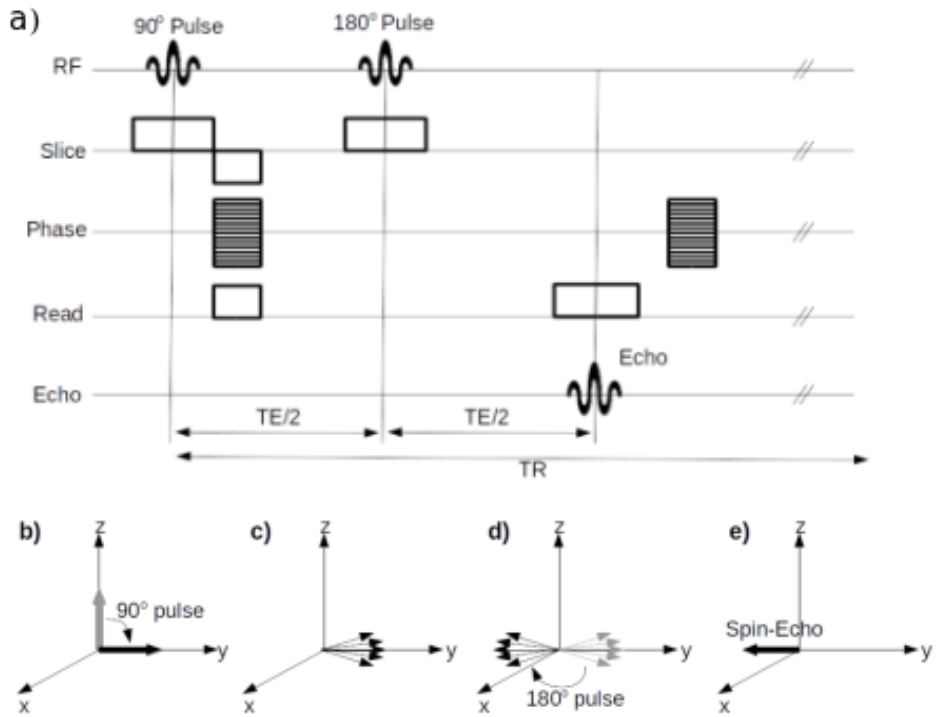

Figure 2.2: Pulse program for a spin echo (a). The sequence is characterized with an initial 90° pulse, followed by a 180^0 pulse at time TE/2. The 180° pulse allows the magnetization to rephase, creating an echo at a time of TE. b-e show the response of the magnetization after the excitation (90°) and refocusing (180°) pulse. In b, the magnetization is tipped into the x-y plane. The spins may precess at different rates due to magnetic field inhomogeneities, causing them to dephase (c). After applying the 180° refocusing pulse (at TE/2), the magnetization begins to rephase, forming an echo at TE. The spin echo will have a stronger signal than a gradient echo since it is able to undo phase dephasing due to magnetic field inhomogenities. The phase-encode gradient is often rewound at the end of acquisition, to reset the phase to its initial value to maintain consistency in the magnetization between repetitions.

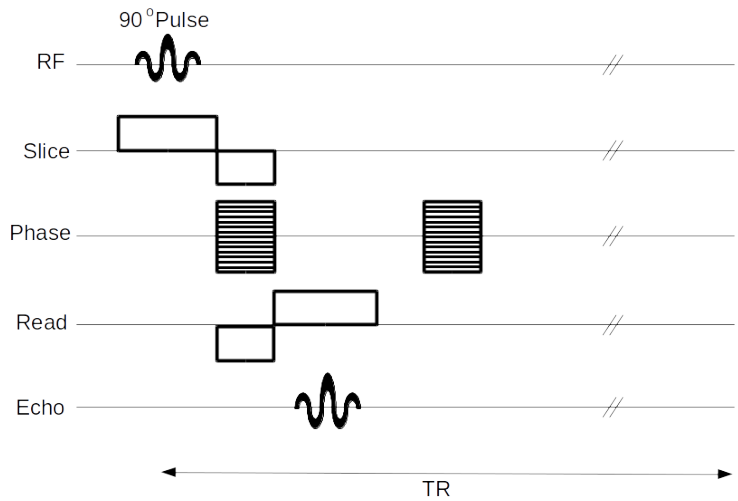

Figure 2.3: Pulse program for a gradient echo. In contrast to a spin echo, the echo occurs from a series of read-encode gradient lobes. De-phasing caused from magnet field inhomogeneities are not refocused, so a gradient echo decays faster than a spin echo.

Gradient Echo

The gradient echo pulse sequence (GRE) creates the echo though application of two gradient lobes along the same gradient channel. The two lobes are referred to as the pre-phase and readout gradients, and have opposite polarities. During the pre-phase lobe, the rate of precession of spins within the sample vary linearly. Spins on one side of the sample will accumulate phase much faster than those on the other side of the sample, resulting in a linearly varying phase distribution across the sample. When the sign of the gradient pulse is inverted, spins continue to precess at the same rate (assuming no magnetic field offsets of inhomogeneities), but in the opposite direction. The GRE forms when the readout gradient area exactly equals that of the prephase gradient lobe. The GRE process is summarized in Figure 2.3.

The GRE pulse sequence allows for faster imaging by using a smaller flip angle for excitation, α. A flip angle less than 90° preserves some longitudinal magnetization, so the repetition time of the experiment can be reduced. If α is chosen to be much less than 90°, such that $sin\alpha \approx \alpha$, the longitudinal signal is $cos\alpha \approx 1 - \alpha^2/2$.

When compared to a spin echo experiment with similar echo times, a gradient echo will have lower SNR. This is a direct result of signal loss from T_2^* relaxation (modulated by e^{-TE/T_2^*}). Without the extra RF pulse, gradient echos can have shorter echo times.

Multiple gradient echos can be played out in succession within a single repetition time. This is the basis for echo planar imaging (EPI). The data acquisition transverses k-space back and forth by inverting the gradient area between successive lobes. The maximum number of echos possible is dependent on how rapidly the signal is lost to T_2^* relaxation.

The sampling locations in k-space are dependent on the net gradient area in the frequency and phase encode directions. To sample multiple lines within one TR, a small area phase-encode gradient must be applied between echo acquisitions. The gradient area is related to the k-space resolution in the phase encoding direction and the desired step size between consecutive k-space lines. These gradients are made as short as possible to maximize the number of echos that may be acquired within the repetition time.

EPI greatly speeds up the total acquisition time by acquiring multiple lines of k-space with each RF pulse. The total acquisition of all echos is referred to as an echo train, and each acquisition referred to as a shot. For multiple gradient echos, the second half of the readout gradient will act as the prephase gradient for the next echo, thug allowing for further time savings. The increased speed, however, comes at the cost of geometric distortions from off-resonant spins and Nyquist ghosts resulting from the alternating k-space trajectories.

Steady-State Magnetization

The recovery of longitudinal signal requires a long time. Data collection may be sped up using a smaller flip angle for the excitation pulse. This in effect reserves a net longitudinal magnetization ($M_o \cos\theta$) for the next pulse, while still providing

sufficient transverse magnetization for imaging ($M_o \sin\theta$). After multiple excitations, the magnitude of the transverse signal approaches a steady state value. For the FLASH pulse sequence, the steady state magnetization, M_{xy}, is [41, 42]:

$$M_{xy} = \frac{M_o(1-e^{-TR/T_1})}{1-\cos\theta e^{-TR/T_1}} \sin\theta e^{-TE/T_2^*} \tag{2.18}$$

Where TR is the repetition time and θ is the flip angle. The optimal angle of excitation, θ_E is determined from the Ernst equation:

$$\theta_E = cos^{-1}(-TR/T_1) \tag{2.19}$$

Where TR is the repetition time of the experiment, and T_1 is the longitudinal relaxation time for the tissue under investigation. With this technique, it is possible to reduce TR, and reach a steady transverse signal between successive excitation pulses. Often, the phase of the B_1 field is adjusted by an integer multiple of a prime-number angle (often 117°) between RF excitations [33] to reduce residual signal from prior excitations. This process is known as RF spoiling.

Flow compensation

A gradient echo occurs when the net phase accumulation of spins within a sample is zero radians [43]. The gradient echo has a maximum magnitude when all spins are stationary. However, in the case of flow, the magnetic environment experienced by a moving spin changes between excitation and acquisition. This results in a non-zero net phase accumulation and a loss of signal at the echo or ghosting artifacts if the flow velocity changes between acquisitions [43]. The goal is to refocus both stationary spins (zeroth order) and those flowing with a constant velocity (first order) at the center of the readout. This technique is referred to as flow compensation or gradient moment nulling (GMN) [33].

Flow compensation attempts to rephase all spins at the echo, whether they are flowing or not, and is performed individually for each logical gradient axes independently [33]. This is achieved by adding additional gradients, such that the higher order phase terms can be nulled at the echo [33]. The number of gradients is dependent on what order we wish to compensate for. For instance, first order

nulling (constant velocity) requires three gradient lobes. Nulling the second order term, for constant acceleration, requires four gradient lobes, and so on [33]. Flow compensation increases the minimum echo time available. Therefore, it is common to use only first order flow compensation in the clinic [33]. For the simple case of a constant velocity, flow compensation attempts to solve [43]:

$$\phi(x,t) = -\gamma \int_{t_1}^{t_2} G(t')[x(t') + vt']dt' = 0 \tag{2.20}$$

Where ϕ is the accumulated phase of the transverse magnetization, γ is the gyromagnetic ratio, G(t) is the time course strength of the gradient lobe, v is the velocity of the flowing spins and t_1 and t_2 are the times at which the flow compensation sequence begins and ends. The echo will form at the end of this sequence.

Flow compensation is generally performed in the slice or frequency-encode directions as the added scan times are much less than for the phase-encode direction [39]. This equation applies for all velocities, as long as it is constant. Higher order moment nulling (second order for acceleration) is possible with additional gradient pulses. However, they are rare in clinical imaging due to the longer echo times [33, 39].

A simple case for flow compensation is to use gradients of equal duration, and assume a perfect rectangular pulse (Figure 2.4). The gradients are played out simultaneously without a break between lobes. The duration of each lobe follows a binomial pattern: the first waveform has amplitude G and duration t, the second has amplitude -2G and duration t, and the third has amplitude G and duration t. For this series, the echo magnitude reaches its maximum as both the zeroth and first order phase accumulations equals 0 at the end of the third pulse.

This is only one specific solution to the problem. It is generally true that to perform GMN in the frequency encoding direction for order N, requires a minimum of N+2 gradient lobes with alternating polarity [33]. For shorter echo times, the gradient strength of the first two gradient lobes can be increased. GMN can only occur at one specific time, which is typically chosen at the peak of the echo.

In reality, the gradient lobes are trapezoids, rather than rectangles. The gradient moment nulling should be calculated for each section of the waveform: ramp up, plateau and ramp down. Further, first-order flow compensation is dependent on the

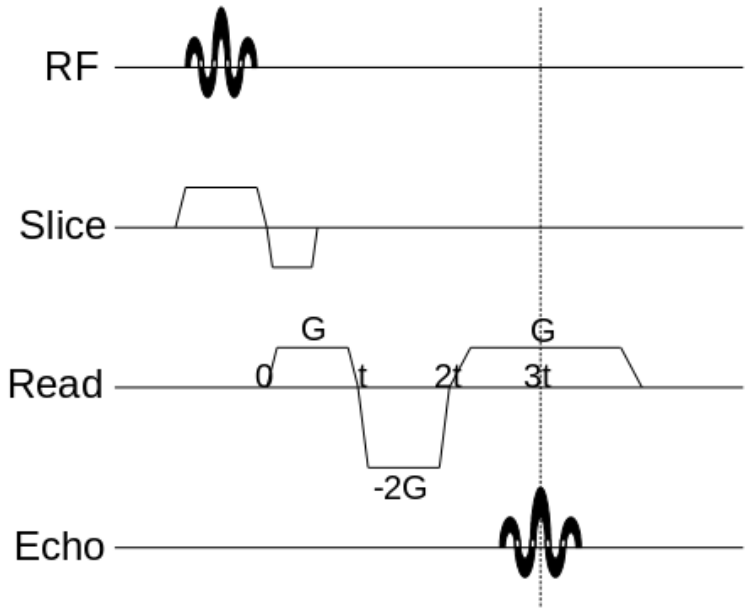

Figure 2.4: Example pulse program for flow compensation. This simple example has three pulse lobes, with alternating polarity and equal duration. At the time of the echo (3t), both the stationary and flowing spins have re-phased.

reference time (center of the readout window) and the delays between the gradient pulses. To simplify the calculations, the net phase accumulation from all gradients can be determined as though the gradient starts at time zero (Table 2.2), then apply a translation [33].

G is the strength of the gradient, τ is the length of the waveform, m_0 is the zeroth order moment and m_1 is the first order moment. Translations of the waveforms to a time $t' = t - \Delta t$ requires the corrections [33]:

$$\tilde{m_o} = m_o \tag{2.21}$$

Table 2.2: Accumulated Phase for Gradient Moment Nulling

Shape	G(t=0)	G(t=τ)	m_o	m_1
Ramp up	0	G	$\frac{G\tau}{2}$	$\frac{G\tau^2}{3}$
Plateau	G	G	$G\tau$	$\frac{G\tau^2}{2}$
Ramp down	G	0	$\frac{G\tau}{2}$	$\frac{G\tau^2}{6}$

$$\tilde{m_1} = m_o \Delta t + m_1 \tag{2.22}$$

Where $\tilde{m_o}$ and $\tilde{m_1}$ represent the zeroth and first order moment for the translated gradient lobes. One interesting property is that the first moment is translation invariant if and only if $m_o = 0$.

Scanning Parameters

The quality of an MRI image can vary dramatically, depending on the imaging parameters, pulse sequence used and other imaging options [39]. This section will briefly look at some of these parameters and how they affect the MRI image in terms of the total scan time, SNR or image contrast.

The size of the imaging matrix describes how many read or phase encode samples are taken. The matrix dimensions may be different in the read and phase encoding directions, depending on the imaging restraints. In general, the read encode dimension will be larger than the phase encode to reduce the total scan time. Exceptions include images that require an ultra short echo time or when geometric distortions, susceptibility effects or motion are an issue [39]. The SNR of the image is inversely proportional to the square root of the matrix size for a given field of view (FOV). Reducing one matrix dimension by a factor of 2 will double the pixel size and lead to an SNR improvement by a factor of 2. The spatial resolution is determined as the ratio of the FOV to the corresponding matrix size.

The FOV defines the spatial extents of the physical image. It may be defined for a 2-D or 3-D image, with the read encode direction typically referring to the larger dimension for rectangular images [39]. The SNR of the image is directly proportional to the FOV for a given matrix size. For instance, doubling the FOV in

one dimension, without chaging the matrix size, will improve the SNR by a factor of 2. However, it is important to select the FOV to cover the region of interest best, as a smaller FOV also provides better spatial resolution. The longer anatomical dimension is typically chosen to correspond with the read encoding gradient to avoid wrap-around artifacts [39]. To acquire data for an off-center FOV, the RF excitation pulse is adjusted to match the central Larmor frequency of the slice. The RF receiver frequency is also adjusted to accommodate this [33].

The strength of the gradient fields is calculated from the FOV, matrix size, slice thickness and relative timings of the pulse sequence.

2.4.1 Cartesian vs. Radial imaging

MRI data may be acquired following any trajectory imaginable. The two most popular techniques include Cartesian and radial sampling.

The first k-space trajectory used in MRI was projection acquisition by Lauterbur [44]. MR data is acquired as radial spokes originating at the center of k-space and radiating outward. Radial sampling is attractive as all spokes are equally important in the image reconstruction [45], all spokes cross the center of k-space (providing contrast information), motion/flow artifacts are suppressed [46, 47] and reducing the number of projections in the image reconstruction does not affect the spatial resolution - though the SNR does decrease. Radial acquisitions require longer scan times to satisfy the Nyquist criterion at the edges of k-space (up to a factor of $\pi/2$ at the edges of k-space for a square FOV). Alternatively, the data may be under-sampled in the angular direction; though this results in the presence of streaking artifacts [48].

Traditionally, radial MR images were constructed with either filtered back-projection, a technique borrowed from CT [49], or by regridding the data onto a Cartesian grid, so that the FFT could be applied [50]. The regridding problem is not intuitive to solve [51], and requires density compensation prior to appying the IFFT [52, 53]. Several new techniques have emerged recently that allow for image reconstruction with an under-sampled data set. This will be the focus of Chapter 5.

The more popular method is Cartesian sampling, in which the data is acquired as a series of parallel lines in k-space. Cartesian sampling has been studied more

extensively and holds several advantages over radial sampling. First, the total scan time can be greatly reduced using echo planar imaging (EPI). Though this sampling method produces ghosting artifacts, they are well documented and correction strategies have been proposed. Generally, imaging artifacts present in Cartesian imaging have known solutions - either preventative or post-processing. Another huge advantage is the ability to apply the FFT directly to the acquired data, thus significantly reducing the reconstruction times.

2.5 Contrast Agents

Contrast agents were first used in the 1980s and showed promise in angiographic studies. Schering was the first company to apply for a patent in 1981 for Gd-DTPA [54].

Observed contrast in MRI signal primarily results from changes in the proton density of tissue or the T_1 or T_2 relaxation time constants. The contrast agents generally used in DCE-MRI experiments are designed to enhance the contrast between normal and diseased tissue by changing the T_1 and T_2 relaxation time constants [55]. These contrast agents interact with the nuclear magnetic moment of protons in nearby tissue, resulting in a change in their phase or orientation with respect to B_o [5]. The interactions responsible for the changes in T_1 and T_2 will be discussed shortly.

A majority of contrast agents used in MRI are stable chelates of a paramagnetic metal ion, such as gadolinium, iron or manganese [5, 55, 56]. These ions contain unpaired electrons in the outer atomic orbits, which creates strong local magnetic fields [5]. Interactions of these fields with the nuclear magnetic moments in tissue selectively induce relaxation. In effect, the effective T_1 and T_2 relaxation time constants are reduced [2].

Low molecular weight agents – generally have molecular weights less than 1000 Da [4] and contain a variety of gadolinium-based agents (including Gd-DTPA) [3]. Due to their small size, these agents rapidly diffuse through vessel walls into the extravascular extracellular space [4, 57]. These agents are commonly used to study angiogenesis in tumours and to monitor the response to antiangiogenic therapy [3].

Gadolinium-based contrast agents have been studied most intensively to date and are commonly used in clinic [58]. Gadolinium ions have seven unpaired electrons in their outer orbit, which makes them the most paramagnetic ion [55]. It has been well established that the change in the relaxation rate (inverse of the relaxation time constants, i.e. $1/T_i$ where i = 1, 2) is directly proportional to the concentration of gadolinium within the region [55]. Assuming that the relaxation rates are known in the presence and absence of gadolinium, the concentration of gadolinium may be determined from the Solomon-Bloembergen equation [42, 59]:

$$1/T_i \;=\; 1/T_{io} + r_i[Gd] \qquad i \;=\; 1,2 \tag{2.23}$$

Where T_i is the relaxation time constant in the presence of a contrast agent, T_{io} is the relaxation time constant in the absence of gadolinium, r_i is the relaxivity of the contrast agent, and [Gd] is the concentration of Gadolinium. The relaxivity may be interpreted as the efficiency at which a paramagnetic ion enhances the relaxation rate of water protons [55]. It is a function of the magnetic field strength and the chemical structure of the agent [42]. The above relation has been verified in-vitro for T_1 and T_2^*, as well as in-vivo for T_1, over a range of concentrations [42]. Here, T_2^* is the transverse relaxation time due to molecular interactions and inhomogeneities in the magnetic field [5].

Changes in the T_1 relaxation rate results from the dipole-dipole interaction between the nuclear magnetic moments and the strong magnetic fields created by the contrast agent [55, 60]. T_1 enhancement effects are only observed in the vicinity of the contrast agent since the dipole-dipole interactions are weak. As a result, enhancement patterns in T_1-weighted images define the regions where contrast agent is present. T_1 enhancement patterns are most strongly observed in areas where there is a uniform distribution of the contrast agent [60]. T_1-weighted images will show an enhanced signal in regions containing the contrast agent [4, 58]. In contrast, changes in the T_2^* relaxation rate are due to susceptibility-induced gradient fields surrounding the contrast agent [60]. The induced fields cause long range magnetic field inhomogeneities, allowing for T_2^* shortening further away from the contrast agent [42]. The effects on the T_1 and T_2^* are complementary, though one often dominates over the other [60]. The T_1 effect is dominant in areas where the

contrast agent is uniformly distributed due to more close range interactions. While, the T_2^* effect is dominant when the contrast agent is compartmentalized as this increases the induced gradient field [60].

Safety concerns and toxicity of Gd-based CA

The unaltered Gd^{3+} ion is known to be highly toxic in humans as it interferes with the calcium channels and protein binding sites [61, 62]. The free ions accumulate in the liver, spleen, kidney and bones. Studies have shown that a 50% lethal dose of free Gd in mice is only 0.20 mmol/kg [61]. With these numbers, it is important to chelate the Gd ions with a larger compound that will limit tissue interactions. Gd forms stable chelates with both ethylenediaminetetraacetic acid (EDTA) and diethylenetnaminepentaacetic acid (DTPA) [63, 64]. Though dissociation in low pH environments is possible, this appears to occur in a very small number of cases [61].

The frequency of acute adverse reactions to Gd^{3+}-based contrast agents is about 0.07-2.4% with doses of 0.1-0.2 mmol/kg. Patients who have had a previous reaction are more likely (eight times greater than the general public) to have a second reaction. The second reaction is often more severe. Patients with allergies to other medications or food, or those with asthma, have a greater risk of a reaction [62].

Acute reactions generally occur within 1 hour of the injection. These range from mild to severe, with most being mild. Late reactions manifest as a skin reaction, and often occur between 1 hour to 1 week post injection. Very late reactions are due to unchelated Gd deposits in the extravascular space. These are most often experienced in patients with renal failure [62]. Use of Gd^{3+}-based contrast agents is not recommended for patients with renal malfunction, where incomplete excretion may be a concern. Studies have shown that a small fraction of these patients may have a serious adverse reaction (nephrogenic systemic fibrosis) to the contrast agent [61].

A more recent safety concern is disposition of gadolinium within the brain. A study by McDonald et al. [65] in 2015 discovered that patients receiving at least four gadolinium based contrast agent (GBCA)-enhanced brain MR examinations had 0.1-58.8 μg gadolinium per gram of neuronal tissue (capillary endothelium and

neuronal interstitium), in a significant dose-dependent manner. These patients all had normal renal function, and the findings were uncorrelated to age. The deposits show up as higher signal intensities of non-enhanced T_1-weighted images. Deposits are observed in a number of brain structures - particularly in the globus pallidus and dentate nucleus within the brain - as well as in the liver, skin and bone [66].

The type on GBCA (linear vs macrocyclic) can impact the quantity of deposits, with greater amounts deposited with linear-type agents [66]. Kang et al. [67] performed a study on multiple-sclerosis patients, receiving either nine (high-exposure) or two injections (low exposure) of a linear GBCA (both non-ionic and ionic) in the first year and an additional dose in the second year. The results showed a strong correlation with the dose, with the high-exposure cohort having enhancement in all regions evaluated, while the low-exposure cohort only had an increase in the dentate nucleus. The additional dose in the second year did not appear to affect the signal intensity in either cohort. Signal increases were greater in the high-exposure cohort when a linear non-ionic contrast agent (such as gadodiamide/Omniscan [66]) injection was administered compared to the linear-ionic contrast agents (such as godopentetate dimeglumine/Magnevist or gadobenate dimeglumine/Multihance [66]).

As of 2018, the effects of gadolinium deposits in the brain are still undetermined [68] and there is no clear evidence that adverse effects reported after administration of the contrast agent is connected with the deposits [66, 68]. The Canadian Association of Radiologist recommends that GBCA administration should be considered with respect to potential risks and benefits and follow the standard dosign guidelines, and that repeat injections should be avoided unless necessary [68]. The University of British Columbia (UBC) no longer allows the use of Omniscan in the clinic.

Chapter 3

Dynamic Contrast Enhanced MRI: Theory and Methods

DCE-MRI is a perfusion-based technique used to evaluate the microvascular structure and function of blood vessels in tissue [7, 8]. Early experiments were performed in the mid-1980s, though true perfusion weighting was not realized until tracer injections and data sampling on the order of seconds was possible. The technique involves the injection of a paramagnetic contrast agent - usually containing a transition element such as gadolinium, manganese or iron - into a peripheral vein and tracking its passage through the capillary bed [3]. By analyzing the biodistribution of the tracer, regions with abnormal vasculature are identified [7]. These regions are often associated with diseases, such as cancer[4, 69].

DCE-MRI operates on the premise that image contrast, caused by the presence of an injected contrast agent, correlates with the vasculature of various tissues [70, 71]. The behavior of the contrast media is monitored through the rapid acquisition of T_1 or T_2^*-weighted images during the first pass of the contrast agent through the tissue [72]. It is expected that any region with highly permeable vasculature or greater blood flow will enhance rapidly as the contrast agent passes through [4, 42]. Depending on the imaging sequence used, this enhancement will reflect an increase (T_1-weighted images) or decrease (T_2^*-weighted images) in signal intensity [60]. Based on the observed characteristics, semi-quantitative or quantitative parameters may be derived to characterize the vasculature [1].

This chapter will summarize the mechanisms for perfusion imaging (angiogenesis) and briefly discuss three common techniques: DCE-MRI, dynamic susceptibility contrast magnetic resonance imaging (DSC-MRI), and arterial spin labeling (ASL). The focus of the thesis is DCE-MRI, so the discussion will focus on this technique in greater depth. The remainder of the chapter will outline Pharmacokinetic (PK) modeling and discuss how physiologically relevant parameters can be derived from the data. But first, it's important to understand angiogenesis, a physiological process that allows us to differentiate healthy and abnormal tissue.

3.1 Angiogenesis

Angiogenesis is the process by which new blood vessels form from a pre-existing host vasculature [3, 69]. Experiments have shown that tumours cannot grow beyond a diameter of $2-3$ mm from the nearest blood supply due to oxygen diffusion limits in tissue [1]. Therefore, it is essential that the tumour develops a system of new blood vessels that will supply the newly developed cells with oxygen and nutrients [69]. This blood supply promotes further growth and metastases [1, 3].

The vasculature of healthy tissue is organized into a system of arteries, capillaries and veins [4, 69]. These vessels are highly efficient in supplying the surrounding tissue with essential nutrients [69]. To promote survival of the tissue, these vessels are highly organized and uniformly spaced, such that metabolites can reach all cells through passive diffusion [5]. We can characterize the vasculature with parameters that describe the mass blood flow, vessel wall permeability and tissue volume fractions [5].

Cancers are known to proliferate rapidly. This requires that new vasculature forms to supply the new cells with nutrients for survival and further growth [73–75]. Due to the temporal demands of rapid growth, the array of angiogenic vessels are disorganized, irregular, fragile, tortuous, have highly permeable walls, and chaotic flow patterns [1, 58]. When compared to healthy tissue, distinct differences are observed related to blood flow and accumulation in the tissues [4]. Scientists can exploit these differences to evaluate the health status of the tissue.

Figure 3.1 illustrates the difference between the vasculature in normal tissue and in a tumour. Angiogenic vessels exhibit large gaps between endothelial cells,

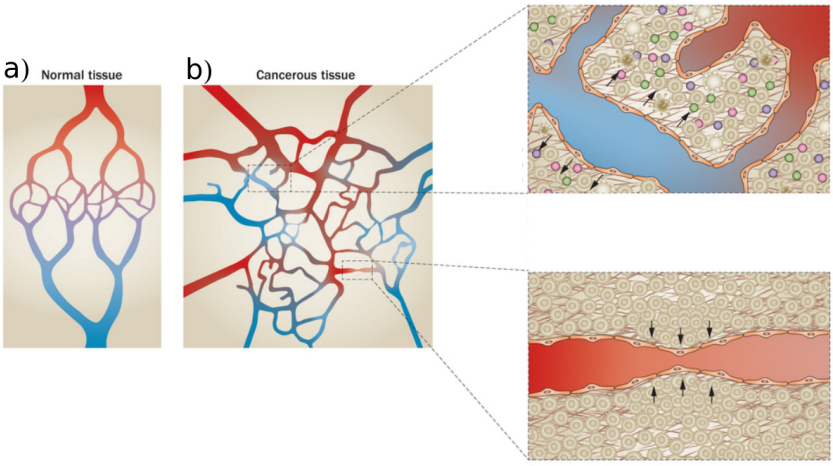

Figure 3.1: Part a) shows the vascualture of healthy tissue. Blood vessels are organized and uniformly distributed. Part b) shows the vasculature of a tumour resulting from angiogenesis. The blood vessels were rapidly developed, meaning that they are tortuous, disorganized and leaky. When a contrast agent is present in the blood plasma, it can perfuse into the interstitial space of the surrounding tissues more rapidly in a tumour. This causes a diffential enhancement pattern between tumour and healthy tissue. DCE-MRI exploits this difference to characterize the health status of tissues. Figure taken from Emblem et al. [76]. Permission for use has been granted from Nature and from Dr. Kyrre Emblem.

within the endothelium and discontinuous basement membranes [3, 69]. As a result, contrast agents perfuse more readily through the vessel walls compared to healthy tissue [3]. This allows us to characterize tumours.

The microvascular density (MVD) (average number of vessels within a small region of tissue) is commonly used to assess angiogenesis in tissue [3, 4, 10]. It has high correlations with the agressiveness of several cancers [77], patient survival and risk of metastases [3]. However, the measurement is invasive as a sample of the tumour is removed, stained and examined by light microscopy [78]. and it does not provide information about blood flow or the hyper-permeability of the vessel walls. DCE-MRI provides a non-invasive alternative that reveals information about the functionality of the vasculature.

3.2 Methods of Imaging Perfusion

Perfusion is defined as the delivery of arterial blood to the capillary bed [79]. Perfusion can be measured from the change in MR signal induced by a contrast agent from a series of rapidly acquired MR images [79]. Perfusion imaging generally falls into one of three categories of scans: DSC-MRI, DCE-MRI and ASL. All three techniques acquire rapid MR images before and after introduction of the contrast agent. The contrast agent is administered through an injection for DSC-MRI and DCE-MRI, and is referred to as a bolus. In the case of ASL, the contrast agent is magnetically labeled blood.

Dynamics Susceptibility Contrast Imaging

Dynamic Susceptibility Contrast Imaging (DSC-MRI) utilizes an exogenous tracer which is injected into a peripheral vein. This technique is used primarily in the brain and looks at signal intensity losses in T_2^*-weighted images. The T_2^* effect is much stronger for intravascular tracers, but suffers from quantification issues if the tracer extravates into the interstitial space as the T_2^* contrast drops significantly [79]. For this reason, DSC-MRI is usually restricted to cases where the contrast agent is compartmentalized. Though most applications are associated with brain imaging [60], DSC-MRI can be performed anywhere in the body.

A blood-pool contrast agent works best as the susceptibility effect extends beyond the vascular space, resulting in a transient signal drop [60]. Since the bolus injection will pass through the tissue in a couple seconds, a fast imaging technique - such as EPI or Fast Low Angle SHot (FLASH) - is used. The temporal resolution of the scans is dictated by the transit time of the bolus through the tissue, and typically a repetition time (TR) of less than 2 s is required [60].

Dynamic Contrast-Enhanced MRI

DCE-MRI is similar to DSC-MRI since an exogenous tracer is used, but it quantifies the change in local T_1. DCE-MRI is by far the most common method for studying perfusion and has applications throughout the body [79]. There has been wide-spread applications in tumour imaging as the angiogenic vessels allow the contrast agent to freely perfuse into the surrounding interstitial space [42].

T_1 interactions are short range and cause an increase in MR signal in a T_1-weighted image. The concentration of agent within the tissue may be deduced from the relative change in local T_1, in which the change in $1/T_1$ and concentration are linearly related [42]. This requires that a high-quality pre-injection T_1 map be acquired in addition to the dynamic T_1-weighted image series. Popular imaging sequences are EPI or turboFLASH, with a temporal resolutions of a few seconds.

DCE-MRI is more sensitive to the leakage of contrast agent into the interstitial space [80]. Low molecular weight contrast agents, commonly used in the clinic, readily perfuse from the vasculature into the interstitial space during the first pass. This is especially prevalent in cancers. In contrast to DSC-MRI, information about vessel permeability can be determined from the slow component of the concentration-time curve in the tissue of interest [79].

Arterial Spin Labeling

Arterial Spin Labeling (ASL) also measures perfusion. It is a competing technique with DCE-MRI, though it is primarily performed to measure blood flow in the whole brain [81] and quantifies absolute cerebral blood flow [82]. ASL avoids the injection, and instead uses tissue water as an endogenous tracer [79]. This makes the technique completely non-invasive [22], and allows for repeat measurements.

The technique may be thought of as an inversion recovery experiment, followed by rapid MR imaging of the tissue of interest. A RF pulse excites the arterial blood located upstream of the tissue of interest. This inverted signal (or 'labeled blood') acts as a temporary contrast agent [22]. The lifetime of the labeled blood is dependent on the T_1 relaxation time of blood, ranging between $1300 - 1750$ ms at clinical field strengths.

After a delay to allow the blood to reach the tissue of interest (TOI), labeled MR images are acquired which contain a mix of signal from the labeled blood and static tissue water [81]. ASL is a differential technique that compares images with and without the labeled blood signal [22]. Any change in tissue magnetization is attributed to perfusion of the excited blood protons into the surrounding tissues. The difference in signal is only a couple percent, so the experiment is performed multiple times to enhance the SNR [22].

3.3 Methods: DCE-MRI

The pioneering experiments on perfusion acquired a single snapshot image of the region of interest post-injection. Though this provided information about the contrast agent distribution, it did not yield any functional information about biological tissue [7]. As faster imaging techniques were developed, analysis across a series of dynamic images became possible.

DCE-MRI operates on the premise that image contrast, caused by the presence of an injected contrast agent, correlates with the vasculature of various tissues [70, 71]. Typical contrast agents contain a paramagnetic ion, such as gadolinium (Gd-DTPA, Gd-DOTA) or manganese ($MnCl_2$, $MnL1$ [83]), though iron oxides can be used as well [75].

DCE-MRI data is acquired with a fast imaging technique before, during and after the rapid administration of a contrast agent (usually gadolinium-based) [57, 69, 84]. Each image provides information of the time-resolved distribution of the contrast agent in the tissue of interest[7, 85]. By analyzing these images, information regarding tissue physiology and pathology may be extracted. This includes the size of the extravascular space (EES), vessel wall permeability and the surface area of the vessel [5, 42].

Three sets of images are acquired in a DCE-MRI experiment [8]. These include the localizer image, pre-contrast T_1-weighted images, and rapid T_1-weighted images acquired before, during and after the contrast inject.

Localizer Images

The localizer images pinpoint the exact location of the region of interest (i.e. tumour) and provide anatomical information. The DCE-MRI slices can be positioned and properly aligned from these images.

Pre-Contrast T-1 weighted images

The pre-contrast images provide a baseline T_1 prior to the injection. The T_1 relaxation time constant can be estimated with an inversion recovery (IR) or saturation recovery (SR) (slow) method, the Look Locker technique or using a variable saturation method, such as gradient echo images with variable flip angles [42]. Though

IR or SR techniques are arguably the most precise methods for estimating T_1, they are time consuming [42]. The Look-Locker technique is a faster method than IR and SR, as it acquires T_1 maps with a single inversion pulse [86]. The T_1 map is often calculated on a per-pixel basis [5]. The pre-injection T_1 times should be acquired with high accuracy, as they are used to estimate the post-injection T_1 times.

IR involves flipping the magnetization by 180°, waiting a variable delay of time, then applying a 90° pulse to flip the magnetization into the x-y plane. The magnitude of the signal is then plotted against the delay time. The T_1 relaxation time is calculated by fitting an exponential curve to the MR signal. The measurement is typically performed with two or three inversion times [87], though more repetition times will improve the accuracy at the cost of longer scan times.

SR is a faster method of estimating the tissue T_1 than IR. The technique involves multiple 90° RF pulses at relatively short repetition times, and measuring the signal intensity for multiple saturation times. A spoiler gradient pulse dephases the residual longitudinal magnetization that remains after the excitation pulse. In 2017, Wang et al. [88] developed a saturation-inversion-recovery (SIR) sequence that measures T_1 times with sharper T_1 resolution than from IR or SR individually.

The Look Locker technique provides a fast and efficient method for estimating the T_1 map [86]. The technique begins with a 180° inversion pulse, then applies a series of small angle excitation pulses at a variety of well known inversion times [89]. Since the angles are small, signal loss along the -z-axis is minimal. The scan is repeated after a period longer than $5T_1$, such that the magnetization has fully recovered. From the acquired data, MR images are produced with varying inversion times. One limitation is that the RF pulses used to acquire the data can affect the longitudinal magnetization, which results in a faster decay rate, termed T_1^*-weighting. This weighting is specific to the pulse sequence. The T_1-map is determined by fitting a smooth curve to the real signal, S ($S = A \cdot e^{-t/T_1^*}$), then performing the correction described in Taylor et al. (2015)[89].

The variable flip angle (VFA) technique is more widely used as it applies to spoiled gradient recalled echo (SPGRE) scans (also known as FLASH). The T_1-weighting is provided by the flip angle and repetition time. Data is acquired for multiple flip angles. T_1 is then determined by fitting a non-linear curve to the signal intensity vs flip angle.

Dynamic Contrast-Enhanced Images

The third set of images is the dynamic scans. These are heavily T_1-weighted images, and acquired rapidly (every $2-15$ s) [69] for at least $5-10$ min. However, there is a trade off between acquiring data rapidly and acquiring images with a higher spatial resolution or tumour coverage [90, 91]. Depending on the goals of the study and tumour model used, some groups will sacrifice the temporal resolution to obtain high quality images [92].

A majority of DCE-MRI experiments use a spoiled GRE pulse sequence. Common protocols are EPI or turboFLASH, which is a T_1-weighted gradient echo (GE) saturation recovery (SR) or inversion recovery (IR) snapshot [4, 42, 69, 79]. These sequences acquire data rapidly, provide sufficient temporal and spatial resolutions, and has a good SNR ratio [5]. Typical spatial resolutions are $100-625$ μ m in preclinical studies in mice ($30-40$ mm FOV length with 64-256 pixels) [15, 93–98] and $0.5-4.0$ mm for in-vivo studies in humans (3.0 T) [99].

To maximize T_1 contrast in the DCE images, the echo time is set to its minimum value (generally $1-2$ ms) [79]. Other pulse parameters, such as the repetition time or flip angle, are then optimized for the desired SNR and temporal resolution. For the case of a FLASH experiment, a flip angle of $30-60^o$ [79] is generally used, as it offers a good balance of SNR and temporal resolution.

A simple DCE-MRI protocol acquires a single proton density weighted image prior to the injection, followed by heavily T_1-weighted MR images for the rest of the experiment [42]. The flip angle is set to a small value for the proton density image, and larger for the T_1 images. repetition time (TR) is short to achieve good T_1 contrast and to allow for a higher temporal resolution.

The concentration of contrast agent within the tissue is estimated from the relative change in MR signal or inverse T_1 relaxation time [42]. In the case of a FLASH experiment, the change in local T_1 is determined from a ratio of the signal intensity from a dynamic MR image and the proton density image. Figure 3.2 shows the T_1-weighted images pre and post-injection, as well as the Look-Locker T_1 map. The Look-Locker map is derived from images with a variety of IR times, and allows for the calculation of the concentration of contrast agent in the tissue of interest.

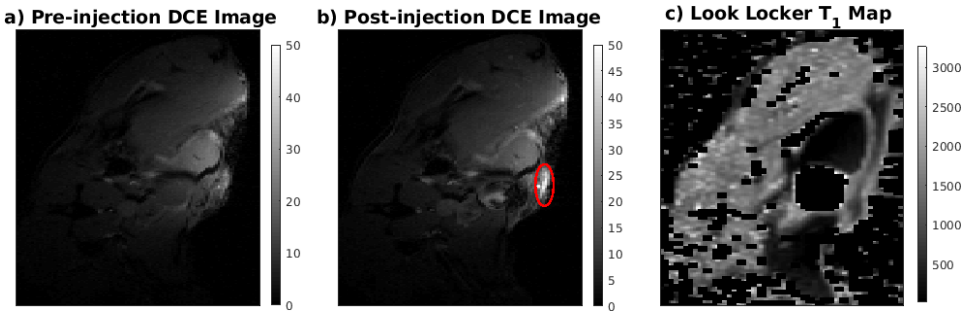

Figure 3.2: T_1-weighted DCE images a) pre and b) post-injection and c) the Look-Locker T_1 map used to calculate the concentration of contrast agent in the tissue of interest. Tissue enhancement is observed within the region outlined in red.

3.3.1 Considerations for Setting up a DCE-MRI Scan

Depending on the maximum expected concentration of contrast agent in the tissue, the signal intensity or T_1 relaxation time may be used for quantification. It is often assumed that the change in the signal intensity is linearly related to the concentration of contrast agent in a small region [8, 91], but is only true at low concentrations [4]. If higher concentrations are expected, it is advantageous to study changes in the relaxivity ($1/T_1$) of the tissue of interest as this parameter correlates directly with the concentration of contrast agent [42].

The relative difference in T_1 is dependent on the native T_1 constant pre-contrast (T_{1o}). In effect, the magnitude of the change is greatest in tissues with larger pre-contrast T_1 values [84]. The change in the T_1 relaxation time constant is converted into a concentration with [42]:

$$1/T_1 = 1/T_{1o} + [CA] \cdot r_1 \tag{3.1}$$

Where T_{1o} and T_1 are the pre and post-contrast relaxation time constants, [CA] is the concentration of the contrast agent, r_1 is the relaxivity of the contrast agent, defined at a particular B_o strength and temperature.

There is a trade off between acquiring data rapidly and acquiring images with a high spatial resolution [90, 91]. Ideally, the DCE data should be acquired with a temporal resolution exceeding the most rapid changes in the tissue [42, 91]. Tissue

coverage and spatial resolution, however, are both sacrificed with high temporal resolution scans [5]. Depending on the goals of the study, some groups choose to sacrifice the temporal resolution in favour of acquiring higher-spatial resolution images to observe heterogeneity in a lesion [92]. Additionally, the temporal resolution must be relaxed when the region of interest is large or when a main artery (used for the AIF estimate) is far from the tissue of interest [5, 42]. If the AIF will be measured, the temporal resolution should be on the order of a second to capture the rapid contrast kinetics in the blood [42]. Conversely, experiments investigating tumour heterogeneity with a semi-quantitative analysis can relax the temporal resolution in exchange for improved spatial resolution [5].

The temporal resolution for DCE-MRI studies are typically on the order of seconds [8, 69], though some groups have relaxed this requirement and used a temporal resolution of 10-30 seconds for higher quality images [5]. The spatial resolutions are typically $100-625\ \mu$m in pre-clinical studies in mice ($30-40$ mm FOV length with 64-256 pixels) [15, 93–98] and $0.5-4.0$ mm for in-vivo studies in humans (3.0 T) [99].

The duration of the scan varies depending on the desired form of analysis. Perfusion weighted scans in human may be acquired in approximately 1 min, while permeability weighted scans require approximately 5 min [79]. The scan duration is typically longer in mice [95, 100, 101]. Studies that wish to investigate the tumour heterogeneity are recommended to favor a higher spatial resolution at the expense of temporal resolution [5].

The change in T_1 in blood and tissue can vary greatly. It is expected that the T_1 of blood may decrease by an order of magnitude at typical clinical doses [102]. Conversely, the change in tissue T_1 can be much smaller [42]. The chosen pulse sequence should have good T_1 sensitivity and dynamic range to capture both changes accurately.

3.3.2 The Contrast Agent Injection

DCE-MRI investigates signal enhancement in T_1-weighted images, induced by an exogenous contrast agent [82]. The bolus of contrast agent is injected into a peripheral vein through a catheter injection. This can be the antecubital in humans,

or the jugular or tail in rodents [5].

Typical contrast agents used in DCE-MRI contain a paramagnetic ion, such as gadolinium (Gd-DTPA, Gd-DOTA) or manganese ($MnCl_2$, MnL1 [83]), though iron oxides have been used as well [75]. Paramagnetic ions contain unpaired electrons that interact with the protons in tissue, causing a reduction in their T_1 and T_2 relaxation times [60]. The magnitude of each effect will categorize the contrast agent into T_1 or T_2 agents, where a T_1 agent has a greater relative effect on the T_1 relaxation time [62]. Most rapid imaging sequences provide greater T_1 contrast, and so a T_1 agent is often used [5, 103].

Conventional contrast agents have concentrations of $0.5-1.0$ M. They are commonly administered to a dose of 0.1 mM/kg body weight. Typical injection protocols in mice involve injecting the bolus $10-20$ s after the start of the scan to allow for pre-injection data to be acquired, and following it with a $20-30$ mL saline flush [79]. The injection is often performed with a power injector to ensure a reproducible injection between studies [69].

The contrast agent only occupies the plasma component of blood [104]. The concentration of contrast agent in the plasma space, C_p, is directly related to that found in the blood, C_b, by:

$$C_p = C_b/(1-Hct) \tag{3.2}$$

Where Hct is the hematocrit, which describes the fractional volume of red blood cells in blood [105]. Generally, a value between 0.4-0.45 is assumed; but this may not be valid in advanced cancers, and is lower in the capillaries [104, 106].

Following injection, the contrast agent circulates freely throughout the vascular plasma space, and diffuses into the interstitial space of surrounding tissue where it interacts with the proton spins of the tissue causing a signal increase in T_1-weighted images. After several hours, the agent is excreted from the body through the kidneys [4]. By analyzing the concentration-time curve in a tissue of interest, perfusion parameters (quantitative or semi-quantitative) can be extracted [104]. As a result of the contrast dynamics, the tissue signal will increase rapidly initially, peak, then slowly return to its baseline value [72].

3.4 Data Analysis

The analysis of DCE-MRI data is based on the principles of tracer kinetics, which describes how blood is transported through the tissue of interest [79, 80]. There are two dominating phenomena that occur simultaneously [107]: the first is the rapid perfusion of contrast agent into the microcirculatory network, and the second is related to the accumulation and slow release of contrast agent from the interstitium. DCE-MRI data attempts to extract meaningful parameters related to the health status of the tissue. The analysis may be quantitative or semi-quantitative.

Semi-quantitative analysis is simple and may be performed quickly. It has applications in characterizing tumour growth and tracking its response to treatment [5]. Semi-quantitative analysis studies the shape of the AIF [7]. It takes place over the first pass of contrast agent through the vasculature [104], which describes the time period beginning with contrast administration and covers a few cardiac cycles [4, 104].

The analysis attempts to derive information about the onset time, peak enhancement, maximum rate of enhancement, gradient of peak enhancement or washout and the signal enhancement ratio from these regions [7, 69]. The simplicity of the analysis, however, comes at the cost of limited physiological information. These descriptors contain information about blood flow, blood volume, contrast agent leakage and v_e, though the contribution of each cannot be distinguished [8]. Further, the reproducibility of the results between trials (within and between institutes) is a major concern [7]. Semi-quantiative parameters have been shown to be dependent on the initial conditions [5, 69], and may not accurately reflect the concentration of contrast agent in the tissue of interest [4]. Some groups choose to calculate the initial area under the enhancement curve (IAUC) [4] as this metric appears to be more reproducible.

Quantitative analysis is preferred by the majority and will be the focus of the remainder of this chapter. Quantitative analysis studies the distribution of contrast agent within the tissue of interest and its elimination from the body, through PK modeling [5]. The chosen PK model provides physiologically relevant parameters by fitting a mathematical model to the time course signal change within a tissue of interest. Most models will include the enhancement characteristics in a blood ves-

sel feeding into the tissue of interest as an input parameter [60]. Theoretically, the derived parameters should be minimally dependent on the injection mode and the patient's physiological status [107], therefore allowing for inter and intra-patient comparisons.

To quantify the observed contrast kinetics, the tissue must be divided into well established regions known as compartments [104]. Most models assume that the contrast agent distributes uniformly throughout the entire compartment for simplicity [5]. Depending on the chosen model, the tissue may be represented with three or four compartments [104], which includes the vascular plasma space, the extravascular extracellular space (EES), the intracellular space, and microscopic tissue components such as cell membranes or fibrous tissue. Often compartments 3 and 4 are grouped together to simplify the model. These compartments may be characterized by their fractional volumes, such that:

$$v_p + v_e + v_i = 1 \qquad and \qquad v_p = (1 - Hct)v_b \tag{3.3}$$

Here, v_p, v_e, v_i and v_b are the fractional volumes of the vascular plasma space, EES, intracellular space and whole blood space respectively, and Hct is the hematocrit.

A majority of contrast agents used in DCE-MRI cannot pass into the intracellular space due to their size, inertness and non-lipophilicity [104]. For this reason, compartments 3 and 4 are often not considered in the analysis of DCE-MRI data. The resulting model is known as the two compartment model. The next section will discuss two popular models used in DCE-MRI studies.

3.4.1 Pharmacokinetic Modeling

PK model parameters describe physical properties of the vessels [108], including blood flow and vessel wall permeability [57]. These may be used to identify the presence of abnormal vasculature [8], such as that observed in tumours [4]. DCE-MRI data is typically characterized with three parameters. The names may vary, depending on the application of the model being used [57], though v_e, K^{trans} and k_{ep} are considered the standard.

v_e is the fractional volume of the EES per unit volume of tissue. It is assumed

to be equal to the space filled by the contrast agent [4]. It is approximately 0.2 - 0.5 in tumours [57].

K^{trans} is the volume transfer constant from the plasma to the EES. It determines the amplitude of the initial response to injection and is calculated from the absolute value of the contrast agent concentration [1]. K^{trans} describes the combination of the endothelial permeability and surface area product, PS, and blood flow, F, to the region [1, 57, 69]. Interpretation of K^{trans} varies depending on the relative contributions from blood flow and tissue permeability, though these components are difficult to separate [8]. It is well established that tumours have high K^{trans} (high permeability and blood flow) [69], while necrotic regions in tumours have small K^{trans} as they have limited blood flow [4].

k_{ep} (= K^{trans}/v_e) is the flux rate constant from the EES to the plasma. It characterizes the rate at which the contrast agent returns to the intravascular space. It is always greater than K^{trans} since v_e is less than 1. The value is generally on the order of minutes to hours [4]. k_{ep} may be determined from the shape of the concentration-time curve.

These parameters act as probes for monitoring tissue status [109], and have shown applications in differentiating malignant from benign tumours, tumour staging and monitoring treatment response. The difference can be subtle, therefore it is essential to acquire high quality data. In fact, several studies have demonstrated that the sensitivity and specificity of DCE-MRI analysis is directly correlated to the accuracy of the fitted PK model parameters[11, 14, 17, 110–112]. The AIF is known to have a dramatic impact on parameter accuracy, making it imperative that a high-quality measurement is obtained [11]. It is therefore suggested to measure the AIF for each experiment [14], including those performed on the same patient multiple times [108].

Two-compartment model

Most pharmacokinetic (PK) models are based on the two compartment model [1, 3], in which the vasculature comprises one compartment, and the extracellular extravascular space (EES), v_e, of the tissue of interest represents the second [110]. It assumes that contrast agent flows readily between the two compartments [1, 57],

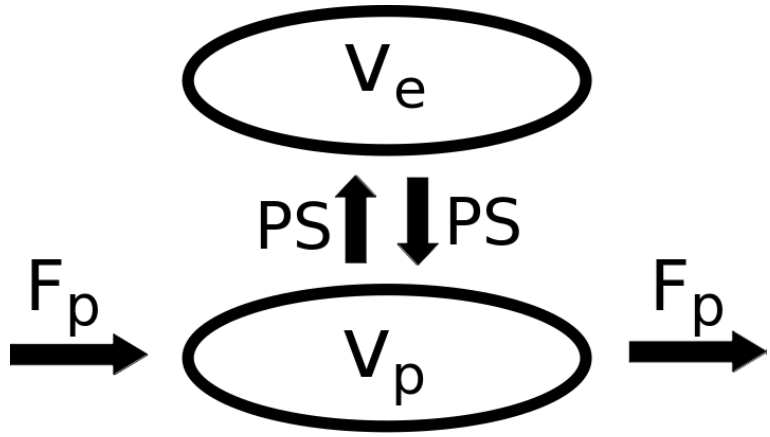

Figure 3.3: Pictorial representation of the two-compartment model. v_e is the volume of the extracellular extravascular space, v_p is the plasma volume within the vessel, PS is the permeability-surface area product relating the rate at which the contrast agent travels between the two regions, and F_p is the plasma flow rate.

with the rate of diffusive transport dependent on the concentration of agent in the two compartments and the permeability of the vessel walls [104]. In addition, the model assumes that the contrast agent is well mixed within each compartment (i.e. uniform distribution) [5]. A pictorial representation of the two-compartment model is shown in Figure 3.3 [113].

Tofts Model

The model proposed by Tofts and Kermode [114] in 1991 offers a simple assessment of the tissue vasculature, and has become the foundation for more complicated PK models [113, 115]. It is important to note that Seymour Kety [116] derived similar equations for the exchanges of inert gases at the lungs and tissue, though Tofts and Kermode were the first to apply the concepts to MRI. The Tofts model, figure 3.4, has the following functional form:

$$C_t(t) \;=\; K^{trans} \int_0^t C_p(t') e^{-K^{trans}(t-t')/v_e} dt' \tag{3.4}$$

Where C_t is the concentration of contrast agent in the tissue, C_p is the con-

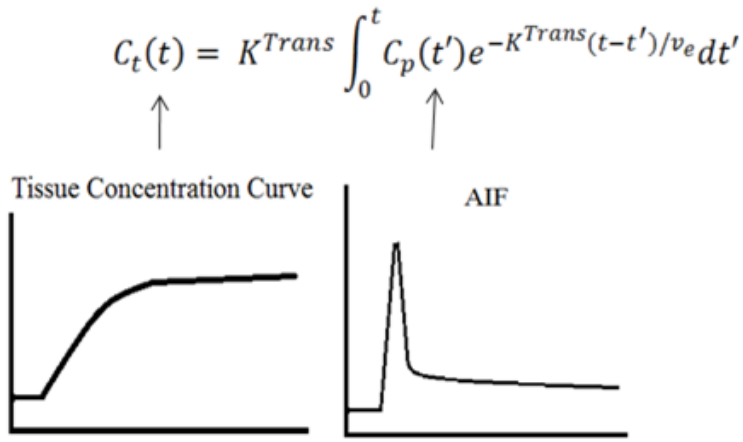

Figure 3.4: The model propsed by Tofts et al. (and various extenstions of it) is one of the most commonly used PK model for analyzing DCE MRI data. The model requires that the concentration-time curves in the tissue of interest, $C_t(t)$, and blood plasma, $C_p(t)$ or AIF, are known. The accuracy of the physiologically relevant perfusion parameters - K^{trans} and v_e - are dependent on the quality of these curves. The AIF needs to be sampled with a high temporal resolution to capture the rapid contrast changes in the blood following the injection.

centration in the blood plasma, K^{trans} is the volume transfer constant relating the rate at which the contrast agent perfuses from the vasculature to the tissue, and v_e is the fractional volume of the EES. These parameters describe physical properties of the vessels [108], and may be used to identify the presence of abnormal vasculature [8], such as that observed in tumours [4].

Model Fitting using the AIF and Tissue C-t Curve

Quantitative analysis involves fitting a PK model to the concentration-time curves [4, 8, 69]. From the fit, physiological parameters, describing the blood flow to the region, and the passage of contrast agent between the plasma space and EES, may be determined [69].

Typical physiological parameters include the blood flow (perfusion), vessel wall permeability, vessel surface area, intravascular and extravascular extracellu-

lar volume fractions [4, 5]. These parameters are independent of the acquisition procedure and only describe tissue properties [8]. Pharmacokinetic (PK) models are concerned with contrast agents that readily diffuse across the vessel walls and remain extracellular [57]. Numerous models may be found in the literature.

The accuracy of the model fit is highly dependent on the quality of the plasma concentration-time curve - often referred to as the AIF. This will be the topic of the next chapter.

Chapter 4

High Temporal Resolution AIF Measurement using the Phase of MR Projections

4.1 The Arterial Input Function

DCE-MRI exams involve the injection of a contrast agent and tracking its distribution within a tissue of interest. Summary parameters, estimated from the images, are known to be dependent on cardiac output, arterial status, injection rate and tissue properties [82]. Even though it is possible to control the injection volume and rate, it will not guarantee that the bolus leading into the tissue of interest will have the same shape. The bolus must first pass through the heart and lungs before being redistributed around the body, which causes it to disperse as it enters the tissue of interest through an artery. If the shape of the incoming bolus is known, information about the microvascular structure of the tissue may be derived. Knowledge of the bolus kinetics (maximum concentration, width, etc.) is especially important when quantitative tissue parameters, such as blood flow or perfusion, are desired.

The AIF describes the time-course concentration of a contrast agent in an artery supplying the tissue of interest [7, 8, 117]. Together with the concentration-time curve within the tissue of interest (TOI), physiological parameters related to tis-

sue perfusion, vessel wall permeability and the volume of the EES, v_e, may be estimated through pharmacokinetic modeling [2]. The AIF is defined in the blood plasma space, not within the whole blood (equation 3.2). The conversion factor between the two spaces is known as the hematocrit (Hct), with typical values ranging between $0.40 - 0.45$ [104].

The earliest known measurement of an AIF was in 1991 by Bruce Rosen and colleagues [118]. In their study, they measured an AIF in the middle cerebral artery of a hypercapnia canine model, using a 1 s single-shot EPI experiment, and compared it with blood samples taken directly from the femoral artery. The results showed good agreement between the two techniques, which suggested that the AIF could be measured non-invasively. Later in 1992, Perman et al. developed a dual-FLASH pulse sequence that allowed for simultaneous AIF and DSC measurements in the neck and brain, respectively [119]. Then in 1996, Fritz-Hansen et al. [102] published a study that confirmed that MRI could be used to non-invasively measure the AIF in the descending aorta. They used an inversion recovery turboFLASH scan and validated their measurement with direct blood samples.

The quality of the AIF can have a significant impact on the accuracy of the modeled parameters [14, 17, 111, 112]. Therefore, the AIF should be sampled with a sufficient temporal resolution and within an artery supplying the region of interest [13, 108]. This can be challenging in situations where a major artery is located far from the imaging site [10] or when partial-volume effects (PVE) affect the concentration measurement within small supplying arteries [120]. The vessel selected for the AIF measurement will depend on the goals of the study [82]. If bolus dispersion is a concern due to major arterial abnormalities - such as a stenosis - then a smaller vessel closer to the tissue of interest is used. Otherwise, a larger vessel further from the site may be the better option to avoid partial volume effects (PVE).

The situation is further complicated when imaging small animals, such as mice, due to their small body size[14, 15] and rapid heart rate [13, 16]. In addition, few vessels in the mouse are of sufficient size to measure the AIF with adequate temporal and spatial resolutions. AIF measurements in mice are often performed in the left ventricle [13, 15, 19, 94, 121], aorta [100], iliac artery [100] or tail vein [20] as these are the largest vessels.

The AIF is known to vary widely due to variations in the contrast injection, cardiac output and blood supply to the tissue of interest between patients [110]. Therefore, it is recommended that the AIF be acquired for each experiment [14, 117], including studies performed on the same patient multiple times [108]. It is, however, technically difficult to acquire the AIF when an acceptable vessel is not present in the imaging field of view [18].

To combat this, multiple groups choose to use a population averaged AIF from the literature [17–19] in their analysis. Even though the population averaged AIF is expected to approximate the true curve, it does not account for inter [13] or intra-individual [5] differences. Nor does it reflect the blood flow to the tumour at the time of the examination [8]. Despite these limitations, the population averaged AIF provides a reasonable estimate when a high temporal resolution is not possible or when a major artery is far from the imaging plane. Care must be taken, however, as the population averaged AIF may only be accurate for a particular pathology [109], specific injection protocol, contrast agent dose and strain of animal.

Two commonly used AIFs in the literature are those proposed by Lyng et al. (mice) [19] and Parker et al. (human) [18].

Population Averaged AIF in Mice by Lyng et al.

One of the more popular population-averaged AIFs in a mouse was published by Heidi Lyng and her team in 1998 [19]. In their study, an amelanotic human melanoma xenograft (A-07 or R-18 cell line) was implanted on flanks of female BALB/c-nu/nu mice of 8-10 weeks old. A bolus of contrast agent (Gd-DTPA) was administered through the tail vein at a constant rate for 5 s duration. The contrast agent had a stock concentration of 0.5 M, and was diluted to 0.03 M with a 0.9% NaCl solution. The injection dose was set to 0.01 ml/g body weight.

Imaging was performed with a 1.5 T Signa whole body tomograph. The AIF was determined from the left ventricle of three separate mice using a T_1-weighted spoiled gradient-recalled sequence with $TR = 50$ ms, $TE = 6$ ms, flip angle = 80° and temporal resolution of 13 s for a total scan duration of 10 min.

Lyng fit a double exponential to the mean concentration-time curve (determined from the relative signal intensity increase), $C_a(t)$, in the left ventricle of

three mice. The functional form is:

$$C_a(t) = Xe^{-xt} + Ye^{-yt} \tag{4.1}$$

Where x, y, X and Y are the fitted constants with values of 2.4 $\pm$ 0.9 min^{-1}, 0.04 $\pm$ 0.02 min^{-1}, 291 $\pm$ 111 mM and 98.6 $\pm$ 3.4 mM, respectively. They used this fitted curve in their analysis rather than the experimental data to minimize noise fluctuations.

Population-Averaged AIF in Humans by Parker et al.

Parker et al. provide a widely used population-averaged curve in humans [18]. In this study, 23 male patients with advanced cancer and demonstrating abdominal or pelvic masses were scanned four or five times for a total of 113 visits. The first two visits were to assess reproducibility of the pharmacokinetic parameters, while the remaining three visits ($N = 67$) were used to calculate the population-averaged AIF.

MR images were acquired on a 1.5 T Philips Intera system with a whole-body coil for transmission and signal reception. The baseline T_1 was determined using three axial spoiled gradient echo scans with flip angles of 2°, 10° and 20°, and four signal averages. The DCE-MRI experiment involved 75 consecutively acquired axial volumes with a flip angle of 20° and temporal resolution of 4.97 s. All scans had 25 slices, $TR = 4.0$ ms and $TE = 0.82$ ms.

A standard dose (0.1 mmol/kg of body weight) of Omniscan 0.5 mmol/ml (Gd-DTPA-BMA; gadodiamide Nycomed) was injected intravenously through the antecubital vein using a power injector at a rate of 3 ml/s. The injection was initiated at the start of the sixth dynamic scan and was followed with an equal volume saline flush.

The AIF was determined in the descending aorta or iliac artery using an automated AIF extraction technique. The user selects the slice for the AIF measurement, while the algorithm extracts the signal time-course of every voxel in the slice. The signal intensity is converted to a concentration using equation 3.1, with an assumed contrast agent relaxivity of 4.5 $s^{-1}mmol^{-1}$. The algorithm then selects curves that reach a maximum concentration within 10 s of the bolus arrival time

and have a peak concentration in the top 5% of all voxels. The second criteria is expected to reduce the impacts of PVE.

Sixty-seven AIFs were used in the population average. Prior to averaging, all AIFs were manually shifted such that the first-pass peak was aligned at the same point. The mean, median and standard deviation were calculated for each time point, and fit with the functional form:

$$C_b(t) = \sum_{n=1}^{2} \frac{A_n}{\sigma_n\sqrt{2\pi}} e^{-\frac{(t-T_n)^2}{2\sigma_n^2}} + \frac{\alpha e^{-\beta t}}{1+e^{-s(t-\tau)}} \tag{4.2}$$

Where A_n (0.809 $\pm$ 0.044, 0.330 $\pm$ 0.040 mmol min), T_n (0.17046 $\pm$ 0.00073, 0.365 $\pm$ 0.028 min) and σ_n (0.0563 $\pm$ 0.0011, 0.132 $\pm$ 0.021 min) are the scaling constants, centers and widths of the nth Gaussian, α (1.050 $\pm$ 0.017 mmol) and β (0.1685 $\pm$ 0.0056 min^{-1}) are the amplitude and decay constants of the exponential, and s (38.078 $\pm$ 16.78 min^{-1}) and τ (0.483 $\pm$ 0.015 min) are the width and center of the sigmoid. The two Gaussian functions represent the first-pass peak and the recirculation peak, while the exponential decay term describes the washout phase.

The results showed that the mean and median curves were similar, thus suggesting that there were no outliers in the data set. From the standard deviation, there was large variability during the transient first pass, but much less in the slow washout phase. Variability in the width and peak of the first pass could result from different doses (determined from the patient mass), heart output and low temporal resolution.

Parker et al. performed their analysis on a pixel-by-pixel basis using the extended Kety model. The population-averaged AIF was used as the input curve for the plasma ($C_p = C_b/(1 - Hct)$). Repeatability was assessed from the 95% confidence interval of a genuine change in a single individual between the first two visits. Repeatability improved by 41.3% for K^{trans}, 41.1% for v_e and 22.6% for v_p (percent change), when the population-averaged curve was used in place of the measured curve. However, this AIF is only valid for tissues in the abdominal region and could lead to inaccuracies if used in other areas of the body.

They concluded that the population-averaged AIF provides greater sensitivity to genuine changes between patients. This is especially important in clinical trials which require sensitivity to a physiologically relevant parameter over accuracy.

Since the temporal resolution was a limiting factor, the population-averaged AIF provided information that may have been missed during the first pass of the bolus.

4.1.1 Requirement for a High Temporal Resolution

To accurately capture the rapid contrast kinetics in the vasculature following injection, a high temporal resolution is required [14, 108, 122]. This will capture important features, such as the bolus arrival time, the rate at which the bolus arrives at the tissue of interest, or the maximum concentration reached.

Due to the smaller diameter of capillaries, not all contrast agent molecules will arrive at the same time [107]. The initial upslope of the AIF therefore provides information about the tissue perfusion flow. This phenomenon is very fast, and requires acquisition speeds exceeding 3-5 s per image.

Although faster imaging techniques are available, the temporal resolution is still a concern [18, 19]. More recent measurements of the AIF focus on improving the temporal resolution. Fruytier et al. [100] measured an AIF in the iliac artery of a mouse with a fast gradient echo, providing a temporal resolution of 1.19 s. Ragan et al. [15], showed that a compressed sensing approach known as cardiac anatomy-constrained temporally unrestricted sampling (CACTUS) can improve the temporal-resolution. They segmented the image into several structures, and updated the images dynamically with two radial projections per measurement. Their AIF, measured in the left ventricle of the mouse heart, had an effective temporal resolution of 84 ms.

Case Study: Interleaved Measurement of the Signal Intensity Curves in Blood and Tissue

Taylor et al. [123], developed a method to simultaneously measure the signal intensity-time curves in blood and tissue using a single-angle projection. This provides a temporal resolution of 50 ms for the blood-based measurement, while also allowing for improved spatial resolution of the tissue of interest (muscle with 0.78 x 1.56 mm^2 resolution). Their technique alternates acquisitions of a 1-D projection for the blood-based curve and a single phase-encode line at the tissue of interest.

The measurements were performed in rats, with an injected dose of 0.1 mmoL/kg

of Gd-DTPA through a tail vein injection. The slice locations for the blood-based and tissue signal intensity-time curves were in the descending aorta and in muscle, respectively. Signal from the aorta was isolated by subtracting the background signal from the corresponding pixels. The background signal was taken from two nearby pixels in the projection data.

The results showed the expected characteristics of an AIF, though the measured curve was for signal intensity rather than concentration. The curve was subjected to a 29-point moving average filter to reduce noise. While their measurements showed great potential in capturing the rapid contrast kinetics following the injection, T_2^* effects resulted in significant signal losses, and thus uncertainty in the measured signal-intensity. Further, the curves need to be converted into a concentration before they may be applied for modelling.

4.1.2 Phase vs Magnitude Derived AIF

The AIF may be derived from the signal magnitude [18, 19, 21, 124, 125] or from the signal phase [16, 126–129]. Traditionally, the AIF was determined from changes in the longitudinal (T_1) or transverse (T_2) relaxation times [19, 21], which was then converted to a concentration with an assumed linear relationship [111]. Magnitude-based AIFs suffer from signal losses from T_2^* relaxation effects at the peak [100, 130], making accurate characterization difficult at high concentrations. Signal truncation becomes a larger problem at higher magnetic field strengths [82]. One solution is to measure the AIF in a smaller vessel, where the maximum concentration is lower, but comes at the cost of greater PVE biases.

Most paramagnetic and superparamagnetic contrast agents will alter the blood susceptibility or shift its resonance frequency. In effect, it is possible to characterize the concentration through phase differences in the MR signal [129]. Recent studies have looked at measuring the AIF from the signal phase [128]. Phase data is advantages as the signal phase evolves linearly with concentration over a wide range [128, 131], it is expected to have an SNR up to a full order of magnitude greater than the magnitude data [14, 128], it is less sensitive to partial-volume effects [100], in-flowing blood and the blood hematocrit [82], and it is relatively insensitive to T_1 and T_2 relaxation [126]. However, raw signal phase has a dynamic

range of 2π radians, meaning that phase wrapping can occur at higher concentrations. The larger dynamic range is thought to be the reason for the significantly higher SNR potential [82], though phase wrapping becomes problematic when the temporal resolution is not sufficient to detect the wrap.

The phase shift, $\Delta\phi$, is dependent on the concentration of contrast agent in the vessel, C, and may be determined as follows [82]

$$\Delta\phi = \frac{4\pi\omega_o\chi_M\zeta CTE}{3} \tag{4.3}$$

Where ω_o is the Larmor frequency, χ_M is the molar susceptibility of the contrast agent, TE is the echo time and ζ is a factor that reflects the geometrical properties of the vascular compartment. For the example of an infinite cylinder, $\zeta = (3\cos^2\theta - 1)/2$, where θ is the angle relative to the static magnetic field. It will have a maximum value, of 1/3, when the vessel is oriented parallel to the main magnetic field, and disappear completely at an angle of 54.7^o. The angular dependence must be taken into account when converting the phase difference into a concentration. This can be done following the method of de Rochefort [129] or by calculating phase coefficients for the expected vessel alignment [100].

Simulating an AIF in a Closed-Loop System by Akbudak et al

Akbudak et al. [126] designed a closed-loop system in which varying concentrations of a contrast agent could circulate freely, without having to move the phantom during the scan. Their phantom was motivated to improve the accuracy of estimating the contrast agent concentration through a difference in phase. As noted in their paper, magnetic field inhomogeneities can be removed through phase subtraction at two unique time points. But, this assumes that the field gradients, and thus the phantom set-up, are consistent.

The phantom includes a long cylindrical tube (for imaging), a mixing reservoir, an attenuation flask and a variable-rate peristaltic driving pump, all connected with transparent Tygon tubing. The cylindrical tube should have a large length to diameter ratio for equation 4.3 to be valid, and be aligned parallel with the main magnetic field to maximize the sensitivity of the scan ($\zeta = 1/3$).

The results showed an AIF of the expected shape for both a parallel and per-

pendicular orientation, but had a slow upward phase drift which leveled out after subtracting the background phase shift. The steady-state concentration was in good agreement with theory and occurred after five complete passes of the bolus around the system. They tested the linearity of the phase change with concentration for four echo times (4.66 ms, 12 ms, 18 ms and 26 ms) and found a strong correlation: $r = 0.99972$ for a plot of $\Delta\phi/TE$ vs C, with a slope of 2.561 ± 0.0023 deg/mM/ms and intercept -0.33 ± 0.40 deg/mM. Since the x-intercept of the graph is within a standard error of 0, they argued that the finite duration of the RF pulse did not significantly affect the $\Delta\phi$ measurements. In addition, they discovered that the phase shift is invariant with T_1, T_2 and the method in which the echo is sampled (including duration and symmetry). This makes a phase-based AIF measurement more robust than a magnitude-based approach.

4.2 Alternative Methods

4.2.1 Dual-bolus

The concentration of the injected bolus must be chosen carefully. A high dose is preferred for improved SNR at the tissue of interest, but also leads to saturation effects which make accurate determination of the AIF difficult. Yet, too low a concentration could mask important signal changes in the tissue of interest, despite providing a better estimate of the AIF. Utilizing the benefits of both the low and high dose injections, Kostler et al. [132] proposed a dual-bolus technique for quantitative multi-slice myocardial perfusion imaging. The technique involves two consecutive injections; a low dose bolus for the AIF measurement, followed with a higher dose bolus for the myocardium measurement for improved signal changes.

In their study, Kostler et al. injected Gd-DTPA into the antecubital vein and measured the signal changes on a 1.5 T Siemens scanner with a multi-slice, saturation recovery trueFISP with TR = 2.6 ms, TE = 1.1 ms and a flip angle of 50°. The two injections were given during two consecutive breath holds with a delay of less than 1 min. As a proof of principle, they injected boluses of 3 ml, 9 ml and 12 ml and compared the AIFs after rescaling for the different doses. The results showed that the up-scaled 3 ml bolus did not match the 12 ml bolus. This con-

firmed that saturation of the blood signal affects the measurement for high dose injections. They argue that a better method would be to represent the high-dose bolus as a summation of several lower dose boluses, temporally shifted by the duration of the injection. This, however, assumes that the system is linear and stationary. They also discovered that the perfusion values were in better agreement with other studies and had smaller standard deviations when a low-dose AIF was used. Li et al. [133] showed improved results when the temporal resolution of the two injection scans were different, provided that the AIF was sampled with a temporal resolution greater than 1 s.

The dual-bolus is attractive as the AIF may be measured at the start of each experiment, but it doubles the effective imaging time required [134], it assumes physiological variations are negligible between the two injections [134] and that the contrast kinetics are identical for the two injections [111]. The dual-bolus technique has been primarily applied to cardiac perfusion studies in humans.

4.2.2 multi-SRT Measurment with Radial Data

An alternative to the dual-bolus technique is to estimate the AIF from the change in signal magnitude in radially reconstructed images [111, 125]. Since every radial spoke passes through the center of k-space, it is possible to reconstruct image series with varying effective saturation recovery times (eSRT), simply by changing the number of projections used in the reconstruction. This technique allows for an AIF measurement with a short eSRT, while maintaining high SNR in the tissue of interest by using a longer eSRT. As there is only one injection [135], the concern of different physiological states is removed and the total scan time is dictated by the DCE experiment. Though this technique shows potential for improving DCE-MRI parameter accuracy, Kholmovski noted that the AIF peak concentration was underestimated in their study.

Kim et al. [135] proposed an extension with a multi-saturation recovery time (SRT) method in which the AIF was estimated from three subsets of radially reconstructed images (24 radial spokes each), having different effective saturation recovery times. They verified that the AIF measured with the multi-SRT technique compared well with the dual-bolus technique in most cases. Since all ra-

dial spokes are acquired in one imaging slice, the supplying blood vessel must be located within the imaging plane; which, as discussed previously, is not always possible.

4.2.3 Reference Region

Gradient-echo sequences are known to be sensitive to vessels of all sizes for the AIF measurement [82]. At typical echo times for DSC-MRI ($35-45$ ms at 1.5 T or $25-30$ ms for 3 T), there is potential for significant signal losses as a result of larger amounts of contrast agent in large vessels. As such, the MR signal is susceptible to strong dephasing, which limits our ability to accurately measuring the AIF. In this situation, measuring the AIF outside the artery could be beneficial.

Kovar et al. borrowed a method from positron emission tomography that avoids the AIF altogether by comparing the enhancement characteristics of two tissues: the tissue of interest, and a reference tissue with known perfusion values [136]. Despite showing promise, the reference region technique did not receive much attention until 2005 when Yankeelov et al. investigated its potential uses via simulations [109]. The main differences between the two methods are that Kovar tried to estimate the AIF from the reference tissue using the differential form of the Kety equation, while Yankeelov developed a theory that is completely independent of the AIF using the integral form of the Kety equation.

The reference region technique uses literature values for K_{trans} and v_e of the reference tissue, typically skeletal muscle, to estimate the perfusion parameters for the tissue of interest. Since the AIF is not measured, the experimental time can be dedicated to obtaining DCE images with greater spatial resolution or SNR. However, the assumption that the AIF is identical for both tissues may not be valid, leading to errors in K_{trans} and v_e [109]. The simulation results from Yankeelov et al. revealed systematic errors in K_{trans} and v_e of the tissue of interest that varied linearly when incorrect values were used for the reference tissue [109]. This can be an issue if there are differences within a cohort of animals in a study.

4.3 Projection-Based AIF Measurement

We develop a novel method for measuring the AIF in a mouse tail using MR projections and the phase of the MR signal. This method involves the acquisition of a single 2-D image pre-injection and a series of projections collected before, during and after the contrast injection. Projection data has a temporal resolution equal to the repetition time, thus offering significant gains in the temporal resolution of the AIF, without compromising spatial resolution along the read-encode direction. Since a projection-based AIF is measured rapidly on an individual basis, it would be applicable to DCE-MRI studies performed in small animals.

The proposed technique is summarized in Figure 4.1. Data from the vessel is extracted from each projection through a subtraction of the background profile. The background profile is obtained from a projection of the pre-injection 2-D image along the direction of phase encode, after removal of the vessel data. This is justified as an application of the central-slice theorem as all projections pass through the center of k-space [137]. The phase of the signal from each projection is then compared to the average pre-injection value and converted into a concentration.

The mouse tail was chosen for our analysis because of its simple geometry. The tail contains four small, isolated point-like vessels in a tissue background void of complicated organs. Since the vessels are located near the surface, the projection may be oriented such that the vessels are well separated in the acquired profile to avoid super-position of signals from two. The tail vessels are relatively straight and have a sufficient diameter for the AIF measurement. The SNR can be improved by increasing the slice thickness, but the vessels must be properly aligned to PVE.

4.4 Experimental Methods

The experiment was performed in three stages: a phantom-based experiment designed to determine the conversion factor between signal phase and concentration of Gd, a flow-phantom experiment to validate our technique in the presence of flow, and a projection-based AIF measurement performed in-vivo.

MRI acquisition took place on a small bore Biospec 70/30 Bruker 7.0 T MRI scanner (Bruker BioSpin Ltd., Etlingen, Germany). A birdcage coil (i.d. = 7.0 cm)

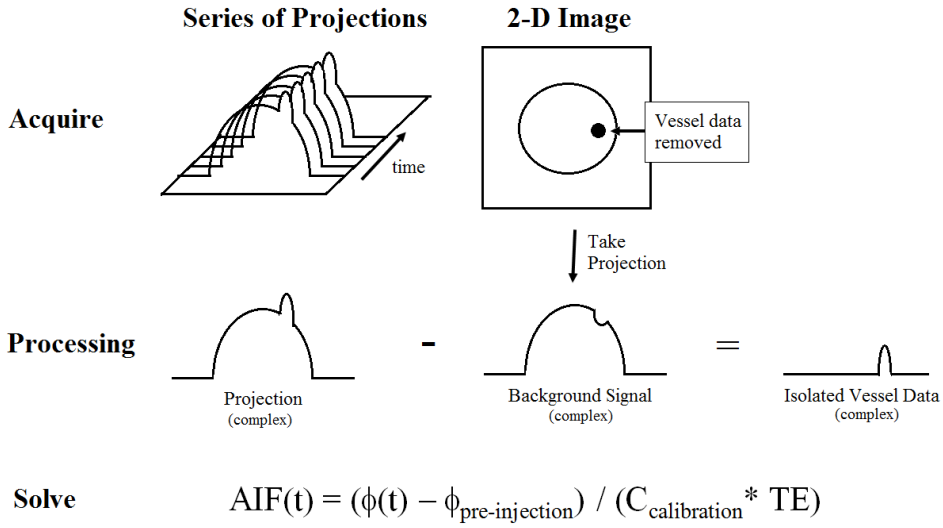

Figure 4.1: Schematic of the projection-based AIF measurement. One 2-D image is acquired pre-injection, followed by a series of projections before, during and after contrast injection. This technique may be used to increase the temporal resolution of the AIF as only one projection is required per data point. The AIF is determined by first subtracting the background signal from each projection, then comparing the signal phase to the pre-injection value.

and an actively decoupled surface coil designed specifically for the mouse tail (width 7 mm, length 18 mm) were used for signal excitation and reception, respectively.

The 2-D pre-injection image and the projections were completed as two separate scans using the standard fast low angle shot (FLASH) pulse sequence. The settings between both acquisitions were identical, except that the phase-encode gradients were set to 0 mT/cm to achieve projections through the center of k-space. The free induction decay (FID) was read into Matlab (The Mathworks, Inc. Natick, MA USA) and centered such that the echo was properly positioned before applying the FFT.

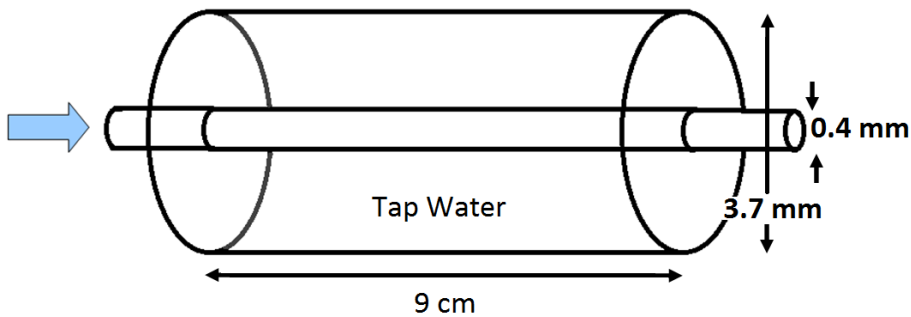

Figure 4.2: Phantom used to validate the linear relationship between signal phase and concentration of Gd-DTPA diluted in saline. The phantom consists of a capillary tube (inner diameter 0.4 mm) placed inside a larger glass tube. The area between the two tubes was filled with tap water.

4.4.1 Relationship Between Concentration and Signal Phase

A calibration phantom was constructed by inserting a capillary tube, with inner diameter (i.d.) 0.4 mm, inside a larger glass spotting tube (i.d. = 3.7 mm). The region between the tubes was filled with tap water [129] to provide additional signal for magnet shimming and a non-enhancing region to correct for hardware-related phase fluctuations [126]. Figure 4.2 depicts the phantom with dimensions.

A number of Gd-based solutions, diluted in saline to concentrations between 2 and 10 mM, were injected through the capillary tube at three physiologically relevant flow velocities [93]: 1) 0 cm/s, 2) approximately 15 cm/s (1.00 ml/min flow rate) and 3) approximately 30 cm/s (2.00 ml/min flow rate). Gd-DTPA has a similar relaxivity in saline and tissue fluids [138], so the same calibration factor can be applied in-vivo.

A KD Scientific power injector (model 780220, Holliston, MA, USA) was used for the injection to reduce variations in injection profile. To investigate the effects of flow within the capillary tube, the experiment was repeated with flow compensation along the slice select direction. Under the assumption of plug flow parallel to the main magnetic field, flow compensation was not applied in the read or phase encode directions to keep echo time (TE) as short as possible.

FLASH data was acquired with $TR = 100$ ms, $TE = (4.6\ or\ 8.0)$ ms, flip

angle 30°, FOV $15x15\ mm^2$ and slice thickness 1 mm. The pre-injection 2-D Cartesian image has a matrix size of $256x256$, while the projections are $256x1$. The two echo times were set to the minimum and a value approximately double, and used to verify if the phase-concentration factor was independent of the echo time. For each scan, 20 repetitions were completed to improve the SNR and allow for reproducibility of the signal temporally (i.e. phase drift during the experiement). A second reference phantom was placed in the field of view to track drifts in phase [126]. This phantom is sufficiently far from the capillary tube that its signal should not be affected by susceptibility effects.

4.4.2 Validation: Colorometry with a Flow Phantom

A colorimetric phantom study was performed to evaluate and cross-validate the projection-based AIF in the presence of recirculating fluid. The flow phantom was constructed, based on the system proposed by Akbudak et al. [126]. It consists of a peristaltic pump (Minipuls 2, Gilson), a recirculation beaker and three types of tubing: latex (inner diameter 3.2 mm), tygon (inner diameter 3.2 mm) and viton (inner diameter 1.0 mm) tubing. To span the length to and from the centre of the scanner bore to the pump in the adjacent room, 8 m of viton tubing was used. Initially, the system was flushed with tap water to clear out any contrast agent residue and improve reproducibility between experiments performed within the same imaging session. The recirculation beaker had an approx. volume of 2 ml and served as a mixing site of the injected solution and water.

A custom-built colorimeter was used to measure dye concentrations of Allura Red 40 dye (Kool-Aid, Kraft Foods). This was constructed with a semi-micro cuvette, through which fluid could flow through, a light emitting diode (LED) (OVLGC0C6B9, Optek Technology Inc.) and a photodiode (MTD5052N, Marktech Optoelectronics). Two operational amplifiers (TL082, Texas Instruments) provided a supplying voltage to the LED and to convert the photocurrent produced by the photodiode into an output voltage. The voltage was recorded with an oscilloscope (TDS 3054B, Tektronix) and converted to a concentration of dye following the procedure of Sigmann and Wheeler [139]. The system was calibrated using a set of known solutions of Allura Red 40 dye. A sketch of the flow phantom is

shown in Figure 4.5a.

The flow phantom allowed us to temporally control the concentration of contrast agent circulating around the system. As such, it is possible to validate the projection-based AIF measurement in the presence of rapid changes in concentration. The flow phantom was filled with water to an initial volume of $24\ ml\ \pm 1$ ml. A 0.8 ml bolus of 0.101 mM Allura Red 40 dye and 10 mM Gd-DTPA was then injected at a rate of 11 ml/min with the power injector. The bolus was allowed to circulate for approx. 8 min to allow for multiple passes of the bolus through the entire system. MRI data was acquired using the standard FLASH experiment, with $TR = 100$ ms, $TE = 3.92$ ms, flip angle 30°, $256x256$ matrix size, FOV $15x15\ mm^2$ and slice thickness 1 mm. The colorimetric data was manually shifted prior to comparison due to the different sampling locations.

4.4.3 In-vivo Measurements

Prior to any experiments, the injection line was prepared. This included a butterfly needle, a 25 μl heparin lock (filled with heparinized saline to prevent blood clots and a pre-mature injection) and PE20 polyethylene tubing (Braintree Scientific, Inc.) containing the bolus injection. The length (l) of the injection line was calculated from the weight of the animal, using $l = V_{CA}/(\pi r^2)$, Where V_{CA} is the desired injection volume and $r = 0.19$ mm for PE20 tubing. For this experiment, 1.0 M Gd-DTPA was diluted with saline to a final concentration of 30 mM, and injected to a volume of 5 μl/g body weight (or dose of 0.15 μmol/g body weight). Premature mixing of the solutions in the line was investigated and shown not to be an issue. Fig.4.3 shows the assembly of the injection line.

All animal-based scans were approved by the Animal Care Committee at the University of British Columbia. Healthy NOD/SCID immune compromised mice were placed inside a custom-build induction chamber. This chamber has two connections for the isoflurane gas, and a v-shaped opening on one side to restrain the animal while performing the tail vein cannulation. While restraining the mouse, a butterfly needle was inserted into the tail vein as far distal as possible. We chose to do the cannulation prior to anesthesia, as the aesthetic is known to reduce the blood pressure, which makes the vein more difficult to see. The needle was secured in

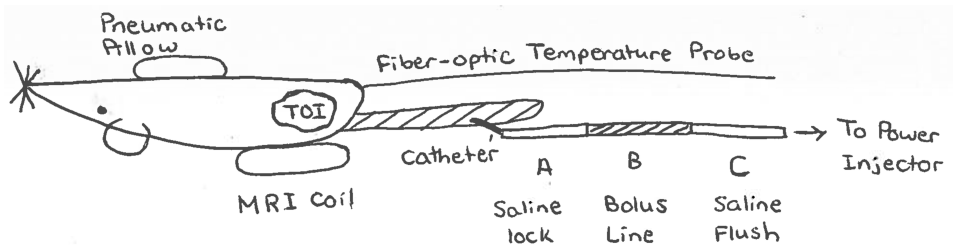

Figure 4.3: Setup for the injection line with a 25 μl heparin lock (segment A), bolus line (segment B), and saline flush (segment C). The heparin lock acts as a buffer between the animal and the contrast-agent volume to prevent a pre-mature injection.

place with fast drying glue.

The mouse was anesthetized with a mixture of 2% isoflurane and oxygen. To maintain a safe body temperature, a heat lamp was shone over the animal during set-up. Once the respiration rate reduced to approx. 100 beats per minute, the mouse was moved to the coil set-up and positioned supine on the animal bed. A subcutaneous saline injection (approx. 0.5 ml volume) was injected into the loose skin behind the neck to reduce dehydration during the scan. Lacri-lube was applied to lubricate the eyes. The tail was positioned over the surface coil, straightened and secured in place with surgical tape (3M Transpore surgical tape). Since the butterfly coil is metal, care was taken to position it as far from the surface coil as possible. The coil was then transported to the scanner where the tail was positioned at the magnet's isocenter.

The animal's respiration rate and body temperature were monitored during MR acquisition using MRI-compatible animal monitoring equipment (Small Animal Instruments, Inc., Stony Brook, USA). This includes a fiber-optic temperature probe (tip diameter = 1 mm) and a pneumatic pillow placed over the lungs. The body temperature was maintained at 37 $\pm$ 0.1^oC using heated air, and the respiration rate between 80-100 beats per minute. Small tweaks to the level of isoflurane were made during the experiment to adhere to these standards.

The AIF was measured using an image-based and projection-based approach on separate days and different mice. The image-based measurement served as

a motivation for our newly developed technique and to estimate the concentration long after the bolus injection. A FLASH pilot scan was performed to ensure that the vessel of interest was aligned along the direction of the main magnetic field [128]. This orientation will maximize the SNR and reduce the presence of fringe fields [129]. For this AIF measurement, a standard multi-slice FLASH protocol was used ($TR = 100$ ms, $TE = 6.874$ ms, flip angle 90°, 5 slices, FOV $15x15\ mm^2$, slice thickness 1 mm) and repeated for eight time points. Each image had an acquisition time of 25.6 s and an inter-acquisition time of approx. 11 s, thus providing a temporal resolution of 37 s. A 115 μl bolus of 60 mM Gd-DTPA, diluted with saline, was injected at the start of the fourth image in the series. This was done with a power injector set to 1.00 ml/min. This corresponds to an approximate flow velocity of 15 cm/s in the tubing (PE 20, i.d. = 0.38 mm). The injection was preceded with a 25 μl heparin lock and followed with a 40 μl saline flush [111].

A projection-based AIF was measured with the acquisition of one pre-injection image (256x256 matrix size), followed by a series of projections ($256x1$ matrix size, 2560 projections) before, during and after contrast injection (TE = 3.92 ms). This AIF was also measured with a standard multi-slice FLASH (TR = 100 ms, TE = 3.096 ms, flip angle 30°, 5 slices, FOV $15x15\ mm^2$, slice thickness 1 mm), but removed the phase-encoding gradients. To prevent signal loss at the peak of injection, a bolus of 30 mM Gd-DTPA, diluted with saline, was injected approximately 25 s into the scan. This provides at least 256 measurements of the baseline phase. Since each projection is one measurement of the AIF, the repetition time (TR) of the scan will dictate the temporal resolution. Projections are much noisier than MR images, so a long TR and optimized flip angle are desired to maintain a sufficient SNR. For the purpose of our study, a repetition time of 100 ms and a flip angle of 30° were used. The long TR will allow for interleaved DCE-MRI data acquisition between individual AIF measurements in the future.

The proposed projection-based method is outlined in Figure 4.1. It involves the acquisition of one 2-D Cartesian image before injection, followed by a series of projections. The projections were acquired under identical scanning conditions, except that the phase-encode gradients were set to 0 mT/m. From the central-slice theorem [137], taking the FT of a projection of a 2-D object along one axis is

equivalent to taking the central line of k-space of the 2-D object. Accordingly, a profile of the surrounding tissue was obtained by projecting the image along the phase-encode direction, after the vessel data had been removed. Using the background profile, we were able to isolate the MR signal from the vessel. The AIF may be determined by comparing the mean phase for each projection with the pre-injection value. This phase difference is then converted to a concentration of Gd using the calibration factor determined previously.

To verify that the concentration at 20 min post-injection is correct, blood samples from four NOD/SCID mice were analyzed for Gd concentration using ICP-MS (inductively coupled plasma mass spectrometry, service provided by Matthew Norman at Exova, Surrey, Canada). These mice were not scanned, but had similar weights to those used for the AIF measurement (range 22.0-30.5 g). The mice were injected with a 30 mM bolus of Gd, mixed in saline, to a dose of 5 μl/g weight. The injection was performed manually over a period of approximately 20 s. The mice were euthanized 20 min post injection, at which time, a cardiac puncture was performed to extract a large volume of blood (volume collected ranged between $200 - 500$ μl). Samples were brought to a final volume of 10 ml with 1% nitric acid (concentration 0.22 M) to prevent bio-degradation [140]. A control sample, consisting of 50 μl of 30 mM Gd and 9.95 ml of 1% nitric acid for a final concentration of 0.15 mM Gd, was also sent for analysis.

4.5 Validation of the Phase-Concentration Relationship

The goal of the calibration experiment was to determine the conversion factor, that relates a phase difference to a concentration of Gd, and to investigate the impact flow compensation has on the measurement. The results from this analysis verified that the phase varies linearly over the range of concentrations chosen. In addition, it is independent of the flow velocity and echo time. Phase-concentration curves for the projection data, at both echo times, are summarized in Figure 4.4.

The slopes of these curves were consistent for all cases studied (three flow velocities, flow compensation absent/present, two echo times, and images/projections) and had a value of (0.213 $\pm$ 0.001) rad/mM/ms. This value is consistent with the predicted value of 0.212 rad/mM/ms ($\Delta\phi$/(Δ[C] TE) = $2\pi\gamma B_0\chi_m/3$)

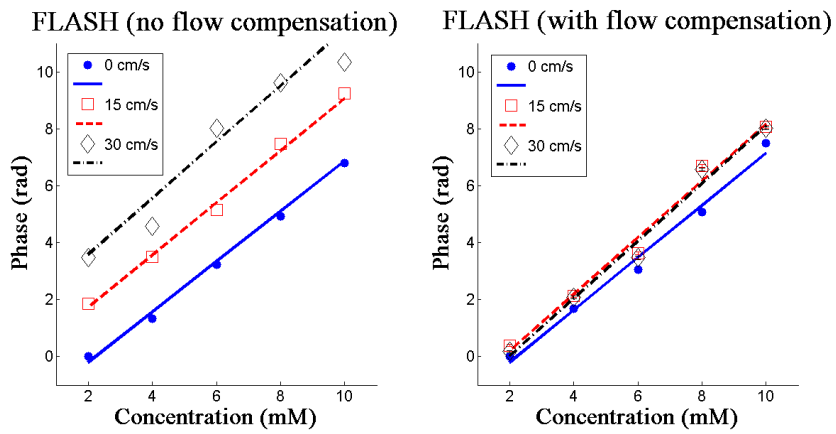

Figure 4.4: Calibration factor converting a phase difference into a concentration of Gd for projections. Gd-based solutions, diluted in saline, were injected through a capillary tube at three biologically relevant flow velocities. The experiment was performed with a standard FLASH pulse sequence, with and without flow compensation.

for a long cylinder oriented parallel to B_0. γ is the proton gyromagnetic ratio ($4.258x10^7$ Hz/T), B_0 is the strength of the main magnetic field (7.0 T), and χ_m is the molar susceptibility of the contrast agent ($3.4x10^{-7}$ mM^{-1} for Gd) [141].

The phase-concentration relationship holds in the presence and absence of flow compensation. However, there appears to be a flow-dependent phase shift that is significantly reduced when flow compensation is used. The extra phase shift between stationary and flowing spins could result from our assumption of plug flow in the capillary tube. The fluid close to the tube walls may have a slower velocity, and therefore bias the phase measurement. Blood flow in the arteries and veins is not likely constant, second order phase compensation would be ideal. But this comes at the expense of longer echo times, which also increases the probability of getting a phase wrap near the peak. First order compensation brought the phase curves closer together, and should be sufficient for a projection-based measurement.

4.6 Validation with Colorimetry

The colorimetry experiment proved that signal phase is superior to magnitude for measuring a change in intra-vascular concentration, as shown in Figure 4.5. A

schematic diagram of the flow system is displayed in the inset of Figure 4.5a.

Figure 4.5a shows the concentration-time curve for the measurement of the dye concentration at different distances downstream from the injection site. Greater dispersion of the bolus (lower peak height and broader width) can be seen in the curve corresponding to the measurement made further downstream.

Figure 4.5b compares the MR measurement of magnitude and phase during bolus passage. The magnitude data does not accurately reproduce the first pass of the bolus, likely a result of signal loss from T_2^* relaxation. Even though the magnitude data does show signs of recirculation, it is not to the same extent observed with the MRI phase-based or colorimetric measurement.

Figure 4.5c shows the optical and phase-based concentration-times curves superimposed on the same graph. Since the location of the colorimetric measurement was approx. 1 *m* downstream from the MR coil, it had to be temporally shifted forward to align with the MRI curve. The first bolus passage is narrower and higher on MR compared to colorimetry. Subsequent recirculation peaks agree very well between the two modalities. The phase curve had peaks at the same locations temporally, but appeared sharper than the cuvette reading. Additional mixing of the dye in the cuvette (located downstream from the MR measurement) could cause this, which would lead to peak dispersion and a lower concentration. peak

4.7 Projection-Based AIF in-vivo

The image-based AIF (temporal resolution 37 s) is shown in Figure 4.6. At this resolution, the shape of the curve is not well characterized, particularly at the peak. Phase data has a dynamic range of 2π radians, so any phases that exceed this value will be reset to a value between 0 and 2π radians. It is unclear if this has occurred in our measurement. As such the peak concentration could be either 1.46 *or* 5.78 mM. Additionally, the time at which the bolus arrives at the measurement site is unknown. These ambiguities will cause severe errors in the model fits if the incorrect concentration is assumed. The lack of temporal information motivated the use of a MR projection-based approach to measure the AIF. The concentration long after the injection is 0.34 mM, which seems reasonable based on other studies[15].

A projection-based AIF, having a temporal resolution of 100 ms, is shown in

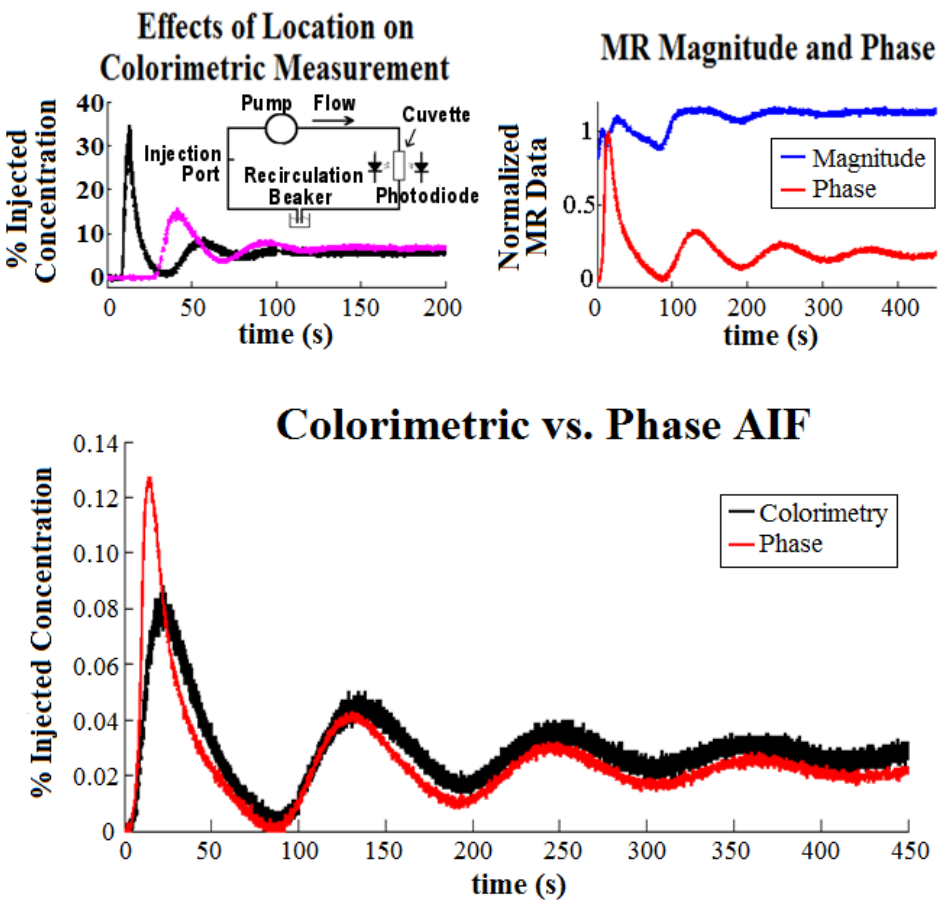

Figure 4.5: Signal-time curves for the colorimetry phantom. a) shows the measured colorimetric concentration-time curves from two cuvettes. The inset is a schematic of the flow phantom used for these measurements. b) is the average magnitude and phase of the MR signal measured in the tygon tubing. c) compares the phase-based AIF measurement and the colorimetric concentration in a simultaneous acquisition. The colorimetric curve has been shifted in time to account for different locations of MR coil and cuvette.

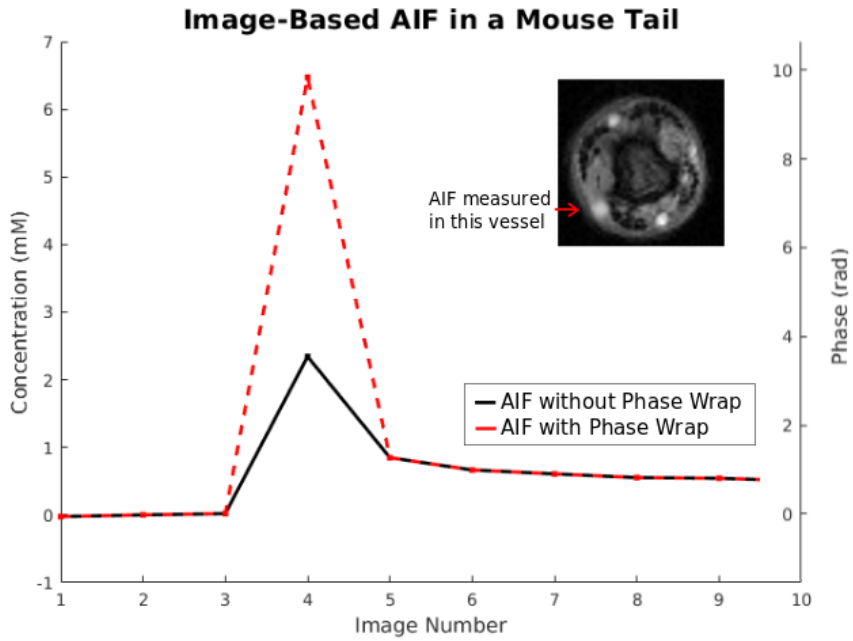

Figure 4.6: Image-based AIF in the mouse tail. The AIF was measured in the vessel indicated by the arrow. At a temporal resolution of 37 s, it is unclear if the measurement at the peak has exceeded the dynamic range of 2π radians and was phase wrapped to a lower angle. By increasing the temporal resolution, phase wraps will become more obvious. In addition, the details of the curve are not well characterized, and the arrival time of the injection is unknown. Increasing the temporal resolution will reduce ambiguities in both.

Figure 4.7. At this temporal resolution, the details of the curve are better characterized throughout the scan, and it is clear when the Gd bolus entered the blood stream. A double exponential [13, 19], modulated by a sigmoid function [18] to fit the injection, was fit to the data, having the functional form:

$$C(t) = \frac{0.8137 \cdot e^{-0.0807t} + 0.3399}{1 + 4.0415 \cdot e^{0.9932t}} \tag{4.4}$$

The double exponential fit, proposed by Lyng et al., is superimposed on the plot [19]. Their AIF was derived from data acquired in the left ventricle of three separate mice, and had a temporal resolution of 13 s. The final concentrations

long after injection are comparable between the two techniques, but there is a large discrepancy at the peak concentration. Lyng determined the concentrations from the increase in T_1 relaxation rate in a T_1-weighted spoiled gradient-recalled (SPGR) experiment, with TR $=$ 50 ms, $TE = 6$ ms and flip angle $= 80^o$. Their injection was 10 μl/g body weight of 30 mM Gd-DTPA diluted in 0.9% NaCl and done at a constant rate over 5 s. In comparison, our dose was 5 μl/g body weight of 30 mM Gd-DTPA, injected over $6-9$ s, depending on the weight of the mouse. With a slower injection, a slightly lower peak concentration is expected. Lavini et al. [117] concluded that effects of flow or T_2^* decay caused them to mis-measure the peak concentration. Measuring the AIF with the signal phase should reduce errors related to signal losses from T_2^* effects. However, the signal from the blood may not rephase fully if the flow velocity is not constant. Higher order flow compensation would reduce this error, but also leads to longer TE. This could be detrimental to the measurement at high concentrations the signal decays rapidly due to T_2^* relaxation.

Figure 4.8 shows four AIFs measured in four different mice. The injection bolus for these mice was 60 mM to see if the higher concentration bolus would affect the shape of the curve. The AIF was obtained by averaging the phase-time curves from all pixels associated with a vessel (typically 2-6 pixels along the projection). The four curves show similarities in shape and peak height, but also differ from one another in terms of the rates of enhancement, wash out and final concentration 10 min post injection. Superimposed on the figure, is the population averaged AIF for this cohort (thick black curve). These results support the observation that the AIF varies between individuals.

The results from mass spectroscopy showed a blood concentration of $0.170-0.195$ mM for the mice of weight $22-24$ g, 0.293 mM for the 30.5 g mouse, and 34.8 mM for the stock solution. These results suggest that the steady-state Gd concentration (20 min post injection) should be approximately $0.2-0.3$ mM, which is consistent with our measured projection-based AIF. Gd clearance in mice is approximately 27 min in mice [5], so we would expect that the concentration would gradually decrease throughout the experiment. For comparison, most AIF experiments were 10:40-38:24 in duration.

If all contrast agent were to remain intra-vascular, we would expect a steady-

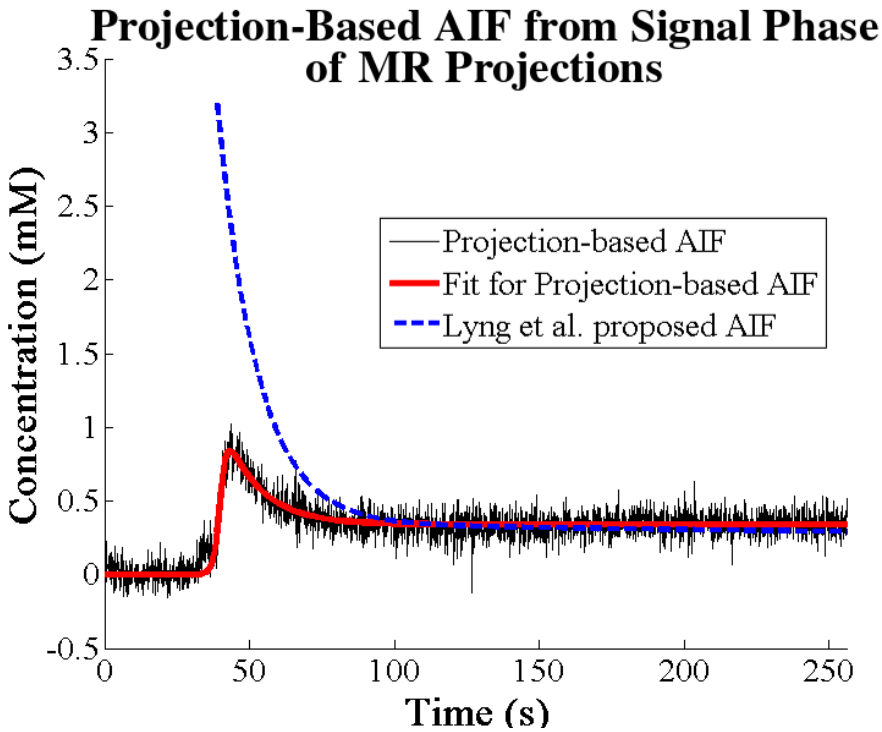

Figure 4.7: Projection-based AIF in a mouse tail with a temporal resolution of 100 *ms*. Our AIF has a functional form as in equation 4.4. The double exponential proposed by Lyng et al. (temporal resolution 13 *s*) is shown for comparison [19]. Their curve has a much higher concentration following injection and appears to be shifted temporally relative to our measurement.

state concentration of 2.0 $\pm$ 0.43 mM Gd. This value was calculated assuming a total blood volume of $6-8\%$ body weight [142] and a 30 mM Gd-DTPA bolus (with error of 5 mM to account for the measured stock concentration) of volume 5 μl/g body weight. The expected concentration is much closer to the observed concentration at the peak than it is the steady-state value. A possible explanation is the extraction of Gd by the kidney and other tissues immediately following injection [4].

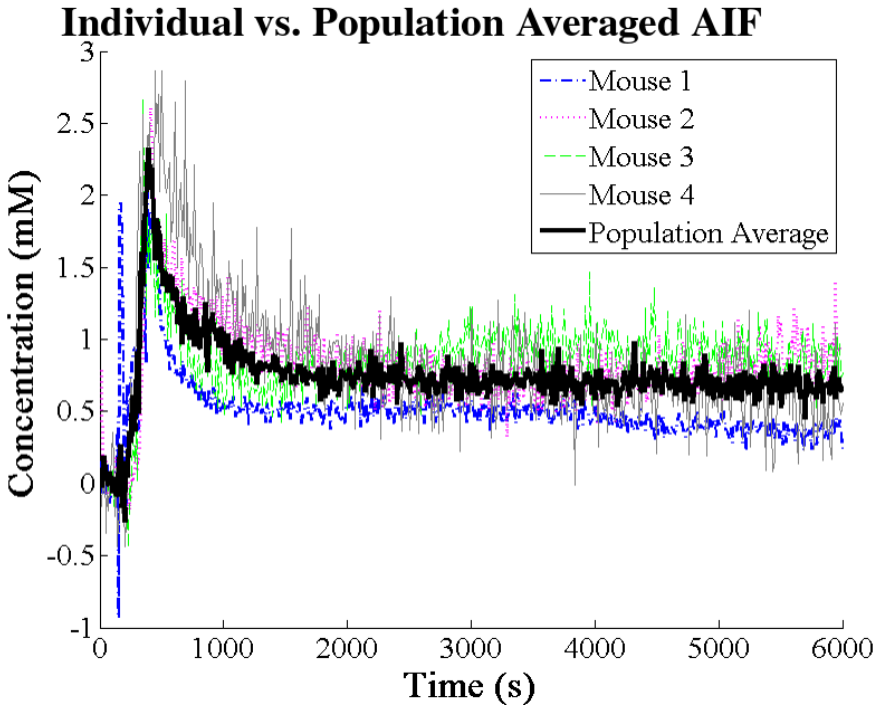

Figure 4.8: AIF measured in four individual mice, with an injection of 60 mM Gd-DTPA (double strength). The AIFs all have a similar shape, but differ around the peak of the AIF. The population averaged result (solid black line) differs from each of the individual curves.

4.8 Discussion

We acquired an AIF in a mouse tail with a temporal resolution of 100 ms using a projection-based approach. Our proposed method involves the acquisition of one 2-D image before injection, and a series of projections before, during and after injection. Scanning parameters (TE, TR, flip angle, etc.) were kept identical for the image and projection acquisitions. This allowed us to isolate the enhancement in the tail vein from the projection through a subtraction of the background profile. Our measurement was performed in a mouse tail due to the simple geometry and absence of additional organs that could complicate the measurement. The mouse tail contains four vessels along the outer perimeter. Care must be taken during set-up of the imaging slice to ensure that two vessels will not overlap within the

projection. As such, the slice was often rotated by a couple degrees to ensure that all vessels could be distinguished in the projection.

The AIF was calculated by comparing the average phase between each projection and the pre-injection value, and then converting the phase change into a concentration with our calibration factor. Despite acquiring data within saline-based solutions, there is evidence that the contrast agent affects the signal phase similarly between blood and aqueous solutions [127].

The AIF may be measured using manual selection of suitable voxels or using an automated searching algorithm [82]. Though the automated procedure is much easier and less time intensive, it could select voxels that do not correlate with a vessel [82]. To avoid this issue, the user must confirm that the selected pixels are valid for the measurement. Manual selection has traditionally been more common. With this method, the user will investigate the concentration-time curves in all voxels within a desired area, and identify those with the most arterial-like features (early and rapid initial slope, narrow peak and high peak concentration) and good contrast-to-noise ratios [82]. This study used manual selection of AIF pixels due to the small size of the vessels in the image. Most vessels would cover 2-10 pixels total. Using an automated algorithm could have introduced PVE biases in the small vessels that cover few voxels.

Concentration-time curves obtained with the signal phase show remarkable agreement with the optical concentration measurements (Figure 4.5c). However, the height and width of the first peak differ between the MR measurement and colorimetry. This could result from the different measurement volumes between MRI and colorimetry. The MRI measurement is made on a 1 mm slice of PE 20 tubing (0.011 ml volume), while the colorimetry measurement is made within a semi-micro cuvette with a volume of 3 ml. The cuvette volume is much larger than the 0.8 ml injection volume, so the maximum concentration of Allura Red 40 dye could be underestimated by as much as a factor 3.75. However, this factor is dependent on the flow rate and the injection speed. Since the mixing is not instantaneous, the peak width of the colorimetric curve increases, its height decreases, and the maximum of the peak is shifted to a later time. Figure 4.5a shows the peak shape in two separate cuvettes within the loop. The first peak for the second cuvette is broader and has a lower peak concentration, which supports our argument.

All subsequent peaks better resemble one another due to bolus mixing in both the cuvette and recirculation beaker.

The AIF proposed by Lyng et al. has become the standard population averaged curve for experiments performed in mice. Their curve has a temporal resolution of 13 s and was determined from changes in T_1 [19]. A double exponential, $C(t) = Xe^{-xt} + Ye^{-yt}$, was fit to the post-injection data where $X = 5.8$ mM, $x = 4.4\ min^{-1}$, $Y = 0.7$ mM, and $y = 0.05\ min^{-1}$. At their temporal resolution, it is unclear when the bolus injection began, how long it lasted, or if a recirculation peak is present. It is therefore difficult to temporally align the Lyng population-average AIF to independently acquired DCE data. Furthermore, when fitting the Lyng curve to DCE data of higher temporal resolution (< 13 s), concentrations following injection may be overestimated, thus leading to errors in pharmacokinetic model parameters.

Attempts to measure murine AIFs have typically been derived from the observed change in the signal intensity [17, 112] or tissue T_1 [111, 128], which are then converted into a concentration using an assumed linear relationship [55]. However, magnitude-based AIFs suffer from a few limitations. There is evidence that the signal intensity only varies linearly with concentration over a narrow range of concentrations. This non-linearity in the signal intensity results from competing T_1 and T_2^* relaxation effects at high concentrations [111, 127]. In addition, the validity of magnitude-based AIFs become questionable when the peak concentrations are sufficiently high to cause the signal magnitude to approach the noise floor. Though this affects both magnitude and phase measurements, magnitude-based measurements incur greater errors. This is shown in Figure 4.5b, where the magnitude data appears to greatly underestimate the peak concentration, while the phase data provides a better estimate. Losses in MR signal, due to T_2^*-relaxation [128], may be partially recovered by minimizing the echo time, using a spin-echo sequence or reducing the concentration of the injected bolus. T_1-based measurements also require a high-resolution pre-injection T_1 map, which will increase the total time of the experiment. With the introduction of faster methods, such as the Look-Locker protocol, the T_1 map may be collected much faster; but still adds to the total scan time.

Some of these limitations are relaxed when evaluating changes in the signal

phase. Though phase-based measurements are relatively new [126], the number of studies using phase have dramatically increased over the last few years [14, 131, 141]. Phase is relatively immune to T_1 and T_2 relaxation times [126], is independent of the blood hematocrit [127], has an increased SNR compared to magnitude data [128] and has an established linear relationship with concentration over a larger range of concentrations [14].

The signal phase can drift slightly through the scan. This may be caused by scanner instabilities, such as drifts in the static field or the transmitter frequency [126]. To compensate, a non-enhancing, external reference phantom was placed next to the mouse tail such that it was close enough to track small field changes near the point of measurement, yet not close enough for susceptibility issues. Analysis of the phase of the reference phantom showed that phase drift was generally negligible for our experiments; but it could be corrected for, if required.

Phase measurements have a dynamic range of 2π radians. At high concentration or long echo times, phase wraps could occur when the phase exceeds 2π radians, and is reset to the modulus of the phase and 2π. Phase wrapping could lead to uncertainties in the actual concentration if the temporal resolution is insufficient. Fortunately, this issue can be avoided using a faster imaging method to increase the temporal resolution, or reducing the echo time to a minimum value.

Maintaining a sufficient temporal resolution to avoid phase wraps becomes increasingly difficult in animals, where the vessel used for the AIF measurement is not located near the tissue of interest (thus requiring two separate areas to image) and the injection time is short. Our results show that the concentration at the peak for a 30 mM bolus injection is approximately 1 mM. At this peak concentration, we could increase the echo time to 29.50 ± 0.14 ms before phase-wrapping becomes an issue at a field strength of 7 T. In general, a longer echo time will allow for greater phase sensitivity to a change in concentration, but will come at the cost of reduced SNR. Increasing the echo time too much could be detrimental to our measurement, as the subtraction of a noisy background profile could introduce additional sources of noise. It should be noted that even if phase wraps were to occur, the high temporal resolution of our approach is sufficient to detect of these wraps, even during the 'difficult', rapid enhancement period.

Contrary to magnitude-based imaging techniques, flow in blood vessels can not

be suppressed with saturation pulses. Our phantom experiment revealed a velocity-dependent phase shift when flow compensation was not used. This shift appeared to be consistent for all concentrations as the slopes of the phase-concentration curves were similar for all cases studied. When flow compensation was applied prior to data acquisition, the phase shift was reduced significantly. As shown in Figure 4.4b, the signal phases at each concentration were nearly identical for flow velocities of 15 and 30 cm/s. However, there was a small offset in phase between the steady-state and kinetic experiments. This could result from our assumption of plug flow through the tubing [126] and suggest that first-order phase compensation may be insufficient in the presence of variable flow velocities, such as observed during an injection or from the associated increases in heart and respiratory rates. Measuring the AIF in a vein would be advantageous for minimizing ambiguities during pulsitile flow.

When measuring the AIF in a vessel, it is important to take into account the relative orientation of the vessel with the main magnetic field. The geometry of the vessel or surrounding organs that contains contrast agent must be known for accurate characterization of the field phase shift. As discussed in the study by de Rochefort et al. [129], the individual phase shift effects can be written as a linear combination from individual organs. In special cases, a simplified model can be assumed. An example is describing the tail vein as an infinite cylinder in our study, which is justified as the length of the vessel is more than four times greater than the diameter [127]. More complicated organs may require that a shape factor is estimated. de Rochefort describes how to do this from MRI intensity images.

Partial volume effects are consistently a concern when the AIF is measured in a smaller artery or when the spatial resolution is limited due to requirements for a higher temporal resolution or tissue coverage. This can be minimized by analyzing only those pixels where the enhancement kinetics are rapid and follow the expected shape. However, the signal from the blood vessel and surrounding tissue are complex values, in which the resulting signal will contain both constructive and destructive contributions [82], thus making it difficult to separate the signal from each component.

van Osch et al. [127], studied the implications of using a gradient echo sequence for the AIF measurement and the impacts of PVEs on the concentration

measurement in the internal carotid artery. In their study, they oriented the vessel parallel and perpendicular to the main magnetic field to observe the effects of each. The signal in the extra-vascular compartment is expected to be time-independent for the parallel orientation, which makes it easier to address PVE issues. van Osch et al. confirmed that the vessel signal follows an inward spiral, where the signal magnitude decreases quadratically with increasing concentration and the phase increases linearly with concentration. When the signal is purely from within the vessel, the spiral is centered at the origin. While it is shifted away from the center as more tissue signal is included. Depending on the magnitude of the shift of the spiral, the AIF may be over or under-estimated, or very distorted [82]. PVE corrections were performed using two calibration curves: a R_2^* vs C curve, and a ϕ vs C curve. The correction was compared with the conventional method of selectively choosing voxels with the desired AIF characteristics. The results showed that the complex correction - using the calibration curves - did a significantly better job than the conventional method did. Our measurement did not address PVEs, but this could be a future area of study.

A major issue with using a metal catheter for the tail vein injection relates to significant SNR losses due to magnetic susceptibility effects. The catheter should be placed far from the sensitive region of the receiver coil to minimize this effect. From initial experiments (results not shown), we found minimal distortion and loss of SNR when the butterfly needle was placed outside the sensitive region of the tail surface coil. This complicates the set up as the injection needs to be done as close to the tip of the tail as possible, and the animal positioned such that the tail coil is closer to the animals body. An alternative is to use a non-metallic catheter. However, plastic catheters are less stiff and require more effort to use.

Bolus delays result from the the AIF and tissue of interest being measured at different locations, and so the AIF is temporally shifted relative to the contrast-uptake in tissue. This issue may be resolved by using a bolus delay-insensitive imaging sequence, a model that includes a bolus delay term, or the shifting all the concentration time curves to remove the delay before uptake [82]. Additionally, the use of a 2-D multi-slice imaging procedure for the DCE images means that each slice is acquired at a different time, and thus have different delay terms. This issue is easier to address as the order at which each slice was acquired is known.

Single MR projections are acquired rapidly and have potential for greatly improving the temporal resolution of the AIF. However, the data from one projection is noisier than a projection of an image. The SNR is known to improve by the square root of the number of lines used to reconstruct an image. As such, a single projection will be eight times noisier than an image acquired with sixty-four phase encode lines. The SNR can be maximized with a strip-line saddle coil for the tail, using a 90° flip angle and a minimum echo time.

Measuring the AIF in small animals is difficult due to the limited number of larger vessels. Some groups have chosen to measure the AIF in the left ventricle of the heart [13, 15, 143] or in the iliac artery [14, 100]. The left ventricle is attractive for its large size and relatively stationary blood for a short period of time. But, proper gating is essential for an accurate measurement. This can be difficult if the heart rate is too rapid. Measuring the AIF in the iliac artery may be advantageous as it is generally closer to the tissue of interest, but aligning it with the main magnetic field is challenging [100], and its proximity to a number of organs will make a projection-based approach more complicated. The tail was chosen for this application as it contains four large, widely spaced vessels (arteries and veins) and fewer anatomic structures in the background. Since the vessels are relatively straight and run the length of the tail, it is possible to increase the SNR with a thicker slice. However, care must be taken during set-up to ensure that the vessel is properly aligned before increasing the slice thickness.

Theoretically, the AIF is defined as the tissue response function for an instantaneous delta function injection. Since the actual injection takes place over a couple seconds, the AIF is determined from the convolution of the injection profile and the tissue response curve [82]. If a power injector is used, the injection profile may be assumed as rectangular. Figure 4.9a shows the expected form of the initial upslope with an assumed rectangular injection pattern with a double exponential. The AIF in the figure was measured in a mouse that weighed 24 g. As such, the Gd-DTPA injection had a volume of 120 μl, and was injected over a period of 7.2 s (1.00 ml/min injection rate). To aid our investigation, the duration of the bolus injection (red line) and the expected time at which a recirculation peak may occur (green line) were plotted. The recirculation time was estimated from an assumed blood volume of $6-8\%$ body weight [142] and a cardiac output of

0.73 ± 0.19 ml/min/g [144].

Comparing the expected upslope with the measured projection-based AIF reveals that the enhancement only follows expectations for approx. 3 s. Beyond this time, the curve levels off rapidly, despite more contrast agent being injected. Possible reasons for the disagreement between the simple model and our observation includes a non-rectangular bolus profile or early contrast perfusion into the extravascular-extracellular space (EES). When two fluids, having different concentrations of Gd-DTPA, share a boundary, diffusion can occur. Though an early test showed that mixing of the saline and contrast agent was minimal, it was never quantified. The duration from setting up the catheter until scanning the animal can be on the order of $30-60$ min. Even in the presence of very slow diffusion, the boundaries of the contrast injection will be smoothed, meaning that the injection profile may not be perfectly rectangular. It is possible that diffusion occurred at both boundaries. As shown in Figure 4.10, this would lead to a more gradual, s-shaped uptake at the start of the injection and a more rounded shape at the end of the injection with a lower maximum concentration. This is consistent with our observations and could result from a lower bolus concentration at the end. The overall impact will greatly depend on the rate and extents of diffusion.

A second issue with diffusion is the ambiguity of the start of the injection if the initial upslope is shallow, which is possible with a trapezoidal injection profile. Early uptake of the contrast agent into the EES would reduce the concentration of contrast agent in the blood plasma. As a result, the maximum concentration reached would be lower than expected. The rate of perfusion is known to be dependent on the concentration gradient between the blood plasma and tissue. At the onset of the injection, the concentration gradient is large, so contrast agent will perfuse at a much faster rate than near the end of the injection when the contrast gradient is smaller as observed. Again, this could cause ambiguity in the location of the start of the injection. Based on the figure, the injection protocol will have a significant impact on the early enhancement characteristics of the curve. As such, the AIF should be measured for each injection protocol used. The projection-based AIF technique will help reduce errors when injections differ between experiments.

The injected bolus will flow through the vasculature towards the heart, where it mixes with blood coming from other areas of the body. This mixing causes

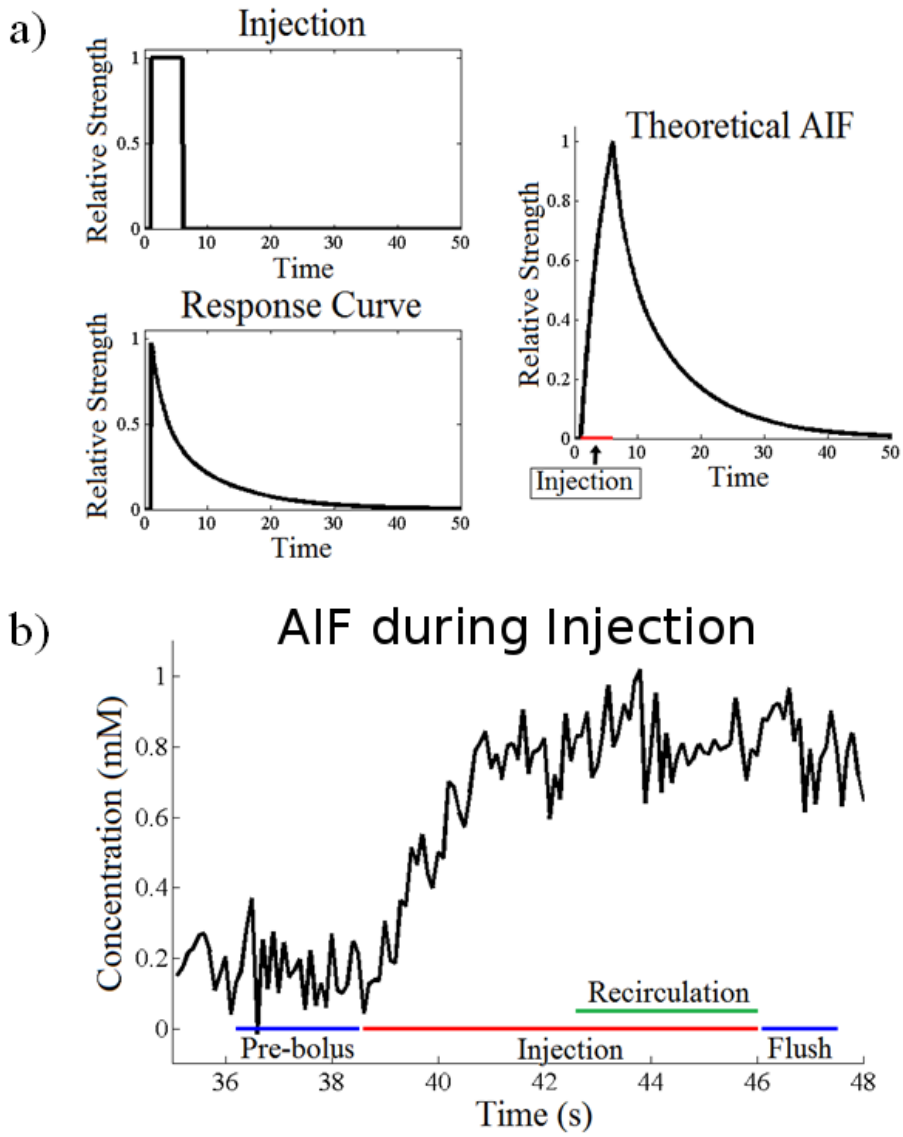

Figure 4.9: Impact of the injection protocol on the expected shape of the AIF. The expected shape for a square injection protocol, with a double exponential clearance from the vasculature, is shown in a), while the observed upslope from the projection-based AIF is shown in b). These results show that the shape of the AIF differs from expectations when measured in-vivo.

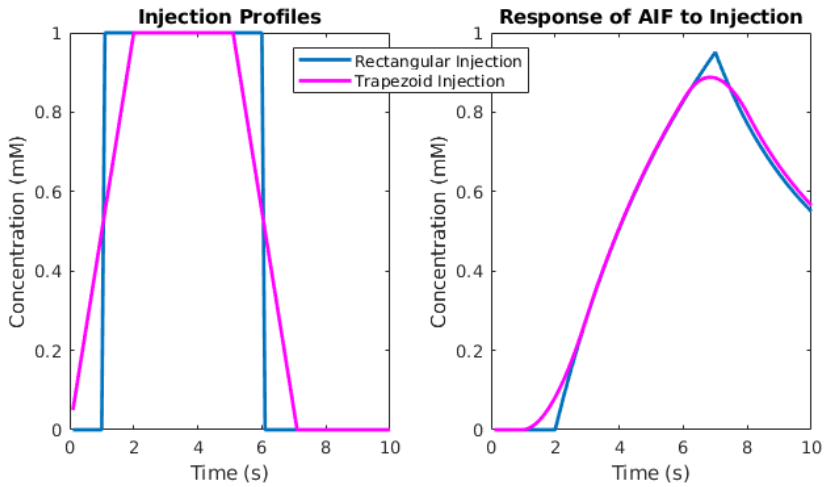

Figure 4.10: Effects of diffusion of the contrast agent in the injection line. A rectangular or trapezoidal injection profile is convolved with a proposed double exponential tissue response curve. The expected rectangular injection profile shows a steady increase in blood concentration for the entire duration of the injection. The trapezoidal injection profile, however, produces a rounded shape at the start and end of the injection, and a lower peak concentration.

dispersion of the bolus, such that a second pass of the bolus will have a lower concentration. The bolus may experience further dispersion after passing through the lungs and left atrium and ventricle. In general, the recirculation peak has a wider width than the first pass. This results from recirculation of blood from all over the body, not just the site of interest. The green line in Figure 4.9b suggests that the recirculation peak may be masked by our injection, and will not be observed in an animal model. This is consistent with another animal-based study [17].

This chapter laid out the frame-work for measuring the AIF from a set of MR projections. We were successful in measuring the AIF in several mice (temporal resolution of 100 *ms*), showing that though the shape is consistent between mice, there are subtle differences representing the physiology of the individual at the time of the scan. One limitation of this technique is the loss of information in a second spatial dimension. Perfusion of the contrast agent into the surrounding tail tissue could lead to local tissue enhancement, and alter the shape of the acquired projec-

tion profile. The projection-based AIF assumes that any change in the projection profile is solely a result of changing signal within the vessel. Not accounting for addition siganl changes in the nearby tissue would lead to a bias in the measured intra-vascular concentration. It is expected that tissue enhancement will occur at a slow rate relative to changes in the blood. Therefore, it may be possible to measure the degree of tissue enhancement temporally and correct the projections for it. This is the focus of the next two chapters.

Chapter 5

Radial MR Imaging

The AIF is typically measured through the change in the T_1 of blood plasma in MR images after a bolus of contrast agent has been administered [5]. The temporal resolution of the AIF measurement is often limited by the time required to collect data for one image, which is typically on the order of seconds [5]. This resolution may not be sufficient if the contrast kinetics in the blood are rapid. As discussed in the previous chapter, the temporal resolution may be accelerated with a projection-based method. Projections are expected to significantly improve the temporal resolution of AIF measurement as only one line in k-space is needed.

The projection-based AIF measurement assumes that all contrast agent remains within the vessel. Under this assumption, any observed change in the projection profile can be attributed directly to a change within the intra-vascular contrast agent concentration. However, most vessel walls are permeable to the contrast agent, thereby allowing some to purfuse into the surrounding tissue [74, 75]. The contrast agent will interact with the tissue protons, leading to local concentration-dependent signal magnitude and phase changes in the tissue[55]. In effect, the shape of the measured projection profile will be biased. These local changes in MR signal are referred to as tissue enhancement. Without compensation for tissue enhancement, the AIF measurement may be incorrect.

The goal of this chapter is to compare three radial reconstruction methods and determine which is best suited for visualizing local tissue enhancement. Radial sampling is attractive since every projection passes through the center of k-space,

and could be used as a single measure for the AIF. Three methods of radial reconstruction were applied to the data: 1) Re-gridding the radial data onto a Cartesian grid, 2) Spatio-Temporal Constrained Reconstruction (STCR) and 3) the Non-Equidistant Fast Fourier Transform (NFFT). In addition, three sampling schemes - uniform, Golden angle and random - were investigated.

5.1 Radial MRI

MRI data is collected as a series of signal projections in k-space. Two common methods of data collection include rectilinear, where series of parallel lines are acquired, or radial sampling in which a set of radial spokes are collected [145]. The reconstruction of MRI images from radial data dates back to the early days for MRI [53]. It was considered undesirable due to non-uniform sampling of k-space data [48], the presence of streaking artifacts [71], longer scan times [146] and the inability to apply the FFT algorithm directly to the k-space data [46, 147, 148].

For these reasons, radial reconstruction has not been studied in great detail until recently, when more advanced techniques, such as highly constrained back projection (HYPR) [149] or FOCal Underdetermined System Solver (FOCUSS) [150], proved to construct high quality images. Radial reconstruction is considered advantageous over rectilinear reconstruction since all radial spokes are equally important for image reconstruction, the spokes always cross the center of k-space, image quality is not significantly deteriorated with the removal of radial spokes, object details can still be visualized, even with few radial spokes [145], and motion and flow artifacts are suppressed [46]. The last point is attractive for studies involving blood flow in a mouse tail.

The first radial images were reconstructed using filtered back-projection [151], a technique borrowed from CT. Filtered back-projection uses the Inverse Radon transform and operates on the principle of the central slice theorem, which states that the 1-D Fourier Transform of a projection is equal to the projection of the 2-D FT of the image along a radial spoke passing through the origin [33, 152]. The radial spoke and projection are both taken for the same angle. In this respect, full images may be reconstructed from a series of radial projections taken from a number of different angles spanning π radians. This technique had limited scope

in MRI, and was later replaced with a gridding method [50, 52].

Re-gridding involves interpolating the k-space data onto a Cartesian grid, compensating for the variable sampling density, and applying the FFT algorithm [50–52]. Radial reconstruction has gained popularity with the introduction of more advanced techniques, include the NFFT [74, 147, 153] and STCR [154, 155].

5.2 Improved Temporal Resolution with Compressed Sensing

compressed sensing (CS) is a technique that allows MR images to be acquired rapidly by only acquiring a subset of k-space. It was first introduced by Lustig et al. with their innovative paper in 2007 [156]. A full analysis of CS is beyond the scope of this thesis, but the main concepts are paramount for our application in which CS is applied in radial MRI. The following section briefly overviews the theory and methodology.

CS operates on the premise that any image with a sparse representation can be recovered from randomly undersampled data, provided an appropriate non-linear recovery scheme is available. The technique was initially motivated by knowledge of image compression, in which an image may be represented with less data without a noticeable loss in visual quality. The compressed image was instead represented as a vector of sparse coefficients that would hold the important image data. This lead to questions about whether it was necessary to collect data over the entire k-space if these images are also compressible. Extending the theory of CS to MRI, Lustig proposed to reconstruct an image from sampled linear combinations of individual Fourier coefficients or k-space samples.

Sparsity means that relatively few voxels ($n \ll N$) have a non-zero value. For the purposes of his article, Lustig focused on images that have sparsity in a fixed mathematical transform domain. Since MRI data is implicitly sparse in k-space, significant reductions in the total scan time is possible by acquiring fewer phase-encode lines. There are three main assumptions regarding the data:

The data requires a sparse representation. This includes pixel sparsity in angiograms, spatial (edges) or temporal finite difference sparsity, sparsity in the images wavelet coefficients or sparsity in k-space.

The data should be randomly sampled, such that it creates incoherent artifacts in the transform domain (appear as additive random noise). Since MRI contrast is found at the center of k-space, variable sampling density (ie. pseudo-random) will selectively sample data more densely here. Radial sampling is unique in that the artifacts from under-sampling are incoherent streaking artifacts [157], even with uniform angular sampling.

A non-linear reconstruction is used to enforce both sparsity of the image representation and consistency with the acquired data.

Under these assumptions, and in the sparse domain, image artifacts become incoherent and may be removed with non-linear thresholding. This leaves only the significant coefficients, which contain information about the desired image. The reconstruction is performed by solving the constrained optimization problem:

$$minimize \|\psi m + P\|_1 \qquad s.t. \qquad \|F_u m - y\|_2 < \varepsilon \tag{5.1}$$

Where ψ is the linear operator that transforms from pixel representation into a sparse representation, m is the reconstructed image, F_u is the undersampled Fourier transform, y is the sampled data, ε controls the fidelity of the reconstruction to the measured data and $\|.\|_{1,2}$ represents the mathematical $L_{1,2}$ norm. P is a penalty term which is commonly the total variation constraint (TV).

To summarize the steps of the optimization, the randomly sampled, sparse data shows the strong components and incoherent artifacts that appear as additive noise. It is known that the strong components leak energy into the surrounding voxels when the Nyquist criteria is not met. This leakage energy is determined by thresholding the raw signal and calculating the interference from the remaining signal using the point spread function. After subtracting off this interference, the interference level is significantly reduced and previously hidden components are discovered. The process is repeated until convergence.

In their paper, they compared Cartesian images reconstructed as low resolution, zero-filled with density compensation and the above algorithm. The results showed that the CS images best reproduced fine details (lost in the low resolution images) and did not suffer from interference artifacts like the zero-filled images did. The image quality was good for high acceleration factors, as long as variable density

sampling was used, and if the sampling pattern differed between slices for the multi-slice acquisition. CS is most effective with high contrast images as the strong coefficients are often sparse. Lustig argues that the worst artifact is loss of low contrast features as these may be submerged within the incoherent artifacts.

5.3 Methods of Radial Image Reconstruction

Local tissue enhancement may be visualized in MRI images acquired for the duration of the DCE study. To maintain the high temporal resolution of our AIF measurement, a radial acquisition scheme is applied. In this sense, every projection is used in the estimation of the AIF and in a sliding-window reconstructed image to assess local enhancement.

Three radial reconstruction techniques are compared in this study: 1) Regridding the data onto a Cartesian grid with Shepard's method of interpolation [158], 2) STCR [155] and 3) NFFT [159].

5.3.1 Regridding

Radially sampled data may be represented in k-space as a set of 'spokes' which intersect at the center [145]. This data often does not fall onto a Cartesian grid, so it must be first interpolated before applying the FFT [160]. The simplest radial reconstruction technique is re-gridding the radial data onto a Cartesian grid [50]. The technique involves the interpolation of the data onto a Cartesian grid, compensating for the non-uniform sampling density across k-space [46], and performing the 2-D FFT [52].

Data interpolation may be done with a convolution Kernel [50]. The performance of the re-gridding method is known to be dependent on the choice of the convolution Kernel. Other interpolation methods, such as Shepard's method or Delaunay triangulation may also be used. Shepard's method involves assigning all data points to a pixel and calculating a weighted sum for each pixel [158]. The weighting is defined as the inverse distance from the center of the pixel.

5.3.2 Spatial-Temporal Constrained Reconstruction

Another technique - STCR - uses spatial and temporal constraints to reconstruct high-quality images from sparse k-space data [154, 155]. Images are reconstructed through the minimization of a cost function:

$$C = ||WFm - d||_2^2 + \alpha_1 ||\sqrt{\nabla_t m^2 + \varepsilon}||_1 + \alpha_2 ||\sqrt{\nabla_x m^2 + \nabla_y m^2 + \varepsilon}||_1 \quad (5.2)$$

The first term represents the data fidelity which quantifies the error between the estimated solution and acquired data. Here, $||.||_2$ represents the L_2 norm, W is the binary under-sampling pattern used to obtain the sparse data, F represents the two-dimensional Fourier Transform, which is applied to each time-frame in the dynamic sequence, m is the estimated image data and d is the acquired k-space data. The second and third terms represent the temporal and spatial total variance (TV) constraint terms, and are regularized by the parameters α_1 ($= 0.04$) and α_2 ($= 0.006$). Here, ∇_t represents the temporal gradient operator, ∇_x and ∇_y are the gradients of the image in the x and y directions, respectively, $||.||_1$ represents the L_1 norm, and ε is a small positive constant used to avoid singularities in the derivative of the functional. The authors chose the TV constraints to help resolve artifacts from under-sampling, while preserving spatial edges and improving the SNR. This technique has been shown to reconstruct high-quality images with as little as 15% of a complete data set (under-sampled in the radial direction) [154]. They define accuracy as the ability to successfully resolve fine details with minimal occurrence of image artifacts.

5.3.3 Non-Equidistant Fast Fourier Transform

The third technique is the NFFT [159], which reconstructs an image from data sampled at non-equispaced nodes [161]. The NFFT is an iterative technique that solves for the image as an inverse problem [162]. The algorithm estimates an MR image from the non-uniformly sampled k-space data [153, 161], then compares its FT domain signal to the acquired k-space data at the known trajectory locations [162]. This comparison involves interpolating the FT data of the image, with triangulation, at the known input node locations.

Since the FT and interpolation steps are linear, they may be combined into a systems matrix, A. This provides the forward problem:

$$\mathbf{y} = \mathbf{A}\mathbf{x} \tag{5.3}$$

Where y is the acquired k-space data (under-sampled), and x is the image vector. This problem is best solved iteratively since the image vector may be large, the problem is ill-imposed due to under-sampling and the data vector could be contaminated with Gaussian noise [162]. The first iteration of the NFFT is equivalent to regridding the data onto a Cartesian grid [160], but without a density compensation. Further iterations enhance the accuracy of the reconstruction with the L_2 norm of the residuum - which is the cost function for the problem [162].

$$\phi(\mathbf{x}) = \frac{\mathbf{1}}{\mathbf{2}}||\mathbf{A}\mathbf{x} - \mathbf{y}||_{\mathbf{2}}^{\mathbf{2}} \tag{5.4}$$

The goal is to find a vector x, that minimizes the cost function ($x = \frac{argmin}{x}\phi(x)$). Block chose a variant of the conjugate gradient method to perform the minimization. Interested readers can refer to Chapter 5 of his thesis ([162]) for specific details.

5.3.4 Sampling Schemes for Radial Data Collection

Radial sampling may be performed in numerous ways. The most common modes are incremental sampling, where all projections are equally spaced and collected in either ascending order or alternating positive and negative angles [163], and Golden angle sampling [164], where the angular spacing between consecutive projections is 111.246^o. Random sampling may be used when a compressed sensing algorithm is used. Albeit, this form of sampling may be less efficient than Golden angle in covering k-space, which could introduce additional artifacts. Figure 5.1 provides an example of the distribution of k-space data for the three sampling methods.

Golden angle sampling is based on the golden ratio [165], but over 180° since parallel opposed projections contain the same MR information. The idea is that the projections will cover the entirety of k-space quickly and quasi-uniformly. For the most efficient coverage, a Fibonacci number of projections should be used. Under

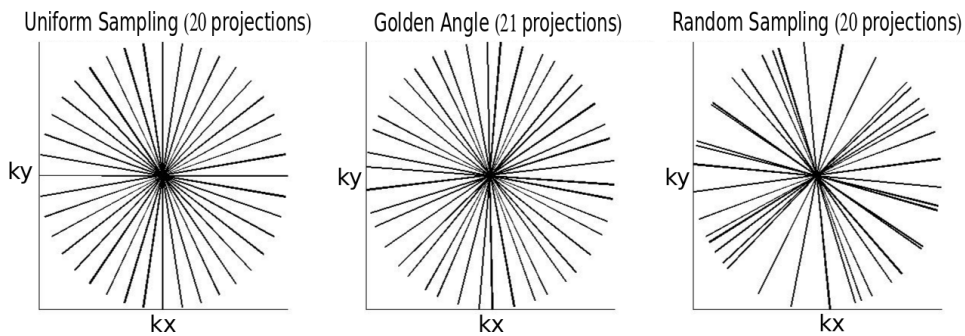

Figure 5.1: The three sampling techniques investigated. For a better visual comparison, the figure shows the sampling distribution for 20 or 21 projections. a) shows uniform spacing between the projections. b) is for Golden Angle sampling where the angular spacing between consecutive projections is 111.246^o. And c) is for random sampling where the chosen angles of acquisition are selected randomly.

these conditions, there are two unique gap sizes (Figure 5.2a): F_{i-1} larger gaps and F_{i-2} smaller gaps, where F_i is the Fibonacci number equal to the number of projections used in the reconstruction. If a non-Fibonacci number of projections are used, there will be three different gap sizes as shown in Figure 5.2b.

5.4 Comparison of Radial Imaging Techniques

The goal of this study is to determine the radial reconstruction technique that is best suited for our application. Suitability is defined as the ability of the technique to reproduce the image with good accuracy (magnitude and phase) and having minimal interference from image artifacts. Since the projection-based AIF measurement requires an estimate of the background signal, a projection of the reconstructed images - perpendicular to the direction of 'read-out' - is performed. These are compared to the expected projection profiles to quantify the effect that tissue enhancement has on the measurement of a projection-based AIF.

5.4.1 Methods

To evaluate the potential of using radial projections to estimate tissue enhancement, a cylindrical phantom of similar dimensions to a mouse tail was used. A

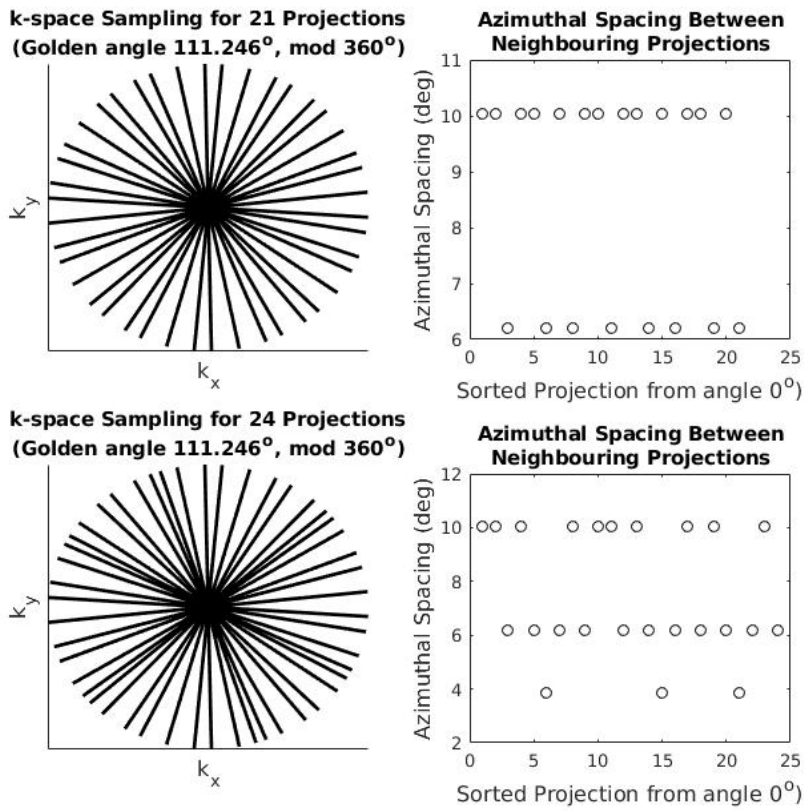

Figure 5.2: Angular gap spacing between neighboring projections when Golden angle sampling (111.246^o spacing) is used. If the number of projections is a Fibonacci number, $F_(i)$, then there are two unique gaps sizes: F_{i-1} of the larger gaps and F_{i-2} of the smaller gaps. But if the number of projections is not a Fibonacci number, then there are three unique gaps sizes. This suggests that a Fibonacci number of projections is required for optimal uniformity in k-space if Golden angle sampling is used.

small capillary tube, of inner diameter 0.4 mm, was placed inside a larger glass tube, having internal diameter 3.7 mm. The larger cylinder was 9.2 cm in length, while the capillary tube was slightly longer to provide attachment points on either side for the injection line. The space between the tubes was filled with saline to act as tissue. Meanwhile, a solution of Gd-DTPA, diluted with saline to a final concentation of 5.0 mM, was injected through the capillary tube to represent blood. To avoid additional artifacts due to motion, the Gd-DTPA solution was stationary for this experiment.

The Cartesian image was acquired with a FLASH experiment on the Bruker 7 T MRI scanner. Signal excitation was done with a volume coil, and signal collection with a custom-made stripline surface coil designed for a mouse tail. The scan parameters were TE = 5.00 ms, TR = 100 ms, flip angle = 30°, FOV of $15x15\ mm^2$, matrix size of $256x256$. Radial data was acquired with the same scan parameters, but with 233 equi-spaced angles over 360°. The number of angles was chosen because it is a Fibonacci number, it is sufficiently small such that the sampling scheme may be repeated in a reasonable amount of time, and has the smallest residual for Golden angle sampling (determined from the modulus of $(1:360) \cdot 111.246^o$ with 360°). The flow compensated FLASH experiment was chosen for this analysis as this will be used to study the mouse tail later.

The k-space data was read manually into Matlab, and processed such that the echo occurred at the center of the projection with phase 0 rad. The Cartesian image serves as the reference scan with which to compare the fully sampled radial reconstructions.

5.4.2 Reconstruction of Radial Images

Radial images were reconstructed with re-gridding, using Shepard's method of interpolation onto a Cartesian grid, STCR and the NFFT. Since Shepard's method of interpolation takes a weighted average of all data points within each pixel, a density compensation filter was not applied.

Reference radial images were constructed with each technique using all 233 unique angles. These serve as the gold standard with which to measure the degree of image degradation when fewer projections were used. This is a better compar-

ison than the Cartesian image as image artifacts and phase distortions observed in the reference image are likely to show up in the under-sampled images as well. All reconstructed images were normalized to have a mean value of 1 as this is more stable than using the image maximum in the presence of noise.

With a repetition time of 100 ms, the time required to construct a fully sampled image is 23.3 s. This may be too coarse to accurately characterize the rate of tissue enhancement following the injection. Radial images were reconstructed with 144, 89, 55, 34 and 21 projections (decreasing Fibonacci numbers) to help identify the optimal temporal resolution for characterizing local tissue enhancement. Three sampling schemes were compared: uniform angular distribution, Golden angle [164], and random angular sampling. The angular increment for uniform sampling was set to $360^o/N$, where $N = 233, 144, 89, 55, 34$ and 111.24^o for Golden angle. With random sampling, the projection numbers were randomly sorted, and the first N projections were selected. This prevented the algorithm from using the same angle twice and allowed for the pattern to be repeated.

For Shepard's method of interpolation, a pixel was defined as the area within 0.5 voxels of the center of a pixel. The value of the pixel was set to the weighted sum of all data points within the pixel area. The weights are the inverse distance of the sampled data location from the center of the pixel. Any sampled data point falling on the Cartesian grid is assumed to be exact and set as the pixel value. The center of k-space was sampled for all projections, so the signal is determined as the mean from all projections. The Nyquist criteria is usually not met at the edges of k-space due to a limited number of projections. As a result, the re-gridding matrix was zero-filled to prevent ringing artifacts due to truncation of data. The 2-D FFT was applied to the data matrix to produce the image.

Matlab code for the STCR [155, 166] and NFFT [159] techniques are available online. The downloaded code was modified for both to allow for Golden angle and random angle sampling over 360°. To adjust for angle dependent shifts in the echo position, the center-of-energy of the first 233 projections was calculated. This is similar to the center of mass, where the 'energy' is related to the signal magnitude. Each projection was individually shifted, such that the echo was properly centered. A zeroth-order phase correction is applied by multiplying each projection by $e^{-i\phi_{echo}}$ where ϕ_{echo} is the phase of the center pixel (i.e. the echo). This

approach generally centered the echo better than the method outlined by Anh and Cho (1987) [167].

All projections were then normalized to have a maximum signal intensity of 1 at the echo. A sinogram of the radial k-space data, which is a plot of the projections along the y-axis and the angle of acquisition along the x-axis, showed that the position of the maximum of each projection followed a sinusoidal curve (amplitude of 1 pixel). The sinusoidal pattern was not an issue with the image reconstruction. In fact, keeping the pattern in the k-space sinogram provided the most consistent phase between the radial reconstructions and the Cartesian image. Smoothing it out often lead to image artifacts due as the appearance of the echo had a jagged appearance with angle.

Images are compared qualitatively and quantitatively to determine the number of radial projections required to produce an image of sufficient quality to accurately visualize tissue enhancement. The qualitative investigation involved visually comparing the Cartesian image with each radially reconstructed image. The images are considered sufficient for our application if the signal contrast between important features (edges, vessel vs. tissue) was correctly represented and no phase artifacts were observed in the object.

Quantitatively, images were compared using the Structural SIMilarity index (SSIM) index [168] (MATLAB code available at http://www.cns.nyu.edu/ lcv/s-sim/). The index attempts to automatically predict perceived image quality by looking at local patterns of pixel intensities and signal dependencies after the image has been normalized for luminance and contrast. Image degradation was based on perceived changes in the structural information within the image.

The SSIM compares the reconstructed image to a reference image on three levels: luminance, contrast, and structure. These are estimated from the mean of the signal intensity, the variability of the data via the standard deviation of the signal and the normalized difference from the mean, $((x-\mu_x)/\sigma_x)$, respectively and are relatively independent of one another. The SSIM is calculated as follows:

$$SSIM = \frac{\sum_{j=1}^{M} [\frac{2\mu_x\mu_y + C_1}{\mu_x^2 + \mu_y^2 + C_1}]^{\alpha} [\frac{2\sigma_x\sigma_y + C_2}{\sigma_x^2 + \sigma_y^2 + C_2}]^{\beta} [\frac{\sigma_{xy} + C_3}{\sigma_x\sigma_y + C_3}]^{\gamma}}{M} \tag{5.5}$$

Where M is the number of voxels, μ_x is the average signal of the reconstructed image, μ_y is the mean signal of the reference image, σ_x is the standard deviation of the signal in the reconstructed image, σ_y is the standard deviation of the signal in the reference image and σ_{xy} is the correlation of the two signals from their respective means $(x - \mu_x)$. α, β and γ are weighting factors for the luminance, contrast and structure comparisons. For our analysis, they were all set to 1. Finally, C_1, C_2 and C_3 are small constants to avoid instability when one of the denominators approaches zero. This equation has a maximum value of 1 when the two images are identical.

The above equation is used to evaluate the global quality of the image. For a local investigation, the statistics are computed for a smaller square window (eg. 8x8 voxels^2), which moves pixel-by-pixel over the entire image. This provides more information about distortions throughout the image from a spatially varying quality map, thus allowing for a more thorough comparison. The mean Structural SIMilarity index (mSSIM) is the average of all the local values spanning the image. See [168] for more details.

The SSIM index is a full-reference image quality assessment, which means that the complete reference image must be known. Our analysis satisfies this condition, as we have a fully sampled Cartesian and Radial images to use as a reference. It is important to note that the SSIM only compares the magnitude of images, leaving phase comparisons to subjective evaluation. Comparing the phase maps of the images may not be resourceful in cases where there is a global phase shift or phase gradient across the image.

5.4.3 Results: Fully Sampled Radial Images

The reference radial images are displayed in figure 5.3. The signal intensity in the reference radial images using Shepard's method of interpolation and STCR differ from the reference Cartesian image. The angle of the signal gradient is greater than that observed in the Cartesian image. As a result, a signal intensity cold spot appears in the top right-hand section of the main phantom and a hot spot in the lower left-hand side. Visually, the NFFT technique best resembles the signal intensity gradient of the Cartesian image in the main part of the phantom. In all

radial images, the signal intensity of the second, smaller phantom is comparable. Though the edges are blurred in the Shepard's interpolated and STCR reference images. Image artifacts are observed in all reference images (including the Cartesian image), however they are low intensity and do not appear to affect the signal representation of the phantom.

The signal intensity of the capillary tube shows a significant drop-off from the center. The signal intensity is comparable between all radial reference images, but lower than that of the Cartesian image (2.27 ± 0.07), even at the center. The signal of the entire capillary tube is 1.48 ± 0.18 for Shepard's method of interpolation, 1.42 ± 0.27 for STCR and 1.43 ± 0.29 with the NFFT algorithm. The signal intensities improve at the center of the capillary tube to 1.90 ± 0.10 for Shepard's method of interpolation, 1.98 ± 0.11 for STCR and 2.02 ± 0.12 for NFFT. This may be attributed to signal smoothing between the high-intensity vessel and the low-intensity annulus surrounding the vessel.

Since all three reference images have the artifact, it is likely a consequence of the radially acquired data. The k-space sinogram - an image of the echos as a function of the angle of acquisition - shows that the echo is well centered for all angles. The location and intensity of the echo does deviate slightly (following a sinusoidal curve with period 233 projections), but it's generally off-set by less than 1 pixel from the desired location. It is possible that the MR trajectory misses the center of k-space for some angles (see Appendix B), which could introduce artifacts into the reconstructed image. The echo was centered with a sub-pixel shift in k-space and a zeroth-order phase correction prior to image reconstruction. Other methods of echo centering also produced the artifact. The chosen centering method produced the best visual images and the largest mSSIM value.

Taking the percent difference between the radial reference images and the Cartesian image, relative to the Cartesian image, confirms the above observations (Figure 5.4). The difference with Shepard's method of interpolation and STCR both have similar characteristics.

The signal intensity difference is greatest on the superior and inferior sides of the phantom, with percent differences on the order of $20-40\%$ and $10-20\%$, respectively. The percent difference drops to $0-10\%$ in the mid-section of the phantom. The difference between the Cartesian reference image and the NFFT

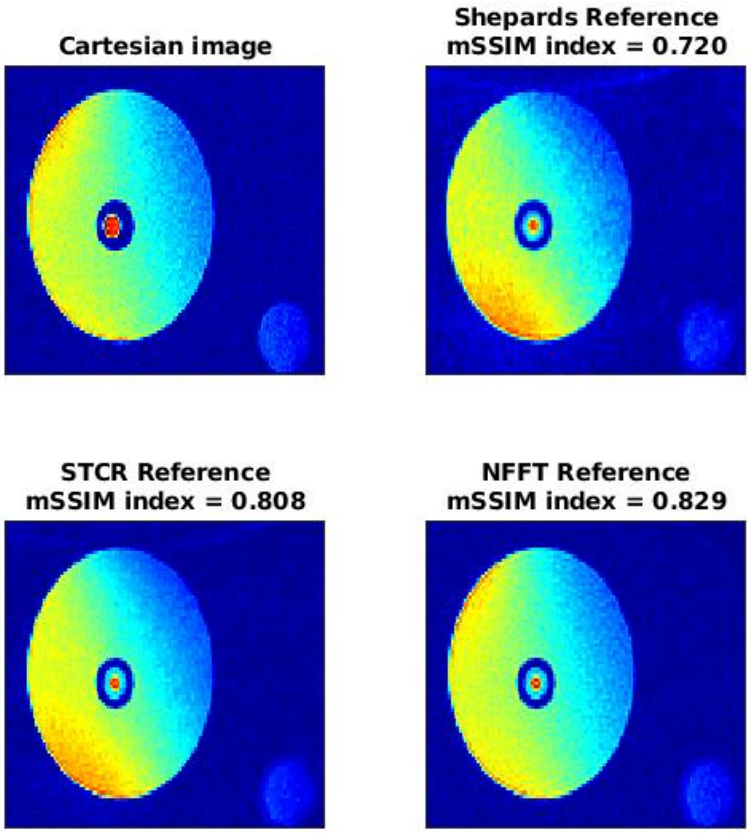

Figure 5.3: Reference radial magnitude images (233 projections) reconstructed with one of Shepard's method of interpolation, Spatial Temporal Constrained Reconstruction (STCR) or the Non-equidistant Fast Fourier Transform (NFFT). The mSSIM indices are recorded in the title, which indicates how closely these images compare with reference Cartesian image in terms of luminance, contrast and structure.

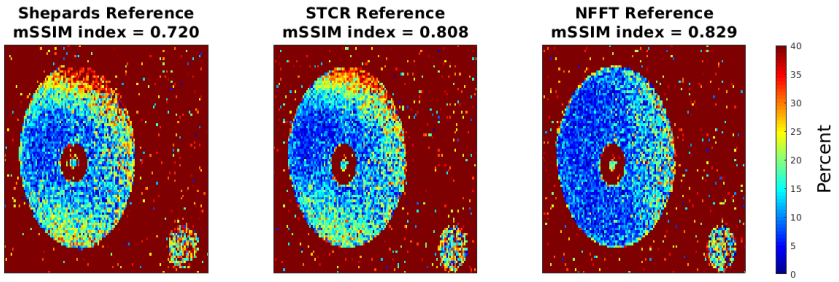

Figure 5.4: Percent difference between the reference Cartesian image and the radial reconstructions, relative to the Cartesian image.

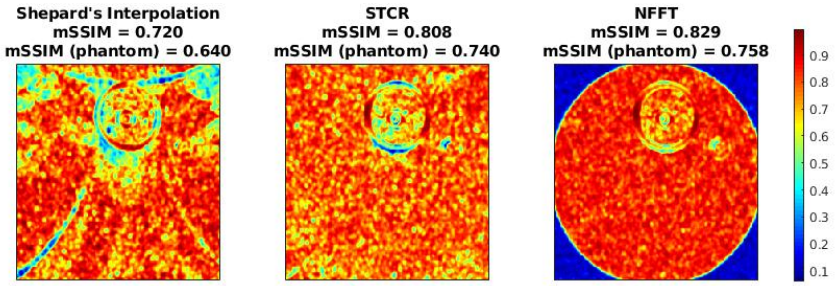

Figure 5.5: Structural SIMilarity (SSIM) index maps for the reference radial images. The mean SSIM (mSSIM) indicies for the entire image and only within the phantom are listed in the title.

reference image is more uniform throughout the main phantom, on the order of $0-10\%$ on the left hand side, and increasing to $10-20\%$ towards the right side. The signal intensity of the phantom is strongest on the left hand side, and gradually decreases towards the right side. The higher percent error on the right hand side of the NFFT image could be a direct result of the signal drop-off. The magnitude difference (Radial - Cartesian) is nearly uniform for the NFFT image, and has hot-spots on the superior and inferior regions with Shepard's method of interpolation or with the STCR reconstruction. Based on these results, the NFFT would be the best reconstruction technique.

Visually, the NFFT produces the most accurate image, followed by STCR, then Shepard's method of interpolation. These rankings are consistent with the mSSIM

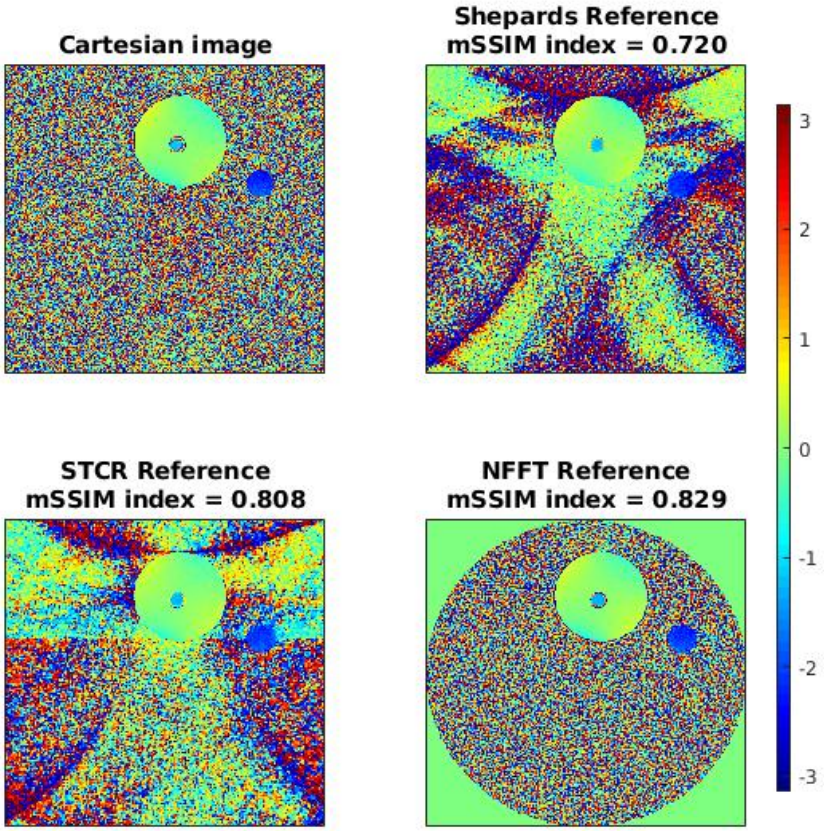

Figure 5.6: Reference radial phase images (233 projections) reconstructed with one of Shepard's method of interpolation, Spatial Temporal Constrained Reconstruction (STCR) or the Non-equidistant Fast Fourier Transform (NFFT). The phase has a similar structure in all images and varies slightly wihtin the capillary tube.

index, with values of 0.720, 0.808 and 0.829 for Shepard's method of interpolation, STCR and NFFT, respectively. Maps of the SSIM index are shown in Figure 5.5.

As shown in the figure, the SSIM index is lowest at the edges of the phantoms and at the image artifacts. This suggests that there may be signal smoothing at the edges or a slight misalignment between the images. It is interesting that the mSSIM

is lower in the phantom than it is across the entire image (exception with the NFFT, in which the region within a radius of 128 voxels was used). The lower intensity of the background, void of structural edges, may cause this. Both Shepard's method of interpolation and STCR had similar intensity features within the phantom, so the lower mSSIM of the Shepard's image is likely related to the increased presence of image artifacts in the background.

The phase images for all three radial reconstructions (Figure 5.6) show similarities with the reference Cartesian image. In all images, the phase appears to have a band structure, with cold spots in the upper right-hand and lower left-hand regions of the phantom. In addition, the phase of the smaller, external phantom appears similar in all images. Streaking artifacts, originating from the phantom, are visible in both the Shepard's method of interpolation and the STCR techniques.

The phase of the capillary tube varies slightly between the four reference images and appears to be consistent across the entire capillary tube. The Cartesian image has an average phase of -1.17 $\pm$ 0.017 rad, while the three radial images have average phases of -1.26 $\pm$ 0.017 rad for Shepard's method of interpolation, -1.28 $\pm$ 0.026 rad in the STCR image and -1.33 $\pm$ 0.018 rad in the NFFT image. The subtle differences between the three radial techniques could be due to the method used for data interpolation and weight compensation. The larger difference could be related to data centering in k-space, which involves one dimension with the radial data and in two orthogonal dimensions with the Cartesian images. Centering for the Cartesian image was done with integer shifting, based on the most probable location for the maximum.

5.4.4 Radial Reconstructions with Fewer Projections

With a temporal resolution of 0.100 s, it would take 23.3 s to acquire data for a complete radial image. This temporal resolution may be too coarse for a DCE-MRI experiment, hence it would be advantageous to reconstruct images with fewer radial projections. Accelerated radial images were reconstructed with descending Fibonacci numbers of projections (144, 89, 55, 34 or 21) with all three reconstruction techniques and sampling schemes. Images are considered sufficient if the boundaries of structures are well defined, contrast between neighbouring regions

is preserved and there are minimal image artifacts. Figure 5.7 summarizes the radial images (both magnitude and phase) reconstructed with 55 projections. Those reconstructed with 144, 89, 34 or 21 projections are reviewed in Appendix A.

The magnitude images with 55 projections reveals that uniform and Golden angle sampling produce similar quality images, and are most comparable with the reference radial image (using all 233 projection angles). Images with random sampling are more blurred, have more artifacts, and in the case of NFFT significantly reduced signal intensity. Images reconstructed with Shepard's method of interpolation or STCR have a hot spot in the lower left-hand quadrant, and a signal cold spot in the upper right-hand quadrant. This is consistent with the reference images, suggesting that the artifact is related to the reconstruction method. The signal intensity of the capillary tube is visibly lower with all three techniques, relative to the reference image: 82.8 (uniform) and 89.0% (Golden angle) for Shepard's, 75.9 (uniform) and 85.0% (Golden angle) for STCR and 82.3 (uniform) and 93.1% (Golden angle) for NFFT.

The phase of the radial images are dependent on the reconstruction method used. All three reconstruction methods have a distinct streaking pattern in the background that radiates out from the main phantom. The patterns are similar between Shepard's method of interpolation and the STCR, while the streaks have greater clarity with NFFT. With all reconstruction methods, the phase is similar when uniform or Golden angle sampling is used, and more blurred for random sampling. The phase of the capillary tube is uniform for all reconstructions, except for random sampling and NFFT where streaking artifacts affect the entire image. In general, the average phase is within 4% of the phase of the reference radial images, which is satisfactory. The phase contrast between the smaller external phantom and the background is best with STCR (uniform and Golden angle sampling) and NFFT (all sampling methods). However, there are spatial modulations in the phase due to background streaking artifacts.

Based on these images, the NFFT appears to be the best radial reconstruction method, followed by STCR, then Shepard's method of interpolation. The image quality is significantly greater with uniform or Golden angle sampling compared with random sampling. Figure 5.8 compares the under-sampled radial images reconstructed with STCR or NFFT and uniform or Golden angle sampling.

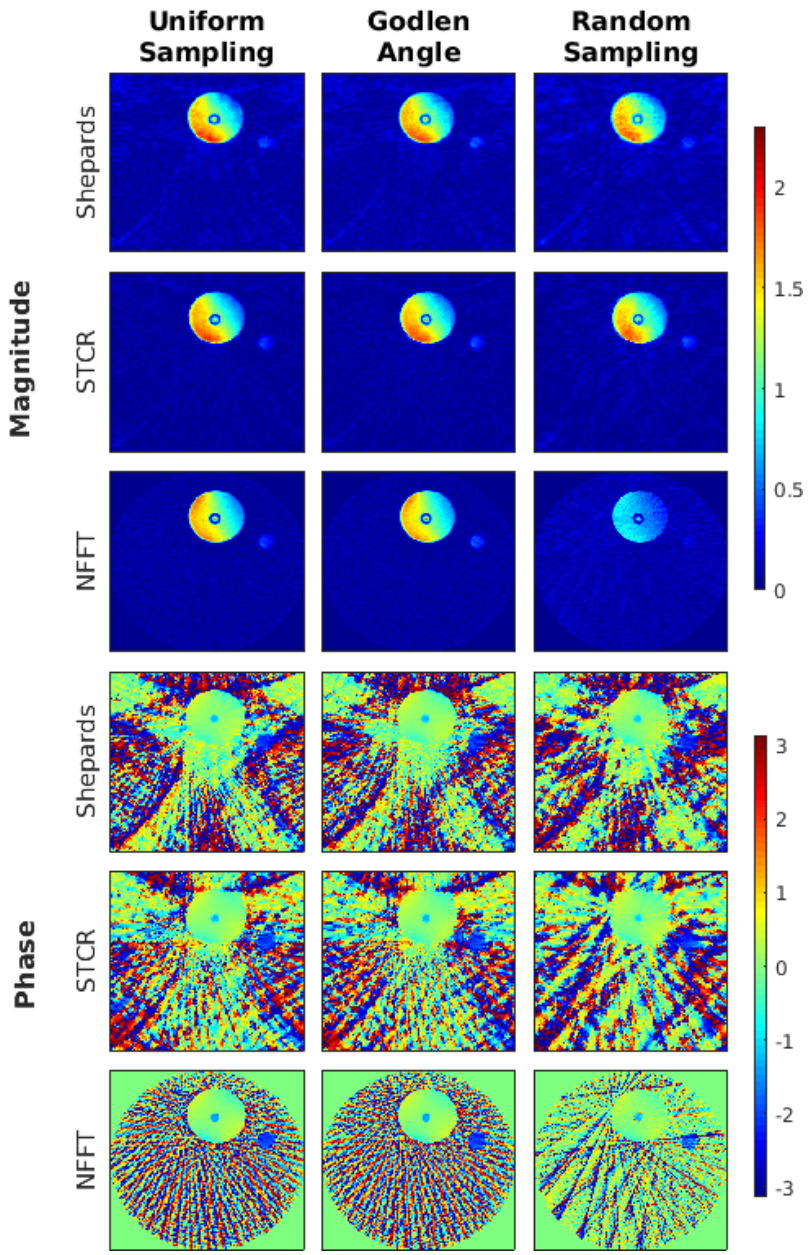

Figure 5.7: Radial reconstructions with 55 projections. Images were reconstructed with Shepard's method of interpolation, STCR or NFFT, and uniform, Golden angle or random sampling. All images are on the same intensity scale.

Qualitative Assessment: Visual Appearance

With STCR, the boundaries of the main phantom and capillary tube are sharp with 89 or 144 projections, and become slightly blurred with 55 projections. Reducing the number of projections to 34 or 21 projections results in severe blurring. The signal contrast between the capillary tube, the surrounding hypo-intense ring and the main phantom is good with 55 or more projections, though the signal within the capillary tube is reduced with fewer projections. The mean signal intensity of the capillary tube is within 10.5% of the reference image when at least 89 projections are used in the reconstruction, and drops to 58.2-72.0% with 34 projections. Contrast of the smaller external phantom is good for the images with 89 or 144 projections, reasonable with 55 projections, and poor with 34 or 21 projections. Streaking artifacts in the background are low intensity, but become more noticeable with 55 and fewer projections. The randomly sampled images (not show due to lower quality) followed a similar trend, though the signal intensity within the phantom has a modulating appearance, and the signal drop-off in the capillary tube is more rapid. With 34 or 21 projections, the shape of the phantom is distorted.

The signal phase of the STCR images are similar within the images reconstructed with 55, 89 and 144 projections. Reducing this number to 34 or 21 results in smoothing around the edges of the main phantom, and a greater appearance of streaking artifacts through the phantom. The average phase of the capillary tube was consistent in the images with 55-144 projections, and deviated with 34 or 21 projections. The phase of all randomly sampled images suffer from steaks throughout the entire image. This could be a result of variable sized gaps in k-space, with some larger regions void of data. In addition, the average phase of the capillary tube started to deviate from the expected phase (from the reference image) with 55 projections and deviated further with fewer projections.

NFFT images with at least 89 projections were visually comparable with the reference images when uniform or Golden angle sampling were used. This was assessed by sharpness of the phantom edges, relative signal contrast between the capillary tube and the surrounding phantom, and visual appearance of image artifacts. The images with 55 projections exhibits some signal smoothing, as observed through the loss of signal in the hyper-intense regions (left hand side) and loss of

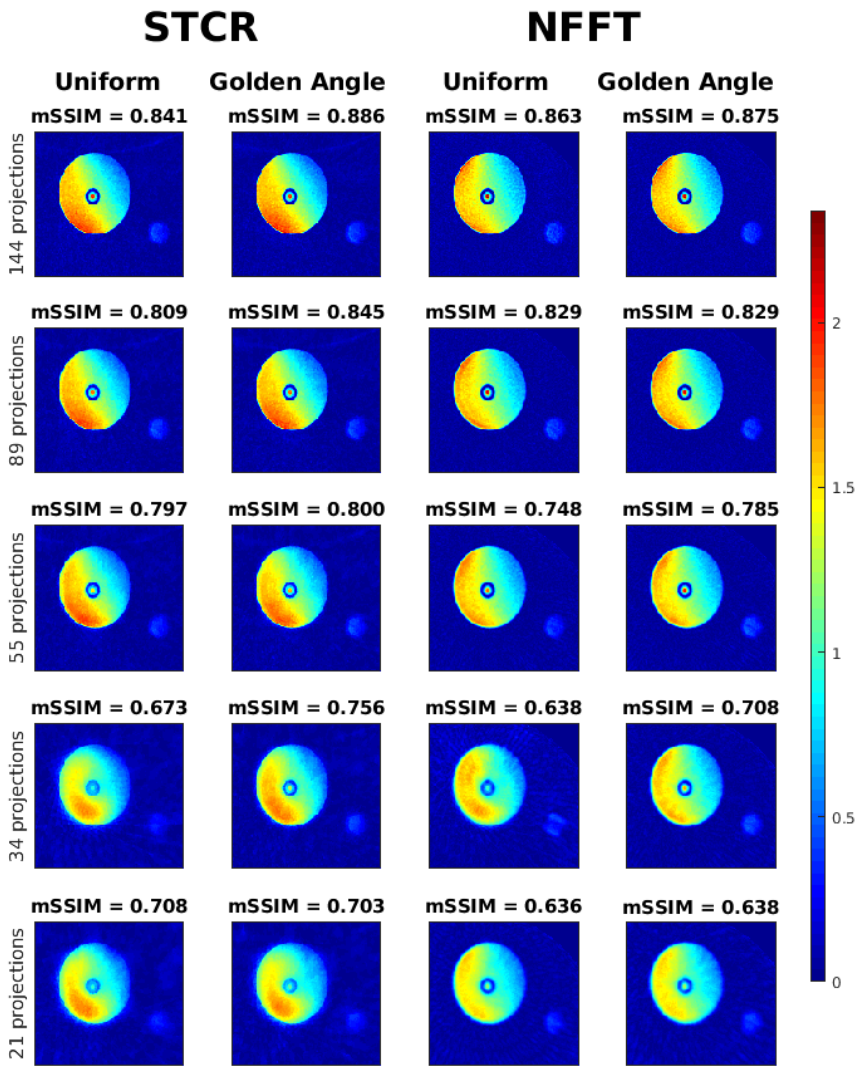

Figure 5.8: Radial images reconstructed with STCR or NFFT and uniform or Golden angle sampling. In general, the image quality between uniform and Golden angle sampling are comparable. Both techniques reproduce the phantom well down to 89 projections, while the image with 55 projections provides a reasonable iamge.

signal contrast between the capillary tube and surrounding phantom. The edges of these images, however, still appear sharp. Reducing the number of projections to 34 or 21 results in more blurring and signal smoothing within the phantom. In addition, the lower intensity region between the capillary tube and phantom has increased signal relative to the images with 55 projections. The signal intensity of the capillary tube gradually decreases as fewer projections are used in the reconstruction. It is within 5.9% of the reference image with 89 projections in the reconstruction, and falls to 54.3-81.8% with 34 projections. The secondary phantom is easily distinguished in images with 89 or 144 projections, with reasonably sharp edges. While the signal intensity of the phantom continues to be sufficiently greater than the background with 55 projections, the edges appear blurred, likely a result of signal smoothing throughout the image. Decreasing the number of projections to 34 or 21 causes further signal smoothing and loss of contrast between the phantom and background due to image artifacts.

Again, the images reconstructed with random sampling (not shown) are of inferior quality. The edges of the phantom are sharp with 89 or 144 projections, but there is an observable signal drop-off within the main phantom and streaking artifacts are present through the phantom. The secondary phantom is distinguishable from the background, but is blurred relative to the uniform and Golden angle images. By 55 projections, the signal is significantly lower than the reference and would not be useful for our application.

The image artifacts appear as rippling at the edges of the phantom (high intensity regions) and streaks originating from the phantoms. With uniform and Golden angle sampling, and 89 or 144 projections, only the rippling effect is visually noticeable with the current windowing. Streaking artifacts are present, but their intensity is low compared to the signal intensity of the phantoms. As we reduce the number or projections to 55, 34 or 21, the streaking artifacts become more noticeable and with a higher frequency. By 21 projections, the magnitude of the signal from the artifacts is similar to that of the secondary phantom. With random sampling, rippling and streaking artifacts are present in all images.

The phase of the main phantom is similar to the reference NFFT image down to 55 projections with uniform or Golden angle sampling. Decreasing this to 34 or 21 resulted in an increased presence of streaking artifacts throughout the phantom.

The background phase changed from being random Rician noise to clear streaks at 55 projections. The density of the streaks appears to be dependent on the number of projections used, as the frequency dropped in the images with 34 and 21 projections. The phase of the smaller reference phantom is comparable in the images with 89 and 144 projections, while streaking artifacts affect the signal with 55 and fewer. The average phase of the capillary tube is more stable than with STCR down to 21 projections, with the maximum deviation being 0.20 rad for the NFFT image with 34 projections and uniform sampling (compared with 0.55-0.63 rad with STCR). The randomly sampled images suffer from streaking artifacts in all phase images, with the severity dependent on the number of projections used in the reconstruction (worse for fewer projections).

The images reconstructed with Shepard's method of interpolation (not shown) are inferior to STCR and NFFT. Only the images with 89 or 144 projections, and uniform or Golden angle sampling, resembled the reference radial image. As the number or projections was reduced to 55 and fewer, the edges of the phantom was noticeably blurred, and the signal within appeared smoothed. In addition the contrast between the capillary tube and the surrounding phantom was greatly reduced as fewer projections were used in the reconstruction. The lower intensity phantom is visible in all images, but suffers from signal losses and blurred edges in the images with 89 and fewer projections. The images with random sampling are again inferior. The shape of the main phantom appears warped in all images with 89 and fewer projections, and signal modulations are observed within the phantom due to streaking artifacts. Similarly to the other sampling methods, the smaller external phantom is distinguishable with 89 and 144 projections, but suffers from signal losses and blurred edges with 89 and fewer projections.

The image artifacts appear as a curved line, originating at the hyper-intense region of the phantom and the lower left-hand corner of the image, and a series of ripples on the lower and left hand sides of the phantom. The structure of the artifacts observed in the images with 89 or 144 projections are consistent with the reference image. This suggests that they could be a result of the chosen techniques for data interpolation and density compensation. As the number of projections is reduced (34 projections for uniform and Golden angle sampling, or 55 with random sampling), more irregularly shaped spots are observed in the background. These

have an intensity of approx 30% of the phantom signal.

The signal phase is similar between the three sampling methods, and has a distinct structure with four bands originating from the main phantom: two approaching each top corner, and two curved features extending towards the lower corners of the image. As the number of projections is reduced, the edges of the phantom become blurred and streaking artifacts are observed within the phase bands in the background. The phase images become more blurred as fewer projections are used in the reconstruction, and streaking artifacts become apparent across the phantom. The average phase of the capillary tube is fairly stable with 55-144 projections (only to 89 projections with random sampling), then deviates with 34 re 21 projections. The deviation is slightly less than that seen with STCR.

Quantitative assessment: mean Similarity Index

The mSSIM provides a more quantitative assessment on how closely the under-sampled radial image compares with the fully sampled radial image reconstructed with the same technique. It is expected that the under-sampled images will have the same characteristic background artifacts as the reference image. By comparing the under-sampled images with their respective reference image, these artifacts are accounted for, and will not further penalize the similarity comparison. The mSSIM was calculated over two regions: the entire image, and only across the main phantom to evaluate if masking would be beneficial for the tissue enhancement correction. The mSSIM values are shown graphically in Figure 5.9, and summarized in Tables 5.1, 5.2 and 5.3.

As expected, the mSSIM index decreases as fewer projections are used in the reconstruction, independent of the reconstruction technique or the sampling method used. In general, the mSSIM was greater across the main phantom, as compared with the entire image. This is likely a consequence of background artifacts. Uniform and Golden angle sampling often produced comparable mSSIM results, and out-performed random sampling. This could result from larger gaps in the periphery regions of k-space, causing a loss of image contrast and detail.

The three tables all confirm that the mSSIM values are generally greater over the main phantom as compared to the entire image, particularly when 55 or more

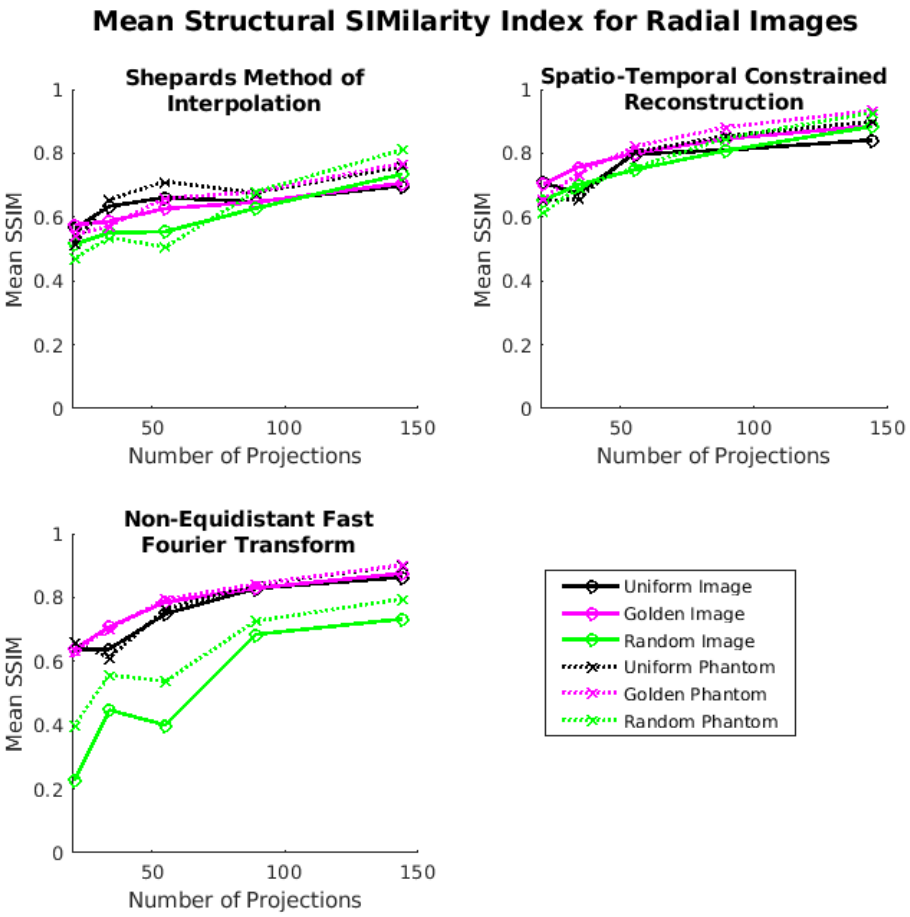

Figure 5.9: Mean Structural SIMilarity Index (mSSIM) comparing radial images reconstructed with fewer projections with the reference image containing 233 radial projections. The mSSIM for the entire images is indicated by the solid line while the dashed line is for phantom only. The curves show that the mSSIM index is greatest with uniform and Golden angle sampling, and lower when random sampling is used.

Table 5.1: mSSIM index for Shepard's Method of Interpolation

Entire Image

Number of Projections	Uniform	Golden Angle	Random
144	0.700	0.706	0.624
89	0.648	0.646	0.662
55	0.661	0.627	0.585
34	0.633	0.586	0.563
21	0.563	0.576	0.541

Within the Main Phantom Only

Number of Projections	Uniform	Golden Angle	Random
144	0.758	0.769	0.705
89	0.676	0.679	0.730
55	0.711	0.658	0.525
34	0.655	0.572	0.612
21	0.517	0.544	0.385

Table 5.2: mSSIM index for Spatio-Temporal Constrained Reconstruction

Entire Image

Number of Projections	Uniform	Golden Angle	Random
144	0.841	0.886	0.877
89	0.809	0.845	0.812
55	0.797	0.800	0.754
34	0.673	0.756	0.662
21	0.708	0.703	0.637

Within Main Phantom Only

Number of Projections	Uniform	Golden Angle	Random
144	0.899	0.933	0.920
89	0.854	0.881	0.826
55	0.804	0.820	0.718
34	0.655	0.734	0.664
21	0.653	0.657	0.622

Table 5.3: mSSIM index for the Non-Equidistant Fast Fourier Transform

Entire Image

Number of Projections	Uniform	Golden Angle	Random
144	0.863	0.875	0.733
89	0.829	0.829	0.684
55	0.748	0.785	0.400
34	0.639	0.708	0.448
21	0.636	0.638	0.226

Within Main Phantom Only

Number of Projections	Uniform	Golden Angle	Random
144	0.901	0.902	0.795
89	0.840	0.842	0.726
55	0.764	0.795	0.537
34	0.611	0.701	0.557
21	0.658	0.633	0.400

projections are used in the reconstruction. For this analysis, a threshold of 0.800 for the mSSIM provides a good comparison, while a value over 0.900 represents an excellent comparison.

With Shepard's method of interpolation, none of the images meet the criteria for a good comparison. The mSSIM had a maximum value or 0.700 and 0.706 with 144 projections and uniform and Golden angle sampling. Since these images were all compared to the reference image with the same reconstruction technique, the lower values could represent loss of resolution or contrast between the different structures (main phantom, capillary tube, external phantom). The mSSIM over the main phantom was improved in the images with 89 or 144 projections, similar with 34 or 55 projections and worse with 21 projections. Again, no image exceeded the threshold of 0.800.

The mSSIM indices for STCR also show a steady decline as the number of projections drops from 144 to 21. This time, the Golden angle sampling scheme performs best, providing the highest mSSIM values for all acceleration rates tested, followed by uniform sampling then random sampling. All radial images with 89

or 144 projections, as well as the image with Golden angle sampling and 55 projections, meet the criteria of a mSSIM greater than 0.800. The image with uniform sampling and 55 projections is close to 0.800 and could be considered sufficient quality if this form of sampling is desired. When considering the mSSIM within the phantom, images with 144 projections have excellent comparability with the reference image, having values of 0.899, 0.933 and 0.920 with uniform, Golden angle and random sampling. Images with at least 55 projections and uniform or Golden angle sampling, or 89 projections and random sampling all have a mSSIM exceeding 0.800. All of these accelerated images would be considered sufficient for compensating for local tissue enhancement as they compare well with the reference image (pre-injection with our technique).

The mSSIM for the NFFT exceeds 0.800 when uniform or Golden angle sampling are used, and 89 or 144 projections. Consistent with the visual analysis, random sampling provides lower mSSIM values. The mSSIM values for the entire image and across the main phantom were similar when uniform or Golden angle sampling were used, and greatly improved for random sampling. Reconstructions with 144 projections and either uniform or Golden angle sampling produced a mSSIM exceeding 0.900, while those with 89 projections exceeded 0.800. The drop-off in the mSSIM is significant as fewer projections are used, thus suggesting that at least 55 projections should be used in the reconstruction. In addition, uniform or Golden angle sampling is required with the NFFT technique.

A more thorough evaluation of the SSIM maps for Shepard's method of interpolation shows that the greatest values occur within the capillary tube and at the edges of both phantoms. The maps with 55 projections, and all sampling schemes is shown in the top row of Figure 5.10. This trend was observed with all sampling methods when at least 55 projections were used in the reconstruction. The region within the two phantoms and in the background appeared as incoherent noise with no obvious structure. These regions cover a majority of the image and will contribute more weight to the mSSIM since it's an un-weighted average. With 34 projections, the mSSIM was greatly reduced in the capillary tube from an average of 0.885 ± 0.007 to 0.702 ± 0.013 (uniform sampling), 0.86 ± 0.02 to 0.61 ± 0.02 (Golden angle) and 0.76 ± 0.02 to 0.55 ± 0.03 (random). In addition, the ring of high SSIM values at the edge of the phantoms faded, indicating signal smoothing.

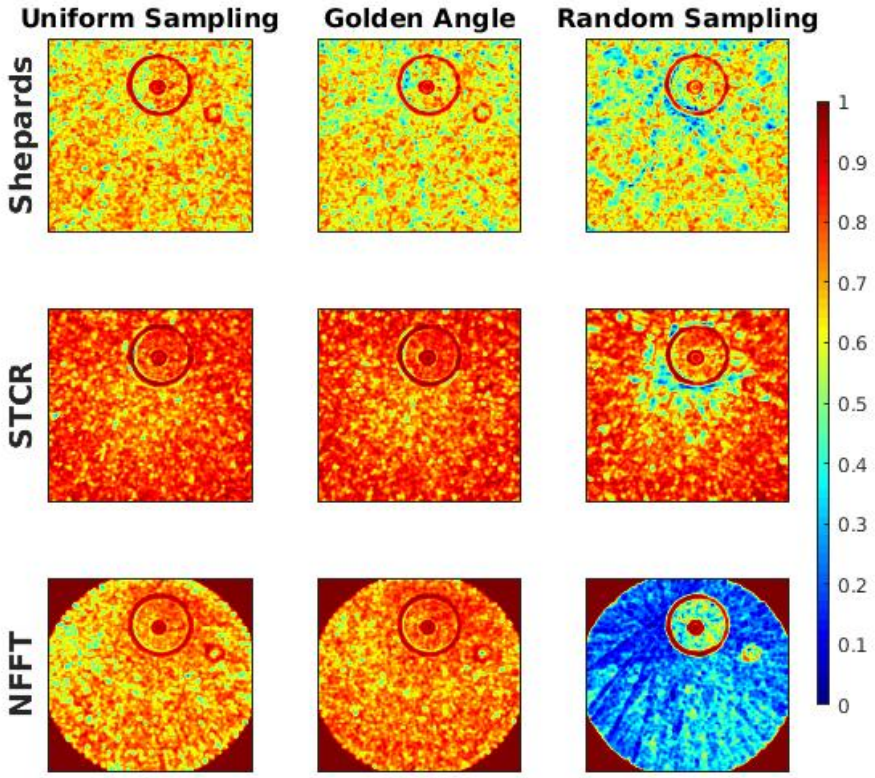

Figure 5.10: Structural SIMilarity Index (SSIM) maps for radial images reconstructed with 55 projections. All images are compared with the reference image (233 projections) with the same technique. The averaging is done for the entire image with Shepard's method of interpolation and STCR, and only within the circular region 128 voxels from the center for NFFT as there is where the image reconstruction is constrained.

These observations are more dramatic with the maps with 21 projections.

The second row of Figure 5.10 shows the SSIM maps for images reconstructed with STCR. The results show that the accelerated images have higher consistency with the reference image in the background and inside the phantom for all cases studied. Similar to Shepard's method of interpolation, the SSIM values were great-

est in the capillary tube and at the edges of the main phantom when at least 55 projections are used. The SSIM values at the edges of the secondary phantom are high with 144 projections, but decrease rapidly as fewer projections are used. The SSIM values inside the capillary tube dropped dramatically with 34 projections and uniform (0.52 ± 0.06) or random sampling (0.65 ± 0.03) and approached values of 0.53 ± 0.05 (uniform), 0.56 ± 0.03 (Golden angle) and 0.47 ± 0.03 (random) with 21 projections. The edges of the main phantom continued to have higher SSIM values down to 21 projections, but they were noticeably reduced from the maps with 55 projections. The SSIM maps show more clearly when image artifacts are present. The region inferior of the main phantom experience a rapid drop-off in SSIM values as the number of projections is reduced. By 34 projections, all SSIM values are below 0.4 due to streaking artifacts in the background.

The third row of Figure 5.10 shows the SSIM maps for NFFT images reconstructed with 55 projections. It is clear that uniform and Golden angle sampling are superior to random sampling across the entire image, though the gains are greatest in the background. The SSIM values have a strong dependence on the number of projections used in the reconstruction, particularly moving down from 89 to 55 projections. Generally, the edges of the phantom were sharp in images with 34 or more projections, as indicated by SSIM values exceeding 0.800. Similar to STCR, the mSSIM in the capillary tube sees a significant drop when the number of projections is reduced from 55 to 34: 0.906 ± 0.008 to 0.52 ± 0.06 for uniform sampling, 0.92 ± 0.01 to 0.812 ± 0.02 for Golden angle and 0.866 ± 0.01 to 0.645 ± 0.03 for random sampling. The SSIM values within the phantoms and in the background decrease rapidly from 89 to 55 projections. The SSIM values in the background are randomly distributed with 144 or 89 projections and uniform or Golden angle sampling. With 55 projections, the background had subtle structured artifacts around the phantom. These became more prominent when using 34 or 21 projections in the reconstruction. The maps of all randomly sampled images had structured artifacts in the background, regardless of the number of projections used.

5.4.5 Recommended Radial Reconstruction Technique

The criteria for good radial reconstruction technique includes good visual similarities (sharp edges, similar signal contrast between distinct regions in the image, and minimal presence of artifacts) and high comparability between images with varying numbers of projections. Based on all results, the STCR or NFFT reconstructions are best suited for a local tissue enhancement correction. For both methods, images reconstructed with fewer projections retain structural similarities to the reference image. This is important as it provides additional flexibility when correcting for local tissue enhancement. The pre-injection image will benefit from using the full data set (233 projections for this experiment) to provide the most accurate image. Meanwhile, the temporal resolution of the post-injection images depends on the rate at which the contrast agent extravasates into the surrounding tissue. A higher temporal resolution is beneficial for rapid changes, but this comes at the cost of blurred structural information. The correction involves a comparison of images before and after the injection, so the comparability of these two images should be good. In addition, image contrast between distinct regions within the image - such as between the capillary tube and surrounding phantom - must be preserved. This is important for an AIF estimation in the mouse tail, as the signal intensities between the vessel and surrounding tissue may be significantly different [169].

Uniform and Golden angle sampling consistently produced images of similar quality for all acceleration rates. Generally, images with 89 or 144 projections had good quality images, with sharp edges and good contrast between the capillary tube and the surrounding phantom. Image artifacts were often not an issue with these acceleration rates. In general, uniform and Golden angle sampling have mSSIM values exceeding that of random sampling. This suggests that either uniform or Golden angle sampling should be used. The significantly different values could reflect the size of gaps in the k-space data, leading to insufficient contrast information at higher acceleration rates.

Re-gridding reconstructions involve a form of data interpolation and weight compensation. Shepard's method of interpolation combines both steps by performing a weighted average of data points within the region of a pixel. The accuracy of the data within a particular pixel becomes a function of the data density. The

center of k-space will be most accurate - as noise may be averaged out during the interpolation step - while the edges of k-space could be sparsely sampled. This can have an impact on the sharpness of details or edges within the image, and thereby reduce the image quality more rapidly.

Zero-filling is a common technique to address the missing data. The zeros should have little effect closer to the edges of k-space, as the signal intensity is already near-zero there. But, it could have more dramatic consequences closer to the center of k-space, where the signal gradient between neighbouring voxels could be large. These sharp edges in k-space could introduce the streaking artifacts commonly seen in radial images, especially with fewer radial projections.

Filtering the data with a mean filter (i.e. 3x3 $pixel^2$ area) or a Kaiser Bessel function can help improve the image quality. The filter has the effect of smoothing the transition between the acquired data and the zero-filled voxels and also reduces the number of zeros near the center of k-space. In effect, the presence of imaging artifacts will be less. However, smoothing the data also causes blurring of the edges of the phantom and further loss of contrast between distinct image features, such as the capillary tube in the center. Density compensation and filtering are often performed simultaneously in regrdidding techniques. The chosen filter emphasizes the importance of the high intensity contrast-containing voxels at the center of k-space, and filters more strongly as it approaches the edges of k-space where most of the voxels have values closer to zero.

Van Vaals [170] introduced the key-hole approach in 1993 as a viable solution. Their method updates k-space with variable temporal resolutions, but filling in the missing data - often in the outer regions of k-space - with acquired data from an earlier time. This is advantageous, as the filled data more closely resembles the actual values. The key-hole approach was applied to the image reconstructions in this study, but did not improve the image quality substantially.

In contrast, STCR and NFFT both reconstruct the image as an inverse problem [154, 162], weighted with a cost function to enforce image continuity spatially and/or temporally. Iterative techniques are attractive as they account for the under-sampling pattern and use prior object knowledge to fill in the missing information [162]. The STCR technique reconstructs a batch of images together to enforce temporal regularity between consecutive images. For 200 images, the re-

construction must be broken up into thirteen batches of 16 images, which takes approximately 15 minutes to complete. The NFFT reconstructs each image separately, and completes the reconstruction of 200 images on the order of 8 minutes. Since these two images produce similar quality results, the time restriction favors the NFFT. Further, the mSSIM values were better over the phantom, rather than the entire image. This suggests that masking of the physical objects is advantageous, especially if image artifacts are observed in the background.

Chapter 6

Compensation for Local Tissue Enhancement

6.1 Local Tissue Enhancement

Local tissue enhancement is a result of contrast agent extravasating from the vascular space into the EES. The contrast agent interacts with the protons in the tissue, causing accelerated T_1 and T_2 relaxation, and thus signal loss and a loss of phase coherence in T_1-weighted images. The projection-based AIF is sensitive to local tissue enhancement as the projection data only contains information along one spatial dimension. Acquiring data at other angles, in particular perpendicular to the AIF projections, would be beneficial for visualizing local tissue enhancement.

MR projections can be acquired at a number of angles spanning the range of $0-360^o$. This enables the concurrent measurement of a high-temporal resolution AIF from the projections, and a series of lower temporal-resolution MR images to visualize tissue enhancement throughout the experiment. The MR projection is a complex summation of all signal perpendicular to the readout direction. As such, some pixels contain information from the vessel and surrounding tissue. When tissue enhancement is present, the shape of the projection profile is affected. If the vessel signal were removed from the projections, then the effects of local tissue enhancement may be evaluated quantitatively. This is where constructing radial images becomes attractive.

Comparing the background profiles (with vessel signal removed), between profile i at time t and a pre-injection profile i (same angle), will provide a quantitative measure of how the profile shape was affected. Using this information, the projections can be corrected for tissue enhancement prior to extracting the AIF.

The goal of this chapter is to demonstrate that local tissue enhancement may be visualized in radial MR images, and then compensated for, in the post-injection projection data. The simulations discussed in this chapter investigates the potential of three radial reconstruction methods - Shepard's method of interpolation, STCR and the NFFT - in effectively visualizing, and then correcting for, local tissue enhancement.

6.2 Methods: Simulated Tissue Enhancement Study

The primary focus of the last chapter was to evaluate three different radial reconstruction techniques and investigate how the number of projections used in the reconstruction and the sampling technique used would affect the image. This study takes the analysis a step closer to correcting for local tissue enhancement.

A simulation study was performed, in which a local tissue enhancement was added to a Cartesian image. Projections were calculated from these images through application of the forward Radon transform. From these projections, radial images were reconstructed temporally to evaluate the effectiveness of each technique in successfully characterizing the tissue enhancement.

The purpose of this study is to evaluate our ability to accurately measure local tissue enhancement from radial MR images, and quantify the effectiveness of using each reconstruction technique discussed in the previous chapter. Only one vessel was used in this study for simplicity in the analysis.

6.2.1 Simulating Local Tissue Enhancement

Capillary walls are permeable, meaning that some contrast agent can extravasate from the vascular space into the surrounding tissue (Figure 6.1). A simulation study was performed, in which extravasation of the contrast agent into the surrounding tissue was added to the Cartesian image of the phantom for 2330 time frames (temporal resolution 0.100 s). These images are referred to as the simulated enhance-

ment images. The phase of the vessel signal was based on the mathematical fit of a previously measured projection-based AIF [171]. Gaussian white noise was applied to the AIF, such that the SNR of the curve was 40, to make the input curve more realistic (i.e. presence of small magnetic field inhomogenetities, non-ideal gradient waveforms, non-uniform distribution of the contrast agent in the vessel, etc.). Perfusion of contrast agent was seeded at the center of the vessel, and grew outward spatially described by the function $0.1 \cdot e^{-5t/230}$, where t is the time from the arrival of the contrast injection and the units are in pixels from the seed position. The shape of the enhancement region was elliptical, in which the radius along the second matrix dimension was 0.8 X that of the first dimension. The concentration of Gd-DTPA in the tissue, C_T, was calculated using:

$$C_T = K^{trans}(AIF * e^{-K^{trans}t/v_e}) \tag{6.1}$$

where $K^{trans} = 0.1/60s^{-1}$ [109, 172], $v_e = 0.5$ [15] and * represents a convolution. The concentration in a given pixel at a radius r from the seed point is a time-shifted version of this curve. The magnitude of enhancement was determined from the change in T_1, (assuming T_{1o} of $900ms$ in muscle [6], relaxivity 3.6 $(mMs)^{-1}$ for Gd-DTPA-BMA (Omniscan) at 7T [109, 173–175], and a FLASH experiment with a flip angle of 30°), while the phase was determined directly from the change in concentration ($\phi = C_T/(0.213\ mM/(rad \cdot ms) \cdot TE)$) with $TE = 5\ ms$ [171]. This result describes the signal phase-shift within a vessel aligned parallel to the main magnetic field, and will be lower for any other orientation as defined by the geometry factor, $\zeta = (3\cos^2\theta - 1)/2$, where θ is the angle between the main magnetic field and the vessel.

This study compared the three sampling techniques to evaluate the benefits and drawbacks of each in a dynamic experiment. Radial images were reconstructed with various numbers of projections. Winkelmann et al. [165] discovered that the most uniform coverage of k-space with fewer projections, and dynamic acquisitions, occurs with Golden angle sampling (angular increment of 111.24^o) when a Fibonacci number of projections is used. In this study, we define accelerations as reconstructing an image with fewer projections. The complete data set contains a total of 233 projections, while the accelerated images were reconstructed with

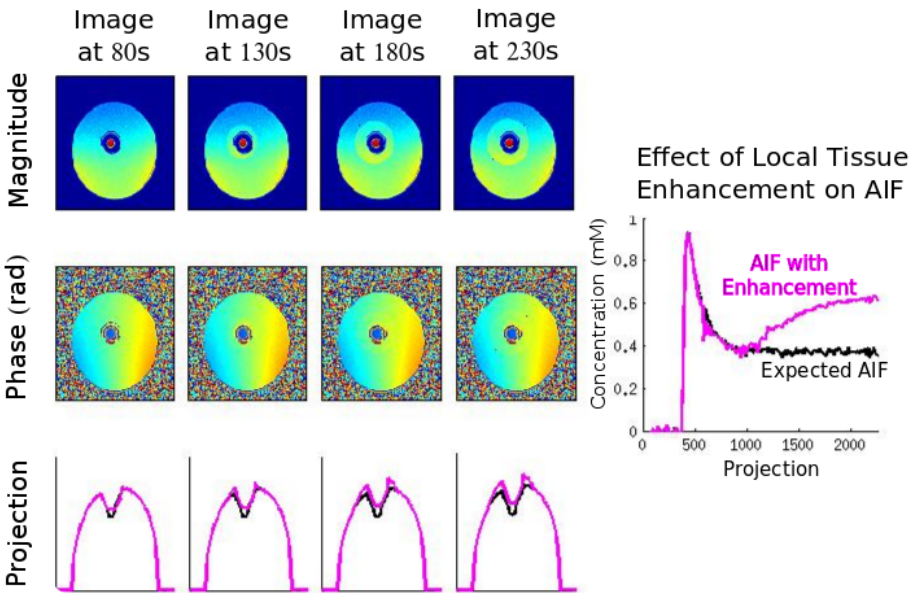

Figure 6.1: This figure shows how perfusion and extravasation of the contrast agent into the surrounding tissue leads to local tissue enhancement. The magnitude images (top row) show varying degrees of local tissue enhancement at 80 s,130 s,180 s and 230 s after the start of the experiment (the injection took place at 25.6 s). The middle row is the corresponding phase images. The bottom row compares the pre-injection background signal (black curve) and the projection of the chosen image (pink curve). It is clearly observed that the tissue perfusion affects the shape of the projection profile in the neighborhood of the vessel. The effects of tissue enhancement on the AIF measurement are shown in the plot on the right hand side, where the black curve is the expected AIF, and the pink curve shows the measured AIF using the projection-based method.

smaller Fibonacci numbers (144, 89, 55, 34 and 21). We chose 233 projections as the full set, as it provided the smallest residual ($mod(233 \cdot 111.246^o, 360) \leq mod(F_N \cdot 111.246^o, 360)$, where F_N are Fibonacci numbers from 21 to 388) from Golden angle sampled data.

For uniform sampling, the angular increment was set to a constant value between consecutive samples. Since the radon transform only provided angles at multiples of $360^o/233$, there may be cases where a projection from the desired angle was not calculated. In such cases, the projection with the closest angle was chosen. Though the data is not perfectly uniformly sampled, it provides a reasonable approximation. The projections for Golden angle sampling were spaced 111.246^o apart between consecutive samples, while the randomly acquired projections randomly selected one of the 233 projections at each time point, and repeated the pattern after 233 samples were collected.

Radial images were reconstructed from a subset of all projections using a sliding-window approach for a total of 200 images (see Figure 6.2). For this study, the sliding window shift was set to a random number to avoid coherent artifacts within the image series. Coherent artifacts appeared as angle-dependent phase fluctuations in the calculated projection-based AIF. Having a random window shift suppressed the artifact.

Radial data was acquired by rotating the image by the desired angle (using bicubic interpolation) and projecting the image along the second dimension (equivalent to the Phase-encode direction). To address variations in the spatial size of the matrix at each angle, the matrix was zero-filled symmetrically to a size of $[\sqrt{2}N_{read}\ x\ \sqrt{2}N_{read}]$, where N_{read} is the number of read-encode points sampled, prior to the rotation. The simulation rotated the image matrix through 233 unique angles, determined from $mod(n * 111.246, 260)$ with n = $1, 2, \cot 233$. This enforces consistency in the sampled angles between the three sampling methods. A 1-D Fourier transform is then applied to convert the projections into k-space data.

The image rotation effectively simulates acquisition of data in a radial MRI experiment. Since the local tissue enhancement can change between sampled time points, the selected projections will contain slightly different information about the local contrast enhancement. It is expected that if tissue enhancement evolves at a sufficiently slow rate, such that the time required to acquire data for an image

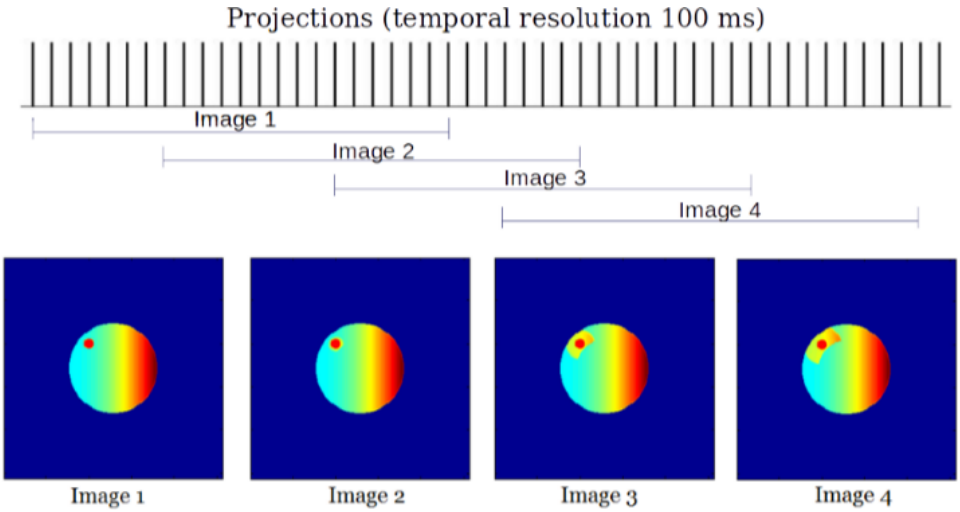

Figure 6.2: Radial data sets, particularly with Golden angle sampling, allow for more flexibility in selecting data for the image reconstruction. A sliding window reconstruction is a popular method for analyzing dynamic data sets. This method allows images to be reconstructed temporally, by shifting the sampling region between consecutive images. To prevent coherent artifacts between images in the series, we used a random number generator to determine the size of the shift.

is fast compared to significant signal changes in the image, than the reconstructed images should provide a good estimate of tissue enhancement temporally. Though this assumption may not be true in DCE-MRI studies with a highly permeable vasculature.

Depending on the rate of local tissue enhancement, sampling data over a finite time interval could cause temporal blurring of the contrast enhancement in the image. To quantify errors related to reconstructing images with projections taken at different times, a second data set - referred to as the 'snap-shot' data - was taken to compare with the dynamic experiment. In the snap-shot data set, all projections were taken from a single enhancement image, at the mean time of the dynamic image data. For instance, if an image was reconstructed from projections taken between times 10.1 s to 15.5 s, with 0.1 s temporal resolution, then a snap-shot image was constructed with all projections taken from the image at time 12.8 s. For a fair comparison, the projection angles exactly matched those sampled in the

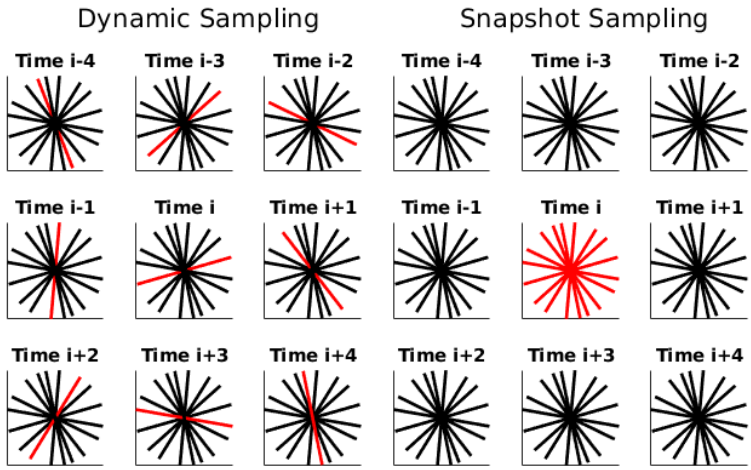

Figure 6.3: Two situations were analyzed to investigate the effects of temporal blurring in the images. The static case involves taking all projections from an image at the central time. While the dynamic case involves taking projections every 0.1 s to more accurately portray a DCE-MRI experiment. The red lines represent the projections that are sampled at a particular time. The black lines are there to show that the sampling scheme is identical for both the dynamic and snapshot data sets.

dynamic case. The 1-D Fourier transform was applied to all projection data prior to image reconstruction. Figure 6.3 illustrates the data sampling for the snap-shot and dynamic experiments.

6.2.2 Quantifying Tissue Enhancement in Radial MRI

Radial image series were reconstructed for the dynamic and snap-shot data sets for re-gridding with Shepard's method of interpolation, STCR and NFFT. The images were normalized, such that the mean intensity of the pre-injection reference images was 1.00. This is more robust than normalizing to the maximum intensity in cases where a single pixel could have a higher intensity due to noise or an image artifact.

Since characterizing the local tissue enhancement is the focus of this project, the first image in the series was subtracted from all following images after blocking out the signal from the vessel. This provided an image of only the enhancement region and some low-intensity residual imaging artifacts. Artifacts in the background

of the image were removed by applying a mask that encompassed the phantom and capillary tube.

The expected enhancement profiles served as the gold standard. They were calculated directly from the initial images of the local tissue enhancement, after subtracting the baseline image from all in the series. The expected projection profile, due to tissue enhancement, was calculated by projecting this difference image along the direction perpendicular to the angle of sampling. The change in signal intensity due to enhancement is directly related to the concentration of contrast agent within the tissue. This means that the changes will be small initially, and increase with time. A quantitative method to compare the enhancement intensity with the expected values is to look at the difference in signals due to enhancement, relative to the pre-injection image (equation 6.2).

$$I_{diff} = \frac{I_X - I_{simulated}}{I_{pre-injection}} \cdot 100 \tag{6.2}$$

Where X represents either the dynamic or snap-shot image series. The units for this analysis are relative to the signal of the pre-injection image to gauge the errors associated with the radial reconstructions. This procedure is outlined in Figure 6.4.

The projection-based AIF method from Chapter 4 may be used to measure the signal in the capillary tube. The 'acquired' projection data came from the simulated enhancement image series. Each image was projected along the second matrix dimension (perpendicular to the read encode gradient). The background profiles are calculated from the radial dynamic images, after applying a mask to remove the signal from the vessel.

The AIF may be corrected with knowledge of how the local tissue enhancement affects the acquired projections. We can get this information by comparing two radial images from the dynamic series, after removal of the signal from the capillary tube: the first image is reconstructed with data prior to the injection, and the second coming from data acquired after. The comparison involved subtracting the pre-injection image from an identically sampled post-injection image. The remaining non-zero signal in the difference image is related to contrast agent enhancement.

The difference image is then projected vertically (second matrix dimension) to

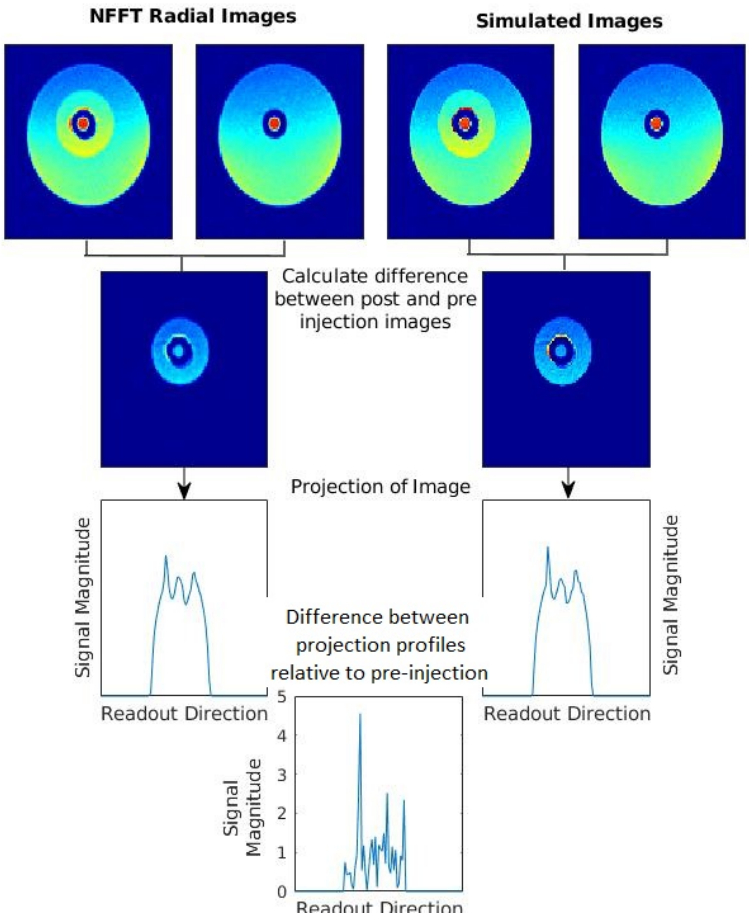

Figure 6.4: Procedure for calculating the error profile for the tissue enhancement region. The radial images are normalized to the mean of the pre-injection image. The tissue enhancement is isolated by subtracting the first pre-injection image from all images in the series. Next, the image of the enhancement is projected along the direction perpendicular to the desired projection angle. This profile is compared to the expected enhancement projection using equation 6.2. The units on the difference between projection profiles plot is the percentage of the maximum signal of the projection profile.

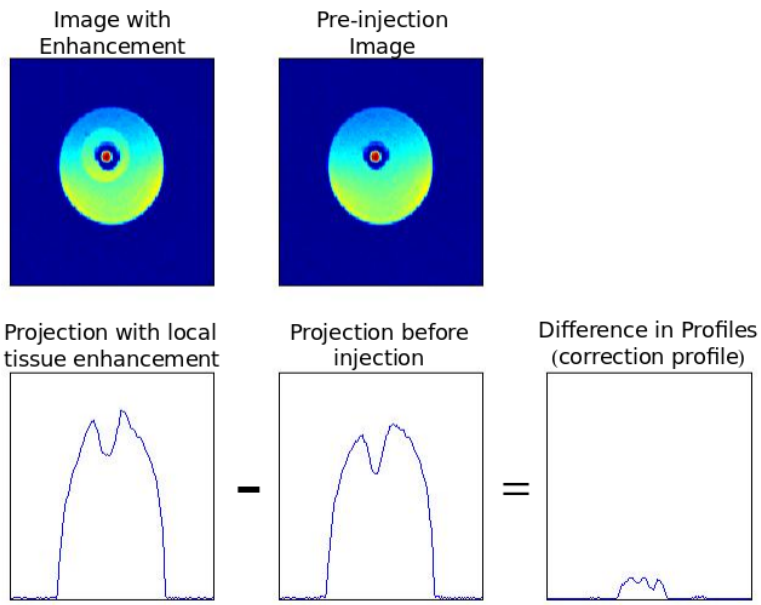

Figure 6.5: Procedure for correcting the AIF for local tissue enhancement. The correction involves comparing radial images from before and after the contrast injection, to isolate any difference between the two situations. The vessel data is zeroed out before projecting the difference image along the second dimension. This provides the correction profile due to local tissue enhancement. Next, the correction profile is subtracted from the acquired data and the projection-based AIF is repeated. The units in the difference in profiles is related to the average signal of the phantom in the pre-injection MR images (mean signal intensity is 1.00). The maximum signal in the projections is dependent on the signal magnitude of the phantom and capillary tube, and the signal intensity gradient in the image.

produce a correction profile. This was added to the post-injection projections and has the effect that it removes the tissue enhancement from the profile and replaces it with the original tissue signal. The projection-based AIF method was repeated to produce a tissue enhancement corrected AIF. The procedure for the correction is outlined in Figure 6.5.

6.3 Quantifying Tissue Enhancement from Radial MR Images: Simulation Study

200 radial images, spanning the 2330 time points, were reconstructed for this analysis with the sliding window method. For a more thorough analysis, and to confirm that the NFFT provides the more accurate results, all three reconstruction methods were studied. This includes the three sampling strategies and five acceleration factors. 200 images were selected as a compromise between spanning the entire range of data with sufficient resolution and computational time and memory. The three radial reconstruction techniques were compared based on their ability to accurately recreate the local tissue enhancement. For this analysis, the first image of each series (pre-injection) was subtracted from images in the series. This left an image of the enhancement pattern and provided insights into potential problematic image artifacts.

Figures 6.6 and 6.7 summarize the local tissue enhancement pattern (magnitude and phase) from all image series reconstructed with 55 and 34 projections. These data sets were chosen as the image series with 55 generally produced images of reasonable quality and the greatest drop-off in visual image quality occurred from 55 to 34 projections. The image series with 89 or 144 projections were of higher quality (more uniform signal distribution and sharper edges), while the images with 21 projections were clearly inferior (significant blurring, loss of contrast between structures and increased presence of artifact). Both figures include the tissue enhancement images from the three image reconstruction techniques and all three sampling methods. As a reference, the simulated enhancement pattern is plotted in the top row. The magnitude scale is identical in both figures to make them easier to compare.

The results show that both STCR and NFFT reproduce the local tissue en-

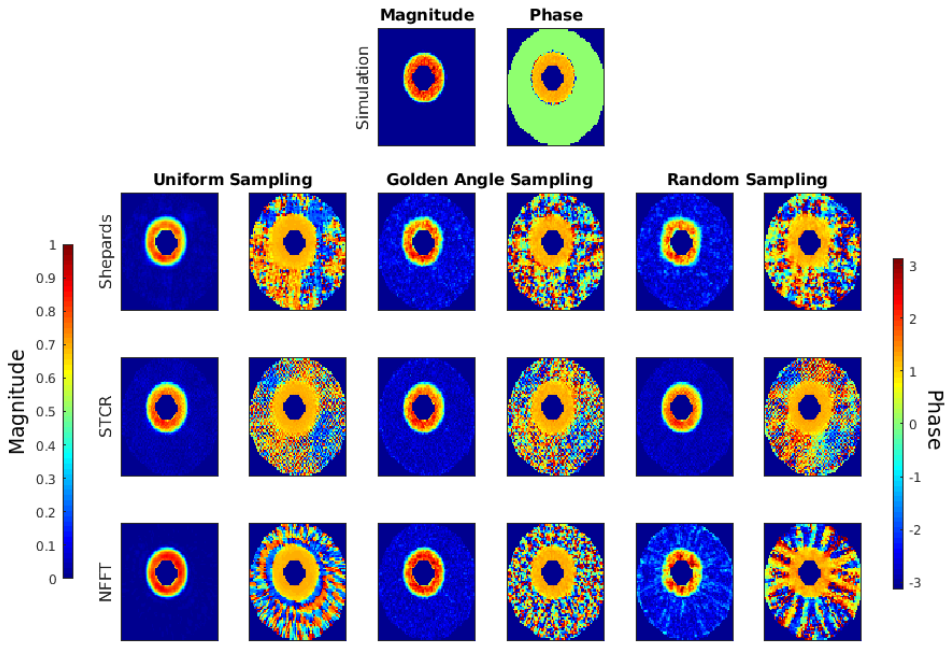

Figure 6.6: Images of the simulated tissue enhancement from radial images reconstructed with 55 projections at time points 1730 s. The top row shows the signal magnitude and phase of the simulated enhancement as a reference. The second, third and fourth rows show the signal magnitude (first, third and fifth column) and phase (second, fourth and sixth column) of the enhancement images for all three radial reconstruction methods. All images were normalized to the mean signal of the phantom in the pre-injection image, and are displayed on the same magnitude scale for an easier comparison.

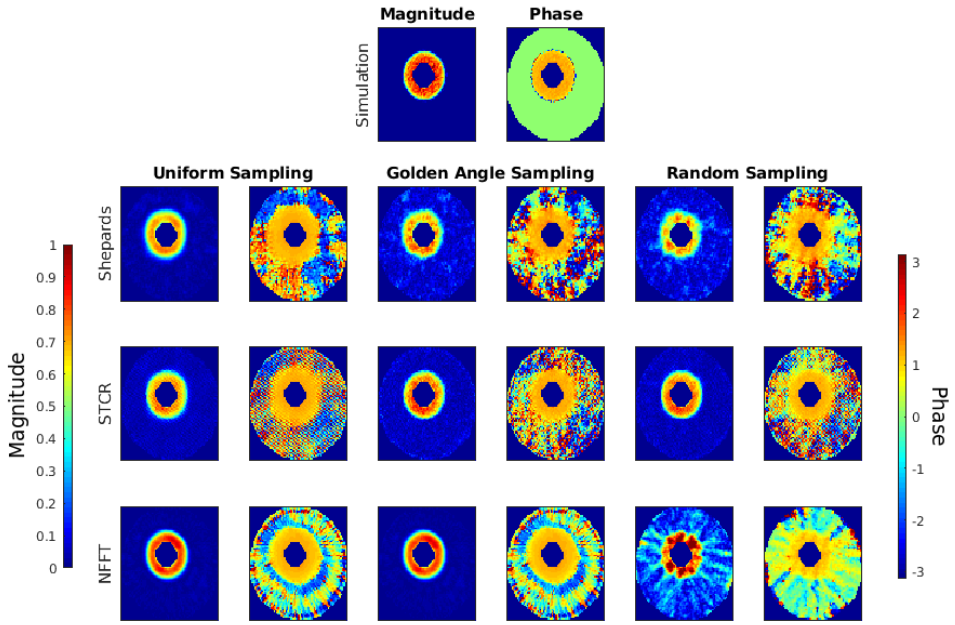

Figure 6.7: Images of the simulated tissue enhancement from radial images reconstructed with 34 projections at time points 1730 s. The top row shows the signal magnitude and phase of the simulated enhancement, as a reference. The second, third and fourth rows show the signal magnitude (first, third and fifth column) and phase (second, fourth and sixth column) of the enhancement images for all three radial reconstruction methods. All images were normalized to the mean signal of the phantom in the pre-injection image, and are displayed on the same magnitude scale for an easier comparison.

hancement well with 55 projections, when uniform or Golden angle sampling is used. For all three radial reconstruction techniques, images reconstructed with uniform or Golden angle sampling have comparable image quality. Between these two techniques, NFFT is visually more similar to the simulation. The signal magnitude of the center of the enhancement region is preserved only with NFFT and uniform or Golden angle sampling. The signal is slightly under-estimated with STCR or Shepard's method of interpolation, with a visible signal variation across the region. With STCR, the signal intensity on the inferior side of the phantom is well represented, while it is underestimated on the superior side. This is consistent in all images, regardless of the method of sampling used. Uniform sampling produces the best results, followed by Golden angle sampling, then random sampling. The signal for the image with Shepard's method of interpolation fades more uniformly, but had a hot and cold zones. The outer edge of enhancement is slightly blurred for all three reconstruction techniques, relative to the simulation.

When using 89 or 144 projections, the image quality is improved (not shown). Both NFFT and STCR outperform Shepard's method of interpolation, when uniform or Golden angle sampling is used. Again, NFFT has a more uniform appearance throughout the entire enhancement region, while STCR shows a slight intensity drop in the upper portion, and Shepard's method of interpolation continues to have hot and cold spots. The signal of the tissue enhancement region for the randomly sampled images is visibly inferior to uniform or Golden angle sampling for Shepard's method of interpolation and NFFT. The image quality is better preserved with STCR, though uniform or Golden angle sampling still produce better images. The outer edge of enhancement is sharp with STCR and NFFT, and slightly blurred with Shepard's method of interpolation, when uniform or Golden angle sampling is used. The enhancement images with random sampling have the greatest visual improvement when more projections are used in the reconstruction. While the edges of the randomly sampled images are sharp, the shape of the enhancement region is slightly warped for Shepard's method of interpolation and with NFFT. Again, the STCR reconstruction provides a higher quality image with random sampling than the other two techniques. In fact, the image quality with all three sampling methods are similar for STCR.

The image quality is visibly degraded after reducing the number of projec-

tions in the reconstruction from 55 to 34. This is especially apparent in the images reconstructed with Shepard's method of interpolation and STCR, both of which show a significant drop in the signal intensity of the enhancement region. While the NFFT images continue to have a higher signal intensity, there is some drop-off near the inner and outer boundaries. In all images with uniform or Golden angle sampling, the edges are blurred. The image quality with random sampling is much lower than with the other two sampling methods. The images with both Shepard's method of interpolation and NFFT had significant signal modulations within the tissue enhancement region and have a warped appearance around the outer boundary. However, STCR maintains a better quality image, that is comparable with the uniform and Golden angle sampled images. These trends are more significant when 21 projections are used in the reconstruction.

Image artifacts are another concern when reconstructing images with under-sampled data. Streaking artifacts are common for radial under-sampling. The artifacts in the tissue enhancement images have a slightly different appearance, which may be related to the subtraction of two radial images (post minus pre-injection). The artifacts are most often observed in the background. With Shepard's method of interpolation, the artifacts become apparent with 89 and fewer projections, when Golden angle or random sampling is used. The artifacts cause the signal magnitude to appear jagged, with variable signal intensity in the angular direction, and shifts the phase relative to the uniformly sampled case. With 55 and 89 projections, the artifacts appear as small spots. These have a streaking appearance with 34 or 21 projections. Surprisingly, the images with uniform sampling remain artifact free down to 21 projections. The artifacts are minimal in all images with STCR, regardless of how the data was sampled. The background artifacts in the NFFT have low signal intensity with uniform (34 or more projections) or Golden angle (55 or more projections) sampling, and are most easily observed in the signal phase. These artifacts may not impact the tissue enhancement correction due to the low intensity, though a mask may be applied to the image to block them out. The randomly sampled NFFT images have an obvious streaking pattern in the background with 55 and fewer projections. These artifacts are observed through the entire image and have a significant effect on the signal of the tissue enhancement.

The projection-based AIF measurement compares complex signals from the

Table 6.1: Average Phase in Tissue Enhancement Image with 55 Projections
Average Phase in Simulation 0.85 $\pm$ 0.46 rad

Technique	Uniform sampling	Golden angle sampling	Random sampling
Shepard's	1.15 $\pm$ 0.34 rad	1.15 $\pm$ 0.44 rad	1.11 $\pm$ 0.37 rad
STCR	1.140 $\pm$ 0.076 rad	1.15 $\pm$ 0.22 rad	1.18 $\pm$ 0.19 rad
NFFT	1.121 $\pm$ 0.033 rad	1.12 $\pm$ 0.20 rad	1.11 $\pm$ 0.40 rad

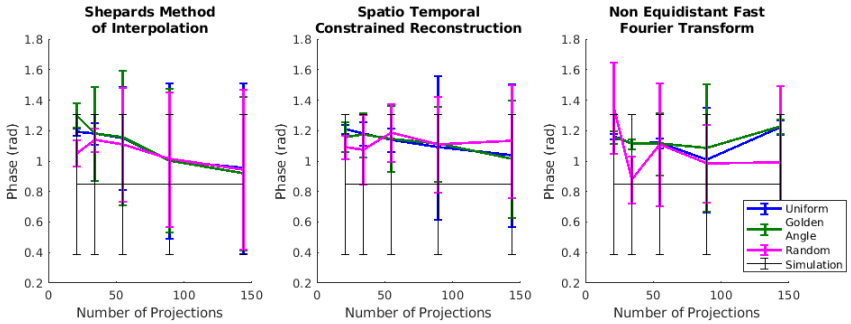

Figure 6.8: Average phase within the tissue enhancement region from the radial images. The uncertainty bars in the figure represent the standard deviation of the phase. The average phase is off-set from the simulated data set (black curve) for all three reconstruction techniques, but are consistent within the reconstruction technique, independent of how the data was sampled.

background and from the acquired projections. Therefore, the phase data must also be conserved as fewer projections are used in the reconstruction. The phase images are more visually similar to the simulation down to 55 projections, when the data is uniformly or Golden angle sampled. Reducing the projections to 34 or 21 does not appear to affect the phase dramatically, but the edges of the tissue enhancement region have a blurred appearance. The phase images with Shepard's method of interpolation (Golden angle or random sampling) and NFFT (random sampling) have visible artifacts through the tissue enhancement region, causing a spotted appearance in the signal phase. Streaking artifacts are present in most NFFT phase images, though these do not appear to impact the tissue enhancement signal when at least 55 projections are used in the reconstruction. The average phase ($\pm$ standard deviation) within the tissue enhancement region is summarized

in Figure 6.8 and Table 6.1 for reconstructions with 55 projections. The average phase appears to be consistently off-set from that of the simulation and is independent of the sampling method used.

The phase mis-representation is consistent with all reconstruction methods, indicating that the issue could be a result of the Radon transform or how the data was interpolated onto the Cartesian grid. The phase off-set with 55 projections is lowest with NFFT (off-set shift 0.26-0.27 rad), and similar between Shepard's method of interpolation and STCR (off-set shift 0.26-0.33 rad). The phase off-set improves slightly with Shepard's method of interpolation and STCR (uniform or Golden angle sampling) as more projections are used in the reconstruction. The average phase for the NFFT images does not have an obvious relationship with the number of projections used. The observed phase off-sets may not affect the AIF measurement, as all radial images will be affected similarly. This will be addressed later in the chapter.

Comparing the enhancement images, through a percent difference, can provide further insights into the effectiveness of each technique in correcting for local tissue enhancement. The enhancement images were compared as a difference between radial and the expected enhancement, and represented as a percent change relative to the signal of the pre-injection image. This, in effect, provides a more quantitative estimate of the errors introduced by the local tissue enhancement and how significant these errors are with regards to a radial AIF measurement. Figure 6.9 summarizes the results for the data set with 55 projections.

The percent difference is lowest with NFFT, followed by STCR, then Shepard's method of interpolation. The percent difference images with NFFT, and uniform or Golden angle sampling, has a more uniform appearance than the other two reconstruction techniques, showing only salt-and-pepper noise. The percent difference increases gradually from 144 to 21 projections, with the most notable change occurring from 34 to 21 projections. The percent difference image for STCR is comparable to NFFT in the lower portion of the tissue enhancement region, but shows a hot spot at the top right hand portion of the enhancement region. This is evident in all images, regardless of the number of projections used or the sampling method employed. The percent difference gradually increases as fewer projections are used (independent of sampling method used), with the most significant changes

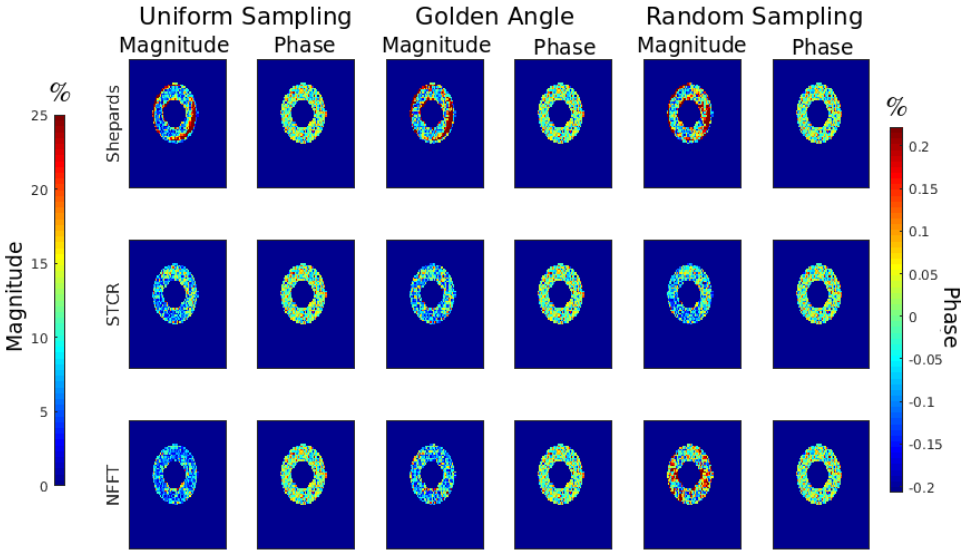

Figure 6.9: Percent difference in the signal between the enhancement images from the radial reconstructions (55 projections) and the simulated enhancement region at time point 225.8 s. The two color bars represent the signal magnitude (left bar - columns 1, 3 and 5) and signal phase (right bar - columns 2, 4 and 6). The signal is presented relative to the signal of the pre-injection image. The results may be interpreted as the percent error in signal associated with the radial reconstruction. For reference, the mean percent signal intensity of enhancement region rises from 3.7% at the first incidence of local tissue enhancement to 66.5% at time point 225.8 s.

occurring between 55 and 21 projections. With Shepard's method of interpolation, a high intensity ring is observed around the outer edge. This is likely a result of signal blurring, as observed from the enhancement images. This large difference could be problematic when compensating for local tissue enhancement, particularly if the region overlaps with the vessel signal in the projection. The percent difference is more uniform closer to the center of the tissue enhancement.

The percent difference, of the signal phase, is shown in columns 2, 4 and 6 in Figure 6.9. The phase of the percent difference has a uniform intensity, and seems to be independent of the sampling method used. The average percent difference

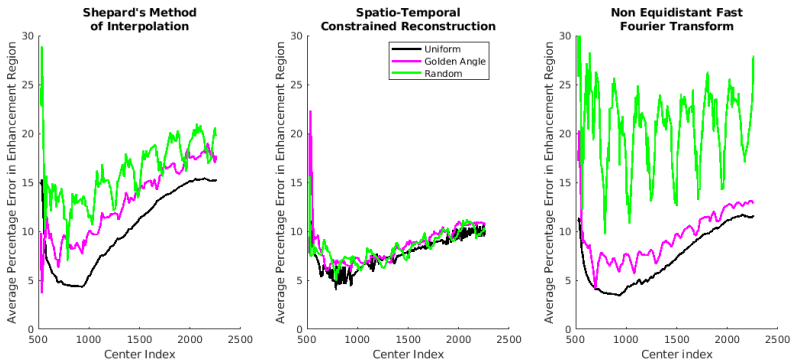

Figure 6.10: Average percent difference in the enhancement region for images reconstructed with 55 projections. The percent difference was normalized to the pre-injection image to provide insights into how much local tissue enhancement affects the signal intensity. These results suggest that the STCR or NFFT (uniform or Golden angle sampling) are the best techniques for compensating for local tissue enhancement.

in phase increases slightly when the number of projections is reduced to 55 with NFFT, or to 34 with Shepard's method of interpolation or STCR.

Figure 6.10 summarizes the average percent difference in the tissue enhancement region temporally, while Tables 6.2, 6.3 and 6.4 summarize the average percent difference ($\pm$ standard deviation) from time points 108.1-225.8 s. This range was selected as the size of the enhancement region was sufficiently strong (size and intensity) to give a good estimate of the differences. As a reference, the average signal intensity of the expected tissue enhancement, relative to the pre-injection image, increases monotonically from 9.3 ± 4.9 at time point 108.1 s to 66.5 ± 4.4 at time point 225.8 s.

The results show that the STCR and NFFT perform better than Shepard's method of interpolation. The average percent error increases as the enhancement region grows, a trend consistent between all sampling methods and number of projections. In general, uniform sampling has the lowest errors, followed closely by Golden angle sampling. And the errors increase as fewer projections are used, with data sets using 89 and 144 projections providing similar results, followed closely by 55 projections. Reduction from 34 to 21 projections resulted in large jumps

Table 6.2: Mean Percent Difference in the signal Magnitude of the Enhancement Region from the Radial Images and the Simulation: 100 x (Shepard's Method of Interpolation-Simulation) / Pre-Injection Image

Number of Projections	Uniform	Golden Angle	Random
144	12.5 ± 2.4	14.0 ± 2.4	15.0 ± 2.1
89	13.3 ± 3.0	15.8 ± 2.8	16.9 ± 2.7
55	12.9 ± 2.8	15.5 ± 2.5	16.5 ± 1.9
34	12.3 ± 2.0	14.4 ± 1.8	18.9 ± 2.2
21	14.3 ± 1.9	16.0 ± 1.8	21.4 ± 2.3

Table 6.3: Mean Percent Difference in the signal Magnitude of the Enhancement Region from the Radial Images and the Simulation: 100 x (STCR-Simulation) / Pre-Injection Image

Number of Projections	Uniform	Golden Angle	Random
144	6.53 ± 0.69	7.49 ± 0.86	7.24 ± 0.85
89	9.3 ± 1.7	10.2 ± 1.8	9.8 ± 1.5
55	8.6 ± 1.2	9.2 ± 1.4	9.0 ± 1.2
34	9.5 ± 1.1	9.1 ± 1.1	9.6 ± 1.0
21	13.7 ± 1.0	9.3 ± 1.0	10.7 ± 1.0

Table 6.4: Mean Percent Difference in the signal Magnitude from the Enhancement Region of the Radial Images and the Simulation: 100 x (NFFT-Simulation) / Pre-Injection Image

Number of Projections	Uniform	Golden Angle	Random
144	4.60 ± 0.26	6.95 ± 0.95	9.8 ± 2.0
89	9.5 ± 2.3	11.2 ± 2.1	13.4 ± 1.7
55	9.5 ± 2.6	9.5 ± 2.6	17.0 ± 2.9
34	9.2 ± 2.3	10.6 ± 1.9	17.88 ± 0.50
21	9.1 ± 2.0	10.6 ± 1.3	18.1 ± 1.1

in the percent difference, suggesting that the image reconstruction should use at minimum 34 projections, though more is better if the temporal resolution is not a constraint.

Based on the results of the tissue enhancement images, STCR (any sampling method) or the NFFT (uniform or Golden angle sampling) are most appropriate for a local tissue enhancement correction. The image series with 144 or 89 projections provide the most accurate results, and are the best candidates for the local tissue enhancement correction. Temporal blurring does not seem to have an impact on the results as signal changes in the region surround the vessel are slow and smooth. The next section will evaluate our ability to accurately correct for local tissue enhancement from projections of the radially reconstructed images.

6.4 Results: Effects of Local Tissue Enhancement on the Projections

The projection-based AIF compares a background signal to the acquired projections. Therefore, it is informative to study the projections of the radial images reconstructed with data acquired post-injection (enhancement images). The enhancement images were summed (complex) along the second dimension to create projections at each particular time. These projections provide information about the evolution of local tissue enhancement across the experiment. Comparing these to the projections from the simulation allows us to assess how effective each reconstruction method would be in compensating for local tissue enhancement.

It is expected that the contrast agent will distribute in the tissue at a slow rate relative to changes in the blood. If true, the lower temporal-resolution of the radial images - from taking data over a finite time interval - may not compromise the accuracy of the local tissue enhancement correction. The goal of this study is to determine the lower limit of the number of projections required to successfully recreate the enhancement pattern and provide a reasonable correction to the post-injection projections. Figure 6.11 shows the enhancement profiles (oriented along the y-axis) for all radial image series with 55 projections (200 images spanning the 2330 sample times).

The projections have two distinct regions in which a sharp change in signal is observed: the first at 58.2 s, which corresponds to the injection, and another at 108.1 s, when local tissue enhancement is observed in the surrounding tissue. Time point 173.0 s is the point at which the signal intensity from the tissue enhancement

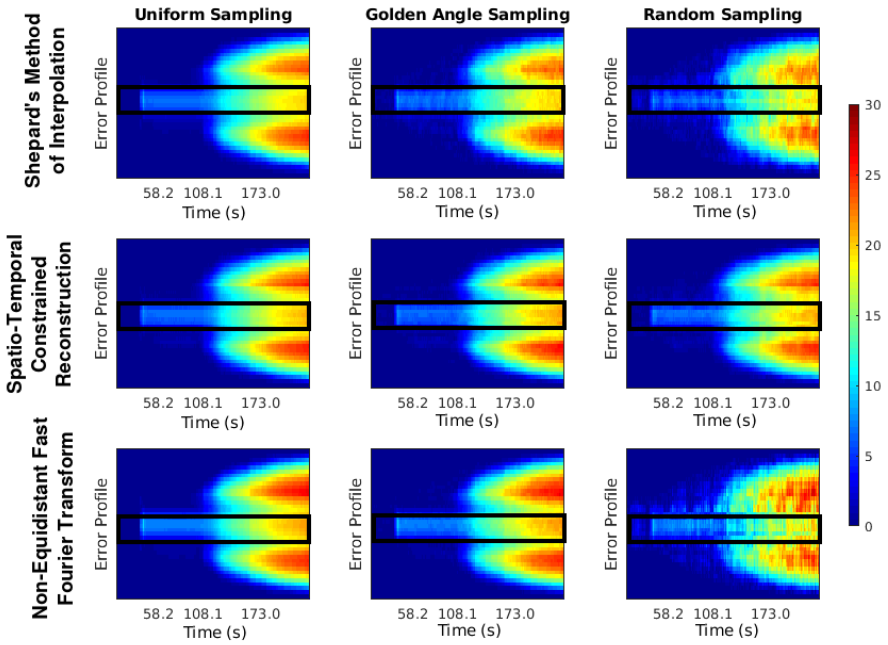

Figure 6.11: Projections of isolated tissue enhancement, from the difference of post and pre-injection radial images reconstructed with 55 projections. The projection profile is oriented along the y-axis and time along the x-axis, with points of interested indicated (injection at 58.2 s, tissue enhancement observed at 108.1 s). The vessel location is outlined with the black box.

approaches its asymptotic value. The black box outlines the region associated with the vessel and is of greatest interest for this study.

The tissue enhancement profiles with uniform and Golden angle sampling are visually superior to those with randomly sampled data. The randomly sampled profiles suffer from signal blurring and intensity modulations in time. None of these are of sufficient quality for a tissue enhancement correction. The enhancement profiles with uniform and Golden angle sampling are comparable with 89 and 144 projections. With 55 projections or less, uniform sampling produces enhancement profiles that vary smoothly across the experiment, while those with Golden angle sampling have slight signal variations between consecutive projections.

Between the three reconstruction techniques (uniform or Golden angle sampling), NFFT appears to slightly outperform STCR, while Shepard's method of interpolation is of much lower quality. With Shepard's method of interpolation, signal intensity modulations are observed in the data sets with 55 and fewer projections, and the signal within the vessel region is lost in the data sets with 34 or 21 projections. Only the data set with 144 projections is visually similar with the simulation. With STCR, data sets with at least 55 projections are comparable with the simulation, though the data set with Golden angle sampling and 55 projections has signal modulations within the region of the vessel. The profiles with 21 or 34 projections suffer from blurring and loss of signal within the region of the vessel. The enhancement profile from the NFFT images are also comparable with the simulation with 55 or more projections, though the data sets with 34 projections are still of reasonable quality. The data sets with 21 projections are clearly inferior, suffering from signal intensity modulations in time, signal blurring and loss of signal within the region of the vessel.

There is a sharp increase in the signal difference within the voxels associated with the vessel that coincides with the timing of the injection (time = 58.2 s). Local tissue enhancement is not observed this early in the simulation, so all changes in the projection signal are associated with a change in the vessel signal. The average pre-injection signal intensity of the vessel, within the projection, is 0.130 ± 0.017. It reaches a maximum intensity of 17.3-17.7 at the center of the vessel or 15.3 ± 2.1 over the entire vessel region. The variability is due to the number of voxels that the vessel spans in the second dimension. Since the vessel is assumed to be cylindrical, the center will sum over more voxels than at the edge. For reference, the average signal intensity of the pre-injection image in the neighbourhood of the vessel is 79.8 ± 3.5. Recall that these profiles are the calculated from the summation of an enhancement image ((post-injection DCE image at time t - pre-injection image)/pre-injection image).

The signal magnitude at the center of the vessel reaches a maximum of 7.02-8.62 with Shepard's Method of interpolation (34-144 projections), 7.10-8.29 with STCR and 8.14-16.50 with NFFT. The maximum value was achieved with 55 projections (uniform or Golden angle sampling) or with 34 projections (random sampling), regardless of the reconstruction technique used. These maxima are much

lower than the expected signal from the simulation, which reaches a peak intensity of 17.3-17.7. The under-estimation in signal intensity may be a result of signal smoothing. The peak of the AIF in the simulation spans 5 time positions; only two of which are selected time-positions for image reconstruction. Further, at most 5 projections in the reconstruction will contain information of the peak concentration, while the rest were acquired with lower intra-vascular concentrations. These results reveal the importance of using a projection-based AIF measurement immediately following the bolus injection. Luckily, tissue enhancement is expected to be minimal at this point, so the uncorrected AIF may be used.

The signal magnitude, for data sets reconstructed with 55-144 projections, tapers off to average values of 6.15-7.01 for Shepard's method of Interpolation, 6.58-6.98 for STCR and 7.14-8.09 for NFFT just before tissue enhancement is observed in the surrounding tissue at 108.1 s. The signal in the simulation averages 6.927 ± 0.034 over this range. The better agreement between the radial images and the simulation further supports the idea that temporal signal blurring may have contributed to the lower signal intensities within the vessel following injection. Further, these results show that the tissue enhancement correction may still be reliable in cases where the the contrast agent extravasates into the surrounding tissue earlier in the experiment.

The next study investigates whether temporal blurring from data collected over a finite time interval impacts our ability to accurately correct for local tissue enhancement. Figure 6.12 compares the profiles for a 'snapshot' and 'dynamic' experiment. Recall that 'snapshot' means that all projections were taken at one specific time point, while 'dynamic' refers to projections taken from a temporal window, centered at the time point of the 'snapshot' image.

The simulated profiles are shown in the top row as the gold standard for comparison. Below it are the projection profiles for the radial reconstructions with 55 projections and uniform sampling. The snapshot and dynamic profiles are both plotted with the same signal intensity scale, while the difference is windowed to a scale set at 1% of the the snapshot and dynamic series. These percentages are very low since the signal of the pre-injection profile is much greater than that of the tissue enhancement.

The difference is quite small, but shows greater values in the vicinity of the ves-

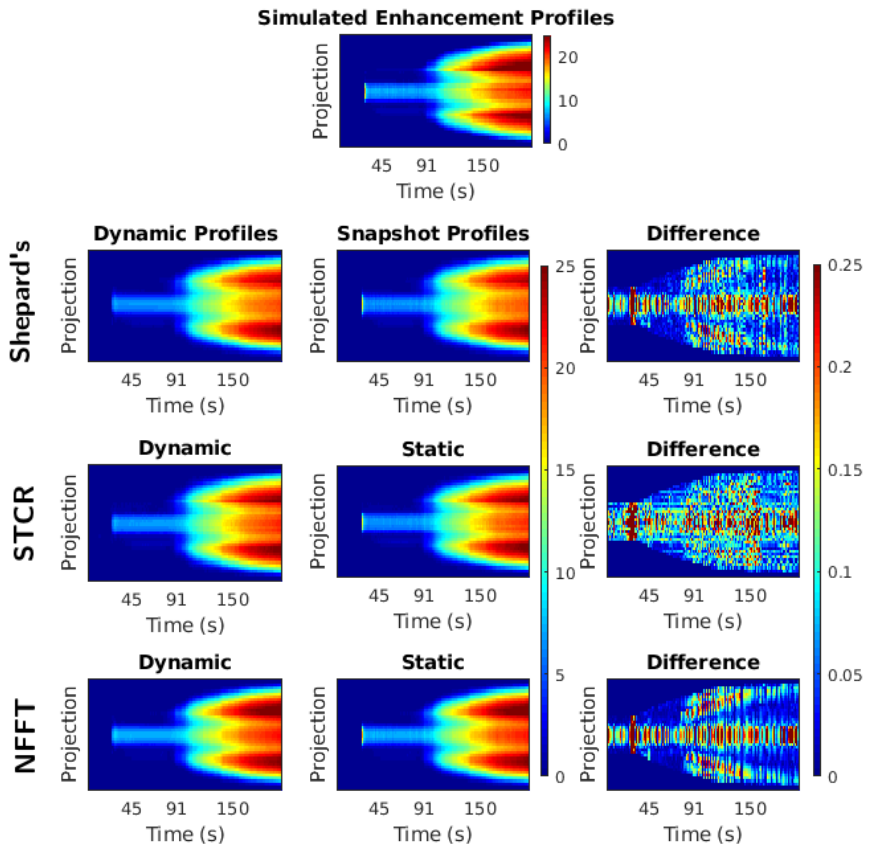

Figure 6.12: Projection profiles of tissue enhancement for the dynamic and snapshot image series, and the difference between them. Images were reconstructed with 55 projections from uniformly sampled data. The k-space data was either acquired all at one time point (snapshot) or over a finite time interval (dynamic), in which one sample is taken over a temporal window centered at the time point of the snapshot image. The dynamic and snapshot series are windowed identically, while the difference is set to a window maximum of 1% of the other Dyanmic and snapshot series. The units are relative, as the radial images were set to have a mean value of 1.0.

sel. The signal within the vessel is on the order of 6.396 $\pm$ 0.010 from time points 44.7-225.8, while the difference is 0.161 $\pm$ 0.013. This equates to differences on the order of 1.46-2.38% (Shepard's method of interpolation), 1.28-2.52% (STCR) or 1.41-2.22% (NFFT) of the vessel signal when 34 or more projections are used in the reconstruction. These errors are relatively small and are not expected to impact the accuracy of the AIF measurement. At the injection, the errors varies widely (with no clear trends), ranging from 3.6-107.6% in the data sets with 34 or more projections. Relying on the projection-based AIF is recommended here.

Table 6.5 calculates the average percent difference from these profiles from time points 93.4-225.8 s, where local tissue enhancement is strong in the background. The percent difference is relative to the projection of the pre-injection image, to better quantify how much of an impact temporal blurring has on the characterization of local tissue enhancement. These results are shown for the data set with Golden angle sampling, though similar values were obtained with uniform and random sampling.

Table 6.5: Percent Difference between Snapshot and Dynamic Profiles in the Enhancement Area (Time points 93.4-225.8 s, Golden angle sampling)

Number of Projections	Shepard's (%)	STCR (%)	NFFT (%)
144	0.023 $\pm$ 0.006	0.030 $\pm$ 0.005	0.016 $\pm$ 0.006
89	0.020 $\pm$ 0.008	0.031 $\pm$ 0.005	0.012 $\pm$ 0.005
55	0.022 $\pm$ 0.010	0.030 $\pm$ 0.005	0.010 $\pm$ 0.005
34	0.015 $\pm$ 0.014	0.027 $\pm$ 0.007	0.009 $\pm$ 0.004
21	0.012 $\pm$ 0.009	0.051 $\pm$ 0.009	0.008 $\pm$ 0.005

The average percent difference is comparable between NFFT and STCR, and slightly greater with Shepard's method of interpolation. They are on the order of 0.006-0.051% from time point 93.4 s to the end of the experiment. These values are very low due to the difference being compared to the pre-injection image, which generally has much higher signal than the difference. The percent difference is greatest around the injection, reaching percent errors as high as 1.60% (range 0.97-1.49 for Shepard's method of Interpolation, 0.80-1.36% for STCR and 0.34-1.60% for NFFT for image reconstructions with 55-144 projections). In general,

the values are greatest with the data sets with 144 projections, and decreases as fewer projections are used. This could be attributed to temporal blurring of signal from data taken over a larger temporal window. To put this into perspective, the injection covers approximately 15 time points (5 to reach the peak concentration, and 10 time points to reach a concentration of 0.655 mM, which is half way between the peak concentration (0.95 mM) and the steady concentration at the end of the experiment (0.37 mM)). Only two of these were randomly selected time-points for image reconstruction.

These results suggest that temporal blurring, due to taking data from different degrees of enhancement (ie. different times), may not be an issue for a smooth, slowly varying enhancement region similar to what was simulated. The percent difference is small for all data sets studied, including those using 144 projections in the reconstruction. Reconstructing images with a larger number of projections will improve the SNR and sharpness of edges of image features, and therefore allow for a more effective local tissue enhancement correction. When the concentration gradient is sharp, as is often observed immediately following the injection, fewer projections may be desired. Local tissue enhancement is expected to be minimal here, but these images could provide information about motion or dilation of the vessel during and immediately after the injection.

A more informative analysis looks at the difference between the profiles from the radial images and the simulation. To estimate the magnitude of errors introduced by the radial reconstruction, the difference is compared to the average pre-injection image and scaled as a percentage. Figure 6.13 shows the percent difference, between the projection profiles from the radial images and the simulated profiles, for all three radial reconstruction techniques with 55 projections and each sampling scheme. All difference profiles are plotted on the same scale, with a maximum set to 5%.

The percent difference profiles are divided into two distinct regions: the first is the region of the vessel, and the second region is the surrounding tissue on both sides. Within the vessel, the maximum percent difference occurs at the start of the injection. This is supported by the previous analysis, in which the signal at the peak of the AIF suffers from temporal blurring due to data taken before, during and after the contrast injection.

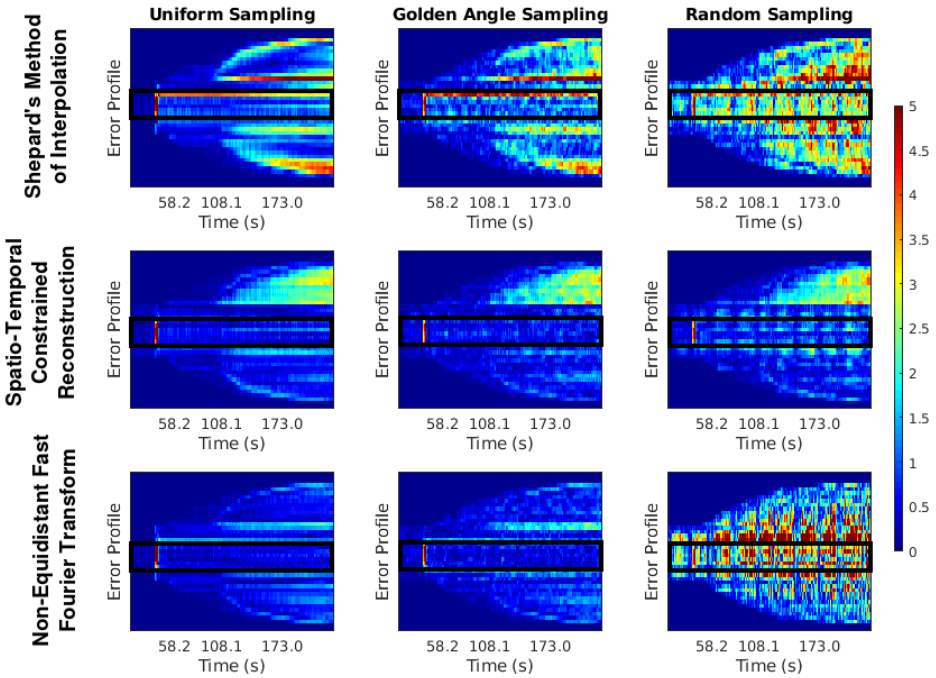

Figure 6.13: Percent difference between the enhancement profiles from the radial images and from the simulated data set, normalized to the signal of the pre-injection image. 55 Projections were used in the reconstruction. STCR (all sampling methods) and NFFT (uniform or Golden angle) are superior to Shepard's method of Interpolation.

Once the concentration within the vessel approaches a steady value, the error within the vessel is significantly reduced (except for NFFT with random sampling). The average percent difference, when using 55 or more projections and either STCR (all sampling methods) or the NFFT (uniform or Golden Angle), is on the order of 0.41-0.92%, between time points 58.2 s to 225.8 s. With Shepard's method of Interpolation, the average percent difference is low at the center of the vessel and increases at the edges, with average percent differences ranging from 1.31-3.33%. Uniform and Golden Angle sampling work best for this technique.

The average percent differences, within the vessel and the entire tissue enhancement, are plotted in Figure 6.14 and Figure 6.15 and summarized in Table 6.6.

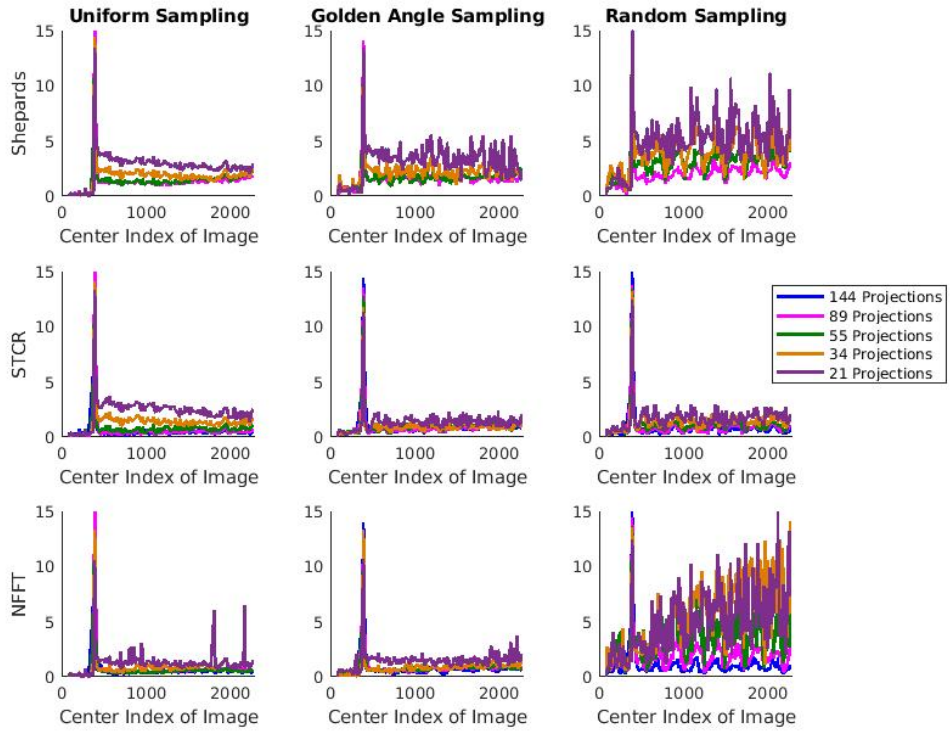

Figure 6.14: Average percent difference in the signal magnitude between the enhancement region of the radial images and the expected signal, for the pixels corresponding to the vessel. The difference is scaled against the pre-injection image, so as to estimate the errors introduced at this stage of the correction. The average percent error consistently shows a sharp peak during the contrast agent injection (58.2 s), then approaches a steady value. It is lowest with 144 projections, and increases as fewer projection are used in the reconstruction.

The average is similar between STCR and NFFT, while Shepard's method of interpolation produces larger values (exception NFFT with random sampling).

Within the vessel, the average percent difference is lowest with 144 projections, and increases as fewer projections are used. This is consistent for all three reconstruction technique. Uniform and Golden angle sampling often produce similar percent differences, while random sampling is greater. Based on the figure, recon-

structions with at least 55 projections (any reconstruction technique and uniform or Golden angle sampling) have similar percent differences. The percent differences increase more rapidly with 34 projections with uniform sampling than it does with Golden angle or random sampling. Among the three techniques, NFFT (followed closely by STCR) has the lowest percent differences within the vessel with uniform and Golden angle sampling, and STCR is the best technique for random sampling.

Table 6.6: Average Percent Difference in Profiles for the Vessel Voxels Golden Angle Sampling (Time points 58.2-225.8 s)

Number of Projections	Shepard's (%)	STCR (%)	NFFT (%)
144	3.33 ± 0.94	0.73 ± 0.18	0.59 ± 0.18
89	1.55 ± 0.25	0.71 ± 0.18	0.74 ± 0.18
55	1.70 ± 0.31	0.92 ± 0.23	0.76 ± 0.16
34	2.18 ± 0.45	0.89 ± 0.23	0.86 ± 0.24
21	3.33 ± 0.93	1.41 ± 0.36	1.54 ± 0.44

Extending the analysis to include the surrounding tissue, the average percent difference is similar with 89 and 144 projections, and increases with fewer projection. This is expected as the signal changes from local tissue enhancement are slow and smoothly varying. In addition, the AIF has reached a near steady value by this point. Therefore, a coarser temporal resolution can still accurately recreate the enhancement region. When uniform or Golden angle sampling are used, the percent errors are comparable with 55-144 projections, and slightly greater with 34 projections. The percent errors increase more rapidly when random sampling is used, particularly with the NFFT.

The percent differences in the surrounding tissue is generally less than 1.5% for NFFT, averaging $0.86 \pm 0.23\%$ (uniform) and $1.01 \pm 0.19\%$ (Golden angle) for images with 55 projections. There is a narrow band of higher percent errors just superior of the vessel, though the differences rarely exceed 3.5% there. The percent differences superior to the vessel are significantly higher with STCR, which may be related to the signal intensity differences observed in the images. For the data sets with 55 projections, the average percent differences inferior and superior to the vessel are $0.63 \pm 0.12\%$ / $2.69 \pm 0.41\%$ (uniform) and $0.70 \pm 0.17\%$ /

2.77 $\pm$ 0.50% (Golden angle). The importance of these values depend on where the vessel is situated. We may have been fortunate that the vessel is located near the center of the phantom, so the average percent differences in the proximity of the vessel are lower (see above). Shepard's method of interpolation produces the largest percent differences, particularly at the outer boundary of enhancement. To illustrate this, the percent difference increases from 1.49 $\pm$ 0.22% (uniform) or 1.77 $\pm$ 0.24% (Golden angle) near the vessel to 4.26 $\pm$ 0.14% / 3.11 $\pm$ 0.25% (uniform) or 5.28 $\pm$ 0.70% / 3.61 $\pm$ 0.48% (Golden angle) at the upper and lower boundaries, respectively.

Since the region within the vessel is of greatest importance, it is imperative to select a reconstruction technique that minimizes errors in this region. Based on this figure, it is clear that STCR and NFFT are superior to Shepard's method of interpolation, and uniform or Golden angle sampling generally produce lower percent errors than random sampling. The largest errors are often found at the boundaries of the vessel, where the signal intensity changes rapidly. This could be attributed to signal smoothing due to limited information at the outer regions of k-space, where image details are stored. It is advisable to use a minimum of 55 projections in the local tissue enhancement correction.

The optimal number of projections used in the reconstruction is dependent on the contrast kinetics (i.e. rate of change) and the temporal resolution of the data. There is a trade off between a higher temporal resolution and accurately modeling the tissue enhancement. In general, if the enhancement curve changes rapidly, it is important to reconstruct images at a high rate to capture key features in the curve. The best example is at the peak magnitude. Reconstructing images with 233 projections could underestimate the degree of enhancement, thus leading to errors in determining the concentration. Alternatively, image reconstruction with too few projections could lead to a greater presence of imaging artifacts and blurring.

The temporal resolution of a radial data set is determined by the number of projections used in the reconstruction. If Golden angle sampling is used, it is possible to retrospectively reconstruct multiple image series with a sliding window reconstruction, each having a different temporal resolution [135, 176]. This is beneficial for DCE experiments as the trade off between having a high quality image - with high spatial resolution - and a high temporal resolution is often a limitation. Image

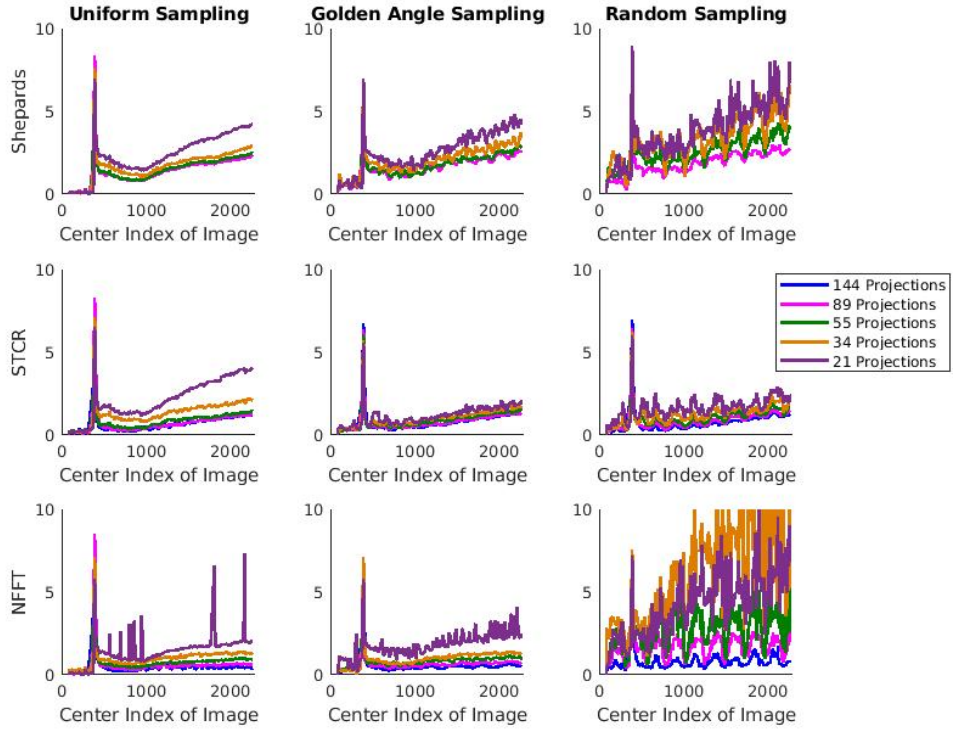

Figure 6.15: Average percent difference in the signal magnitude between the enhancement region of the radial images and the expected signal. The difference is scaled against the pre-injection image. The results show that STCR and NFFT have the lowest percent errors, which increases as the number of projections used in the reconstruction is reduced. For all cases, the average percent error has a sharp peak during the contrast agent injection (58.2 s), then increases again beyond time point 108.1 s, when local tissue enhancement becomes more apparent.

series using a larger number of projections (144, 233, etc.) will provide high contrast images for visualizing the anatomy, while image series with fewer projections (34 or 55, etc.) can better capture rapid changes between images. By analyzing multiple data sets in this way, it is possible to extract more information about the rate and shape of enhancement.

An estimate of the peak concentration in the mouse tail would greatly improve our ability to assess errors in our measurements in-vivo. The simulations involved adding a local contrast perfusion to an anatomical image and taking one radial projection from each time point. This study shows that a minimum of 55 projections are required to produce a satisfactory image and provide a reasonable estimate of local tissue enhancement; but this could be greatly dependent on the rate of contrast kinetics in the vasculature.

6.5 Correcting the Projection-Based AIF for Local Tissue Enhancement

The final stage of analysis involves measuring the AIF with the projection-based AIF technique detailed in Chapter 4, then correcting it for local tissue enhancement with radial images. The radial tissue enhancement correction involves a comparison of a post-injection image with its sister pre-injection image. Both images use the same sampling technique (angles of acquisition and number of projections) to minimize reconstruction-related factors, such as artifacts. The difference between these images is then projected along the dimension perpendicular to the angle of acquisition, after removing the data from the vessels. This provided an estimate of how the post-injection profiles were affected by the local tissue enhancement. By subtracting the difference profile from the sampled projections, we effectively replace the tissue enhancement with the original signal pre-injection. The projection-based AIF approach is then applied to get the tissue-enhancement corrected AIF.

The tissue enhancement corrected radial AIF's, with images reconstructed with 55 and 34 projections, are shown in Figure 6.16 and Figure 6.17. Both Figures use Golden angle sampling. The sampling pattern is shown in the inset of the Figure.

The uncorrected AIF follows the expected trend of the input curve until time point 103.1 s, at which point, it diverges due to local tissue enhancement. The

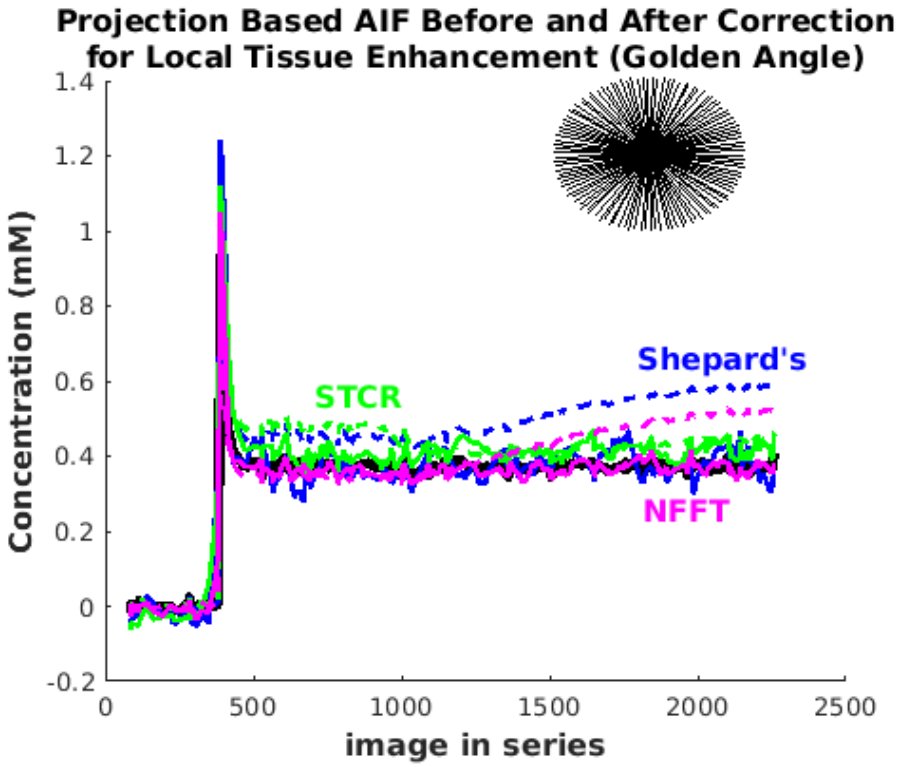

Figure 6.16: Radial projection-based AIFs measured before and after correction for local tissue enhancement. The dashed lines represent the raw, uncorrected AIF, while the solid lines represent the tissue enhancement corrected AIFs. In this study, a subset of 55 projections, with Golden angle sampling, were used in the radial reconstruction. The correction, which is outlined in Figure 6.5, was effective in removing the divergence caused by the tissue enhancement for all three reconstruction methods. The curves with Shepard's method of interpolation and the NFFT are in good agreement with the input curve, while STCR over-estimates the concentration.

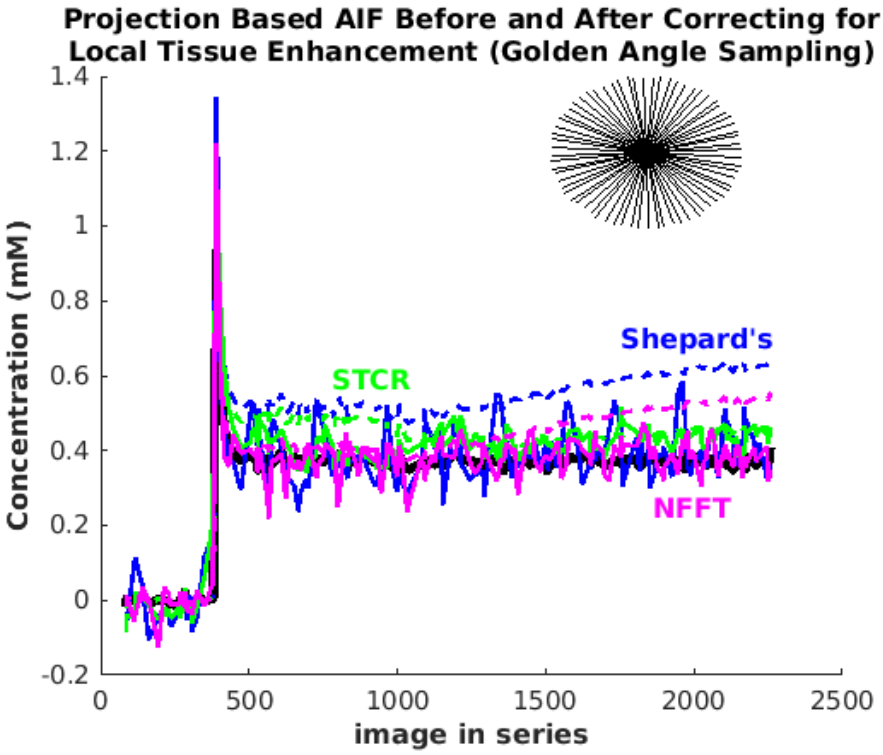

Figure 6.17: Radial projection-based AIFs measured before and after correction for local tissue enhancement. The dashed lines are the uncorrected AIFs, while the solid lines are the tissue enhancement corrected AIFs. In this figure, 34 projections were used in the reconstruction, with Golden angle sampling. Local tissue enhancement was corrected using the method outlined in Figure 6.5 and was effective at removing the divergence for all three radial reconstruction techniques. The results are similar to the case with 55 projections, though the corrected curves are noisier.

divergence is the greatest with Shepard's method of interpolation (final concentration of 0.650 mM, or 1.76x greater), then NFFT (final concentration of 0.573 mM, or 1.55x greater), and the lowest with STCR (final concentration of 0.552 mM, or 1.49x greater) in the data sets with 55 projections. There are slight differences in the uncorrected AIF as the sampling scheme changes or when a different number of projections are used in the reconstruction. This is likely related to image artifacts that would carry errors through to the AIF measurement.

The tissue enhancement correction was effective in removing the bias for all radial reconstruction techniques. The corrected AIF with Shepard's method of interpolation and the NFFT most closely matched the input AIF, whereas the STCR over-estimated the concentration past the peak by a factor of 1.19-1.34 mM (uniform sampling), 1.19-1.26 mM (Golden angle) or 1.21-1.41 mM (random sampling). Consistent with previous results, the corrected AIF is most comparable with the simulated curve with uniform or Golden angle sampling, and 55 or more projections used in the image reconstruction. With 34 or 21 projections, the corrected AIFs are either noisy or over-estimate the concentration when local tissue enhancement is present. The corrected AIFs with random sampling (Shepard's method of Interpolation or NFFT) are very noisy with 55 and fewer projections, and would not be effective in modeling DCE-MRI data.

The average difference between the tissue enhancement corrected projection-based AIFs and the input curve from time points 108.1 s to the end of the experiment are summarized in Tables 6.7 and 6.8.

The differences are consistently the lowest when 55, 89 or 144 projections are used in the image reconstruction. The average difference between uniform and Golden angle sampling are comparable (within uncertainty), suggesting little difference between the two sampling methods or all three techniques. Between the three image reconstruction methods, the NFFT reconstruction most closely agrees with the input AIF, followed closely by Shepard's Method of interpolation. The average difference for the STCR reconstruction is consistently greater, by 0.055-0.090 mM. This is a significant amount as the expected intra-vascular concentration is 0.371 $\pm$ 0.010 mM over this time frame.

The ratio of the tissue-enhancement corrected projection-based AIF to the input AIF provides insightful information on the effectiveness of the correction. If the ra-

Table 6.7: Average Difference Between the Corrected Radial AIF (Uniform Sampling) to the Input AIF from time points 108.1-225.8 s

Number of Projections	Shepard's (mM)	STCR (mM)	NFFT (mM)
144	0.021 ± 0.028	0.088 ± 0.036	-0.002 ± 0.017
89	0.004 ± 0.025	0.086 ± 0.022	0.001 ± 0.016
55	0.020 ± 0.022	0.073 ± 0.022	0.003 ± 0.016
34	0.067 ± 0.026	0.124 ± 0.027	0.056 ± 0.020
21	0.031 ± 0.046	0.114 ± 0.046	0.091 ± 0.051

Table 6.8: Average Difference Between the Corrected Radial AIF (Golden angle) to the Input AIF from time points 108.1-225.8 s

Number of Projections	Shepard's (mM)	STCR (mM)	NFFT (mM)
144	0.010 ± 0.034	0.068 ± 0.022	-0.001 ± 0.018
89	0.021 ± 0.042	0.083 ± 0.024	0.008 ± 0.017
55	0.026 ± 0.039	0.082 ± 0.023	0.012 ± 0.021
34	0.058 ± 0.070	0.099 ± 0.030	0.056 ± 0.020
21	0.091 ± 0.162	0.101 ± 0.034	0.063 ± 0.085

tio is flat beyond the peak of enhancement, then the tissue enhancement correction was effective, save a scaling factor. Figure 6.18 shows the ratios for the corrected AIF curves to the input curve, in which Golden angle sampling was used.

The ratios are close to 1.00 with Shepard's method of interpolation and the NFFT, when at least 55 projections are used in the reconstruction. Reducing this number causes the ratio to increase, as a result of over-estimating the intra-vascular concentration. Since local tissue enhancement resulted in an over-estimation of the measured concentration post-injection, it is likely that the image quality of the images with 34 and 21 projections was insufficient for accurately accounting for the effects of local tissue enhancement. The measured AIFs with STCR significantly over-estimated the concentration, yielding ratios between 1.1-1.3. This is interesting as the enhancement images with STCR were most similar to the simulation. The scaling factor for the correction was calculated with the same method for all three reconstruction techniques.

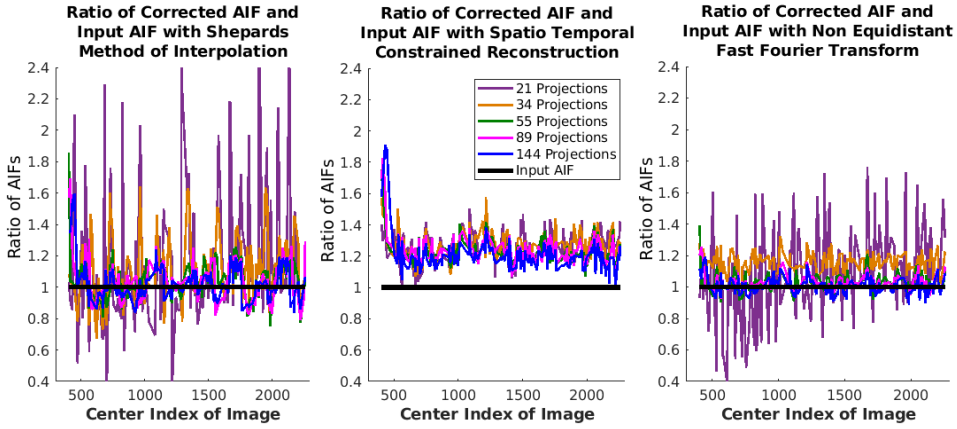

Figure 6.18: Ratio of the radial projection-based AIF (Golden angle sampling), after correction for local tissue enhancement, to the input curve. The results show that STCR overestimates the concentration, while Shepard's method of interpolation and NFFT are more accurate.

The over-estimation in concentration is present for all STCR-corrected AIFs, regardless of the sampling method used. Since the ratio is consistent throughout the experiment, these curves could be re-scaled if STCR is the preferred reconstruction technique. However, the AIFs with NFFT (55 or more projections and uniform or Golden angle sampling) agree with the input curve better. Using the NFFT over STCR would be beneficial, as the scaling factor could introduce additional uncertainties. Tables 6.9 (uniform sampling) and 6.10 (Golden angle sampling) summarize the ratios of the corrected AIF to the input AIF from time point 108.1 s to the end of the experiment, where local tissue enhancement is observed in the images.

The concentration at the peak is over-estimated post-correction when uniform or Golden angle sampling was used. The degree of over-estimation is related to the number of projections used in the reconstruction. In both cases, the over-estimation increases gradually as the number of projections is reduced from 144 to 34, but not in a linear fashion. The data sets with random sampling have conflicting results, with most AIFs under-estimating the concentration with Shepard's Method of Interpolation, over-estimating with STCR, and having good agreement with the NFFT. In comparison, the simulated peak concentration is 0.929 mM, while the

Table 6.9: Average Ratio of the Corrected Radial AIF (Uniform Sampling) to the Input AIF from time points 108.1-225.8 s

Number of Projections	Shepard's	STCR	NFFT
144	1.06 ± 0.08	1.25 ± 0.07	1.00 ± 0.04
89	1.01 ± 0.06	1.25 ± 0.06	1.01 ± 0.04
55	1.06 ± 0.06	1.21 ± 0.06	1.02 ± 0.04
34	1.18 ± 0.07	1.34 ± 0.08	1.16 ± 0.06
21	1.08 ± 0.12	1.32 ± 0.13	1.25 ± 0.14

Table 6.10: Average Ratio of the Corrected Radial AIF (Golden angle sampling) to the Input AIF from time points 108.1-225.8 s

Number of Projections	Shepard's	STCR	NFFT
144	1.03 ± 0.09	1.19 ± 0.06	1.00 ± 0.05
89	1.06 ± 0.11	1.23 ± 0.06	1.03 ± 0.05
55	1.07 ± 0.11	1.23 ± 0.06	1.04 ± 0.06
34	1.16 ± 0.19	1.28 ± 0.08	1.16 ± 0.06
21	1.25 ± 0.44	1.28 ± 0.09	1.18 ± 0.23

uncorrected AIFs have peak concentrations ranging from 0.870-1.175 mM (uniform), 0.890-1.115 mM (Golden angle) and 0.929-1.148 mM (random). Though these do not all agree with the input AIF, the uncorrected AIF was consistently closer to the input AIF at the peak than the tissue enhancement corrected ones.

The over-estimation in the corrected curves could be a result of insufficient image quality to accurately model the tissue enhancement, or from added noise introduced by the tissue enhancement correction. The technique involves correcting the acquired projections using a projection of a difference of two images. The correction profile will be noisier with images reconstructed with fewer projections due to signal smoothing and a higher probability of reconstruction artifacts.

Radially reconstructed images all contain information about the local enhancement, and could be used to determine at what stage the correction must be applied. It is recommended to first identify the point at which local tissue enhancement becomes problematic, and only apply the correction beyond that point. In this study,

local tissue enhancement is observed in the radial images as early as time point 108.1 s. Only from this point, will the measurement of the AIF benefit from a local tissue enhancement correction. Building on this point, if the onset of the local tissue enhancement is rapid, it is advantageous to use fewer projections in the reconstruction and correct the AIF with a higher temporal resolution despite the risk of lower image quality. But when the rate of enhancement is slower, more projections may be used as temporal blurring is less of a concern.

The presence of image artifacts could limit our ability to successfully correct the AIF. This can be seen with the Golden angle data set where the uncorrected AIF with the NFFT reconstruction does not show significant tissue enhancement, and the corrected curve has an apparent sinusoidal artifact (results not shown). It is important that the window shift is set randomly between the reconstructed images. Failure to do so, could result in a coherent oscillating concentration (observed during study, but not shown here).

6.6 Measuring the Radial AIF with Acquired MRI data

The chapter, to this point, has studied the impact selected radial image reconstruction techniques had on the AIF measurement. The results showed that the NFFT reconstruction was most effective. However, this analysis assumed that all projections were acquired at the same orientation (i.e. 0°) to isolate the errors introduced by the tissue enhancement correction. If a high temporal resolution is desired, it would be beneficial to measure the AIF directly from the radial data, rather than alternating AIF and correction profiles. The rest of the chapter, and Appendix C, focuses on measuring the AIF with radial projections.

6.6.1 AIF Measurement using MRI Data

A cylindrical phantom was imaged with a FLASH protocol on a Bruker 70/30. The data was acquired as radial acquisitions at 233 unique angles, and equi-spaced in the angular direction. Both uniform and Golden angle sampling were investigated to see if changing the gradients significantly between measurements had any impact on our measurement. The pulse parameter settings were $TR = 100\ ms$, $TE = 5ms$, flip angle = 30°, $1.5x1.5\ cm^2$ FOV and 256 read-encode samples. The

data is acquired with the stripline surface coil for improved SNR.

An injection, of 30 mM Gd-DTPA in saline, was initiated with a peristaltic pump (Minipuls 2, Gilson: set to 700 which corresponds to an injection rates of approx. 10 ml/min). The bolus circulated around the system multiple times after passing through a mixing beaker. The temporal resolution of the sampled data is 0.1 s, which is consistent with previous measurements. The measured radial projection-based AIF is shown in Figure 6.19. The curve shows well characterized peaks, and gradually approaches a final steady-state concentration of 0.873 $\pm$ 0.082 mM Gd-DTPA. The projection-based AIF is very noisy, so a moving average filter (window size of 5) is applied for display purposes.

The baseline phase for the first 233 points - defined as the average phase of the signal from the vessel after it is sorted by angle - has an angular dependence. This is clearly observed in Figure 6.20. The pattern is not a simple sinusoid, but does repeat every 2π radians. The baseline pattern appears to be consistent between all angular sampling methods used in the experiment. However, the observed pattern seems to be dependent on the set-up, as it changes between scan sessions. This may indicate a position-dependent artifact in the placement of the phantom within the bore. Care was taken to ensure that the phantom was properly centered prior to imaging, but the phase fluctuations continue to change between sessions.

Knowing that the baseline fluctuations are repetitive over 2π radians, and that they are consistent for all scans within a study, a baseline-phase correction could be applied. This entails calculating the phase of the first N samples, and using a sliding window of size N. After subtracting the baseline-phase from all remaining projections, the AIF will be smoother, with a significant improvement in the SNR. The baseline-phase corrected AIF is shown in Figure 6.21.

Comparing the noise level (standard deviation) of the original and corrected AIFs, the measurement benefits significantly at the pre-injection and late stage time-points. At the pre-injection stage, the magnitude of the noise, in concentration, reduced from 0.359 mM to 0.049 mM post correction (reduction by a factor of $7.4X$). Meanwhile, the late stage concentration changed from 0.874 ± 0.334 mM to 0.873 ± 0.082 mM (An improvement in SNR by a factor of 4).

Figure 6.22 was created to help identify and rule out potential sources of the baseline phase. The figure shows the sinograms (magnitude on the first row, and

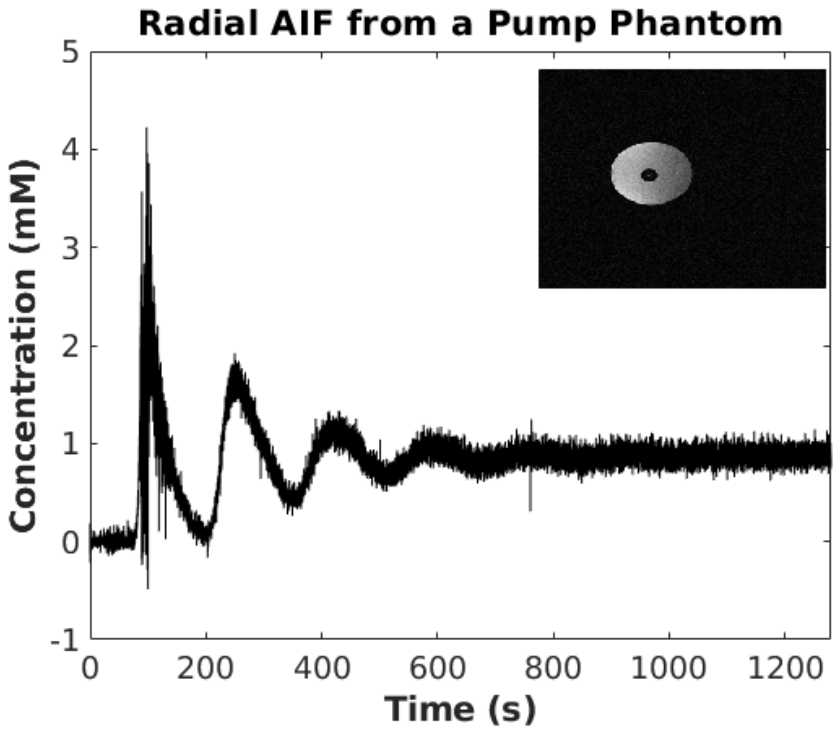

Figure 6.19: Measured AIF in the tail phantom using the pump phantom to generate a series of contrast agent passes. The contrast agent was injected into the tubing with a power injector at a rate of 1.000 ml/min, and allowed to circulate for the duration of the experiment. We observe a series of peaks that eventally trend towards an equilibrium value. The inset shows a DCE image of the phantom, which is located 5 mm from the location of the AIF slice.

phase on the second row) of 233 acquired projections, the estimated background projections, and the difference between these two images (isolated signal from the vessel). As a reminder, the sinogram is a plot of the radial data as a function of the angle of acquisition. Both sinograms were normalized to have a mean magnitude of 1.00 before calculating the difference.

The sinograms of the acquired data and the background projections show similarities in magnitude and phase. However, the magnitude of the background has a couple signal hot-spots near the edges of the phantom. These are more easily ob-

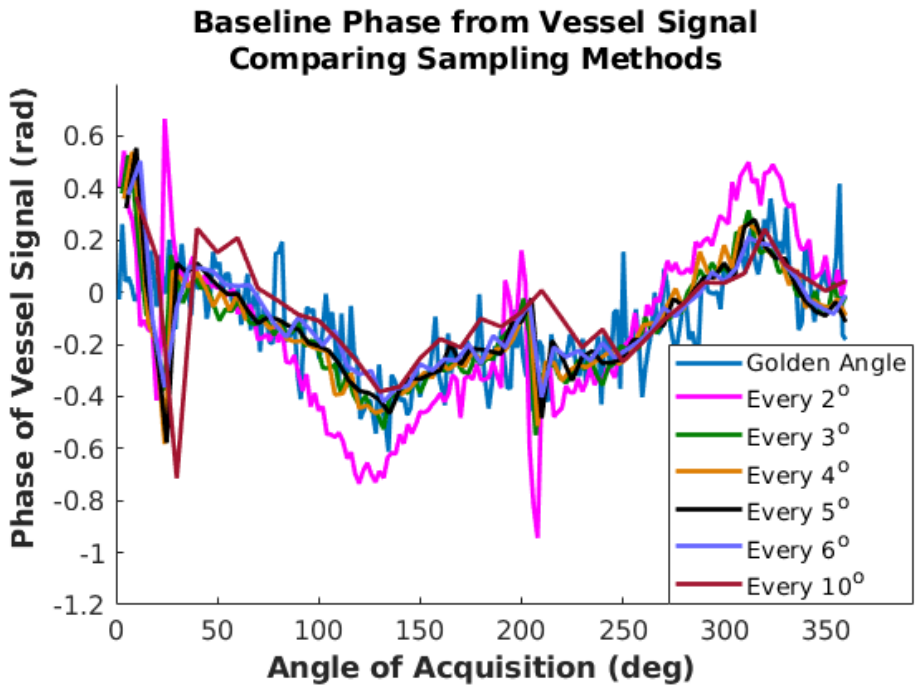

Figure 6.20: The baseline phase of the vessel signal, resorted based on the angle of acquisition, shows an angular dependence. The pattern is independent of the echo time and sampling technique chosen. In addition, it is repetitive after 2π radians, but does not follow a simple sinusoidal curve.

served in the vessel signal sinogram, which is the difference between the acquired projections and the background. The hot-spots appear to be well separated from the vessel (narrow band through the middle of the phantom) and are of lower intensity. It is unlikely that these directly contribute to the baseline phase.

The signal phase reveals a banding structure, in which the phase in the upper and lower halves of the phantom are close to being conjugates (Figure 6.23). The measured phase of the vessel will depend on where it falls within the banding structure. In addition, there are a couple angles with a different phase from the data acquired at a near-by angle (observed as the brighter vertical lines). These projections were acquired at the start of the experiment, so the signal may not have reached steady-state by this point. Another possibility is a mis-centering of

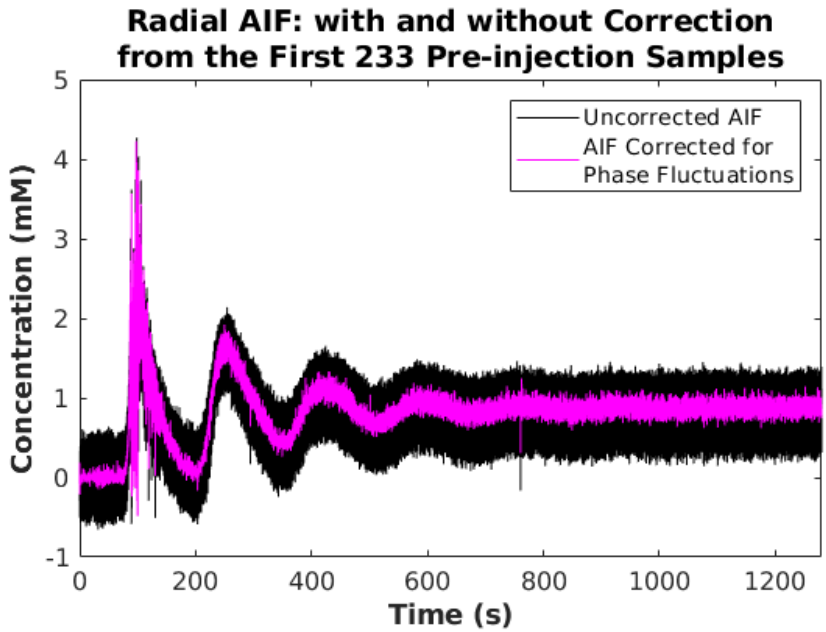

Figure 6.21: Measured AIF in the tail phantom using the pump phantom to generate a series of contrast agent passes. A baseline-phase phase correction was applied by subtracting the baseline phase from all remaining projections. The correction significantly improved the SNR of the measrued AIF, confirming that the phase fluctuations have an angualar dependence.

the echo in k-space by a sub-pixel value. This typically leads to a phase gradient across the image. The phase of the acquired projections is not symmetric about 180°, which could support this claim.

When the radial data is read in, it is centered with a global phase shift. Centering each projection individually caused a jagged edge in the k-space sinogram, which in turn produced radial images of lower quality. It is possible that the gradient in one dimension is slightly stronger/weaker than expected. In response, the k-space sinogram will be centered appropriately, but have a small shift at some angles (i.e. sinusoidal pattern). Using this data in the radial reconstruction could cause signal blurring as the center of k-space will be spread over a larger area. In more severe cases, the echo may not pass through the center of k-space, which

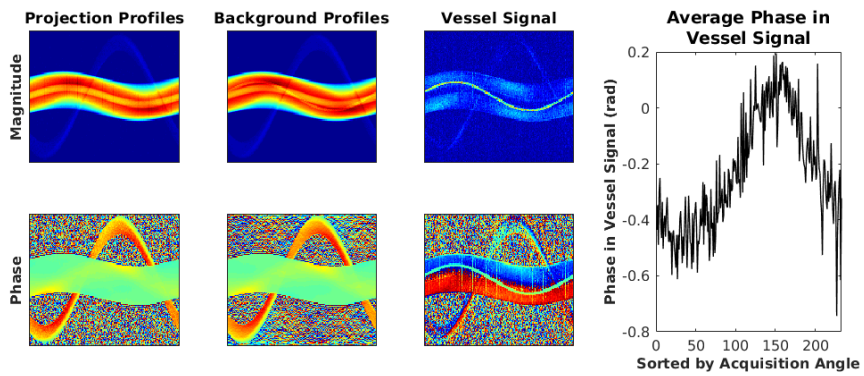

Figure 6.22: Sinograms of the acquired projections, background profiles and difference between the two. There appears to be a step-like phase artifact in the difference signal. The phase of the vessel appears to be affected by the location of the vessel within these two phase bands.

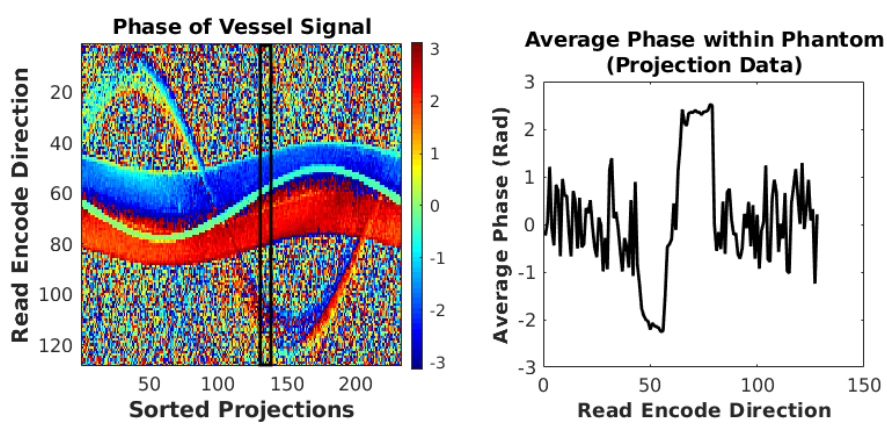

Figure 6.23: Sinogram of the phase of the vessel signal and a cross-sectional plot of the data from within the black box. The phase jumps have a steady phase, transitioning from a phase of -2.13 ± 0.07 rad in the upper region of the phantom to 2.35 ± 0.05 rad in the lower region. The measured phase of the vessel signal appears to vary slightly angularly. This correlates with the positioning of the vessel within each of these phase bands.

would also impact the signal intensity of the echo.

Since the background images are all derived from the same data set, any temporally varying change in the acquired projections would be smoothed out. The radial images may have artifacts that consistently occur in the same spatial location, which would impact the background signal differently as each angle. This means that the background signal would differ from the acquired data with an angular dependence. Two possible explanations are eddy currents [177] or gradient timing delays [178]. Appendix B investigates both issues. The results of these studies were not sufficient for removing the phase baseline in the radial projection-based AIF.

6.6.2 Concluding Remarks

This chapter evaluated three radial reconstruction methods for their effectiveness in correcting the projection-based AIF for local tissue enhancement. The analysis of the enhancement images shows that STCR best reproduced the local enhancement region, followed by the NFFT. This observation carried through the investigation of the projection profiles, created from a projection of the enhancement images perpendicular to the readout direction. In both analyses, Shepard's method of interpolation was inferior. The final investigation measured the projection-based AIF, after the sampled projections were corrected for local tissue enhancement. The results showed that Shepard's method of interpolation and the NFFT technique best agreed with the input curve, while the concentrations with STCR were consistently over-estimated by a factor of 1.19-1.25 when 55 or more projections are used in the reconstruction.

Taking all results into consideration, the NFFT seems to be the best technique for correcting for local tissue enhancement, when at least 55 projections are used in the radial reconstruction. Though it is beneficial to use more projections in the image reconstruction if local tissue enhancement evolves slowly. In addition, the data should be sampled with Golden angle sampling, so that radial images may be reconstructed retrospectively at a variety of temporal resolutions.

The measurement of the radial projection-based AIF with acquired projections revealed issues in the isolated vessel signal. There appears to be an angular-

dependent phase shift, of which the source remains unknown. Attempts to uncover the issue are presented in Appendix B, though the results were inconclusive. Future work on this project involves further investigation into the source of the phase banding in the isolated vessel signal. Appendix C explores limitations in the radial projection-based AIF measurement due to imperfect phantom set-up, off-sets of the k-space data, and multiple vessels.

The projection-based AIF may be used in current in-vivo AIF-DCE experiments, though the best results require that the same angle of acquisition is used. It may be possible to measure a radial AIF in a larger object - such as a rat tail if spatial resolution is high - but this is beyond the scope of this thesis.

Chapter 7

Interleaved AIF and DCE Measurement

7.1 Interleaving a DCE and AIF Measurement

PK model parameters are most specific to a patient and exam if the AIF and DCE data are acquired simultaneously. This often requires that the blood vessel feeding the tissue of interest is located close or within the imaging plane [108]. For pre-clinical studies on small animals, this is often difficult to achieve as there are a limited number of vessels of a sufficient size to avoid partial volume effects, and common locations for tumour implants are distant from these vessels.

Animal-based AIFs have been successfully measured in the left ventricle of the mouse heart [15], in the iliac artery [100], and in the mouse tail [20]. While the heart and iliac artery may be closer to a tumour implanted in the mammary fat pad or on the hind flank, these sites would require an image-based measurement. In addition, the estimate within the heart would require a gated scan. This could further impede the temporal resolution of the DCE experiment. The mouse tail provides a good compromise for being closely located to a tumour implanted on the hind flank, and simple anatomy to allow a projection-based AIF measurement.

The sensitivity and specificity of the DCE-MRI model fit parameters are highly correlated with the spatial and temporal resolutions of the acquired data. Great care should be taken to ensure that the spatial resolution is sufficient to capture tumour

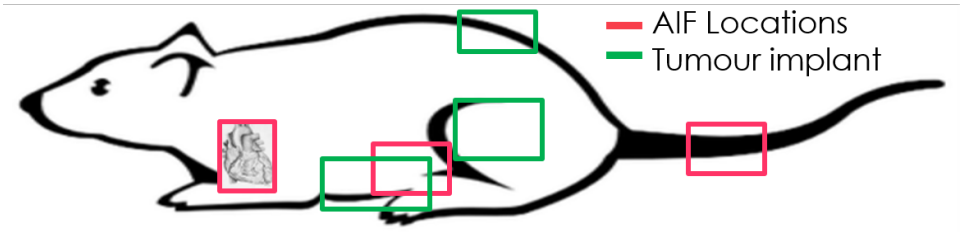

Figure 7.1: Typical locations for implanting tumours in mice (green) and where the AIF has been successfully measured in mice (red). There is little overlap between the two regions, making it difficuilt to acquire an AIF throught the DCE experiment without compromising the temporal resolution.

inhomogeneity and to reduce partial volume effects [42], while also attaining a sufficiently high temporal resolution to capture the rapid contrast kinetics in the vessel [5, 91]. Satisfying these two conditions is already a challenge when only DCE-MRI data is acquired, so adding an image-based AIF to the scan time is undesirable. The projection-based AIF has the advantage that TE can be set much shorter than TR, thereby allowing us to integrate the AIF measurement into a DCE experiment with minimal effects on the temporal resolution.

Multiple studies have concurrently acquired data for the AIF and DCE experiments, though most of them are performed in humans. One animal-based study was performed by Dominick McIntyre and his colleagues [21], where they performed an interleaved AIF and DCE acquisitions in rat tumours. Similar to our study, the AIF was measured in the tail.

Case Study: McIntyre et al

McIntyre [21] and colleagues recognized the importance of acquiring the AIF for each experiment, and performed this study to show that an interleaved AIF and DCE experiment is possible in rats. They looked at both the reproducibility of the AIF measurement in two Wistar Furth rats (no prolactinomas and tail only scans) imaged at 0, 4 and 8 days, as well as the potential for an interleaved AIF-DCE scan with two separate coils. The interleaved experiment was performed on six rats. These rats had GH3 prolactinomas grown on the flanks.

Data was acquired on a 4.7 T Varian Unity Ivova spectrometer. The experiment utilized two coils; a nine-turn solenoid tail coil (length 24 mm, inner diameter 8 mm, and oriented with its long axis perpendicular to the main magnetic field) to acquire the AIF and a three-turn solenoid coil wrapped around the tumour (diameter 25 mm, length 11 mm and oriented with its long axis vertically) for the DCE data. The rat was positioned on its side and its tail led through the tail coil. A SPDT PIN diode switch was constructed to alternate between the tumour and tail acquisitions and was remotely controlled by the spectrometer. McIntyre et al. observed three distinct vessels in the images of the rat tails (one large artery and two large veins). The AIF was measured in any one of these, though the veins produced the most reliable results.

For the reproducibility study, a saturation-recovery gradient-echo pulse sequence was utilized to avoid signal intensity alterations due to the inflow of unsaturated spins between the excitation and refocusing pulse. Slice-selective saturation pulses, with a saturation recovery time of 50 ms, were oriented to saturate the full length of the tail within the coil volume. A total of 32 scans were obtained prior to injecting a bolus of 0.1 mmol/kg Omniscan to get an accurate measure of the baseline values. 140 images were acquired after the injection. The results from this study showed that the variability of fitted parameters was comparable within and between rats. This further confirms that the AIF should be taken during each DCE-MRI scan.

DCE-MRI images of a tumour and AIF data at the tail were acquired with a T_1-weighted gradient echo pulse sequence with $TR = 105$ ms, $TE = 4$ ms and flip angle of 90° (tail) or 50° (tumour). This produced a temporal resolution of 6.72 s. The repetition time was selected to allow for three tumour slices to be imaged, while saturating the signal from the tail to minimize inflow effects. The rat was positioned such that the tumour was a couple cm beyond the geometric center of the magnet. This allowed the tail to lie within the linear region of the gradients. Magnetic field shimming was optimized for the X, Y and Z shims at the tumour, while no shimming was performed on the tail.

Their results show that the AIF measurement had superior SNR (standard error estimates of 2-3%) compared to a measurement in the aorta or vena cava using a volume coil (standard error estimates of 10%). This confirms that a dual-coil

approach is superior, despite the two coils being off-center. In addition, the AIF measurements taken with the interleaved scan were comparable to those from the reproducibility study. This suggests that interleaving the two data sets does not significant impact on the reliability of the data.

McIntyre calculated K_{trans} maps for both a literature AIF (from Rozijn [179]) and their individually acquired interleaved AIF. The results show dramatic differences in both the average value and the skewness of the histograms. In addition, the values of v_e appear to be more strongly affected. They quote that 48% of pixels lies outside the range of $0 \leq v_e \leq 1$ with Rozijn's AIF [179], while only 13% lie outside the range with the interleaved AIF.

Our interleaved dual-coil AIF-DCE experiment was inspired by this study.

7.1.1 Interleaved AIF-DCE Pulse Sequence

The pulse program used for the interleaved AIF-DCE experiment is shown in Figure 7.2. The pulse program is split into two blocks: one for the AIF measurement, and the second for the DCE experiment at the region of interest (ROI) (often a tumour). Within each repetition time, one line of k-space for the AIF and each of the DCE slices is acquired. When setting up the experiment, two slice packs are defined. The first slice in the series is always associated with the AIF measurement, while all others are associated with the DCE experiment.

The AIF is measured using a flow-compensated FLASH acquisition. The flow compensation is only applied in the direction of the slice select as the tail is oriented parallel to the main magnetic field. In addition, a radial acquisition is used so that local tissue enhancement may be assessed throughout the experiment, and compensated if required.

Conversely, the DCE experiment follows the standard protocol used in our lab. This consists of a multi-slice FLASH acquisition with Cartesian sampling. The interleaving works by acquiring one line of k-space for the AIF, followed by a single line of k-space for each DCE image within the repetition time. For a TR of 100 ms, up to five DCE slices may be acquired. Interleaving the two experiments in this way allows us to maintain a high temporal resolution for both the AIF and DCE data. Future studies can use compressed sensing or multi-echo procedures to

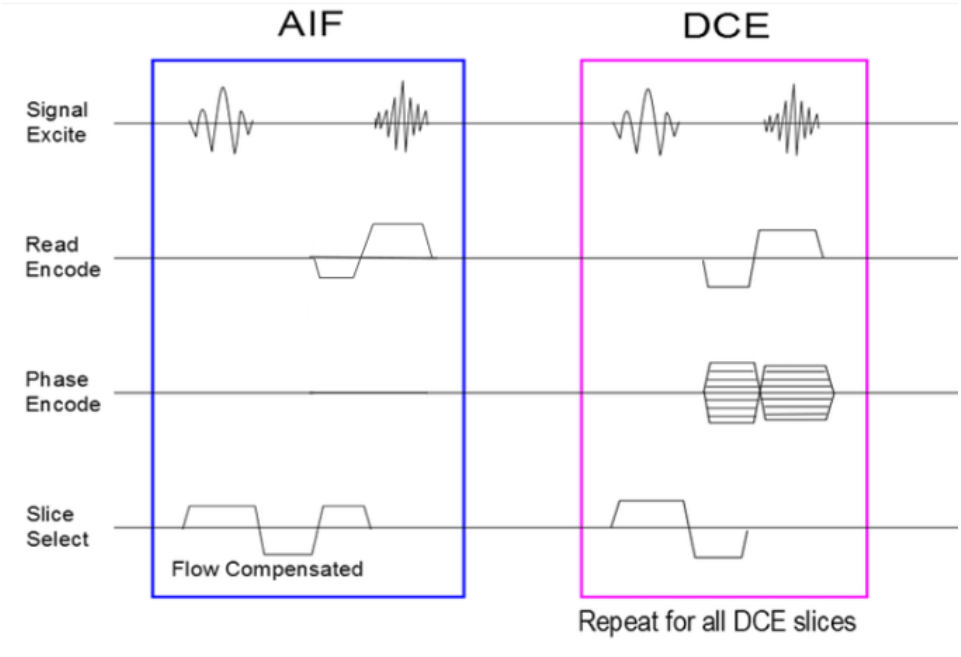

Figure 7.2: Pulse program for the interleaved AIF and DCE measurement. During each TR, one line of k-space is acquired for the AIF measurement and one line of k-space for each slice in the DCE experiment. This pattern continues until all data has been collected.

acquire the DCE data faster though this could impact the temporal resolution of the AIF if the acquisition window for each slice is increased.

7.1.2 Two-coil set-up

With an interleaved experiment, where the AIF and DCE slices are located far apart. The data can be sampled with a single coil at two locations or with two separate coils which are optimized for the anatomy of interest. The dual-coil approach is superior as the two coils can have smaller sensitive regions, and thus improve the SNR of the data. It also for more flexibility for difference sized mice, or locations of the DCE-ROI and catheter for the tail vein injection. However, care must be taken to ensure that both coils fall within the linear region of the gradient fields [21] and that there is minimal cross talk between the two. Our lab grows

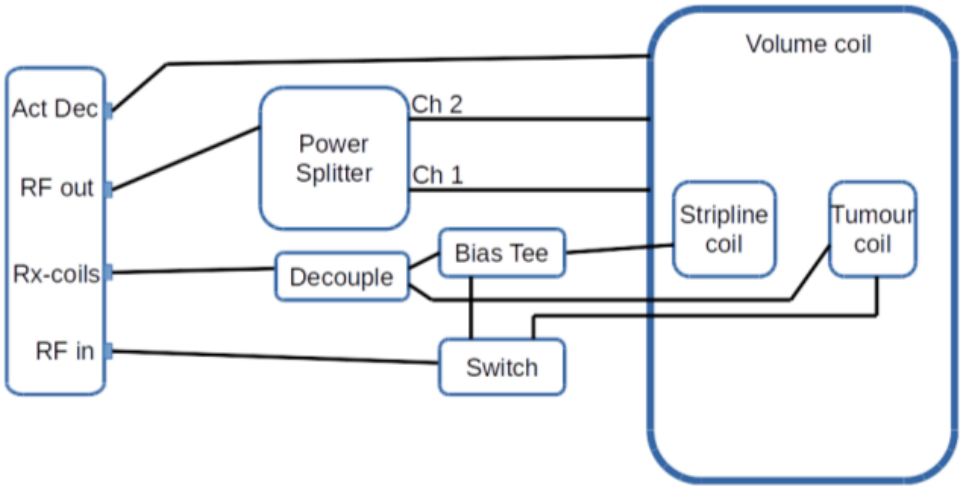

Figure 7.3: Scematic for the Two coil set-up. Surface coils, specific for the AIF and DCE data acquisitions, were used to maximize the SNR of the signal at each location. The electronic switch allowed us to selectively choose which coil was active during the acquisition window, and thus enabling data collection for the AIF and DCE experiments separately.

tumours on the hind flank of the mouse, while the AIF is located approximately $2-5$ cm away on the average adult mouse. This is within the limits of the linear region of the volume coil for signal excitation, while the large spacing between AIF and DCE measurements benefits from a dual-coil set-up.

Having two distinct data collection blocks in the pulse sequence, an electronic switch was added to select which surface coil is active during the acquisition window. Following the example by McIntyre, a SPDT PIN diode switch was constructed. The switch operation is based on low and high voltages at the input to the surface coils, such that one coil will perceive a closed circuit, while the other perceives an open circuit. The switch settings are prescribed within the pulse sequence and is controlled remotely by the scanner. Since one coil is part of an open circuit at any instance, cross talk between these two coils is not a concern. Both surface coils are actively decoupled from the volume coil (used for signal excitation).

7.2 Data Acquisition

An in-vivo measurement was performed on a healthy mouse on a Bruker Biospec 7 T MRI scanner. To replicate a DCE experiment, the mouse was set up using the same procedure outlined in Chapter 4. This included a tail cannulation and an injection bolus of 5 ml/g of 30 mM Omniscan. A pre-bolus of 25 ml heparinized saline was used to prevent an early injection. The image slice was oriented such that no two tail vessels would overlap in the projection.

A specialized strip-line coil was used for signal collection at the tail and a single loop surface coil was used for signal collection of the DCE-data, located at the kidney. Since the mouse tail tends to be small, we chose to orient the tail coil's long axis parallel to the main magnetic field to allow for better shimming.

In this study, projection data was acquired with an angle of acquisition of 0° for the AIF measurement, as the phase artifact from the radial data is still unresolved. The DCE slices (N=5) were acquired using the standard FLASH experiment with Cartesian sampling. The AIF and DCE data were interleaved, such that one line of k-space was acquired for each DCE slice between AIF acquisitions. This provided temporal resolutions of 100 ms for the AIF projections and 12.8 s DCE images (128 phase-encoding lines), respectively. The scan was set-up for 80 repetitions (total time 17:04), with the injection initiated after 60 s.

7.3 Results from Interleaved Study

Interleaved AIF-DCE data was acquired with four DCE slices and one AIF slice. The locations of the two slice packs was chosen from a multi-slice FLASH scan at each location. For the AIF, the selected slice had at least three well defined vessels and minimal signal from the surrounding tissue. The slice was oriented such that no two vessels would overlap in the projection profile. The DCE slices covered the majority of the kidney volume with 1 *mm* thick slices, and 2 *mm* spacing. The center of the two slice packs were separated by 4.6 cm. Images from slice 2 of the DCE pack are shown in Figure 7.4. These images have a temporal resolution of 12.8 s and a spatial resolution of 31.2 x 31.2 μm^2. The injection took place 60 s into the experiment, meaning that the first four DCE images are pre-injection, and the sixth to eightieth are post-injection.

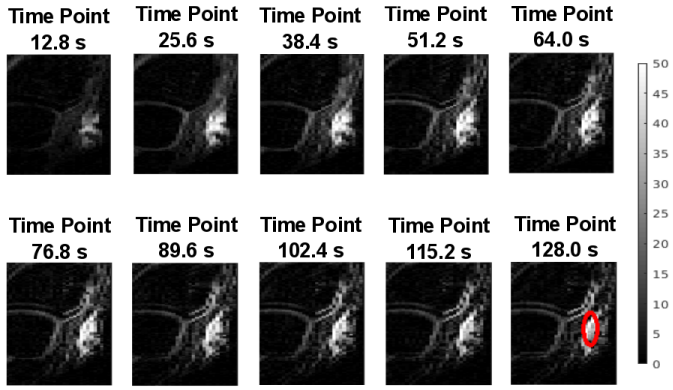

Figure 7.4: Signal magnitude of the DCE-MRI images of the ROI at slice 2. The temporal resolution of this experiment is 12.8 s. The bolus of Gd-DTPA was injected 60 s into the experiment, which is during the acquisition of the 5th DCE image (data collected between 51.3 s - 64.0 s). This figure shows one pre-injection image, the image during the injection, and six post-injection time points. The signal throughout the animal enhances after injection, though the ROI (outlined with red oval) enhances to the greatest degree.

The AIF was measured in each of the four vessels. Only the curves that had the characteristic shape of an AIF - initial sharp uptake after the injection, followed by a gradual decrease to a steady concentration - were used in the measurement. The phase of the external reference phantom tracked phase drift in the imaging plane, and was used to correct the AIF. The vessel located at readout pixels 151-155 produced the most AIF-like curves, with pixel 151 selected for the measurement. Other pixels had a large phase shift artifact during the injection, which may have resulted from movement or a reaction to the injection. The maximum measured concentration, for each pixel of the projection corresponding to the vessel, ranged between $0.8 - 1.7$ mM. The selected AIF had a concentration of 0.93 mM at the peak and a long time concentration around 0.25 mM. This is consistent with the projection-based AIF discussed in Chapter 4.

The ROI for the DCE study was selected by evaluating the concentration-time curves in locations of significant enhancement over time. The concentration was calculated from the relative change in T_1 (equation 3.1), in which the pre-injection

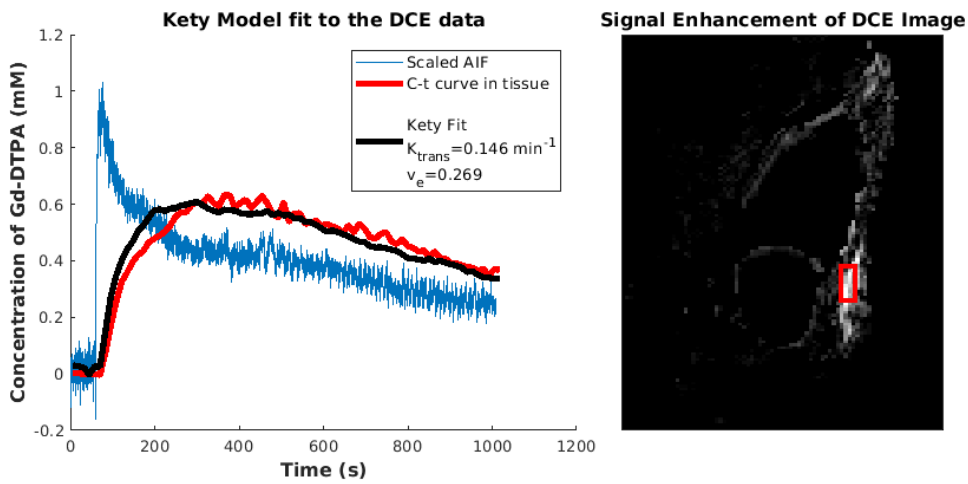

Figure 7.5: The Tofts model was fit to the DCE-MRI data from slice 2. The region of interest (ROI) is outlined in red on the right, while the red curve on the plot to the left is the concentration of Gd-DTPA within this area. The projection-based AIF (blue curve) was used in the model fitting (black curve). The Tofts model fit overestimates the concentration early, but is considered a reasonable fit.

value was measured with a fit to the signal-intensity vs inversion time of a Look-Locker experiment, and the post-injection value calculated from equation 2.18 and a proton density image as an estimate of M_o.

The Tofts model was fit to the concentration-time curve from the selected ROI, indicated with the red box on the right side of Figure 7.5. Since this model appears to fit the data well, and adding a third parameter for the plasma volume (v_p) did not improve the fit, the two-parameter Tofts model would be considered sufficient.

The average concentration-time curve for this ROI is the red curve on the left, and the projection-based AIF is in blue. The fit parameters, K_{trans} and v_e, have values of 0.145 min^{-1} and 0.269, respectively. These are consistent with the literature values. [98, 109, 180–183].

Pre and post injection images of the mouse tail can be instructive in confirming that the injection was successful and in assessing local tissue enhancement. The tail images from the in-vivo study are shown in Figure 7.6. The post-injection image (36 : 30 after the injection) shows that the blood vessels are all dilated post-

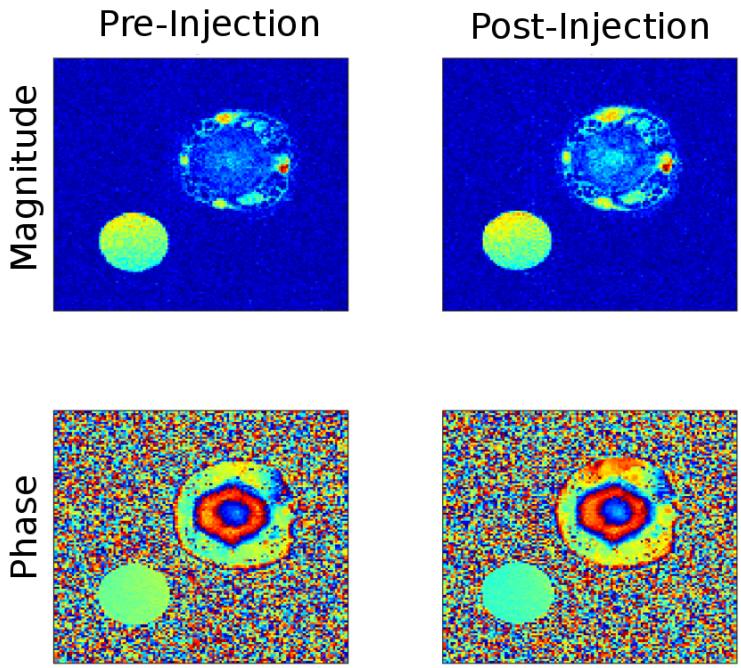

Figure 7.6: Magnitude and phase signal of the mouse tail before and after (approx. 36 : 30 after the injection) the DCE experiment. The injection was performed through the superior vessel. These images show that the superior vessel is enlarged post-injection, and there are subtle changes in the signal of the surrounding tissue. The phase images shows that there was some phase drift during the experiment.

injection. Had the AIF projections been acquired radially, the point at which the vessels dilated could be assessed from a sliding window reconstruction. The vessel mask may need to be redefined post-injection to compensate for the enlarged vessel area or account for any minor shift in position.

The tissue surrounding the vessels has changed slightly in the surrounding tissue, but it is not clear if this affects the measurement of the AIF as the vessel is only a few pixels in diameter. If the signal contrast between the vessel and surrounding tissue is low, then the relative contribution of the vessel to the total signal will be low. This means that changes in the surrounding tissue could be detrimental to the AIF measurement, even though it does not appear to change significantly between pre and post-injection images.

The presence of local tissue enhancement may be assessed from the complex difference of the post and pre injection images. Figure 7.7 compares the signal magnitude of the vessels, and from local tissue enhancement. Depending on the location, the signal magnitude of the local tissue enhancement varies from 8.7% to 178.0% of that from the vessel (50.8% to 76.7% in the vessel used for the AIF). Both are complex signals, so the effect on the signal phase depends on the relative angle of each. In the best case scenario, the tissue enhancement signal has the same phase as the vessel, and so the measured AIF is unaffected. The maximum phase difference occurs when the two signals are parallel-opposed, and the tissue enhancement signal is stronger than the vessel.

For this study, the AIF projections were all acquired at the same angle, so only motion along the projection may be assessed. Movement perpendicular to the acquired projection could be a concern if its due to a rotation, as this would change the background profile of the surrounding tissue. Comparing the FLASH images before and after the DCE experiment, it appears that the mouse shifted slightly (11.8 μm (2 pixels) to the right and 5.9 μm (1 pixel) down). However, it is unknown when this shift occurred during the experiment. The projection profiles show a linear shift towards the right by 5-6 pixels during the scan. The movement was corrected by first identifying the edges of the projection profiles using the Sobel filter. The shift in the edge location, s, relates to the required phase adjustment in k-space, through the phase term $e^{-i2\pi xs/256}$, where x ranges from -128 to 127 in the readout direction. This correction removed the shift in the readout direction, and produced a more uniform phase across the reference phantom in time.

7.4 Final Thoughts and Directions for Future Study

A projection-based AIF is inherently noisy compared to one measured from MR images. Averaging multiple measurements will improve the SNR, but at the expense of reduced temporal resolution. Taylor et al. [123] averaged 29 sampled together to significantly improve the SNR of their measurement. With a moving average approach, the temporal resolution (0.050 s) is unaffected, through fine details will be lost. With our technique, averaging as few as 5 time points together appeared to be effective in greatly reducing the noise. The contrast changes in

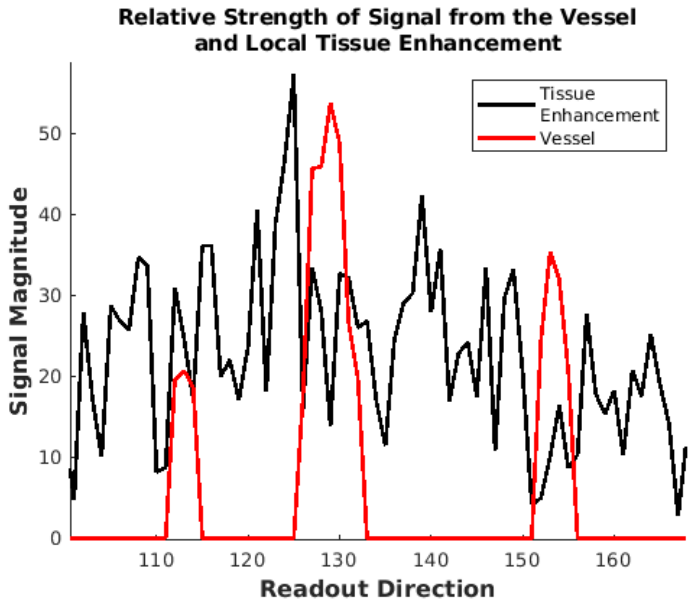

Figure 7.7: Signal from the vessel and local tissue enhancement from the projections of the post and pre-injection FLASH images. The FLASH images were first masked for either the vessel or the surrounding tissue, then the difference (post-pre) was taken. The plot shows the projection of the difference for the vessel and local tissue enhancement masked images. The results show that the relative strength of the tissue enhancement signal, to that of the vessel, varies. With the vessel chosen for the AIF, the relative strength is $60.6 \pm 11.1\%$, suggesting that local tissue enhancement should be accounted for. The vessel from pixels 151-156 was used for the AIF measurement.

blood are influenced by the injection rate. With a rate of 1.00 ml/min, the changes occur on the order of seconds. Therefore averaging 3 or 5 samples with a moving average filter should not affect the accuracy of our projection-based AIF.

If the DCE data were sampled with a radial technique, a sliding window reconstruction may be used to adjust the temporal resolution of the data series. The sliding window reconstruction is advantageous as it allows for the reconstruction of multiple image series with varying temporal resolutions. There is a trade-off between higher temporal resolutions and higher quality images. With fewer projections, more information regarding the contrast kinetics may be extracted. How-

ever, this comes at the cost of larger gaps in k-space, resulting in blurred edges and loss of image contrast. Kholmovski et al. [125] discusses how several image series may be studied to gain further insights.

It is expected that only a small fraction of voxels will enhance in the image. Wavelet or independent component analysis (ICA) both have potential in reducing the number of significant variables in the analysis, making interpretation of the results more specific to observable changes in the DCE images. Mehrabian et al. [184–186] show that an AIF may be extracted from the complex-signal of DCE images using ICA. With their approach, the AIF and DCE curves will have the same temporal resolution. The projection-based AIF measurement allows for a much higher temporal resolution, and has higher potential to capturing the peak concentration. However ICA could be applied to radially reconstructed images at the tail to both validate the projection-based AIF measurement and track local tissue enhancement more accurately (i.e. ICA could remove noise from the analysis). Multiple groups have studied DCE-MRI data sets with wavelet analysis [176, 187]. These would be interesting avenues to explore with future studies.

Compressed sensing techniques can significantly reduce scan times as only a fraction of the full data set is measured. Fast imaging with Cartesian sampling are well established based on randomized data collection [156]. Further accelerations are possible with the techniques such as Grappa [188], where the use of multiple coils allow for a combination of parallel imaging and compressed sensing. Improving the temporal resolution of the DCE data is beyond the scope of this thesis, though it is an area for further investigation.

For the best results, we recommend that the tail vein injection is performed with a plastic catheter or is located as distal as possible to the surface coil to minimize susceptibility artifacts from metallic components in the catheter. Since the diameter of the mouse tail tapers off as we move towards the tip, the plastic catheter is a more attractive alternative. However, the plastic catheter is more flexible than a needle, which could be more challenging for those less experienced with tail cannulations.

Chapter 8

Concluding Remarks

The work detailed in this thesis attempted to improve the temporal resolution of the AIF, by measuring it from a series of MR projections. We present a projection-based AIF measurement, in which the AIF is extracted from the phase information of a single MR projection. This approach has a temporal resolution of 100 ms (the repetition time), and allows for an interleaved AIF-DCE experiment without compromising the temporal resolution of either data set.

In Chapter 4, we present the projection-based technique, which measured the AIF from the phase of MR projections. The phase accumulation with concentration of Gd-DTPA was validated in-vivo to provide a scanner conversion factor for future experiments. This result ($(0.213 \pm 0.001)\ rad/mM/ms$) agreed with the theoretically expected value ($0.212\ rad/mM/ms$) for concentrations ranging between 1-10 mM. A projection-based AIF was measured within a tail phantom, concurrently with a colormetric measurement. The results from this analysis showed that the phase data accurately captures changes in intra-vascular concentration. Finally, an AIF was successfully measured in-vivo. The measurement had a temporal resolution of 100 ms. The long term concentration was validated with a cohort of 4 mice, using mass spectrometry.

Chapters 5 and 6 studied three radial reconstruction techniques and evaluated how they performed with varying numbers of projections and sampling methods with and without local tissue enhancement present. The results of these chapters suggest that STCR and the NFFT techniques are superior to Shepard's method of

interpolation, and that uniform or Golden angle sampling are best. Image series with at least 89 projections agreed well with the simulation, though 55 projections may be used for a reasonable estimation of local tissue enhancement. Uniform sampling produced the best results, though Golden angle sampling has the advantage of retroactively reconstructing images with different temporal resolutions. The NFFT technique was selected for further analysis, with Golden angle sampling.

Related to this chapter, Appendix C explores potential limitations with the radial projection-based AIF measurement under imperfect data acquisition. The results show that the measurement is minimally affected with translations of the object in image space. The AIF measurement is compromised when fewer projections are used in the tissue-enhancement correction (55 or fewer, in general) or if the k-space data is shifted by a small amount (1.3-2.6 pixel shift in a 256x256 image), in which the concentration near the peak was under-estimated, and the tissue-enhancement correction was ineffective at the later stages. The location of the vessel within the coils sensitivity zone could also impact the measurement, with vessels closer to the coil being more accurate. The chapter closes with a discussion of an issue that presented with the radially acquired data. The difference between the acquired data and the background profiles (from an NFFT reconstruction) has two distinct phase bands. The AIF then has an angular dependence, with the size of the effect dependent on the location of the vessel within the phantom. Attempts to correct the issue - limiting effects from eddy current (longer TE, varying sampling methods, etc.), gradient mis-timing measurements or trajectory measurements - were unsuccessful. Resolving the issue continues to be an area for future studies.

Chapter 7 detailed the interleaved AIF and DCE measurements with a dual-coil set-up. The phantom experiments verified that the interleaved sequence acquired data rapidly at the tail and tissue of interest with a temporal resolution of 0.100 s. However, the results showed a phase baseline artefact, that was repeatable within an experiment, but varied between experiments. Until this issue is resolved, it is recommended to acquire the AIF projections at a single angle. The AIF slice location was determined with a multi-slice FLASH experiment. The best location had good signal contrast between the vessels and surrounding tissues. An interleaved acquisition was successfully applied in-vivo with the single angled projection-based AIF, providing temporal resolutions of 0.100 s and 12.8 s for the AIF and DCE

data, respectively. Measuring both curves within the same experiment is expected to improve the accuracy of model fit parameters. This would be beneficial in studies attempting to differentiate between two or more known populations, and identify trends between them. Since the projection data is noisy, it is best to measure the AIF in areas with fewer anatomical structures. We chose the mouse tail for our experiments for this reason, though other areas are possible. Further the use of flow compensation improved the contrast between the vessel and surrounding tissue, providing a more accurate measure of the intra-vascular concentration. Future studies could address the issues with the radial data acquisition (AIF) or attempt to speed up the DCE image acquisition (current temporal resolution of 12.8 s).

Bibliography

[1] Peter L Choyke, Andrew J Dwyer, and Michael V Knopp. Functional Tumor Imaging With Dynamic Contrast- Enhanced Magnetic Resonance Imaging. *Journal of Magnetic Resonance Imaging*, 17:509–520, 2003. doi:10.1002/jmri.10304.

[2] Lindsay W Turnbull. Dynamic contrast-enhanced MRI in the diagnosis and management of breast cancer. *NMR in Biomedicine*, 22:28–39, 2009. doi:10.1002/nbm.1273.

[3] Tristan Barrett, Martin Brechbiel, Marcelino Bernardo, and Peter L Choyke. MRI of Tumor Angiogenesis. *journal of magnetic resonance imaging*, 26:235–249, 2007. doi:10.1002/jmri.20991.

[4] Anwar R Padhani and Janet E Husband. Review Dynamic Contrast-enhanced MRI Studies in Oncology with an Emphasis on Quantification, Validation and Human Studies. *Clinical Radiology*, 56: 607–620, 2001. doi:10.1053/crad.2001.0762.

[5] Thomas E. Yankeelov and John C. Gore. Dynamic Contrast Enhanced Magnetic Resonance Imaging in Oncology: Theory, Data Acquisition, Analysis, and Examples. *Current Medical Imaging Reviews*, 3(2):91–107, 2009. doi:10.2174/157340507780619179.Dynamic.

[6] Donald B Plewes and Walter Kucharczyk. Physics of MRI: a Primer. *Journal of Magnetic Resonance Imaging*, 35:1038–1054, may 2012. ISSN 1522-2586. doi:10.1002/jmri.23642. URL http://www.ncbi.nlm.nih.gov/pubmed/22499279.

[7] Vanessa N Harry. Novel imaging techniques as response biomarkers in cervical cancer. *Gynecologic Oncology*, 116:253–261, 2010. ISSN 0090-8258. doi:10.1016/j.ygyno.2009.11.003. URL http://dx.doi.org/10.1016/j.ygyno.2009.11.003.

[8] J P B O Connor, A Jackson, G J M Parker, and G C Jayson. DCE-MRI biomarkers in the clinical evaluation of antiangiogenic and vascular disrupting agents. *British journal of cancer*, 96:189–195, 2007. doi:10.1038/sj.bjc.6603515.

[9] Jelle O Barentsz, Marc Engelbrecht, Gerrit J Jager, J Alfred Witjes, Jean de LaRosette, Boudewijn P.J. van der Sanden, Henk-Jan Huisman, and Arend Heerschap. Fast dynamic gadolinium-enhanced MR imaging of urinary bladder and prostate cancer. *Journal of magnetic resonance imaging*, 10:295–304, sep 1999. ISSN 1053-1807. URL http://www.ncbi.nlm.nih.gov/pubmed/10508289.

[10] Mark A Zahra, Kieren G Hollingsworth, Evis Sala, David J Lomas, and Li T Tan. Dynamic contrast-enhanced MRI as a predictor of tumour response to radiotherapy. *Lancet Oncology*, 8:63–74, 2007.

[11] Linda Knutsson, Danielle van Westen, Esben T Petersen, Karin Markenroth Bloch, Stig Holtås, Freddy Ståhlberg, and Ronnie Wirestam. Absolute quantification of cerebral blood flow: correlation between dynamic susceptibility contrast MRI and model-free arterial spin labeling. *Magnetic Resonance Imaging*, pages 1–7. ISSN 0730-725X. doi:10.1016/j.mri.2009.06.006.

[12] Xiangyu Yang, Jiachao Liang, Johannes T Heverhagen, Guang Jia, Petra Schmalbrock, Steffen Sammet, Regina Koch, and Michael V Knopp. Improving the pharmacokinetic parameter measurement in dynamic contrast-enhanced MRI by use of the arterial input function: theory and clinical application. *Magnetic Resonance in Medicine*, pages 1448–1456, jun . ISSN 0740-3194. doi:10.1002/mrm.21608.

[13] Stephen Pickup, Rong Zhou, and Jerry Glickson. MRI estimation of the arterial input function in mice. *Academic Radiology*, 10:963–968, sep 2003. ISSN 10766332. doi:10.1016/S1076-6332(03)00291-5. URL http://linkinghub.elsevier.com/retrieve/pii/S1076633203002915.

[14] Anders Garpebring, Ronnie Wirestam, Nils Östlund, and Mikael Karlsson. Effects of inflow and radiofrequency spoiling on the arterial input function in dynamic contrast-enhanced MRI: A combined phantom and simulation study. *Magnetic Resonance in Medicine*, pages 1670–1679, jun . ISSN 07403194. doi:10.1002/mrm.22760.

[15] Dustin K Ragan, Stephen Y Lai, and James a Bankson. Fast, reproducible measurement of the vascular input function in mice using constrained

reconstruction and cardiac sampling. *NMR in biomedicine*, 24:373–384, sep 2011. ISSN 1099-1492. doi:10.1002/nbm.1601. URL http://www.pubmedcentral.nih.gov/articlerender.fcgi.

[16] Emeline Julie Ribot, Eric Thiaudiere, Richard Roulland, Pierre Brugieres, Alain Rahmouni, Pierre Voisin, Jean Michel Franconi, and Sylvain Miraux. Application of MRI phase-difference mapping to assessment of vascular concentrations of BMS agent in mice. *Contrast Media & Molecular Imaging*, 3:64–71, 2008. ISSN 15554317. doi:10.1002/cmmi.232.

[17] Deirdre M McGrath, Daniel P Bradley, Jean L Tessier, Tony Lacey, Chris J Taylor, and Geoffrey J M Parker. Comparison of model-based arterial input functions for dynamic contrast-enhanced MRI in tumor bearing rats. *Magnetic Resonance Imaging*, pages 1173–1184, may . ISSN 1522-2594. doi:10.1002/mrm.21959.

[18] Geoff J M Parker, Caleb Roberts, Andrew Macdonald, Giovanni A Buonaccorsi, Sue Cheung, David L Buckley, Alan Jackson, Yvonne Watson, Karen Davies, and Gordon C Jayson. Experimentally-derived functional form for a population-averaged high-temporal-resolution arterial input function for dynamic contrast-enhanced MRI. *Magnetic Resonance in Medicine*, 56:993–1000, nov 2006. ISSN 0740-3194. doi:10.1002/mrm.21066. URL http://www.ncbi.nlm.nih.gov/pubmed/17036301.

[19] Heidi Lyng, Gro A. Dahle, Olav Kaalhus, Arne Skretting, and Einar K. Rofstad. Measurement of Perfusion Rate in Human Melanoma Xenografts by Contrast-Enhanced Magnetic Resonance Imaging. *Magnetic Resonance in Medicine*, 40:89–98, 1998. URL http://onlinelibrary.wiley.com/doi/10.1002/mrm.1910400113/abstract.

[20] Arvind P Pathak, Dmitri Artemov, and Zaver M Bhujwalla. Novel System for Determining Contrast Agent Concentration in Mouse Blood In Vivo. *Magnetic Resonance in Medicine*, 51:612–615, 2004. doi:10.1002/mrm.10727.

[21] Dominick J O McIntyre, Christian Ludwig, Amit Pasan, and John R Griffiths. A method for interleaved acquisition of a vascular input function for dynamic contrast-enhanced MRI in experimental rat tumours. *NMR in biomedicine*, 17:132–143, may 2004. ISSN 0952-3480. doi:10.1002/nbm.868. URL http://www.ncbi.nlm.nih.gov/pubmed/15137038.

[22] J Ferré, E Bannier, H Raoult, G. Mineur, B. Carsin-Nicol, and J.Y. Gauvrit. Arterial spin labeling (ASL) perfusion : Techniques and Clinical Use. *Diagnostic and Interventional Imaging*, pages 1211–1223. ISSN 2211-5684. doi:10.1016/j.diii.2013.06.010.

[23] O. Arcangioli, L. Arrive, B. Aubert, R. Benacerraf, J.M. Bigot, J. Bittoun, S. Blangy, A. Bonnin, J. Broussin, D. Buthiau, J.N. Buy, A.E. Cabee, J.M. Caille, S. Chagnon, J. F. Chateil, A. Chevrot, C. Coffre, D. Couanet, E. Despres, J. De Treuf, J. Ecoiffier, L. Engelholm, G. Frija, F. Gires, N. Grenier, P. Grenier, C. Guinet, F. Heran, I. Idy-Peretti, J. Jean-Mart, P. Kien, H. Kressel, R. Lavayssiere, J. Leclere, A. Leroy-Willig, L. Malbec, M. Marichez, J. Masselot, E. Meary, Y. Menu, G. Pallardy, R.A. Parienty, J.D. Piekarski, J.C. Roucayrol, E. Schouman-Claeys, C. Segebarth, A. Sibert, E. Somveille, A. Taieb, V. Taviere, D. Vadrot, C. Vallee, D. Vanel, M. Zalcman, and M. Wybier. *MRI of the Body*. Springer-Verlag, Paris, France, 1 edition, 1989. ISBN 9783642875588.

[24] Alfred L. Horowitz. *MRI Physics for Radiologist: A Visual Approach*. Springer, New York, New York, USA, 3rd edition, 1995. ISBN 9780387943725.

[25] Lars G Hanson. Is Quantum Mechanics Necessary for Understanding Magnetic Resonance? *Concepts in Magnetic Resonance Part A*, 32A(5): 329–340, 2008. ISSN 00178012. doi:10.1002/cmr.a.

[26] Brian M Dale and Jeffrey L Duerk. The Use Of Measured K-Space Trajectory For Reconstruction Of Radial MRI Data. *Proceedings International Society of Magnetic Resonance in Medicine*, 10, 2002.

[27] Robert W Brown, Yu-Chung N.Cheng, E. Mark Haccke, Michael R. Thompson, and Rames Venkatesan. *Magnetic Resonance Imaging*. John Wiley & Sons Inc, Hoboken, New Jersey, second edition, 2014.

[28] F. Bloch, W. W. Hansen, and M. Packard. The Nuclear Induction Experiment. *Physical Review*, 70(7 and 8):474–485, 1946.

[29] Brian M Dale, Mark A Brown, and Richard C Semelka. Production of net magnetization. In *MRI Basic Principles and Applications*, chapter 1, pages 1–9. John Wiley & Sons, Ltd, Chichester, UK, 5th edition, 2015.

[30] Muhammed Elmaoğlu and Azim Çelik. Fundamentals of Magnetic Resonance Imaging. In *MRI Handbook*, chapter 2, pages 7–23. Springer, New York, New York, USA, 2012. ISBN 978-1-4614-1095-9.

doi:10.1007/978-1-4614-1096-6. URL
http://link.springer.com/10.1007/978-1-4614-1096-6.

[31] Brian M. Dale, Mark a. Brown, and Richard C. Semelka. Concepts of magnetic resonance. In *MRI Basic Principles and Applications*, volume 0, chapter 2, pages 10–16. John Wiley & Sons, Ltd, Chichester, UK, 5th edition, oct 2015. ISBN 9781119013068. doi:10.1002/9781119013068. URL http://doi.wiley.com/10.1002/9781119013068.

[32] Stephen Balter. An Introduction Magnetic to the Physics Imaging of Resonance. *RadioGraphics*, 7(2):371–383, 1987.

[33] Matt A Bernstein, Kevin F King, and Xiaohong Joe Zhou. *Handbook of MRI Pulse Sequences*. Elsevier Inc, 2004.

[34] Stuart Currie, Nigel Hoggard, Ian J Craven, Marios Hadjivassiliou, and Iain D Wilkinson. Understanding MRI: basic MR physics for physicians. *Postgraduate medical journal*, 89:209–223, apr 2013. ISSN 1469-0756. doi:10.1136/postgradmedj-2012-131342. URL
http://www.ncbi.nlm.nih.gov/pubmed/23223777.

[35] Paul Heckbert. Fourier Transforms and the Fast Fourier Transform (FFT) Algorithm. *Computer Graphics*, 2:15–463, 1998.

[36] J W Cooley and J W Tukey. An Algorithm for Machine Calculation of Complex Fourier Series, 1965. ISSN 00255718.

[37] A. Dutt and V Rokhlin. Fast Fourier Transforms fpr Nonequispaced Data. *SIAM Journal Scientific Computing*, 14(6):1368–1393, 1993.

[38] Robert A Pooley. AAPM / RSNA Physics Tutorial for Residents Fundamental Physics of MR Imaging 1. *RadioGraphics*, 25:1087–1099, 2005.

[39] Muhammed Elmaoğlu and Azim Çelik. MR Imaging Parameters and Options. In *MRI Handbook*, chapter 5, pages 69–89. Springer, New York, New York, USA, 2012. ISBN 978-1-4614-1095-9. doi:10.1007/978-1-4614-1096-6. URL
http://link.springer.com/10.1007/978-1-4614-1096-6.

[40] S. MeiBoom and D. Gill. Modified Spin-Echo Method for Measuring Nuclear Relaxation Times. *The Review of Scientific Instruments*, 29(8): 688–691, 1958.

[41] A Haase, J Frahm, D Matthaei, and K Merboldt. FLASH Imaging . Rapid NMR Imaging Using Low Flip-Angle Pulses. *Journal of Magnetic Resonance*, 67:258–266, 1986.

[42] David L Buckley and Geoffrey J M Parker. Measuring Contrast Agent Concentration in T 1 -Weighted Dynamic Contrast-Enhanced MRI. In Leuven A.L. Baert and Heidelberg K.Sartor, editors, *Dynamic Contrast-Enhanced Magnetic Resonance Imaging in Oncology*, chapter 5, pages 69–79. Springer, 2005.

[43] E Mark Haacke and Gerald W Lenz. Improving MR image quality in the presence of motion by using rephasing gradients. *American Journal of Roentgenology*, 148:1251–1258, jun 1987. ISSN 0361-803X. URL http://www.ncbi.nlm.nih.gov/pubmed/3495155.

[44] Paul C Lauterbur. Image Formation by Induced Local Interactions. *Nature*, 242:190, 1973.

[45] Jeff L Zhang, Henry Rusinek, Louisa Bokacheva, Qun Chen, Pippa Storey, and Vivian S Lee. Use of cardiac output to improve measurement of input function in quantitative dynamic contrast-enhanced MRI. *Journal of Magnetic Resonance Imaging*, pages 656–665, sep . ISSN 1053-1807. doi:10.1002/jmri.21891.

[46] M Louis Lauzon and Brian K Rutt. Effects of Polar Sampling in k-Space. *Magnetic Resonance in Medicine*, 36:940–949, 1996.

[47] M I Altbach, T P Trouard, and A F Gmitro. Radial MRI techniques for obtaining motion-insensitive high-resolution images with variable contrast. In *2002 IEEE*, pages 125–128, 2002. ISBN 078037584X.

[48] Rafael L O'Halloran, Zhifei Wen, James H Holmes, and Sean B Fain. Iterative projection reconstruction of time-resolved images using highly-constrained back-projection (HYPR). *Magnetic Resonance in Medicine*, pages 132–139, jan . ISSN 0740-3194. doi:10.1002/mrm.21439.

[49] Eli Benveniste and L. Yaroslavsky. Comparison Of Two-Dimensional Rebinning Algorithms For Image Reconstruction From Projections. Technical report, Tel Aviv University, Tel Aviv, 2003. URL http://www.eng.tau.ac.il/{~}yaro/EliBenveniste/EliBenvenisteSummary.pdf.

[50] H Schomberg and J Timmer. The gridding method for image reconstruction by Fourier transformation. *IEEE Transactions on Medical Imaging*, 14(3):

596–607, jan 1995. ISSN 0278-0062. doi:10.1109/42.414625. URL http://www.ncbi.nlm.nih.gov/pubmed/18215864.

[51] J D O'Sullivan. A fast sinc function gridding algorithm for fourier inversion in computer tomography. *IEEE Transactions on Medical Imaging*, 4(4):200–207, jan 1985. ISSN 0278-0062. doi:10.1109/TMI.1985.4307723. URL http://www.ncbi.nlm.nih.gov/pubmed/18243972.

[52] John I Jackson, Craig H Meyer, Dwight G Nishimura, and Albert Macovski. Selection of a Convolution Function for Fourier Inversion Using Gridding. *IEEE Transactions on Medical Imaging*, 10(3):473–478, 1991.

[53] Peter M Joseph. Sampling Errors in Projection Reconstruction MRI. *Magnetic Resonance in Medicine*, 40:460–466, 1998.

[54] Muhammed Elmaoğlu and Azim Çelik. A Brief History of Magnetic Resonance Imaging. In *MRI Handbook*, chapter 1, pages 3–6. Springer, New York, New York, USA, 2012. ISBN 978-1-4614-1095-9. doi:10.1007/978-1-4614-1096-6. URL http://link.springer.com/10.1007/978-1-4614-1096-6.

[55] Éva Tóth, Lothar Helm, and André E Merbach. Relaxivity of MRI Contrast Agents. In Werner Krause, editor, *Contrast Agents 1: Magnetic Resonance Imaging*, volume 221, pages 61–101. Springer Berline Heidelberg, Berlin, 2002.

[56] Erez Eyal and Hadassa Degani. Model-based and model-free parametric analysis of breast dynamic-contrast-enhanced MRI. *NMR in biomedicine*, 22:40–53, jan 2009. ISSN 0952-3480. doi:10.1002/nbm.1221. URL http://www.ncbi.nlm.nih.gov/pubmed/18022997.

[57] Paul S Tofts, Gunnar Brix, David L Buckley, Jeffrey L Evelhoch, Elizabeth Henderson, Michael V Knopp, Henrik B W Larsson, Ting-yim Lee, Nina A Mayr, Geoffrey J M Parker, Ruediger E Port, June Taylor, and Robert M Weisskoff. Estimating Kinetic Parameters from Dynamic Contrast-Enhanced T1-Weighted MRI of a Diffusable Tracer: Standardized Quantities and Symbols. *Journal of Magnetic Resonance Imaging*, 10: 223–232, 1999.

[58] Maya Dadiani, Edna Furman-Haran, and Hadassa Degani. The application of NMR in tumor angiogenesis research. *Progress in Nuclear Magnetic Resonance Spectroscopy*, 49:27–44, aug 2006. ISSN 00796565.

doi:10.1016/j.pnmrs.2006.06.001. URL http://linkinghub.elsevier.com/retrieve/pii/S0079656506000343.

[59] Eva Tóth, Lothar Helm, and André Merbach. Relaxivity of Gadolinium (III) Complexes: Theory and Mechanism. In Lothar Helm Andre Merbach and Eva Toth, editors, *The Chemistry of Contrast Agents in Medical Magnetic Resonance Imaging*, chapter 2, pages 25–81. John Wiley & Sons, Ltd, New York, New York, USA, second edition, 2013.

[60] Fernando Calamante. Quantification of Dynamic Susceptibility Contrast T2* MRI in Oncology. In Leuven A.L. Baert and Heidelberg K.Sartor, editors, *Dynamic Contrast-Enhanced Magnetic Resonance Imaging in Oncology*, chapter 4, pages 53–67. Springer, 2005.

[61] Zhuxian Zhou and Zheng-Rong Lu. Gadolinium-Based Contrast Agents for MR Cancer Imaging. *Wiley Interdisciplinary Reviews. Nanomedicine and Nanobiotechnology*, 5(1):1–18, 2013. doi:10.1002/wnan.1198.

[62] Brian M Dale, Mark A Brown, and Richard C. Semelka. Contrast Agents. In *MRI Basic Principles and Applications*, chapter 15, pages 189–195. John Wiley & Sons, Ltd, Chichester, UK, 5th edition, 2015.

[63] Hanns-Joachim Weinmann, Robert C Brasch, Wolf-R Press, and George E Wesbey. Characteristics of Gadolinium-DTPA Complex: A Potential NMR Contrast Agent. *American Journal of Roentgenology*, 142:619–624, 1984.

[64] D. H. Carr, J. Brown, G. M. Bydder, H. J. Weinmann, U. Speck, D. J. Thomas, and I. R. Young. Intravenous Chelated Gadolinium As a Contrast Agent in NMR Imaging of Cerebral Tumours. *The Lancet*, March 3: 484–486, 1984. ISSN 01406736. doi:10.1016/S0140-6736(84)92852-6.

[65] Robert J. McDonald, Jennifer S. McDonald, David F. Kallmes, Mark E. Jentoft, David L. Murray, Kent R. Thielen, Eric E. Williamson, and Laurence J. Eckel. Intracranial Gadolinium Deposition after Contrast-enhanced MR Imaging. *Radiology*, (3):772–782. ISSN 0033-8419. doi:10.1148/radiol.15150025.

[66] Bang J. Guo, Zhen L. Yang, and Long J. Zhang. Gadolinium Deposition in Brain: Current Scientific Evidence and Future Perspectives. *Frontiers in Molecular Neuroscience*, 11(September):1–12, 2018. doi:10.3389/fnmol.2018.00335.

[67] H. Kang, M. Hii, M. Le, R. Tam, A. Riddehough, A. Traboulsee, S. Kolind, M. S. Freedman, and D. K.B. Li. Gadolinium deposition in deep brain structures: Relationship with dose and ionization of linear gadolinium-based contrast agents. *American Journal of Neuroradiology*, 39(9):1597–1603, 2018. ISSN 1936959X. doi:10.3174/ajnr.A5751.

[68] Andreu F. Costa, Christian B. van der Pol, Pejman Jabehdar Maralani, Matthew D.F. McInnes, Jason R. Shewchuk, Raman Verma, Casey Hurrell, and Nicola Schieda. Gadolinium Deposition in the Brain: A Systematic Review of Existing Guidelines and Policy Statement Issued by the Canadian Association of Radiologists. *Canadian Association of Radiologists Journal*, (4):373–382. ISSN 14882361. doi:10.1016/j.carj.2018.04.002.

[69] Bariş Türkbey, David Thomasson, Yuxi Pang, Marcelino Bernardo, and Peter L Choyke. The role of dynamic contrast-enhanced MRI in cancer diagnosis and treatment. *Diagnostic and Interventional Radiology*, pages 186–192, sep . ISSN 1305-3612. doi:10.4261/1305-3825.DIR.2537-08.1.

[70] M. O. Leach, B. Morgan, P. S. Tofts, D. L. Buckley, W. Huang, M. A. Horsfield, T. L. Chenevert, D. J. Collins, A. Jackson, D. Lomas, B. Whitcher, L. Clarke, R. Plummer, I. Judson, R. Jones, R. Alonzi, T. Brunner, D. M. Koh, P. Murphy, J. C. Waterton, G. Parker, M. J. Graves, T. W J Scheenen, T. W. Redpath, M. Orton, G. Karczmar, H. Huisman, J. Barentsz, and A. Padhani. Imaging vascular function for early stage clinical trials using dynamic contrast-enhanced magnetic resonance imaging. *European Radiology*, 22:1451–1464, 2012. ISSN 09387994. doi:10.1007/s00330-012-2446-x.

[71] A L Martel, R W Chan, E Ramsay, and D B Plewes. Removing undersampling artifacts in DCE-MRI studies using independent components analysis. *Magnetic Resonance in Medicine*, 59:874–884, apr 2008. ISSN 0740-3194. doi:10.1002/mrm.21552. URL http://www.ncbi.nlm.nih.gov/pubmed/18302238.

[72] Jie Zheng, Kyongtae T Bae, Pamela K Woodard, E Mark Haacke, and Debiao Li. Efficacy of Slow Infusion of Gadolinium Contrast Agent in Three-Dimensional MR Coronary Artery Imaging. *Journal of Magnetic Resonance Imaging*, 10(5):800–805, 1999.

[73] D Checkley, J J Tessier, J Kendrew, J C Waterton, and S R Wedge. Use of dynamic contrast-enhanced MRI to evaluate acute treatment with ZD6474 ,

a VEGF signalling inhibitor, in PC-3 prostate tumours. *British Journal of Cancer*, 89:1889–1895, 2003. doi:10.1038/sj.bjc.6601386.

[74] M V Knopp, E Weiss, H P Sinn, J Mattern, H Junkermann, J Radeleff, A Magener, G Brix, S Delorme, I Zuna, and G van Kaick. Pathophysiologic basis of contrast enhancement in breast tumors. *Journal of magnetic resonance imaging*, 10:260–266, sep 1999. ISSN 1053-1807. URL http://www.ncbi.nlm.nih.gov/pubmed/10508285.

[75] Tristan Barrett, Hisataka Kobayashi, Martin Brechbiel, and Peter L. Choyke. Macromolecular MRI contrast agents for imaging tumor angiogenesis. *European Journal of Radiology*, 60:353–366, 2006. ISSN 0720048X. doi:10.1016/j.ejrad.2006.06.025.

[76] Kyrre E. Emblem, Christian T. Farrar, Elizabeth R. Gerstner, Tracy T. Batchelor, Ronald J. H. Borra, Bruce R. Rosen, A. Gregory Sorensen, and Rakesh K. Jain. Vessel calibre—a potential MRI biomarker of tumour response in clinical trials. *Nature Reviews Clinical Oncology*, pages 566–584. ISSN 1759-4774. doi:10.1038/nrclinonc.2014.126.

[77] Vladimir V. Iakovlev, Manal Gabril, William Dubinski, Andreas Scorilas, Youssef M. Youssef, Hala Faragalla, Kalman Kovacs, Fabio Rotondo, Shereen Metias, Androu Arsanious, Anna Plotkin, Andrew H F Girgis, Catherine J. Streutker, and George M. Yousef. Microvascular density as an independent predictor of clinical outcome in renal cell carcinoma: An automated image analysis study. *Laboratory Investigation*, (1):46–56. ISSN 00236837. doi:10.1038/labinvest.2011.153.

[78] Noel Weidner, Joseph P. Semple, William R. Welch, and Judah Folkman. Tumor Angiogenesis and Metastasis - Correlation in Invasive Breast Carcinoma. *The New England Journal of Medicine*, 324(1):1–8, 1991.

[79] Steven Sourbron. Technical aspects of MR perfusion. *European Journal of Radiology*, 76:304–313, 2010. ISSN 0720048X. doi:10.1016/j.ejrad.2010.02.017. URL http://dx.doi.org/10.1016/j.ejrad.2010.02.017.

[80] Tong San Koh, Sotirios Bisdas, Dow Mu Koh, and Choon Hua Thng. Fundamentals of tracer kinetics for dynamic contrast-enhanced MRI. *Journal of magnetic resonance imaging*, 34:1262–1276, dec 2011. ISSN 1522-2586. doi:10.1002/jmri.22795. URL http://www.ncbi.nlm.nih.gov/pubmed/21972053.

[81] David C Alsop, John A Detre, Xavier Golay, G Matthias, Jeroen Hendrikse, Luis Hernandez-garcia, Hanzhang Lu, Bradley J Macintosh, Laura M Parkes, Marion Smits, Matthias J P Van Osch, and Danny J J Wang. Recommended Implementation of Arterial Spin-Labeled Perfusion MRI for Clinical Applications : A Consensus of the ISMRM Perfusion Study Group and the European Consortium for ASL in Dementia. *Magnetic Resonance in Medicine*, 00(October 2013), 2014. doi:10.1002/mrm.25197.

[82] Fernando Calamante. Arterial input function in perfusion MRI: A comprehensive review. *Progress in Nuclear Magnetic Resonance Spectroscopy*, 74:1–32, oct 2013. ISSN 1873-3301. doi:10.1016/j.pnmrs.2013.04.002. URL http://www.ncbi.nlm.nih.gov/pubmed/24083460.

[83] Peter Caravan, Christian T Farrar, Luca Frullano, and Ritika Uppal. Influence of molecular parameters and increasing magnetic field strength on relaxivity of gadolinium- and manganese-based T1 contrast agents. *Contrast media & molecular imaging*, 4:89–100, 2009. ISSN 1555-4317. doi:10.1002/cmmi.267. URL http://www.pubmedcentral.nih.gov/articlerender.fcgi?artid=3995751.

[84] J A Brookes, T W Redpath, J Gilbert, G Needham, and A D Murray. Measurement of spin-lattice relaxation times with FLASH for dynamic MRI of the breast. *The British Journal of Radiology*, 69:206–214, 1996.

[85] A Jackson, G C Jayson, K L Li, X P Zhu, D R Checkley, J J L Tessier, and J C Waterton. Reproducibility of quantitative dynamic contrast-enhanced MRI in newly presenting glioma. *The British Journal of Radiology*, 76: 153–162, mar 2003. ISSN 0007-1285. doi:10.1259/bjr/70653746. URL http://bjr.birjournals.org/cgi/doi/10.1259/bjr/70653746.

[86] D C Look and D R Locker. Time Saving in Measurement of NMR and EPR Relaxation Times. *Review of Scientific Instruments*, 41(2):250–251, feb 1970. ISSN 0034-6748. doi:10.1063/1.1684482. URL http://aip.scitation.org/doi/10.1063/1.1684482.

[87] Yantian Zhang, Matthew O'Donnell, and Paul L Carson. Determination of Sample Time for T1 Measurement. *Journal of Magnetic Resonance Imaging*, 8:675–681, 1998.

[88] Hongzhi Wang, Ming Zhao, Jerome L Ackerman, and Yiqiao Song. Saturation-inversion-recovery : A method for T 1 measurement. *Journal of*

Magnetic Resonance, 274:137–143, 2017. ISSN 1090-7807. doi:10.1016/j.jmr.2016.11.015. URL http://dx.doi.org/10.1016/j.jmr.2016.11.015.

[89] Andrew J. Taylor, Michael Salerno, Rohan Dharmakumar, and Michael Jerosch-Herold. T1 Mapping: Basic Techniques and Clinical Applications. *JACC: Cardiovascular Imaging*, 9(1):67–81, 2016. doi:10.1016/j.jcmg.2015.11.005.

[90] M. Keara Boss, N. Muradyan, and D. E. Thrall. DCE-MRI: A review and applications in veterinary oncology. *Veterinary and Comparative Oncology*, 11(2):87–100, jun 2011.

[91] Jeffrey L Evelhoch. Key factors in the acquisition of contrast kinetic data for oncology. *Journal of magnetic resonance imaging*, 10:254–259, sep 1999. ISSN 1053-1807. URL http://www.ncbi.nlm.nih.gov/pubmed/10508284.

[92] Hee Kwon Song and Lawrence Dougherty. Dynamic MRI With Projection Reconstruction and KWIC Processing for Simultaneous High Spatial and Temporal Resolution. *Magnetic Resonance in Medicine*, 52:815–824, 2004. doi:10.1002/mrm.20237.

[93] Elodie Parzy, Sylvain Miraux, Jean-Michel Franconi, and Eric Thiaudière. In vivo quantification of blood velocity in mouse carotid and pulmonary arteries by ECG-triggered 3D time-resolved magnetic resonance angiography. *NMR in biomedicine*, 22:532–537, jun 2009. ISSN 1099-1492. doi:10.1002/nbm.1365. URL http://www.ncbi.nlm.nih.gov/pubmed/19156686.

[94] Julien Vautier, Nadine El Tannir El Tayara, Christine Walczak, Joël Mispelter, and Andreas Volk. Radial multigradient-echo DCE-MRI for 3D Ktrans mapping with individual arterial input function measurement in mouse tumor models. *Magnetic Resonance in Medicine*, 70:823–828, 2013. ISSN 07403194. doi:10.1002/mrm.24504.

[95] Jae-Hun Kim, Geun Ho Im, Jehoon Yang, Dongil Choi, Won Jae Lee, and Jung Hee Lee. Quantitative dynamic contrast-enhanced MRI for mouse models using automatic detection of the arterial input function. *NMR in Biomedicine*, 25:674–684, 2012. ISSN 1099-1492. doi:10.1002/nbm.1784. URL http://www.ncbi.nlm.nih.gov/pubmed/21954069.

[96] Thomas E Yankeelov, Laura M DeBusk, D Dean Billheimer, Jeffrey J Luci, P Charles Lin, Ronald R Price, and John C Gore. Repeatability of a reference region model for analysis of murine DCE-MRI data at 7T. *Journal of Magnetic Resonance Imaging*, 24:1140–1147, nov 2006. ISSN 1053-1807. doi:10.1002/jmri.20729. URL http://www.ncbi.nlm.nih.gov/pubmed/17024660.

[97] Martin Pellerin, Thomas E Yankeelov, and Martin Lepage. Incorporating contrast agent diffusion into the analysis of DCE-MRI data. *Magnetic Resonance in Medicine*, 58:1124–1134, dec 2007. ISSN 0740-3194. doi:10.1002/mrm.21400. URL http://www.ncbi.nlm.nih.gov/pubmed/17969007.

[98] Tormod A M Egeland, Kristine Gulliksrud, Jon-Vidar Gaustad, Berit Mathiesen, and Einar K Rofstad. Dynamic contrast-enhanced-MRI of tumor hypoxia. *Magnetic resonance in medicine*, 67:519–530, feb 2012. ISSN 1522-2594. doi:10.1002/mrm.23014. URL http://www.ncbi.nlm.nih.gov/pubmed/21661044.

[99] Andrew B Rosenkrantz, Christian Geppert, Robert Grimm, Tobias K Block, Christian Glielmi, Li Feng, Ricardo Otazo, Justin M Ream, Melanie Moccaldi Romolo, Samir S Taneja, Daniel K Sodickson, and Hersh Chandarana. Dynamic contrast-enhanced MRI of the prostate with high spatiotemporal resolution using compressed sensing, parallel imaging, and continuous golden-angle radial sampling: preliminary experience. *Journal of Magnetic Resonance Imaging*, 41:1365–1373, may 2015. ISSN 1522-2586. doi:10.1002/jmri.24661. URL http://www.pubmedcentral.nih.gov/articlerender.fcgi?artid=4233205.

[100] A.-C. Fruytier, J. Magat, F. Colliez, B. Jordan, G. Cron, and B. Gallez. Dynamic contrast-enhanced MRI in mice at high field: estimation of the arterial input function can be achieved by phase imaging. *Magnetic resonance in medicine*, 71:544–550, feb 2014. doi:10.1002/mrm.24682. URL http://www.ncbi.nlm.nih.gov/pubmed/23440927.

[101] Igor Jacobs, Gustav J. Strijkers, Henk M. Keizer, Henk M. Janssen, Klaas Nicolay, and Matthias C. Schabel. A novel approach to tracer-kinetic modeling for (macromolecular) dynamic contrast-enhanced MRI. *Magnetic Resonance in Medicine*, 75:1142–1153, 2016. ISSN 15222594. doi:10.1002/mrm.25704.

[102] Thomas Fritz-hansen, Egill Rostrup, Henrik B W Larsson, Lars Sandergaard, Poul Ring, and Ole Henriksen. Measurement of the Arterial Concentration of Gd-DTPA Using MRI : A Step Toward Quantitative Perfusion Imaging. *Magnetic Resonance in Medicine*, 36:225–231, 1996.

[103] Matthias C Schabel and Dennis L Parker. Uncertainty and bias in contrast concentration measurements using spoiled gradient echo pulse sequences. *Physics in Medicine and Biology*, 53(9):2345–2373, may 2008. ISSN 0031-9155. URL http://www.pubmedcentral.nih.gov/articlerender.fcgi?artid=2894639.

[104] Geoffrey J M Parker and David L Buckley. Tracer Kinetic Modelling for T 1 -Weighted DCE-MRI. In Leuven A.L. Baert and Heidelberg K.Sartor, editors, *Dynamic Contrast-Enhanced Magnetic Resonance Imaging in Oncology*, chapter 6, pages 81–92. Springer, 2005.

[105] L.J. Liu and M. Schlesinger. MRI contrast agent concentration and tumor interstitial fluid pressure. *Journal of Theoretical Biology*, 406:52–60, 2016.

[106] Torfinn Taxt, Radovan Jiřík, Cecilie Brekke Rygh, Renate Grüner, Michal Bartoš, Erling Andersen, Fitz Roy Curry, and Rolf K. Reed. Single-channel blind estimation of arterial input function and tissue impulse response in DCE-MRI. *IEEE Transactions on Biomedical Engineering*, 59(4): 1012–1021, 2012. ISSN 00189294. doi:10.1109/TBME.2011.2182195.

[107] C A Cuenod and D Balvay. Perfusion and vascular permeability : Basic concepts and measurement in DCE-CT and DCE-MRI. *Diagnostic and Interventional Imaging*, 94:1187–1204, 2013. ISSN 2211-5684. doi:10.1016/j.diii.2013.10.010. URL http://dx.doi.org/10.1016/j.diii.2013.10.010.

[108] Mark Rijpkema, Johannes H. A. M. Kaanders, Frank B. M. Joosten, Albert J van der Kogel, and Arend Heerschap. Method for quantitative mapping of dynamic MRI contrast agent uptake in human tumors. *Journal of Magnetic Resonance Imaging*, 14:457–463, oct 2001. ISSN 1053-1807. URL http://www.ncbi.nlm.nih.gov/pubmed/11599071.

[109] Thomas E Yankeelov, Jeffrey J Luci, Martin Lepage, Rui Li, Laura Debusk, P Charles Lin, Ronald R Price, and John C Gore. Quantitative pharmacokinetic analysis of DCE-MRI data without an arterial input function: a reference region model. *Magnetic Resonance Imaging*, 23: 519–529, may 2005. ISSN 0730-725X. doi:10.1016/j.mri.2005.02.013. URL http://www.ncbi.nlm.nih.gov/pubmed/15919597.

[110] Xiaobing Fan and Gregory S Karczmar. A new approach to analysis of the impulse response function (IRF) in dynamic contrast-enhanced MRI (DCEMRI): a simulation study. *Magnetic resonance in medicine*, 62: 229–239, jul 2009. ISSN 1522-2594. doi:10.1002/mrm.21995. URL http://www.pubmedcentral.nih.gov/articlerender.fcgi?artid=2927981.

[111] Eugene G Kholmovski and Edward V R DiBella. Perfusion MRI with radial acquisition for arterial input function assessment. *Magnetic Resonance Imaging*, 57:821–827, may 2007. ISSN 0740-3194. doi:10.1002/mrm.21210. URL http://www.ncbi.nlm.nih.gov/pubmed/17457875.

[112] Xia Li, E Brian Welch, Lori R Arlinghaus, A Bapsi Chakravarthy, Lei Xu, Jaime Farley, Mary E Loveless, Ingrid A Mayer, Mark C Kelley, Ingrid M Meszoely, Julie A Means-Powell, Vandana G Abramson, Ana M Grau, John C Gore, and Thomas E Yankeelov. A novel AIF tracking method and comparison of DCE-MRI parameters using individual and population-based AIFs in human breast cancer. *Physics in Medicine and Biology*, pages 5753–5769, sep . ISSN 1361-6560. doi:10.1088/0031-9155/56/17/018.

[113] Steven P. Sourbron and David L. Buckley. Classic models for dynamic contrast-enhanced MRI. *NMR in Biomedicine*, 26:1004–1027, 2013. ISSN 09523480. doi:10.1002/nbm.2940.

[114] Paul S Tofts and Allan G Kermode. Measurement of the blood-brain barrier permeability and leakage space using dynamic MR imaging. 1. Fundamental concepts. *Magnetic Resonance in Medicine*, 17(2):357–367, feb 1991. ISSN 0740-3194. URL http://www.ncbi.nlm.nih.gov/pubmed/2062210.

[115] Rujirutana Srikanchana, David Thomasson, Peter Choyke, and Andrew Dwyer. A Comparison of Pharmacokinetic Models of Dynamic Contrast Enhanced MRI. In *Proceedings of the 17th IEEE Symposium on Computer-Based Medical Systems*, pages 1–6, 2004.

[116] Seymour S Kety. The Theory and Applications of the Exchange of Inert Gas at the Lungs and Tissues. *Pharmacological Reviews*, 3(1):1–41, 1951.

[117] Cristina Lavini and Joost J C Verhoeff. Reproducibility of the gadolinium concentration measurements and of the fitting parameters of the vascular input function in the superior sagittal sinus in a patient population.

Magnetic resonance imaging, pages 1420–1430, dec . ISSN 1873-5894. doi:10.1016/j.mri.2010.06.017.

[118] Bruce R Rosen, John W Belliveau, Bradley R Buchbinder, Robert C McKinstry, Leena M Porkka, David N Kennedy, Michelle S Neuder, C Richard Fisel, Hannu J Aronen, Kenneth K Kwong, Robert M Weisskoff, Mark S Cohen, and Thomas J Brady. Contrast Agents and Cerebral Hemodynamics. *Magnetic Resonance in Medicine*, 19(2):285–292, 1991.

[119] William H Perman, Mokhtar H Gado, Kenneth B Larson, and Joel S Perlmutter. Simultaneous MR Acquisition of Arterial and Brain Signal Time Curves. *Magnetic Resonance in Medicine*, 28:74–83, 1992.

[120] Adam E Hansen, Henrik Pedersen, Egill Rostrup, and Henrik B W Larsson. Partial volume effect (PVE) on the arterial input function (AIF) in T1-weighted perfusion imaging and limitations of the multiplicative rescaling approach. *Magnetic resonance in medicine*, 62:1055–1059, oct 2009. ISSN 1522-2594. doi:10.1002/mrm.22098. URL http://www.ncbi.nlm.nih.gov/pubmed/19672948.

[121] Rong Zhou, Stephen Pickup, Thomas E Yankeelov, Charles S Springer Jr, and Jerry D Glickson. Simultaneous Measurement of Arterial Input Function and Tumor Pharmacokinetics in Mice by Dynamic Contrast Enhanced Imaging : Effects of Transcytolemmal Water Exchange. *Magnetic Resonance in Medicine*, 52:248–257, 2004. doi:10.1002/mrm.20143.

[122] Wei Lin, Junyu Guo, Mark A Rosen, and Hee Kwon Song. Respiratory motion-compensated radial dynamic contrast-enhanced (DCE)-MRI of chest and abdominal lesions. *Magnetic Resonance in Medicine*, 60: 1135–1146, nov 2008. ISSN 1522-2594. doi:10.1002/mrm.21740. URL http://www.ncbi.nlm.nih.gov/pubmed/18956465.

[123] N J Taylor, I J Rowland, S F Tanner, and M Leach. A Rapid Interleaved Method for Measuring Signal Intensity Curves in Both Blood and Tissue during Contrast Agent Administration. *Magnetic Resonance in Medicine*, 30:744–749, 1993.

[124] Sabine Heiland, Wolfgang Reith, Michael Forsting, and Klaus Sartor. How do concentration and dosage of the contrast agent affect the signal change in perfusion-weighted magnetic resonance imaging? A computer simulation. *Magnetic Resonance Imaging*, 19:813–820, jul 2001. ISSN 0730-725X. URL http://www.ncbi.nlm.nih.gov/pubmed/11551721.

[125] E G Kholmovski, E V Dibella, and A A Samsonov. Perfusion MRI with Radial Sampling : Arterial Input Function and Tissue Enhancement Curve Assessment. In *Proceedings International Society of Magnetic Resonance in Medicine*, volume 13, page 252, 2005.

[126] Erbil Akbudak, Richard E Norberg, and Thomas E Conturo. Contrast-agent phase effects: an experimental system for analysis of susceptibility, concentration, and bolus input function kinetics. *Magnetic resonance in medicine*, 38:990–1002, dec 1997. ISSN 0740-3194. URL http://www.ncbi.nlm.nih.gov/pubmed/9402201.

[127] Matthias J P van Osch, Evert-jan P A Vonken, Max A Viergever, Jeroen van der Grond, and Chris J G Bakker. Measuring the arterial input function with gradient echo sequences. *Magnetic Resonance in Medicine*, 49: 1067–1076, jun 2003. ISSN 0740-3194. doi:10.1002/mrm.10461. URL http://www.ncbi.nlm.nih.gov/pubmed/12768585.

[128] Melanie S Kotys, Erbil Akbudak, Joanne Markham, and Thomas E Conturo. Precision, Signal-to-Noise Ratio, and Dose Optimization of Magnitude and Phase Arterial Input Functions in Dynamic Susceptibility Contrast MRI. *Journal of magnetic resonance imaging*, 25:598–611, 2007. doi:10.1002/jmri.20859.

[129] Ludovic de Rochefort, Thanh Nguyen, Ryan Brown, Pascal Spincemaille, Grace Choi, Jonathan Weinsaft, Martin R. Prince, and Yi Wang. In vivo quantification of contrast agent concentration using the induced magnetic field for time-resolved arterial input function measurement with MRI. *Medical Physics*, (12):5328–5339. ISSN 00942405. doi:10.1118/1.3002309.

[130] Shiyang Wang, Xiaobing Fan, Milica Medved, Federico D. Pineda, Ambereen Yousuf, Aytekin Oto, and Gregory S. Karczmar. Arterial input functions (AIFs) measured directly from arteries with low and standard doses of contrast agent, and AIFs derived from reference tissues. *Magnetic Resonance Imaging*, 34:197–203, feb 2016. ISSN 0730725X. doi:10.1016/j.mri.2015.10.025. URL http://linkinghub.elsevier.com/retrieve/pii/S0730725X15002623.

[131] Egbert J W Bleeker, Mark A van Buchem, Andrew G Webb, and Matthias J P van Osch. Phase-based arterial input function measurements for dynamic susceptibility contrast MRI. *Magnetic resonance in medicine*, 64:

358–368, aug 2010. ISSN 1522-2594. doi:10.1002/mrm.22420. URL http://www.ncbi.nlm.nih.gov/pubmed/20665779.

[132] Herbert Köstler, Christian Ritter, Michael Lipp, Meinrad Beer, Dietbert Hahn, and Jörn Sandstede. Prebolus quantitative MR heart perfusion imaging. *Magnetic resonance in medicine*, 52:296–299, aug 2004. ISSN 0740-3194. doi:10.1002/mrm.20160. URL http://www.ncbi.nlm.nih.gov/pubmed/15282811.

[133] Ka Loh Li, Giovanni Buonaccorsi, Gerard Thompson, John R. Cain, Amy Watkins, David Russell, Salman Qureshi, D. Gareth Evans, Simon K. Lloyd, Xiaoping Zhu, and Alan Jackson. An improved coverage and spatial resolution-using dual injection dynamic contrast-enhanced (ICE-DICE) MRI: A novel dynamic contrast-enhanced technique for cerebral tumors. *Magnetic Resonance in Medicine*, 68:452–462, 2012. ISSN 07403194. doi:10.1002/mrm.23252.

[134] Jacob U Fluckiger, Matthias C Schabel, and Edward V R DiBella. Constrained estimation of the arterial input function for myocardial perfusion cardiovascular magnetic resonance. *Magnetic resonance in medicine*, 66:419–427, aug 2011. ISSN 1522-2594. doi:10.1002/mrm.22809. URL http://www.ncbi.nlm.nih.gov/pubmed/21446030.

[135] Tae Ho Kim, Nathan A Pack, Liyong Chen, and Edward V R DiBella. Quantification of myocardial perfusion using CMR with a radial data acquisition: comparison with a dual-bolus method. *Journal of cardiovascular magnetic resonance*, 12:45–52, 2010. ISSN 1532-429X. doi:10.1186/1532-429X-12-45. URL http://www.pubmedcentral.nih.gov/articlerender.fcgi?artid=2920886.

[136] David A Kovar, Marta Lewis, and Gregory S Karczmar. A new method for imaging perfusion and contrast extraction fraction: input functions derived from reference tissues. *Journal of Magnetic Resonance Imaging*, 8(5): 1126–1134, 1998. ISSN 1053-1807. URL http://www.ncbi.nlm.nih.gov/pubmed/9786152.

[137] N Srinivasa, K. R. Ramakrishnan, and K. Rajgopal. Two-Dimensional Spectral Estimation : A Radon Transform Approach. *IEEE Journal of Oceanic Engineering*, OE-12(1):90–96, 1987.

[138] Kathleen M Donahue, Deborah Burstein, Warren J Manning, and Martha L Gray. Studies of Gd-DTPA Relaxivity and Proton Exchange Rates in Tissue. *Magnetic Resonance in Medicine*, 32:66–76, 1994.

[139] Samuella B. Sigmann and Dale E. Wheeler. The Quantitative Determination of Food Dyes in Powdered Drink Mixes. *Journal of Chemical Education*, (10):1475–1478, oct . ISSN 0021-9584. doi:10.1021/ed081p1475.

[140] David E. Nixon, Mary F Burritt, and Thomas P Moyer. The determination of mercury in whole blood and urine by inductively coupled plasma mass spectrometry. *Spectrochimica Acta Part B*, 54:1141–1153, 1999.

[141] Claire Foottit, Greg O Cron, Matthew J Hogan, Thanh Binh Nguyen, and Ian Cameron. Determination of the venous output function from MR signal phase: feasibility for quantitative DCE-MRI in human brain. *Magnetic resonance in medicine*, 63:772–781, mar 2010. ISSN 1522-2594. doi:10.1002/mrm.22253. URL http://www.ncbi.nlm.nih.gov/pubmed/20187184.

[142] William T Golde, Peter Gollobin, and Luis L Rodriguez. A rapid , simple , and humane method for submandibular bleeding of mice using a lancet. *Lab Animal*, 34(9):39–43, 2005.

[143] D Stab, J Tran-Gia, C O Ritter, D Hahn, and H Kostler. AIF Determination for Quantitative Myocardial Perfusion Imaging Using a Model Based Reconstruction of Radially Acquired Data. In *Proceedings International Society of Magnetic Resonance in Medicine*, volume 19, page 1341, 2011.

[144] Michael C Kreissl, Hsiao-Ming Wu, David B Stout, Waldemar Ladno, Thomas H Schindler, Xiaoli Zhang, John O Prior, Mayumi L Prins, Arion F Chatziioannou, Sung-Cheng Huang, and Heinrich R Schelbert. Noninvasive measurement of cardiovascular function in mice with high-temporal-resolution small-animal PET. *Journal of Nuclear Medicine*, 47:974–980, jun 2006. ISSN 0161-5505. URL http://www.ncbi.nlm.nih.gov/pubmed/16741307.

[145] Shuo Zhang, Kai Tobias Block, and Jens Frahm. Magnetic Resonance Imaging in Real Time: Advances Using Radial FLASH. *Journal of Magnetic Resonance Imaging*, 31:101–109, 2010. doi:10.1002/jmri.21987.

[146] Rachel W Chan, Elizabeth A Ramsay, Charles H Cunningham, and Donald B Plewes. Temporal stability of adaptive 3D radial MRI using

multidimensional golden means. *Magnetic resonance in medicine*, 61: 354–363, feb 2009. ISSN 1522-2594. doi:10.1002/mrm.21837. URL http://www.ncbi.nlm.nih.gov/pubmed/19165897.

[147] Potts D., Steidl G., and Tasche M. Fast Fourier transforms for nonequispaced data: A tutorial. In Benedetto J.J. and Ferreira P.J.S.G., editors, *Modern Sampling Theory. Applied and Numerical Harmonic Analysis*, chapter 12, pages 247–270. Birkhäuser, Boston, MA, 2001. ISBN 978-1-4612-0143-4. doi:https://doi.org/10.1007/978-1-4612-0143-4_12.

[148] Jeffrey A Fessler and Bradley P Sutton. Nonuniform Fast Fourier Transforms Using Min-Max Interpolation. *IEEE transactions on signal processing*, 51(2):560–574, 2003.

[149] Charles A Mistretta. Undersampled Radial MR Acquisition and Highly Constrained Back Projection (HYPR) Reconstruction: Potential Medical Imaging Applications in the Post-Nyquist Era. *Journal of Magnetic Resonance Imaging*, 29:501–516, 2009. doi:10.1002/jmri.21683.

[150] Sungho Tak, Jaeheung Yoo, and Jong Chul. High Resolution Projection Reconstruction MR Imaging using FOCUSS. In *SPIE-IS&T*, volume 6498, page 64981A, 2007.

[151] Kai Tobias Block, Martin Uecker, and Jens Frahm. Undersampled radial MRI with multiple coils. Iterative image reconstruction using a total variation constraint. *Magnetic Resonance in Medicine*, 57:1086–1098, 2007.

[152] Avinash C. Kak and Malcolm. Measurement of Projection Data- The Nondiffracting Case. In Robert E. O'Malley Jr., editor, *Principles of Computerized Tomographic Imaging*, chapter 4, pages 113–175. SiAM, Philapelphia, PA, first edition, 2001.

[153] Leslie Greengard and June-Yub Lee. Accelerating the Nonuniform Fast Fourier Transform. *SIAM Review*, 46(3):443–454, 2004.

[154] Ganesh Adluru, Ross Whitaker, and Edward V.R. Dibella. Spatio-Temporal Constrained Reconstruction of Sparse Dynamic Contrast Enhanced Radial MRI Data. *2007 4th IEEE International Symposium on Biomedical Imaging: From Nano to Macro*, pages 109–112, 2007. doi:10.1109/ISBI.2007.356800. URL http://ieeexplore.ieee.org/lpdocs/epic03/wrapper.htm?arnumber=4193234.

[155] Ganesh Adluru, Chris McGann, Peter Speier, Eugene Kholmovski, Akram Shaaban, and Edward V R Dibella. Acquisition and Reconstruction of Undersampled Radial Data for Myocardial Perfusion MRI. *Journal of Magnetic Resonance Imaging*, 29(2):466–473, 2009. doi:doi:10.1002/jmri.21585.

[156] Michael Lustig, David Donoho, and John M Pauly. Sparse MRI : The Application of Compressed Sensing for Rapid MR Imaging. *Magnetic Resonance in Medicine*, 58:1182–1195, 2007. doi:10.1002/mrm.21391.

[157] K.T. Block and M. Uecker. Simple Method for Adaptive Gradient-Delay Compensation in Radial MRI. In *Proceedings International Society of Magnetic Resonance in Medicine*, volume 19, page 2816, 2011.

[158] Donald Shepard. A two-dimensional interpolation function for irregularly-spaced data. In *Proceedings of the 1968 ACM National Conference*, pages 517–524, New York, New York, USA, 1968. ACM Press. doi:10.1145/800186.810616. URL http://portal.acm.org/citation.cfm?doid=800186.810616.

[159] Jens Keiner, Stefan Kunis, and Daniel Potts. Using NFFT 3 – a software library for various nonequispaced fast Fourier transforms. *ACM Transactions on Mathematical Software*, V(N):1–23, 2008.

[160] Tobias Knopp, Stefan Kunis, and Daniel Potts. A note on the iterative MRI reconstruction from nonuniform k-space data. *International Journal of Biomedical Imaging*, 2007:24727, jan 2007. ISSN 1687-4188. doi:10.1155/2007/24727. URL http://www.pubmedcentral.nih.gov/articlerender.fcgi?artid=2271125.

[161] Jens Keiner, Stefan Kunis, and Daniel Potts. NFFT 3.0 - Tutorial. Technical report, University of Lubeck, Institute of Mathematics and Chemnitz University of Technology, Department of Mathematics, Chemnitz, Germany, 2006. URL http://www.tu-chemnitz.de/potts/nfft.

[162] Kai Tobias Block. *Advanced Methods for Radial Data Sampling in Magnetic Resonance Imaging*. PhD thesis, der Georg-August-Universitat Gottingen, 2008.

[163] Wei Lin, Feng Huang, Enrico Simonotto, George R Duensing, and Arne Reykowski. Off-resonance artifacts correction with convolution in k-space (ORACLE). *Magnetic Resonance in Medicine*, pages 1547–1555, jun . ISSN 1522-2594. doi:10.1002/mrm.23135.

[164] Stefanie Winkelmann, Tobias Schaeffter, Holger Eggers, and Olaf Doessel. SNR enhancement in radial SSFP imaging using partial k-space averaging. *IEEE Transactions on Medical Imaging*, 24(2):254–262, feb 2005. ISSN 0278-0062. URL http://www.ncbi.nlm.nih.gov/pubmed/15707251.

[165] Stefanie Winkelmann, Tobias Schaeffter, Thomas Koehler, Holger Eggers, and Olaf Doessel. An optimal radial profile order based on the Golden Ratio for time-resolved MRI. *IEEE Transactions on Medical Imaging*, 26 (1):68–76, jan 2007. ISSN 0278-0062. doi:10.1109/TMI.2006.885337. URL http://www.ncbi.nlm.nih.gov/pubmed/17243585.

[166] Ganesh Adluru, Suyash P Awate, Tolga Tasdizen, Ross T Whitaker, and Edward V R Dibella. Temporally constrained reconstruction of dynamic cardiac perfusion MRI. *Magnetic resonance in medicine*, 57:1027–1036, jun 2007. ISSN 0740-3194. doi:10.1002/mrm.21248. URL http://www.ncbi.nlm.nih.gov/pubmed/17534924.

[167] Z H Ahn, C B, Cho. New Phase Correction Method in NMR Imaging Based on Autocorrelation and Histogram Analysis. *IEEE transactions on medical imaging*, MI-6(1):32–36, 1987.

[168] Zhou Wang, Alan Conrad Bovik, Hamid Rahim Sheikh, and Eero P Simoncelli. Image Quality Assessment : From Error Visibility to Structural Similarity. *IEEE Transactions on Image Processing*, 13(4):600–612, 2004.

[169] Greg J. Stanisz, Ewa E. Odrobina, Joseph Pun, Michael Escaravage, Simon J. Graham, Michael J. Bronskill, and R. Mark Henkelman. T1, T2 relaxation and magnetization transfer in tissue at 3T. *Magnetic Resonance in Medicine*, 54:507–512, 2005. ISSN 07403194. doi:10.1002/mrm.20605.

[170] Joop J van Vaals, Marijn E Brummer, W Thomas Dixon, Hans H Tuithof, Hans Engels, Rendon C Nelson, Brigid M Gerety, Judith L Chezmar, and Jacques A den Boer. ”Keyhole” method for accelerating imaging of contrast agent uptake. *Journal of Magnetic Resonance Imaging*, pages 671–675. ISSN 1053-1807.

[171] Jennifer Moroz, Andrew C Yung, Piotr Kozlowski, and Stefan A Reinsberg. Estimation of the Arterial Input Function in a Mouse Tail from the Signal Phase of Projection Profiles. In *Proceedings International Society of Magnetic Resonance in Medicine*, volume 20, page 239, 2012.

[172] Patrik Brynolfsson, Jun Yu, Ronnie Wirestam, Mikael Karlsson, and Anders Garpebring. Combining phase and magnitude information for

contrast agent quantification in dynamic contrast-enhanced MRI using statistical modeling. *Magnetic Resonance in Medicine*, 74:1156–1164, 2015. ISSN 15222594. doi:10.1002/mrm.25490.

[173] Yaqi Shen, Frank L Goerner, Christopher Snyder, John N Morelli, Dapeng Hao, Daoyu Hu, Xiaoming Li, and Val M Runge. T1 Relaxivities of Gadolinium-Based Magnetic Resonance Contrast Agents in Human Whole Blood at 1.5, 3, and 7 T. *Investigative Radiology*, 50(5):330–338, 2015. ISSN 15360210. doi:10.1097/RLI.0000000000000132.

[174] C. Kalavagunta and G.J. Metzger. A field comparison of r1 and r2 * relaxivities of Gd-DTPA in aqueous solution and whole blood : 3T versus 7T. *Proceedings International Society of Magnetic Resonance in Medicine*, 18:4990, 2010.

[175] Iris M Noebauer-huhmann, Pavol Szomolanyi, Oliver Kraff, and Siegfried Trattnig. Gadolinium-Based Magnetic Resonance Contrast Agents at 7 Tesla. *Investigative Radiology*, 45(9):554–558, 2010.

[176] Rachel W Chan, Elizabeth A Ramsay, Edward Y Cheung, and Donald B Plewes. The influence of radial undersampling schemes on compressed sensing reconstruction in breast MRI. *Magnetic resonance in medicine*, 67: 363–377, feb 2012. ISSN 1522-2594. doi:10.1002/mrm.23008. URL http://www.ncbi.nlm.nih.gov/pubmed/21656558.

[177] Hao Tan and Craig H Meyer. Estimation of k-Space Trajectories in Spiral MRI. *Magnetic Resonance in Medicine*, 61:1396–1404, 2009. doi:10.1002/mrm.21813.

[178] Dana C. Peters, J. Andrew Derbyshire, and Elliot R. McVeigh. Centering the projection reconstruction trajectory: Reducing gradient delay errors. *Magnetic Resonance in Medicine*, 50:1–6, 2003.

[179] T. H. Rozijn, B. P J Van Der Sanden, A. Heerschap, J. H N Creyghton, and W. M M J Bovée. Influence of the pharmacokinetic model on the quantification of the Gd- DTPA uptake rate in brain tumours using direct T1 measurements. *Magnetic Resonance Materials in Physics, Biology and Medicine*, 6(1):37–43, 1998. ISSN 13528661. doi:10.1016/S1352-8661(98)00008-8.

[180] Jonathan M. Bernstein, Jarrod J. Homer, and Catharine M. West. Dynamic contrast-enhanced magnetic resonance imaging biomarkers in head and neck cancer: Potential to guide treatment? A systematic review. *Oral*

Oncology, 50:963–970, 2014. ISSN 18790593. doi:10.1016/j.oraloncology.2014.07.011.

[181] Chong Duan, Jesper F. Kallehauge, G. Larry Bretthorst, Kari Tanderup, Joseph J.H. Ackerman, and Joel R. Garbow. Are complex DCE-MRI models supported by clinical data? *Magnetic Resonance in Medicine*, 77 (3):1329–1339, 2017. ISSN 15222594. doi:10.1002/mrm.26189.

[182] Andriy Fedorov, Jacob Fluckiger, Gregory D. Ayers, Xia Li, Sandeep N. Gupta, Clare Tempany, Robert Mulkern, Thomas E. Yankeelov, and Fiona M. Fennessy. A comparison of two methods for estimating DCE-MRI parameters via individual and cohort based AIFs in prostate cancer: A step towards practical implementation. *Magnetic Resonance Imaging*, pages 321–329. ISSN 18735894. doi:10.1016/j.mri.2014.01.004.

[183] Xiaoguang Li, Yongshan Zhu, Houyi Kang, Yulong Zhang, Huaping Liang, Sumei Wang, and Weiguo Zhang. Glioma grading by microvascular permeability parameters derived from dynamic contrast-enhanced MRI and intratumoral susceptibility signal on susceptibility weighted imaging Head & neck imaging. *Cancer Imaging*, 15(1):1–9, 2015. ISSN 14707330. doi:10.1186/s40644-015-0039-z.

[184] Hatef Mehrabian, Chaitanya Chandrana, Ian Pang, Rajiv Chopra, and Anne L Martel. Arterial input function calculation in dynamic contrast-enhanced MRI: an in vivo validation study using co-registered contrast-enhanced ultrasound imaging. *European radiology*, 22: 1735–1747, aug 2012. ISSN 1432-1084. doi:10.1007/s00330-012-2418-1. URL http://www.ncbi.nlm.nih.gov/pubmed/22752523.

[185] Hatef Mehrabian, Rajiv Chopra, and Anne L Martel. Calculation of intravascular signal in dynamic contrast enhanced MRI using adaptive complex independent component analysis. *IEEE Transactions on Medical Imaging*, 32(4):699–710, 2013. ISSN 0278-0062. doi:10.1109/TMI.2012.2233747;10.1109/TMI.2012.2233747.

[186] Hatef Mehrabian, Masoom A. Haider, and Anne L. Martel. Using Independent Compenents Analysis to Calculate Intravascular Contrast Agent Concentration in Prostate Cancer. In *IEEE 10th International Symposium on Biomedical Imaging*, pages 966–969, 2013. ISBN 9781467364553.

[187] Robert Marc Lebel, Jesse Jones, Jean-Christophe Ferre, Meng Law, and Krishna S Nayak. Highly accelerated dynamic contrast enhanced imaging.

Magnetic Resonance in Medicine, pages 635–644. ISSN 1522-2594. doi:10.1002/mrm.24710.

[188] Mark A Griswold, Peter M Jakob, Robin M Heidemann, Mathias Nittka, Vladimir Jellus, Jianmin Wang, Berthold Kiefer, and Axel Haase. Generalized Autocalibrating Partially Parallel Acquisitions (GRAPPA). *Magnetic Resonance in Medicine*, 47:1202–1210, 2002. doi:10.1002/mrm.10171.

[189] Chao Ma and Xiaohua Jiang. A New Eddy-current Compensation Method in MRI. *PIERS Online*, 3(6):874–878, 2007. ISSN 1931-7360. doi:10.2529/PIERS061006031452. URL http://piers.mit.edu/piersonline/piers.php?year=2007{&}volume=3{&}number=6{&}page=874.

[190] Amir Moussavi, Markus Untenberger, Martin Uecker, and Jens Frahm. Correction of gradient-induced phase errors in radial MRI. *Magnetic Resonance in Medicine*, 71:308–312, 2014. ISSN 07403194. doi:10.1002/mrm.24643.

[191] Ian C. Atkinson, Aiming Lu, and Keith R. Thulborn. Characterization and correction of system delays and eddy currents for MR imaging with ultrashort echo-time and time-varying gradients. *Magnetic Resonance in Medicine*, 62:532–537, 2009. ISSN 07403194. doi:10.1002/mrm.22016.

[192] Yantian Zhang, Hoby P Hetherington, Ernest M Stokely, Graeme F Mason, and Donald B Twieg. A novel k-space trajectory measurement technique. *Magnetic Resonance in Medicine*, 39:999–1004, jun 1998. ISSN 0740-3194. URL http://www.ncbi.nlm.nih.gov/pubmed/9621924.

[193] Peter Latta, Zenon Starcuk Jr., Marco L H Gruwel, Michael H. Weber, and Boguslaw Tomanek. K-space trajectory mapping and its application for ultrashort Echo time imaging. *Magnetic Resonance Imaging*, 36:68–76, 2017. ISSN 18735894. doi:10.1016/j.mri.2016.10.012.

[194] Marine Beaumont, Laurent Lamalle, Christoph Segebarth, and Emmanuel L Barbier. Improved k -Space Trajectory Measurement With Signal Shifting. *Magnetic resonance in medicine*, 58:200–205, 2007. doi:10.1002/mrm.21254.

[195] Jennifer Moroz, Piotr Kozlowski, and Stefan A Reinsberg. Determination of Local Tissue Enhancement from Radially Reconstructed Images. In *Proceedings International Society of Magnetic Resonance in Medicine*, volume 21, page 3074, 2013.

Appendix A

Comparing Radial Reconstruction Techniques

This appendix shows all of the radial images reconstructed with Shepard's method of interpolation, STCR and NFFT, with three sampling methods and five acceleration rates.

A.1 Shepard's Method of Interpolation

Radial images reconstructed with Shepard's method of interpolation are presented in Figures A.1, A.2, and A.3 for reconstructions with 233, 144, 89, 55, 34 or 21 projections, and uniform, Golden angle or random sampling.

In general, the image quality decreases as fewer projections are used in the reconstruction. At least 89 projections are required for the radial image to be visually comparable with the reference image (using all 233 radial projections). Reducing the number of projections to 55 and fewer often causes a loss of contrast between the capillary tube and the rest of the phantom, and blurring of the outer edges of the phantom. The smaller external phantom to the right of the main one is visible in all images with uniform or Golden angle sampling, but only in the images with 55 or more projections with random sampling. Blurry, curved streaking artifacts are observed in the background for all images, though the structure is consistent with the reference image. These artifacts are likely due to the chosen interpolation

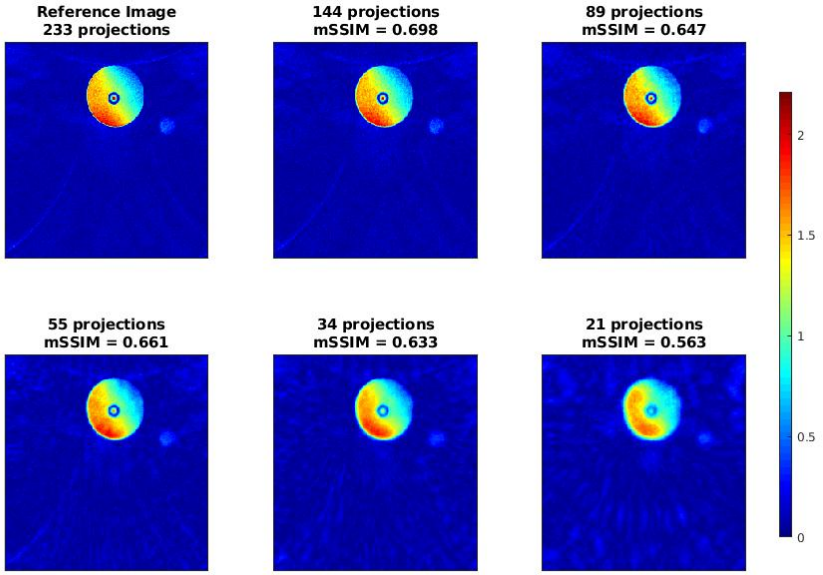

Figure A.1: Radial magnitude images created with Shepard's method of interpolation with uniform angluar sampling over 180°. The reconstructions were done with 233 (reference), 144, 89, 55, 34 or 21 projections. Visually, the images with 89 or 144 projections are comparable with the reference image. As the number of projections is reduced, the image becomes blurred and the contrast between the capillary tube and surrounding region is reduced. The signal intensity gradient across the phantom is preserved down to 34 projections. The mSSIM index, relative to the reference image, gradually decreases from 0.698 with 144 projections to 0.563 with 21 projections. Faint artifacts are observed in the background in all images. These are likely a result of how the data is interpolated onto the Cartesian grid. Additional artifacts are observed in the images with 89 and fewer projections. These appear as blotches.

method and density correction. Additional artifacts are observed as the number of projections in the reconstruction are reduced.

Figure A.4 compared the signal magnitude and phase of the reconstructed images with 55 projections. The magnitude images are similar between the uniform

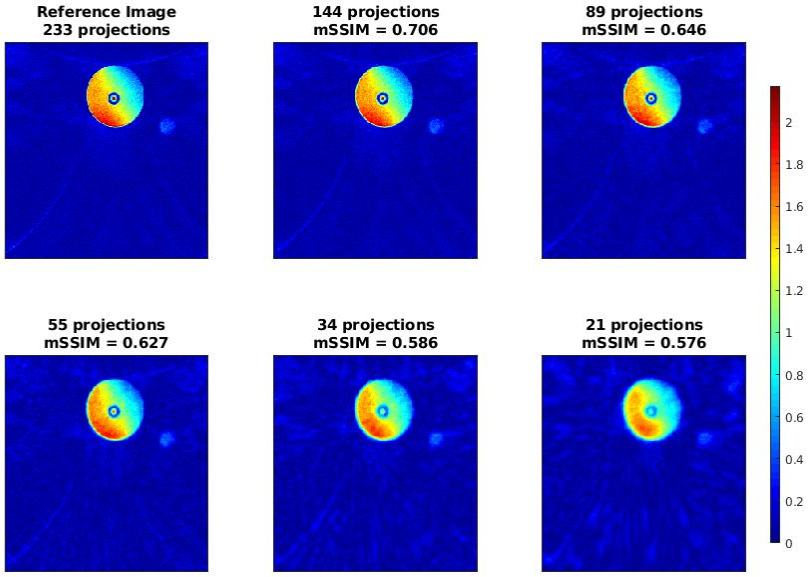

Figure A.2: Radial magnitude images created with Shepard's method of interpolation and Golden angle sampling (having an angular increment of 111.246^o). 233 (reference), 144, 89, 55, 34 or 21 projections are used in the reconstruction. Similar to the uniformly sampled data set, the images with 89 and 144 are visually similar to the reference image. With fewer projections, the images become blurry and the contrast between the capillary tube and surrounding phantom decreases. The mSSIM values, relative to the reference image, are listed in the title, and decreases from 0.706 with 144 projections to 0.576 with 21 projections. Additional background artifacts are observed in the images with 89 and fewer projections. They are more apparent in the images with 21 or 34 projections.

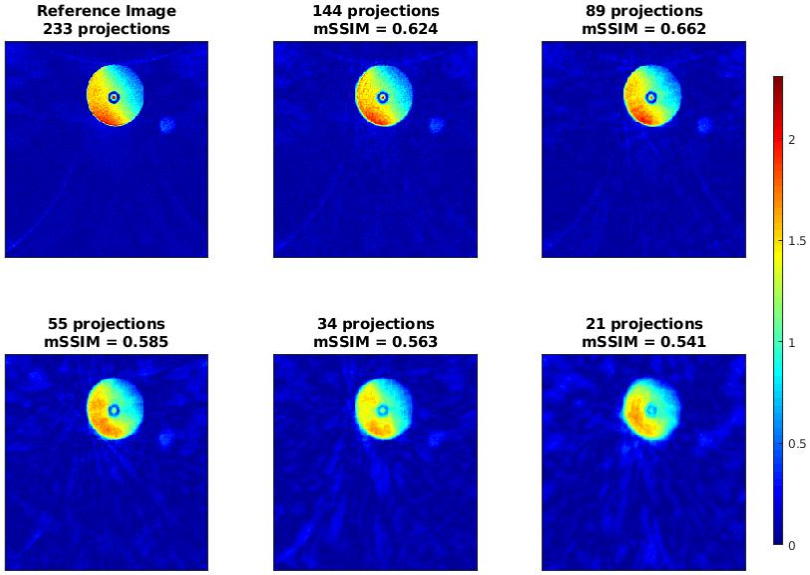

Figure A.3: Radial magnitude images created with Shepard's method of interpolation and randomly sampled data over the angular range of $0 - 180^o$. The images were reconsturcted with 233 (reference), 144, 89, 55, 34 or 21 projections. Only the image with 144 projections is visually similar to the reference image. As the number of projections drops from 89 to 21, image contrast between the capillary tube and the rest of the phantom decreases rapidly and edges are blurred. The external phantom to the right of the main one is visible in the images with at least 55 projections. Beyond this, it blends in with the additional image artifacts in the background. These artifacts are present in all images, but are more visually apparent as the number of projections is reduced. The mSSIM values listed in the titles decrease from 0.624 with 144 projections to 0.541 with 21 projections.

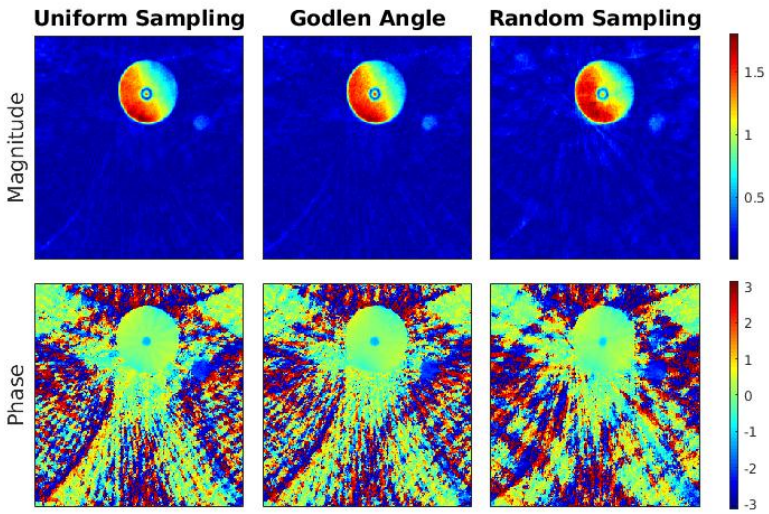

Figure A.4: Radial magnitude images created with Shepard's method of interpolation, 55 projections in the recontruction and uniform, Golden angle (angular increment 111.246^o) or random data sampling. The uniform and Golden angle sampling schemes produce a simlar images in terms of phantom edge sharpness, contrast between the main phantom and capillary tube, and structure of the artifacts. The artifacts appear as blurry curves, not the typical streaking artifacts seen in radial images. The intensity is low, but they are more apparent in the phase image. The randomly sampled image has a stronger presence of image artifacts and appears more blurred than the other two. This is likely a result of larger gaps near the centre of k-space that influence the image contrast.

and Golden angle sampled images, but inferior with random sampling (likely due to larger gaps in near the center of k-space where contrast information is stored). The phase of all images are similar. There are obvious curved artifacts originating from the phantom in the phase image.

A.2 Spatial-Temporal Constrained Reconstruction

Figures A.5, A.6, and A.7 show the reconstructed images using 233, 144, 89, 55, 34 or 21 projections, and using uniform, Golden angle or random sampling.

The STCR reconstructed images showed similarities to the reference image (233 projections) when at least 89 projections are used in the reconstruction for uniform and Golden angle sampling and 144 projections for random sampling. As the number of projections is reduced to 55 or fewer, the edges of the phantom became blurry and contrast between the capillary tube and the main phantom degrades. The small external phantom to the right is visible in all images. However, it starts to blend in with background image artifacts when 34 or 21 projections are used in the reconstruction for uniform and random sampling. The image set with Golden angle sampling has good visibility of the phantom down to 34 projections.

All images have two circular artifacts, the intersect with the edge of the phantom. These artifacts have a low magnitude, and seem to only affect the background. As the number of projections is reduced to 55 or less, additional artifacts appear. These artifacts appear as elongated spots that radiate outward from the phantom. Their presence is most noticeable in the images with 34 or 21 projections. The data sets with Golden angle or random sampling also show artifacts within the main phantom. These appear to be streaking artifacts, which originate at the capillary tube, and are easily observed in the top-right (low intensity) and lower-left (high intensity).

Figure A.8 shows the STCR magnitude and phase images reconstructed with 55 projections. In general, the images with uniform or Golden angle sampling provide similar quality, while the randomly sampled image has greater loss of contrast between the capillary tube and surrounding vessel and presence of artifacts in the background. The phase images are similar. All three sampling methods show radial streaks from the main phantom. The phase of the smaller phantom differs between the sampling method. However this is more likely a result of the imaging artifacts within the background.

A.3 Non-Equidistant Fast Fourier Transform

Radial images reconstructed with the NFFT algorithm are shown in Figures A.9, A.10, and A.11. The reconstructions used 233, 144, 89, 55, 34 or 21 projections, and one of uniform, Golden angle or random sampling.

NFFT images with at least 89 projections are visually similar with the reference

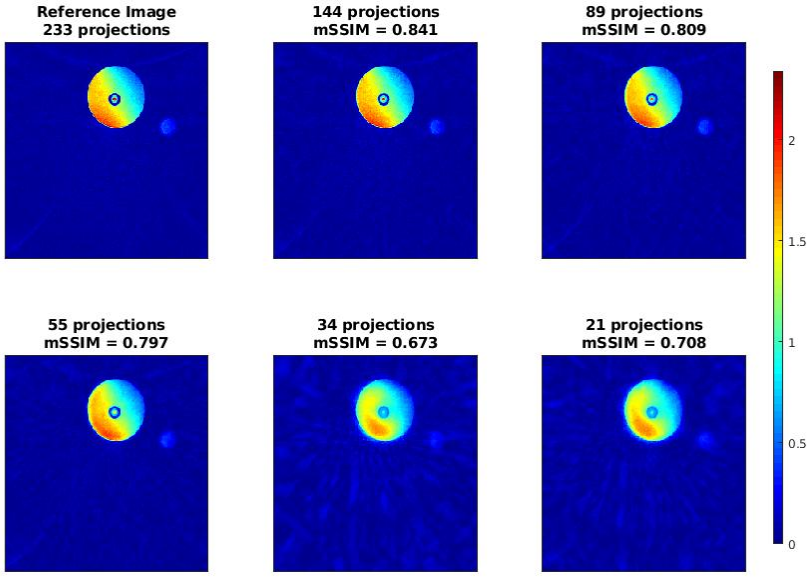

Figure A.5: STCR magnitude images reconstructed with 233 (reference), 144, 89, 55, 34 or 21 uniformly spaced projections. Visually, the images are comparable with the reference image when at least 89 projections are used in the reconstruction. Signal contrast between the capillary tube and the main phantom is reduced in all images, relative to the reference image. However the most dramatic loss of contrast is observed from 89 to 55 projections. Edge sharpness is good with 55 or more projections, then degrades significantly with 34 or 21 projections. The smaller external phantom, on the lower right side, is visible in all images, though the contrast is best with at lesat 55 projections. The mSSIM index, relative to the reference STCR image, gradually decreases from 0.841 with 144 projections to 0.708 fwith 21 projections. If the threshold for a clinical-quality image was set to 0.800, then the STCR reconstruction requires at least 89 projections.

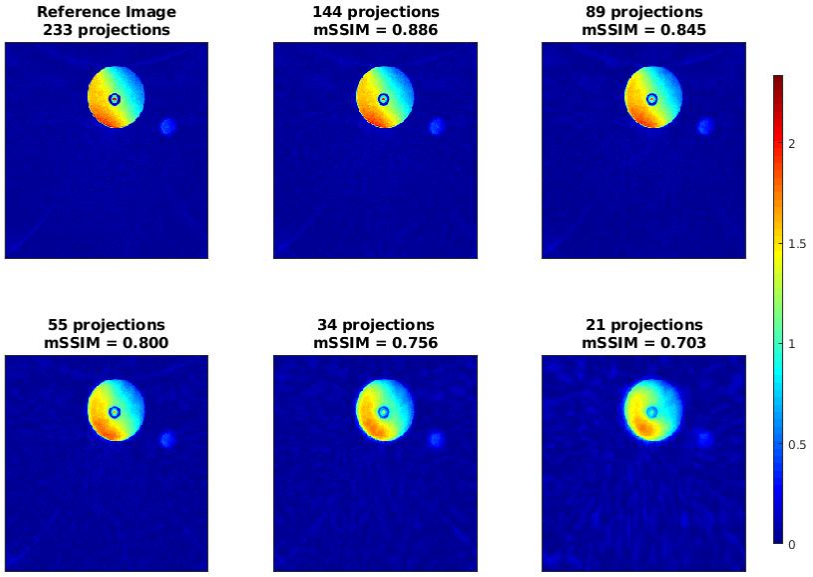

Figure A.6: STCR magnitude images reconstructed with 233 (reference), 144, 89, 55, 34 or 21 projections and Golden angle sampling (with an angular increment of 111.246^o). Visually, the images are comparable with the reference image when at least 89 projections are used in the reconstruction. As with the uniformly sampled data, the contrast between the capillary tube and the rest of the phantom degrades as the number of projections drops from 89 to 55 and the edges around the main phantom become blurry. The smaller external phantom is visible in all images, but is faint in the image with 21 projections. The mSSIM index gradually reduces from 0.886 with 144 projections to 0.703 with 21 projections. Images with 55 or more projections have an SSIM index exceeding 0.800.

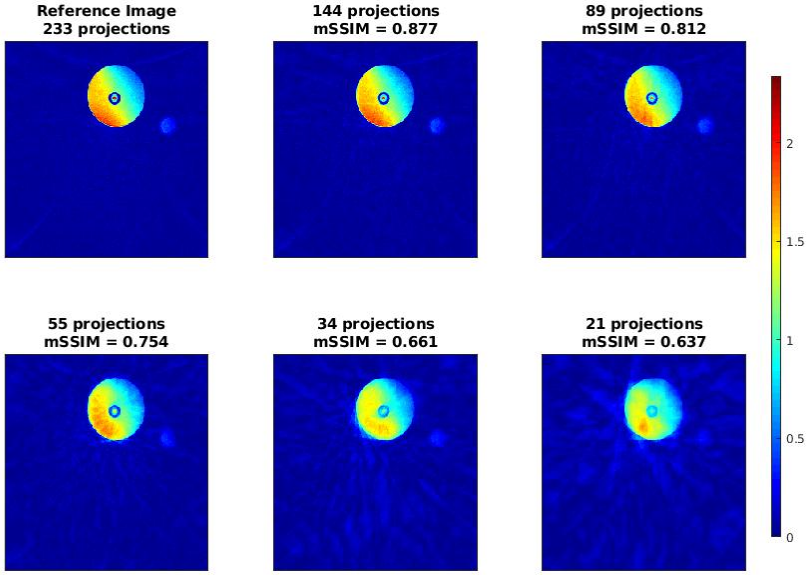

Figure A.7: STCR magnitude images reconstructed with 233 (reference), 144, 89, 55, 34 or 21 randomly selected projections over 180°. The image with 144 projections is comparable with the reference image, but as the number of projections is reduced, image contrast with the capillary tube and surrounding phantom is reduced and the edges of the phantom get blurry. Streaking artifacts are observed within the main phantom with 55 and fewer projections. The external phantom to the right is visible in all images, but with less contrast when 55 or fwere projections are used. The mSSIM index gradually reduces from 0.877 with 144 projections to 0.637 with 21 projections. Only the images with 89 and 144 projections have a mSSIM exceeding 0.800, and it has a sharp drop from 0.754 to 0.661 when the number of projections is reduced from 89 to 55.

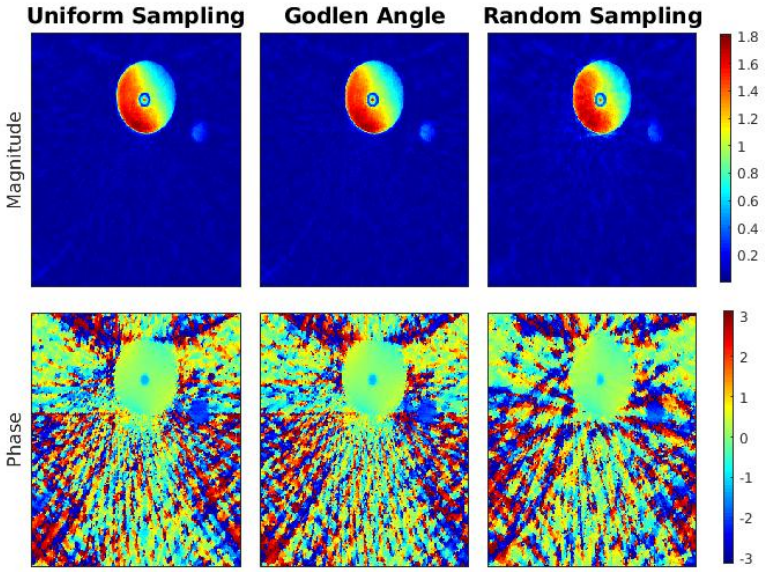

Figure A.8: Magnitude images reconstructed using Spatial-Temporal Constrained Reconstruction (STCR), 55 projections and uniform, Golden angle (angular increment 111.246^o) or random samlping. The uniform and Golden angle sampling schemes both produce an image of comparable quality (contrast, presence of artifacts). The randomly sampled image is more blurred, lower contrast and has a greater presence of artifacts. This likely results from the non-uniform sampling of k-space, resulting in larger gaps that contain image contrast and detail information.

images when uniform or Golden angle sampling were used. This was assessed by sharpness of the phantom edges, relative signal contrast between the capillary tube and the surrounding phantom, and visual appearance of image artifacts. Although the signal contrast was slightly lower for the image with 89 projections, the rest of the image seemed to compare well. This contrast was lost when 55 or fewer projections were used in the reconstruction. The image quality is poor for the images with 34 and 21 projections to the point that they are unusable. The edges of the phantom were significantly blurred and streaking artifacts are seen in the

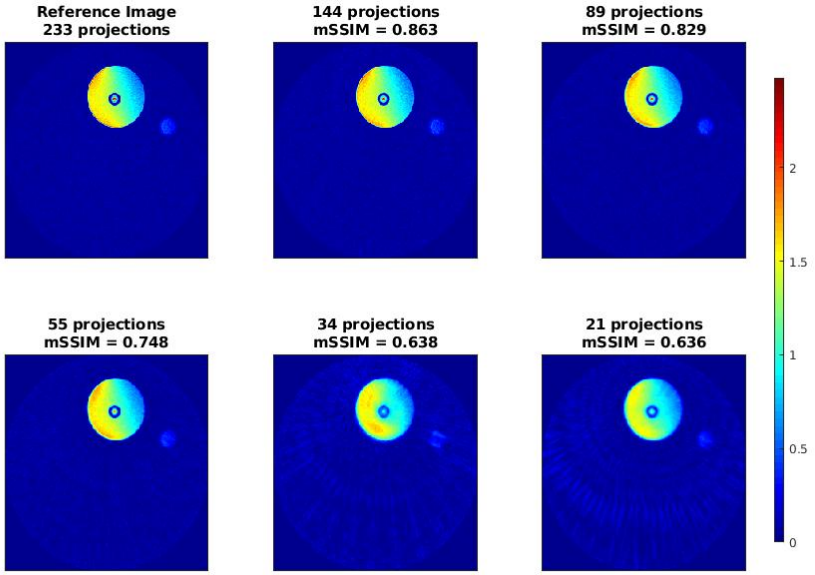

Figure A.9: NFFT magnitude images reconstructed with 233 (reference), 144, 89, 55, 34 or 21 uniformly spaced projections over 180°. Images with 89 and 144 projections are comparable with the reference radial image, having a mSSIM index of 0.829 and 0.863, respectively. Reducing this number to 55 resulted in loss of contrast between the capillary tube and surrounding phantom. With 34 or 21 projections, there is significant blurring of the phantom edges and significant loss of contrast between the capillary tube and surrounding phantom. Streaking artifacts are visually apparent in the images with 34 or 21 proejctions.

background. Random sampling was clearly inferior for this technique. The image quality degraded rapidly as fewer projections were used in the reconstruction, with none of the images resembling the reference NFFT image.

The NFFT magnitude images, reconstructed with 55 projections and uniform, Golden angle or random sampling, are shown in Figure A.12. The uniformly sampled and Golden angle images are comparable visually, and are of much higher quality than the randomly sampled image. The phase of the image is consistent between the three sampling methods, though all three have streaking artifacts and

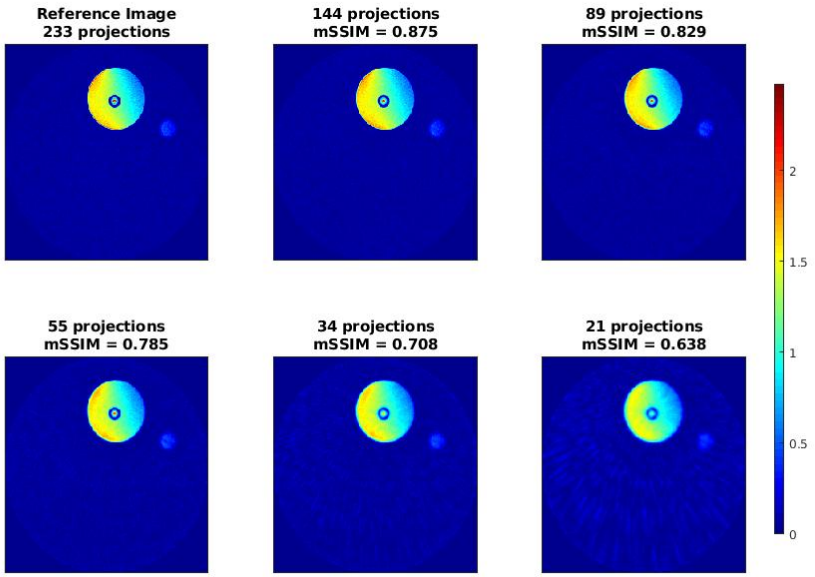

Figure A.10: NFFT magnitude images reconstructed with 233 (reference), 144, 89, 55, 34 or 21 projections, and Golden angle sampling. Images reconstructed with at least 55 projections are visually comparable with the reference image, though the contrast between the capillary tube and the surronding phantom is lost with 55 projections. Streaking artifacts are observed in the background as early as 55 projections, though they are of low intensity. Images with 34 and 21 projection are of low quality as the phantom edges are blurry, signal contrast of the capillary tube is lost and streaking artifacts are observed in the background. The images with at least 89 projections have a mSSIM value exceeding 0.800.

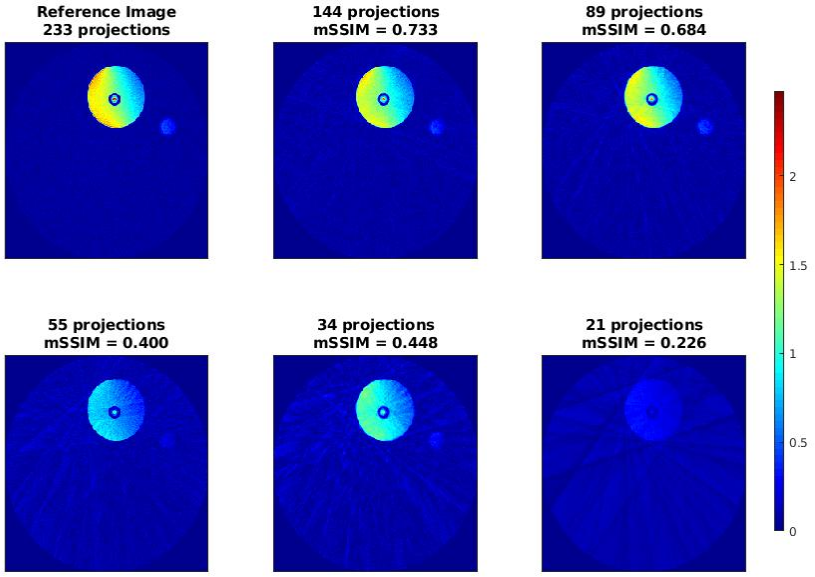

Figure A.11: NFFT magnitude images reconstructed with 233 (reference), 144, 89, 55, 34 or 21 randomly selected projections over 180°. The quality of the image degrades as fewer projections are used in the reconstruction. For this sampling method, no image resembles the reference NFFT image: the signal intensity is lower in all images, contrast of the capillary tube and surrounding phantom is lost and the edges of the phantom are blurry. The smaller phantom is observed in images with at least 34 projections, though the contrast with the background is low with 34 and 55 projections. Streaking artifacts are present in images with 89 and fewer projections, and can be seen in both the phantom and background. The mSSIM index is 0.733 with 144 projections and 0.684 with 89 projections. It drops significantly to 0.400 with 55 projections, meaning that this image is not of sufficient quality.

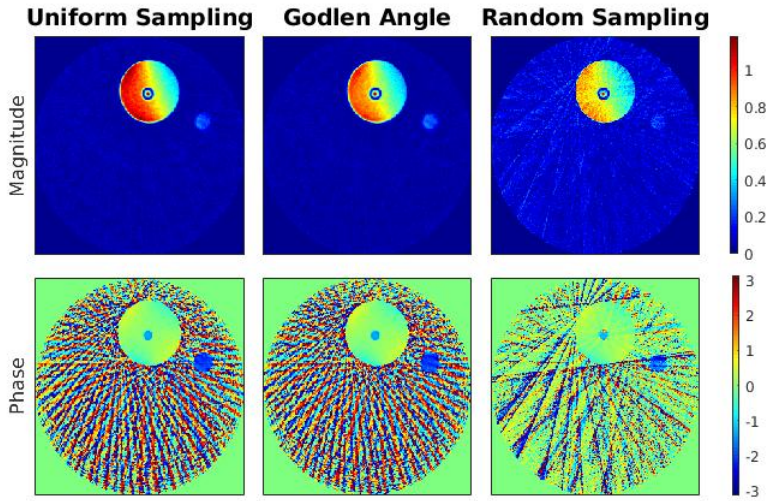

Figure A.12: Radial images reconstructed with the NFFT, 55 projections and uniform, Golden angle (angular increment 111.246^o) or random sampling. The images with uniform or Golden angle sampling are comparable, while the randomly sampled image appears blurry and suffers from image artifacts. The phase images look similar for all techniques, though the streaking artifacts in the background are more pronounced with random sampling. The phase of the smaller phantom is varied as a result of these artifacts.

affect the phase of the smaller side phantom.

Appendix B

Radial Acquisition Correction Techniques

B.1 Observed Issues with Radial Sampling

Theoretically, all radial samples should pass through the center of k-space. This is not guaranteed as magnetic field inhomogeneities, off-resonance effects, imperfect gradient profiles, scanner timing delays and residual eddy currents are all known to introduce errors in data positioning. This section will address common issues with radial data sampling and discuss methods to minimize or compensate for them.

A simple technique to correct for zeroth and first order phase issues is outlined in the paper by Ahn and Cho [167]. Their technique is based on the statistical phase properties and distributions of the image and provides a more accurate representation of the phase information. Examples include inversion recovery imaging, spectroscopic imaging, phase-modulated velocity imaging and fast imaging techniques that make use of the conjugate symmetry of the FID. Since the projection-based AIF measurement compared the background profile from an image to an individual projection, the phase data must be preserved.

Phase information may be distorted due to mis-adjustment of the reference phase, delays in the acquisition time, or be introduced by electronic filters. The correction provided by Ahn and Cho [167] involves two parts: first, the first-order phase distortions are addressed, then the zeroth-order phase distortions are

removed. The correction is applied to the MR image, not to the k-space data. The first-order correction factor, ε_1, is determined from the phase of the auto-correlation of the image, $F(x,y)$, between neighboring pixels in the direction of the read-encode gradient. For instance, if the read-encode is along the x-direction, then the x-directional auto-correlation is used. The image data is then multiplied by the correction factor $e^{-i\varepsilon_1 x}$. The zeroth-order correction is determined from the peak of the phase histogram of the first-order corrected image. The entire image is multiplied by the exponential of the zeroth-order conjugate phase.

B.1.1 Eddy Currents

Eddy currents are induced electric currents in the conducting structures of the MR scanner when changes in the amplitude of the gradient fields occur [189]. By Lenz's law, the eddy currents work against the original current and disturb the gradient field experienced by the sample [190]. Though they are often more severe in permanent magnets than in a superconducting magnet [189], significant artifacts and distortions can degrade the image quality at higher field strengths and when stronger, rapidly changing gradients are used [191]. The magnitude of the eddy currents decays in time, resulting in a temporally varying off-resonance effect. They are observed as streaking artifacts in the reconstructed image, originating from the object.

Most clinical and research scanners are equipped with active shielding coils, which are designed to minimize fringe fields [189], though further correction is often required. An easily implemented improvement is to add gradient pre-emphasis lobes to the gradient waveform. However, these only accommodate a small number of time constants, so eddy currents can persist at short echo times [191]. Linear eddy current effects present as k-space trajectory distortions (often along the read-encode direction), while B_o eddy currents provide unwanted phase accumulation. Higher order terms and cross-talk have minimal effects on the image and are often ignored [190].

Compensation for eddy currents is essential in under-sampled, non-Cartesian FLASH acquisitions at higher field strengths due to the rapidly changing strong gradients. Typical eddy current models represent the system response as a sum of

decaying exponential functions, and convolve this with the time-varying gradient waveform. Ma et al. [189] suggested a model that compensates for both zeroth-order (spatially invariant) and first-order eddy currents. Their method calculates the time derivative of the phase of the echo after a known delay time (range 0-1 s).

B.1.2 Gradient Timing Delay Correction

Projection data is acquired as a series of radial spokes in k-space, consisting of N_r readout points. Typically, the readout is symmetric, in which the center of k-space is acquired as the $N_r/2$ readout point if N_r is even, or $(N_r \pm 1)/2$ readout if N_r is odd. But if the gradient timing is miscalculated, such that the actual start time of the gradient readout is different from the requested time, the center of k-space will be shifted and thus changing the effective echo time. The shift can be different between the three gradient channels, resulting in an angular-dependent shift. This would cause a blurring of the center of k-space and blurring in the reconstructed image if not corrected.

Peters et al. [178] introduced a one-time calibration to apply to future radial scans. Their technique involves acquiring equally spaced radial projections over 180° on a homogeneous spherical phantom placed at the scanner isocentre. The delays can be determined from the relative shift of the maximum from the expected location. Peters achieved this by applying a Fourier transform to each projection, then determining the shift with the procedure outlined by Ahn and Cho [167]. They assume that there are no other sources of linear phase shift due to the object or the imaging procedure. The shift is then converted into a time delay.

Peters suggests fitting a sinusoidal curve to the delay vs angle plot. The data at $0^o/180^o$ and 90° will relay information about the two gradient channels. By comparing the results from two slice orientations, the delay time may be verified. From that information, the compensatory gradient area can be calculated. This area is then added to the pre and rephasing gradient areas. The compensation areas only need to be measured once for a gradient set. For future use, the areas for each angle could be placed in a look up table.

Peters measured the timing delays in phantom to be as great as 5 μs. However, after adding the compensatory gradient areas, the time delay was reduced to less

than 1 μs, and image artifacts were greatly reduced in both phantom and volunteer data.

B.1.3 Trajectory Measurements

The trajectory of MR data is sensitive to imperfections in the gradient amplifier performance, readout timing and eddy currents induced by the gradient pulse [192, 193]. In their presence, the spatial locations of the data points are not consistent with expectations, which leads to image rotation and artifacts [194]. As scanner demands (stronger gradients and faster acquisition times) increase and the trajectory becomes more complicated - such as spiral imaging - knowing the exact location where the data was collected is essential.

Several techniques have been presented to measure the k-space trajectory. Generally, the pulse sequence is altered such that slice selection is in the same direction as the read encode gradient, and often limits the measurement to a single physical gradient channel at a time for accuracy (to avoid data sampling in areas with little signal). For instance, if measuring the trajectory along the physical x-gradient, the slice and read encode gradients are both oriented in that direction. This requirement limits slice selection to coronal, sagittal or axial orientations. Only one gradient channel is on during the acquisition, which occurs while the read encode gradient is played out. Once the trajectory is known, the information may be used in the image reconstruction to reduce artifacts (blurring, rotation, intensity variations, etc.).

The next two sections will discuss the trajectory measurements introduced by Zhang et al., Beaumont et al. and Latta et al.

Trajectory Measurement using Phase Differences from Adjacent Images

Zhang et al. proposed a technique that determines the actual k-space trajectory using the phase difference between acquired MR signals of adjacent slices along the gradient axis of interest. A homogeneous spherical object should be used for this measurement, as spatially varying susceptibility induced magnetic field inhomogeneities could introduce errors in the measurement. The results of their study showed that the trajectory could be accurately determined and provided significant

improvements in the reconstructed image.

Beaumont et al. [194] provide an extension to the technique introduced by Zhang et al. [192]. They identified a limitation at high k-space values where the signal is close to the noise floor. This caused unreliable data for measuring the trajectory. Beaumont suggested acquiring three trajectories measurements, with two offset by a known amount, and averaging them. The pulse sequence is similar to that from Zhang, but includes an added gradient area along the gradient channel of interest prior to the acquisition window. This, in effect, forces the center of k-space to be shifted such that the maximum can cover an area where a signal null was present.

Most slice profiles are symmetric, so the the critical points where a signal null occurs will be symmetric about the center. Beaumont's technique involves the acquisition of three trajectories; one with no shift (0), and two offset measurements (+G and -G). Their results showed artifacts in the trajectory measurements at the nulls when the added gradient was not applied. But after averaging the three signals (-G, 0 and +G), the trajectory was much cleaner and did not present the same artifacts. Images without correction appeared to be rotated by a few degrees relative to those corrected with the trajectory. They predicted that this was due to an uncontrolled delay between the gradient-waveform and data acquisition. They also found that the trajectories appeared compressed slightly, likely due to a mis-setting of the gradient calibration setting or eddy currents.

Trajectory Measurement Proposed by Latta el al

An alternative approach is to measure the trajectory with a spin-echo, while utilizing a phase-encode gradient [193]. Their method maps the point-by-point k-space trajectory of the examined gradient waveform (X, Y or Z). Slice-selection is done parallel to the measured gradient axis. After slice-excitation, the phase-encoding gradient, G_{PE}, is applied to introduce spin de-phasing along the chosen gradient direction prior to the measurement. The phase encoding step is performed in such a way that the measured k-space trajectory crosses the origin at different times, as observed through the echo position. The measurement is completed by turning on the desired gradient waveform, G_W, simultaneously with the acquisition window.

The trajectory is reconstructed from a plot of the the applied pre-phased gradient area, G_{PE}, and the estimated crossing of the k-space origin. This technique is optimized for short readout gradients, such as radial acquisition. Longer sequences (spiral imaging) would have limited scope.

Latta suggests using an adaptive phase encoding gradient such that the trajectory has uniform spacing. He argues that the data along the ramp-up and ramp-down sections of the G_W waveform are under-sampled if the phase encoding steps are all equally spaced in area. The adaptive phase encoding gradient is outlined in their paper. In addition, they used a variable echo time to ensure that all off-resonance effects were compensated for by adjusting the timing between the excitation pulse and the refocusing RF pulse.

Latta tested their method on phantom and healthy volunteers. The trajectory measurements were successfully applied to reconstruct a radial 2-D ultra-short echo time (UTE) image with significantly improved quality. Prior to correction, the UTE images showed ghosting artifacts. The images were further improved with gradient delay and linear eddy current parametric model corrections. These were applied to compensate for missing data at the gradient onset and also reduce the number of measurements required to perform the correction. The technique was also shown to work well on off-center images of a patient knee offset by 70 mm from the scanners isocentre.

B.2 Attempts at Correcting the Acquired Radial Data

The radial projection-based AIF measured at the end of Chapter 6 showed an angular dependence on the measured concentration of Gd-DTPA. The organization of this Appendix follows the order in which the correction attempts were made. Post-processing corrections were done first, in hopes of reducing the phase baseline to a point that the AIF may be used for modeling. The focus then shifted to improving the quality of the acquired data.

B.2.1 Post-processing k-Space to Center Echo

Having identified the angular dependent artifact, we tested three echo correction techniques. The first two involved a global shift of all projections by either an in-

teger or a sub-pixel amount. The global integer shift involves finding the pixel at which the greatest signal intensity was achieved, and calculating the mean position across all angles. Next, all of the projections were shifted by $round(N_{readenc}/2) - N_{pixelofecho}$. For the sub-pixel shift, the data was up-sampled by a factor of 10, and the position of the echo was determined from the maximum signal intensity. The projections were globally shifted to center the data in k-space, before down-sampling back to its original size. The third technique redefined the locations of the nodes in the NFFT reconstruction so that the maximum in projections k-space coincided with the center of k-space for the image. To accomplish this, we calculate the difference in the expected and actual positions of the echo for each projection and then update the NFFT node positions with that information. Finally, the phase of the echo was reset to 0 radians. The resulting vessel signal and AIFs are summarized in Figure B.1 before and after applying the three correction techniques.

The phase baseline of the corrected AIF varies between the three correction techniques, but the amplitude of the phase fluctuations are significantly reduced. These results strongly suggest that a k-space correction should be applied to the k-space data prior to proceeding with the projection-based measurement. The small fluctuations that persist could be a consequence of imperfect centering of the echo.

Quantitatively, the phase of the uncorrected AIF covers the range -3.069 to -0.176 rad. It also appears to have a rapid phase jump, which is a consequence of vessels spatial location within the projection. Applying either the global integer or sub-pixel shift significantly reduced the phase fluctuations (range -1.652 to -1.010 rad and -1.576 to - 1.133 rad, respectively). The baseline phase still has the step in phase, but the difference is a factor of 0.222 and 0.153 of that of the uncorrected curve. Adjusting the positions of the NFFT nodes significantly improved the quality of the baseline as well. However, the phase fluctuations were greater with a range from -1.813 to -0.972 rad. From this analysis, it appears that the sub-pixel shift provides the best results, followed by the global integer shift. The phase fluctuations are not desirable, and should be further reduced if possible.

The NFFT images from the above analysis are compared in Figure B.2 to gain a better understanding of what causes the angular phase dependence. The magnitude image of the uncorrected data has a hot spot at the center of the phantom, which is not as dominant after applying a centering correction. Since the background data

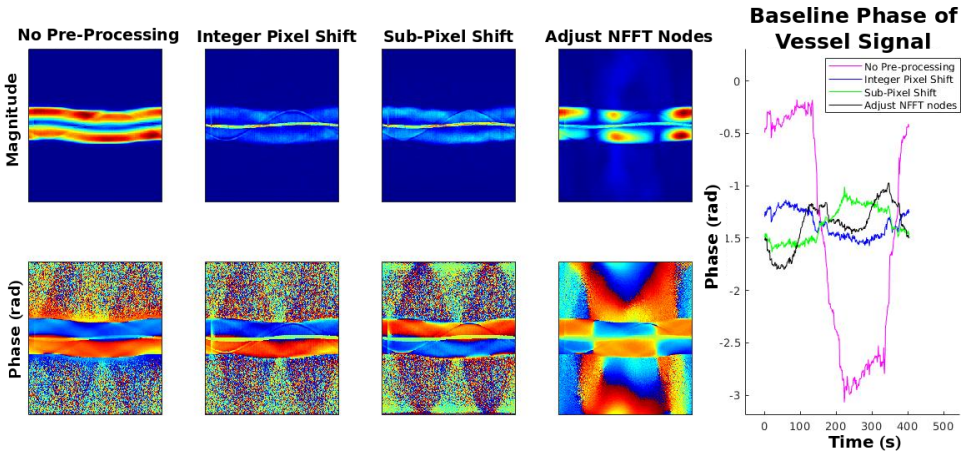

Figure B.1: Magnitude and Phase of the vessel data (acquired projections - background), and the average signal phase within the vessel (sorted by angle), for four situations: 1) no pre-processing of the k-space data of the projections, 2) applying a global integer pixel shift, 3) applying a global sub-integer shift, and 4) adjusting the NFFT node positions based on the expected echo position. The results show that the acquired k-space is not acquired as expected, and requires some post-processing before carrying out the projection based AIF measurement. Of the techniques investigated, a global pixel shift (either sub-pixel or integer value) performs best.

is determined from the summation of many complex signals, regions with higher signal intensity contribute more strongly to the summation. As a result, the phase of the background projection could be artificially biased towards the phase of the hot spot signal. The hot spot shifted towards the bottom of the phantom when a global shift (integer or sub-pixel) was applied to the data. This would affect the background signal differently at each angle as the strongest signal is off-center in image-space. Since the vessel signal is a difference between the acquired data and the background signal, this angular signal difference could carry a bias through the remainder of the AIF estimation. The NFFT images from the two shifted cases were similar, which would explain the similar background measurements. When the NFFT nodes were adjusted, the hot spot shrunk and shifted to the lower right-hand side of the phantom. The superior region of the phantom has hypo-intense

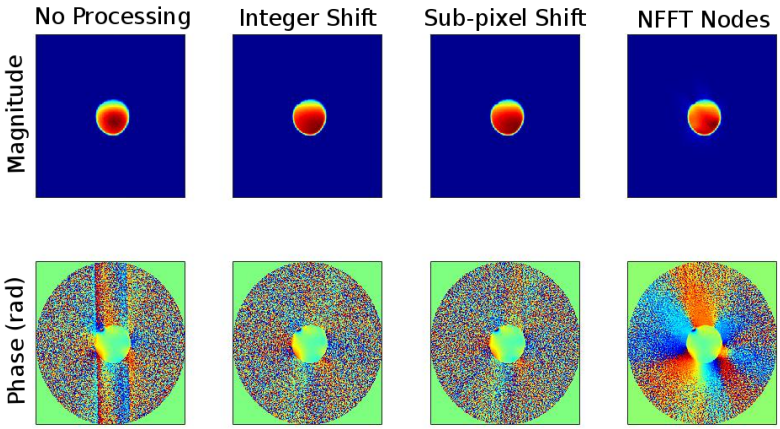

Figure B.2: Magnitude and phase of the reconstructed NFFT image of a cylindrical phantom. The first column shows the reconstructed images when the raw projection data is used. The remaining three columns correspond to one of the following corrections: global integer pixel shift, global sub-pixel shift, or adjusting the locations of the NFFT nodes. Streaking artifacts are observed in all cases, though they are least impactful when the global pixel shift is applied (integer or sub-pixel).

signal relative to the other three cases. This again will impact the AIF measurement in an angular dependent manner.

The second row shows the phase of the NFFT images. Within the phantom, the phase is similar in all cases, although there are slight differences along the perimeter of the phantom. In general, the phase has three hot-spots: two on the left-hand side and a smaller on the lower right-hand side. The phase of the uncorrected data set shows a distinct vertical streak. Similarly, the correction with adjustments to the NFFT nodes has obvious streaks in the background. These originate from the phase hot spots in the phantom. Even though the signal intensity is lower in the background, these artifacts could have an impact on the background summation as phase of the complex signal of these voxels all point in the same direction. The phase of the background signal would again have an angular dependence as the summation will have varying amounts of vectors in the 'hot phase' and 'cold phase' setting.

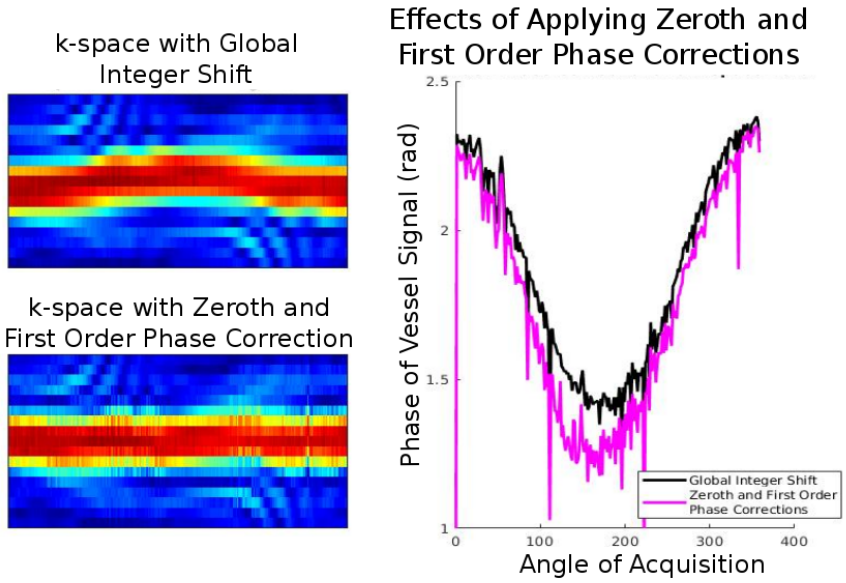

Figure B.3: Effects on the baseline phase after centering the k-space data with one of two techniques. a) shows the k-space sinogram for the correction with a global phase shift and setting the phase of the echo to 0 rad, with the corresponding phase baseline in black (c). b) is the k-space sinogram for the correction following the methods of Ahn and Cho, which results in the magenta curve. The k-space sinograms have distinct differences in appearance, but provide a similar phase baseline. For this experiment, the global phase shift performs slightly better than the first order phase shift.

Ahn and Cho [167] outline a technique that corrects radial data for zeroth and first order phase errors. The effectiveness of the first-order phase shift had conflicting results with our data. In some cases, it significantly reduced the phase baseline, while in others it had a limited effect. This illustrates an instability in the radial data acquisition that needs to be addressed in future studies. Figures B.3 and B.4 show data from two experiments performed on different days.

Figure B.3 compares k-space and the baseline phase of the projection-based AIF after centering the data with two techniques. Figure B.3a represents the k-space sinogram after applying a global integer shift to better center the k-space data, and then a zeroth order phase correction to set the phase of the echo to 0 rad.

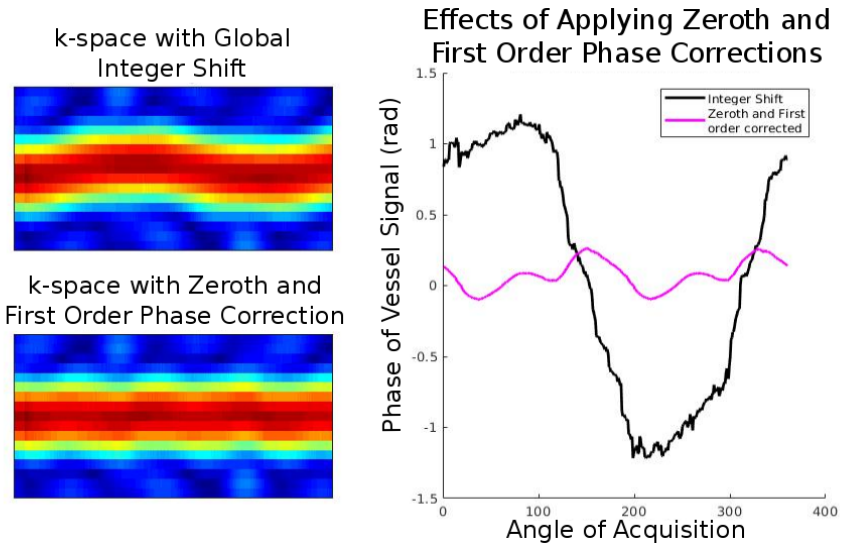

Figure B.4: Effects on the baseline phase after centering the k-space data with one of two techniques. a) shows the k-space sinogram for the correction with a global phase shift and setting the phase of the echo to 0 rad, with the corresponding phase baseline in black (c). b) is the k-space sinogram for the correction following the methods of Ahn and Cho, which results in the magenta curve. For this data set, the first order phase shift significantly improves the phase-baseline, reducing the range of phase from 1.21 to 0.181 rad.

The sinogram has an oscillating pattern with an amplitude of 2 pixels. The resulting phase baseline covers a range of 1.415 to 2.338 rad. Figure B.3b shows the k-space data after a first (shift determined from image-space data) and zeroth order phase correction [167]. The k-space sinogram no longer had a sinusoidal pattern, though the edges appeared jagged and the amplitude of the echo varied with angle. When put into the NFFT reconstruction, this would put more emphasis on some projections over others. The phase baseline was noisier than with the global shift, and covered a larger range of 1.180 to 2.349 rad.

The data set used in Figure B.4 was significantly improved with the first order phase correction. Similar to the previous example, the k-space echo was centered with either a global phase shift and zeroth order phase correction, or following the methods of Ahn and Cho. The k-space sinogram in Figure B.4a again has an os-

cillating pattern with an amplitude of 2 pixels. The resulting phase baseline (black curve) covers a range of 1.21 radians (from -1.217 to 1.208 radians). The k-space sinogram in Figure B.4b still has an oscillating pattern, but with a much smaller amplitude. In addition, the signal intensity at the center is more uniform across all angles. In contrast to Figure B.3, the range of the phase baseline was significantly reduced to 0.181 radians after (range -0.099 to 0.262 radians). Interestingly, the baseline phase with the first order correction appears to be repetitive over 180° instead of 360° with the global phase shift. This could be a consequence of the correction, in which we take the auto correlation of a projection with its conjugate, shifted by one pixel.

The effectiveness of the first-order phase correction could be related to how closely the echo approaches the center of k-space. This may be observed from the strength of the signal at the echo in the two examples. When the signal intensity is more uniform at the echo, the phase baseline is significantly improved. In addition, the transition of signal between consecutive angles is smoother; not having rough edges like the first example. Despite having mixed results with the first-order phase correction, a majority of data sets benefit from it. As such, it is recommended to apply both zeroth and first-order corrections to k-space. However it is important that the echo passes as close as possible to the center of k-space. This may be achieved by ensuring a good magnetic field shim prior to data acquisition, or through minimizing eddy currents, gradient mis-timing effects and deviations from the expected trajectory through k-space. These techniques will be discussed shortly.

Figure B.5 takes the investigation further by adding in sinograms of the real and imaginary data. The top row shows the signal of the acquired projections after re-centering k-space with a global phase shift and setting the phase of the echo to 0 rad. The second row is the background profiles. This is calculated as the projection of 233 NFFT radial reconstructions - all using the same data, but adjusting the angle of acquisition by $-I \cdot 360/233$, where I is an integer from $1-233$ - after removing the signal from the vessel. The imaginary data of the acquired projections has a hot and cold-signal region in the later angles of acquisition, which is not observed as strongly in the background profiles. This is an effect of the NFFT taking data over the full 2π radians range, and thereby averaging out the hyper-intense regions. This presents as two distinct regions in the background profiles

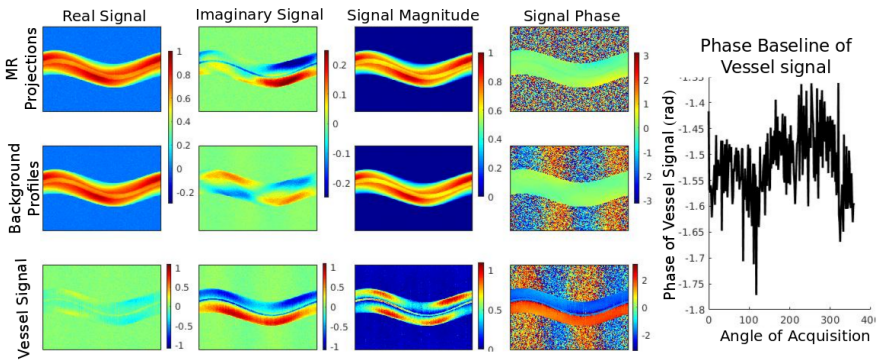

Figure B.5: Real, imaginary, magnitude and phase signal of the acquired projection profiles (first row), the background profiles from the NFFT images (second row) and the vessel signal (third row). The real and magnitude data appear as expected, with slowly varying signal intensity with angle. However, the imaginary data shows a hot and cold spot from projections 130 to 215. This affects the phase of these projections, and hence will lead to phase fluctuations in the AIF.

with hot/cold spots, separated by π radians.

For the projection-based AIF to be accurate, the signal should be consistent between the two rows. This is evaluated by taking the difference between the two, the so called vessel signal. Ideally, only those pixels associated with the vessel should have a significant magnitude, while the remainder of the image is noise. However, the results from this example show that there are slight differences in the real and imaginary signal, which in effect carries through to the magnitude and phase data. Most notable, is the higher signal intensity hot/cold spots of the imaginary data. The artifact appears as two distinct regions of high and low-intensity signal, in which the signal magnitude is comparable in the upper and lower portions of the phantom, but the phase differs.

The two distinct phase bands in the vessel signal correlate well with the signal difference in the imaginary signal. Although the real signal has slight differences with angle (that is along the x-axis), it does not impact the phase as significantly due to the lower intensity. The location of the vessel relative to these phase bands will dramatically impact the baseline phase. A vessel that is located near the center

of the phantom will have a much smaller baseline phase range compared to a vessel that is located closer to the edge of the phantom and passes through both phase bands. For the example shown, the vessel fortunately falls near the center of the phantom, and does not cross between the two phase bands. As a result, the phase fluctuation is small, covering 0.402 rad (range -1.752 to -1.350 rad).

The fact that the hyper-intense hot and cold spots in the imaginary signal occur only in the regions from π-2π rad is problematic. Typically a phase gradient in the image-space is indicative of a shift in k-space. This could suggest that a global pixel shift is not sufficient in centering k-space; but instead the global pixel shift could be done for data from 0-π rad and another from π-2π. NFFT images were reconstructed with half of the data, and provided AIF curves with less phase fluctuations. This could be a short term fix, but essentially ignores the underlying issue altogether. An alternative is to average parallel opposed projections together to smooth out inconsistencies in acquiring data π radians apart. This would reduce the temporal resolution by a factor of 2. Depending on the maximum rate of contrast changes in the vessel of interest, a lower temporal resolution may not be detrimental to the AIF measurement.

B.2.2 Effects of NFFT Node Prescription

In this study, the acquired projections are replaced with projections from one of the reconstructed NFFT image. The Radon transform was applied to a pre-injection NFFT image for 233 equally spaced angles (i.e. angular increment $360/233^o$). Since the projections are all derived from one image, signal inconsistencies from data acquired from parallel-opposed directions is minimized. The projection-based AIF method was applied to the NFFT-derived projections. This involved a second NFFT reconstruction, zeroing out the signal from the vessel, then taking the difference of the projection and background signals. The results of this study established an estimate on the impacts imperfect echo centering can have on the projection-based AIF measurement. The results are summarized in Figure B.6. The first column of the figure shows the NFFT-derived projections, the second column for the background signal from the NFFT reconstruction with the NFFT-derived projection, the third column is the difference between the projections and background,

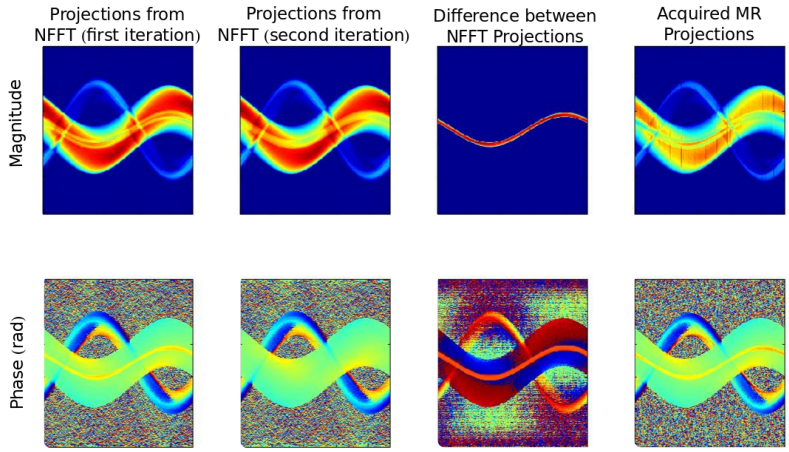

Figure B.6: The radial projection-based AIF was calculated from an idealized data set, in which the input data are projections of the original NFFT images for 233 unique equi-distant angles. After subtracting the background from the input projections, a near-zero signal intensity was observed in the main phantom.

and the fourth is the acquired projections as a reference.

The results show much greater consistency between the projections of the NFFT images and the corresponding background profiles. The vessel signal (third column) has a narrow high intensity band through the center that correlates with the capillary tube of the phantom, while the rest of the image has significantly lower signal intensity. The phase of the vessel signal still has a banding structure. Though the phase of the bands appears to flip after 180°, the signal intensity is negligible relative to that of the vessel. The phase of the vessel is stable, fluctuating between -1.397 to -1.376 rad. This is a difference of 0.016 rad, compared to 0.402 rad with the acquired data, or an 25-fold improvement.

The results of this analysis showcase the effects imperfect MR data can have on the AIF measurement. It is essential to minimize errors in the data acquisition, as post-processing of the projection data is limited to shifting it along the readout direction. The remainder of the chapter explores techniques that could improve the data quality.

B.3 Pre-Acquisition Techniques to Correct Radial Data

B.3.1 Magnetic Field Shimming

A common issue in MR imaging is B_o inhomogeneities. These can be minimized with active shimming before starting the experiment. Figure B.7 shows the k-space and corresponding projection sinograms for a good and poor shim at two different echo times. The magnetic field was shimmed up to the second order prior to the start of the experiment. This state is defined as the good shim. The poor shim manually adjusted the strengths of the first order shim gradients by a small amount.

With the poor shim, the echo is missed entirely at some angles, resulting in severe signal loss in the projection signal. Surprisingly, acquiring the echo early/late by 5 readout positions in k-space only had a minor impact on the NFFT image. This includes a 2 pixel shift to the left, a lower maximum signal intensity and reduced contrast of the capillary tube with the poor shim. The signal phase of both images were similar. Despite the minimal effect on the NFFT images, the poor shim affects the projection profiles significantly, particularly the signal magnitude. Due to the signal magnitude differences, the vessel signal will be greatly influenced by the background. This could lead to an inaccurate AIF measurement.

The results of this analysis suggests that the quality of the NFFT reconstruction is somewhat robust to imperfect k-space data. However, it is recommended to shim the magnet prior to the start of the experiment if the projection-based AIF measurement is to be accurate.

Gradient Timing Delays

A majority of pulse sequences are designed to have the echo occur at the center of the acquisition window. For this to happen, the gradient area of the pre-wind gradient must be exactly equal to the acquisition gradient area at the center of the readout. However, the echo can occur early or late due to gradient mis-timings. The mis-timing may result from a delay in the gradient ramp up/down or from a calculation error in the gradients strengths. Figure B.9 shows how a small change in the gradient strength impact the location of the echo. Trim 4 describes the percentage strength (maximum 100%) of the pre-wind gradient, and trim 5 is the gradient ap-

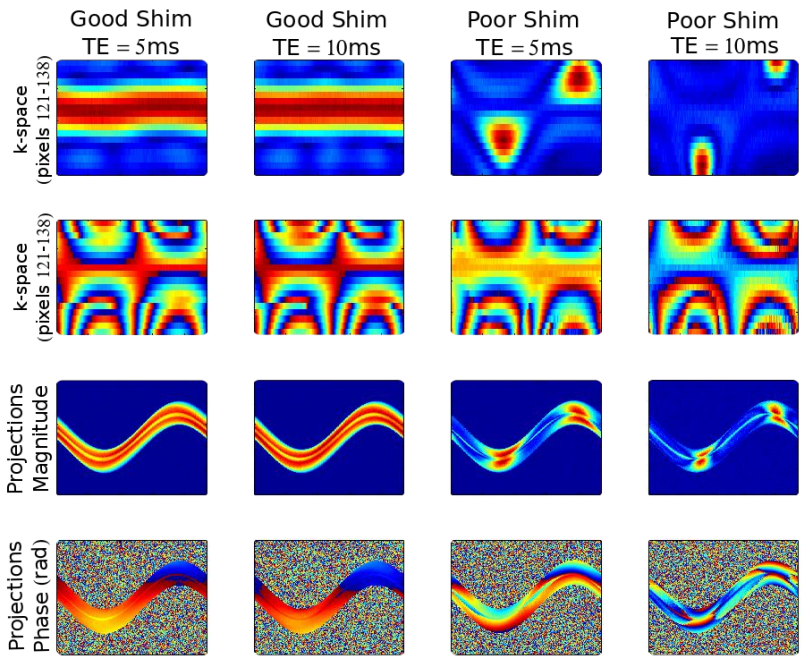

Figure B.7: k-Space and projection data with a good shim and poor shim. Rows one and two are the signal magnitude and phase of the k-space data, while rows three and four are the signal magnitude and phase of the projections. The figure shows that the good shim centers the echo effectively, but with a phase off-set. With a poor shim, the center of k-space may be missed at some angles. This impacts the appearance (magnitude and phase) of the projections, making the data unusable for the projection-based AIF measurment.

plied during the acquisition (see Figure B.8). Here, trim is the term used by Bruker to describe the percentage strength of the gradient, with the maximum being 100%.

The left plot in the Figure shows how the echo location varies with angle of acquisition after adjusting the trim values. The echo does not refocus at the same point globally. However, the shape is consistent between all data sets, just shifted by a couple pixels as determined by the relative change in the gradient areas. The echo location seems to follow a similar trajectory between $0-180^o$ and $180-360^o$, but flipped after 180°. The difference is about 0.5 pixels and may be related to a

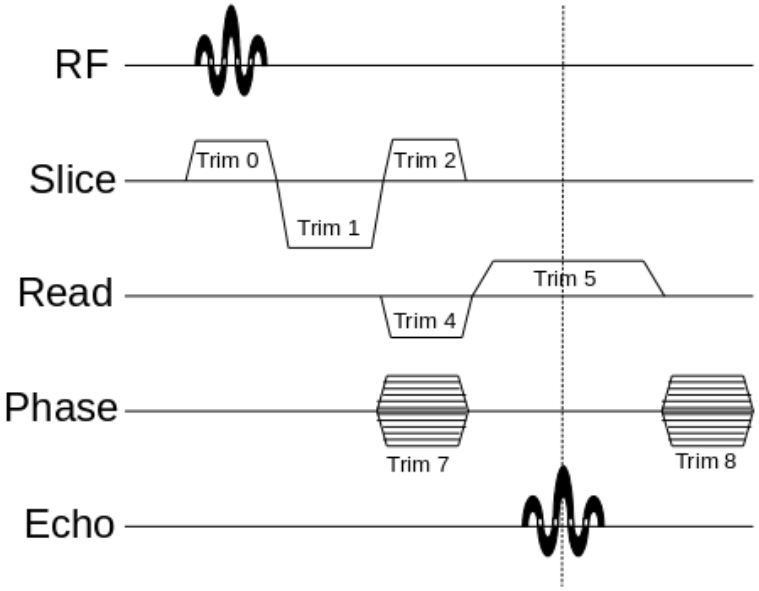

Figure B.8: Pulse Sequence for Radial Projection-based AIF showing trim definition. The echo position is dependent on the relative strengths of trims 4 and 5.

mis-calculation in one of the gradient areas. The plot on the right side shows the echo location after averaging the data from similar trim adjustment, but opposite signs.

If the mis-calculation is primarily along the gradient of the readout, the global pixel shift may be be sufficient for centering the echo. As long as the global pixel shift is small, shifting a couple pixels at the edge of k-space to the opposite side (as the circshift function in Matlab does) should not significantly affect the image as the magnitude is near zero. For the data sets in this analysis, the echo location is offset by at most 8 pixels. Since the readout length is 256 samples, this is not expected to impact the reconstructed image as the signal intensity is very close to 0 at the ends of k-space. However, the missing data could be copied from the

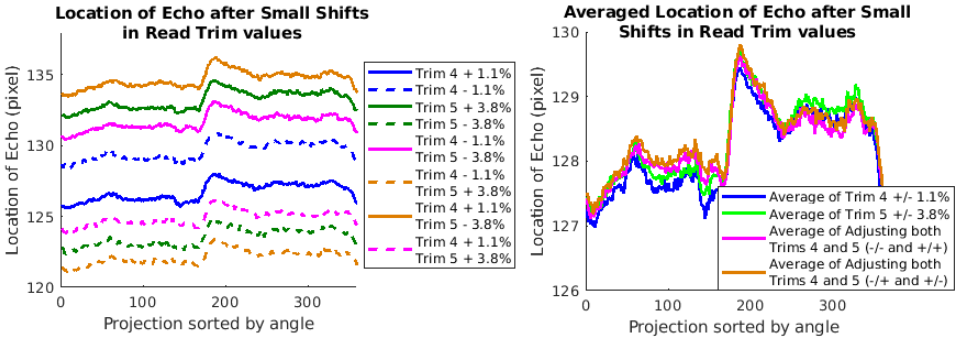

Figure B.9: Echo position after introducing small changes in the gradient strengths in the readout direction (trim 4 is the prewind and trim 5 is the readout). The changes were equivalent to a 1.1 or 3.8% change in the gradient strength. The plot on the left shows the angular dependence on the echo position before attempting to center the echo. The shape of the angular dependence is similar for all cases. The right side figure shows the average echo position after averaging the data with similar changes in the trim values (positive vs. negative).

acquired side, with a phase adjustment, if required.

Any acquisition that uses radial or spiral sampling will require two or more physical gradients for data sampling. The physical gradients are all independent of one another, so mis-timing artifact will affect each radial trajectory differently. This means that the echo location would have an angular dependence, which is repetitive over 180°. If both gradients are affected, then the proximity to the center of k-space will have an angular dependence.

As described in [178], the echoes may refocus along an ellipsoid centered at the center of k-space where all the contrast information is stored. This can have dramatic effects on the image quality if the timing delay is significant (more than a couple pixels). If the projection-based AIF uses only a single angle of acquisition, each projection will be affected identically. If only one physical gradient is used for the readout, then the projection should pass through the center of k-space at some point. The timing delay will be determined from how far off-set the echo occurs from expectations.

Radial sampling has the benefit that two physical gradients are used. It is then possible to track the echo position, and assess how it changes with the angle of

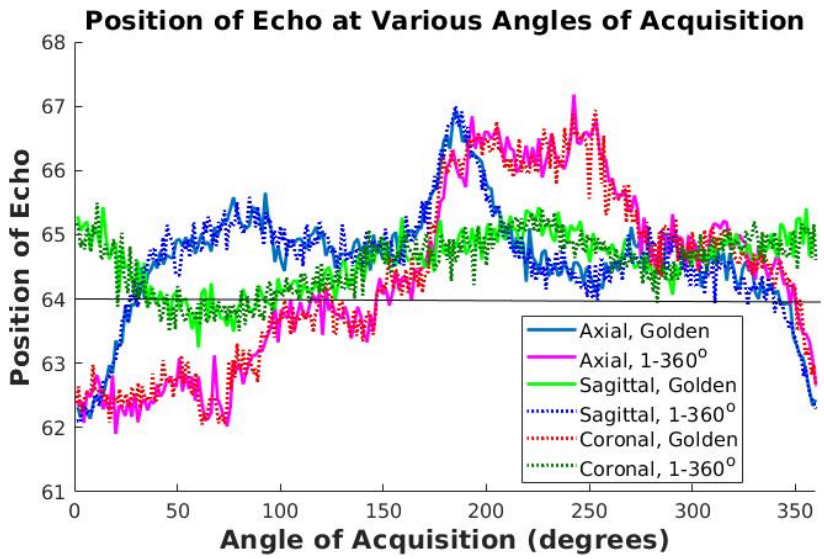

Figure B.10: Gradient timing delays for the radial AIF pulse program, for the three standard slice orientations and Golden angle or uniform angular sampling. The phantom - a homogeneous, spherical glass ball filled with 2 *mM* Gd-DTPA - was placed at the scanners isocenter to within 1 mm using a localization scan. The results reveal an angle-dependent pattern, though it is not a simple sinusoidal and repeats every 360° rather than the expected 180°. The pattern is consistent within an experiment (for any angular sampling density or sampling method used (i.e. uniform, Golden angle)), but changes between experiments.

acquisition. If a gradient delay is present - and the slice orientation is axial, coronal or sagittal - then the echo follows a sinusoidal pattern, repetitive every 180°. This is a result of the same gradients being used for acquisitions at angle N and angle N + 180°; only the sign differs. The timing delays are then read off the graph at angles 0 and 90° for the two physical gradients in use, and may be verified by comparing the results from two orthogonal slice orientations. Figure B.10 shows the timing delay measurements for the three slice orientations (axial, coronal and sagittal) and Golden angle or uniform angular sampling. The phantom for this experiment was a homogeneous, spherical phantom filled with 2 mM Gd-DTPA diluted in a saline solution. The spatial location of the center of the phantom was verified to be within 1 mm of the magnets iso-centre with a tri-pilot localization

scan.

The results show an angular offset in the position of the echo, but the pattern is not sinusoidal and is repeated every 360° rather than the expected 180°. The observed pattern may be sensitive to the phantom positioning and/or shape as it changed slightly between experimental days. The timing offset is insensitive to the angular sampling density or method used (i.e. uniform, Golden angle), as shown with the solid and dashed lines in the Figure. The timing delay does not follow a simple sinusoidal pattern, which indicates that the issue is more complicated. Magnetic field inhomogeneities is another explanation. The areas affected with hot or cold spots would map to another location in k-space during the readout and phase encoding steps, and thereby affect the profile of the acquired radial data. Trajectory measurements probe the locations of sampling, and may be performed at the start of the scanning session. The next section describes two techniques. Susceptibility effects should be negligible with the homogeneous, spherical phantom used in the measurements.

k-Space Trajectory Measurements

This section describes two MR trajectory measurement techniques presented by Beaumont et al. [194] and Latta et al. [193]. Both techniques are performed on a homogeneous, spherical phantom centered at the scanners isocentre. The magnetic field is shimmed to the second order prior to the measurement.

With the method by Beaumont, three data sets are acquired. This involves adding a small gradient area to the readout gradient that shifts the entire trajectory by a known amount to avoid the zero-crossings of the excitation pulse - a sinc waveform for this measurement. The summation of all three scans provides a more definitive trajectory measurement as the SNR is sufficient over the entire sampling domain. Figure B.11 shows the trajectories measured using this method. The second column is the trajectory measured without any additional gradient areas (technique first proposed by [192]), while the first and third columns are with the additional gradient area. The fourth column is the summation of all three, and is used for the trajectory measurement.

As observed in the figure (column one, two and three), the phase data can

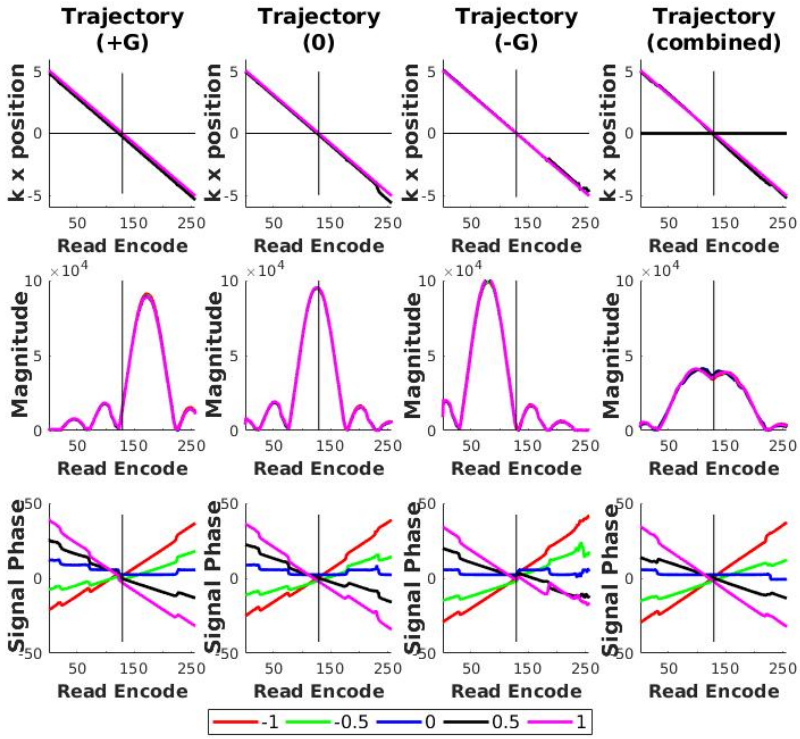

Figure B.11: Trajectory measurements followed the method by Beaumont et al. The first three columns shows the results from the three data sets; the first and third with an additional gradient area to off-set the peak of the sinc pulse to a zero-crossing of the data in column two. The fourth column is the summation of these, and is used for the trajectory measurement. The trajectories are linear near the center of k-space, but can jump slightly when a phase wrap was not detected (ie. at the zero-crossings of the sinc pulse). Changing the strength of the readout gradient (to simulate a radial measurement) also changed the echo location (see Figure B.12).

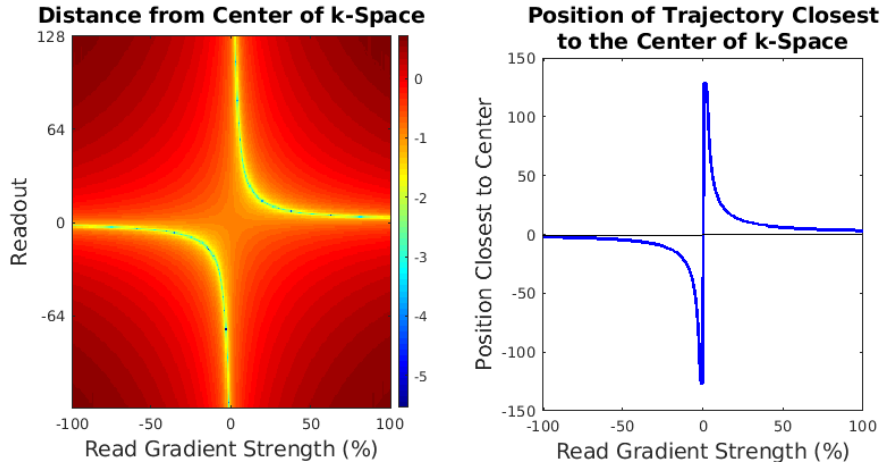

Figure B.12: Distance of the measured trajectory from the center of k-space (displayed on a log10 scale for better visibility) as the readout gradient strength varies from its maximum positive value to its maximum negative value. The figure on the left shows the distance of each trajectory position from the center of k-space, and the figure on the right shows the voxel at which the trajectory crosses the zero (ie. gradient fields are balanced). The center of k-space appears to diverge as we get closer to a gradient strength of 0 mT and follows an inverse relationship with readout gradient strength.

jump abruptly when the excitation pulse profile crosses zero and has a small signal magnitude. The phase is defined relative to the center of k-space, so phase wraps are determined by comparing the phase of neighboring readout points. If the phase jump exceeds π radians, then all readout points from there to the edge are adjusted by $\pm\, 2\pi$ rad. Near the zero-crossings, the signal phase is unreliable (low SNR), so the phase wrap may not be detected.

To simulate a radial acquisition, the strength of the readout gradient was adjusted from its maximum positive value to the maximum negative value in 256 steps. If the trajectory is off-set from the center of k-space, it is expected that this offset will gradually approach 0 as the readout gradient strength is reduced, then increase again with the opposite sign. A closer look at the center of k-space reveals that this is not the case. The zero-crossing of the trajectories does not change linearly, but seem to be somewhat random. This is problematic for radial acquisitions

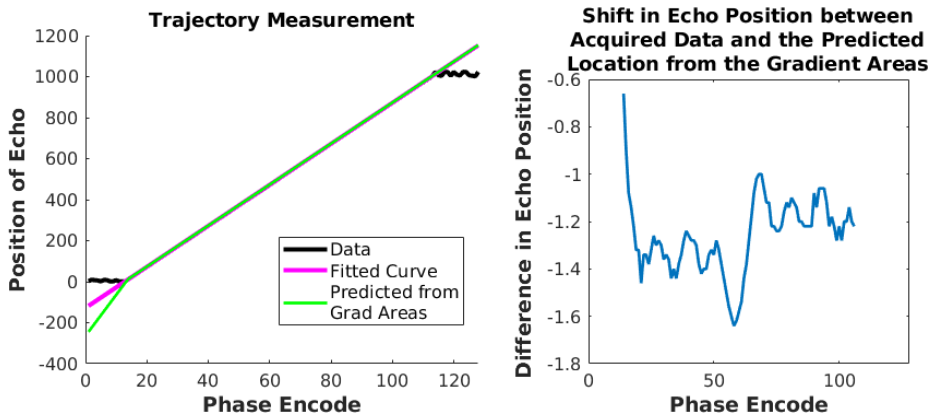

Figure B.13: Trajectory measurement following the method by Latta et al. The results show the measured trajectory (location of echo in black), the expected position based on the gradient area (green) and the best fit curve to the acquired data (magenta).

as the trajectory is dependent on two physical gradients played out concurrently.

Figure B.12 maps the displacement of the trajectory from zero as the strength of the readout gradient varies from its maximum positive value to its maximum negative value. The displacement is plotted on a log10 scale for better visibility of the zero-crossing. The echo appears to be sampled early, when the read encode gradient has a positive value, and late for negative values. When the magnitude is close to zero, the echo position diverges.

The method by Latta uses a spin echo pulse sequence for better SNR, and allows for measurements along the ramp-up lobe of the readout gradient. Figure B.13 shows the trajectory for a coronal slice, with the readout in the head-foot direction.

Comparing the measured trajectory with the desired k-space locations (calculated from the gradient areas) suggests that the echo occurs about 1.2 pixel steps early. In addition, the offset is fairly stable on either side of the center of readout, but it differs by approximately 0.2 pixels. Knowing this, the gradient strengths of the readout could be adjusted slightly to better center the echo, or the trajectory locations could be used in the reconstruction. The NFFT node locations were updated based on the trajectory measurements in both the readout and phase encode directions. The results of this analysis are displayed in Figure B.14.

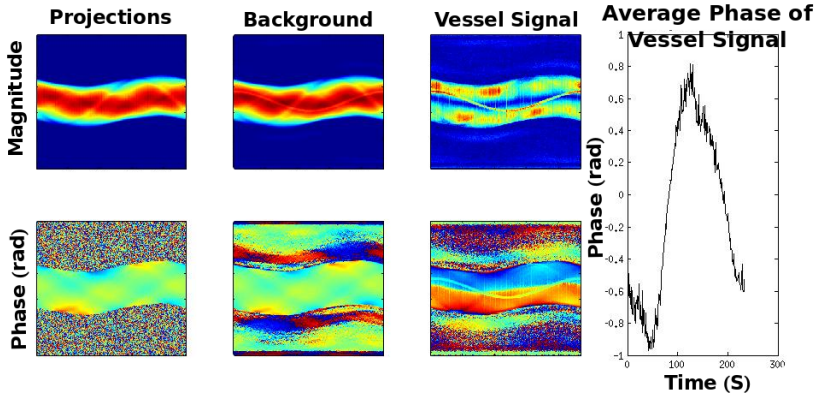

Figure B.14: The Latta trajectory locations were used in the NFFT image reconstruction. The vessel signal still has non-zero signal intensity outside the capillary tube, the phase bands are still present and the phase baseline of the AIF continues to have an angular dependence. These results suggest that the trajectory correction is not sufficient for correcting the AIF on its own.

The new locations did not improve the AIF measurement. The vessel signal still has a higher intensity signal outside the region of the capillary tube, and continues to have the two phase bands (though the phase varies with angle slightly). The phase baseline still shows an angular dependence, covering a range from -0.95 rad to $+0.75$ rad. This result suggests that updating the trajectory locations in the reconstruction is not sufficient on its own. Noting the difference on the two sides of the zero-crossing of the trajectory, it would be worthwhile looking further into its cause. This likely contributes to the phase bands observed in the vessel signal.

Appendix C

Radial Projection-Based AIF with Imperfect Radial Data: Simulation Study

This Appendix outlines the simulation study performed on a digital phantom to test the radial projection-based AIF measurement. The offsets and imperfections studies were motivated from the results of the projection-based AIF baseline artifact. These include measuring data from a phantom off-center in image-space, a mis-centering of the k-space data, multiple vessels in the phantom which could overlap with one another and a sharp rectangular shaped injection profile. Simulations are advantageous as the input AIF is known, and may be used to characterize the errors in the measured projection-based AIF. In addition, the phantom can be made increasingly more complicated to provide a more thorough investigation of the limits of our technique.

C.1 Methods: Correcting the AIF for Local Tissue Enhancement

The simulations were performed on a digital phantom with one 'vessel' to identify the limits of our technique. The phantom consisted of a circular object, of radius 32 voxels and centered in the image plane, with a small circular vessel (radius 1.5

voxels), in the top left hand corner. The vessel was offset 16 voxels up and to the left of the center of the phantom (equivalent to a shift of 22.6 voxels from the center of the phantom). To make the phantom more reflective of a mouse tail, a vertebral mask, having radius 16 voxels from the center of the phantom, was created. The signal intensity and phase were not affected, but the mask will prevent the contrast agent from extravasating into this region.

The magnitude of the phantom was determined from the steady state flash equation, with $T_1 = 1000$ ms, $TR = 100$ ms, $TE = 5$ ms and a flip angle of 30°. S_o was set to 500 and the phase remains at 0 rad for simplicity. An intensity gradient was applied to the phantom to simulate acquisition with a surface coil. The slope of the gradient was determined from a fit of the signal intensity from a Cartesian image acquired with our mouse tail (gradient strength $= [d+5]/6.3+150$, where d is the distance from the surface coil). Finally, Gaussian white noise was added to complex signal of all images to achieve an SNR $= 50$.

The magnitude of the vessel signal was set to 500, while phase followed the model fit of one of our measured projection-based AIFs [195], but with double the magnitude and added Gaussian white noise to have an SNR of 50. The high SNR provided an environment to test the proposed tissue enhancement correction and identify potential limitations. The AIF had 256 pre-injection samples to cover at least one complete data set of 233 unique angles. This is important for determining the base-line background profiles.

Next, local tissue enhancement was added to the phantom using a similar method to the previous study. The enhancement covered 1398 time steps (6 full repetitions of the 233 sampling angles). The extravasation was seeded at the center of the vessel and grew outward at a rate of $0.1 \cdot e^{-2.5t/1398}$, where t is the time step number. The concentration of contrast agent was calculated from the convolution of the AIF and an exponentially decaying function ($e^{-K_{trans}t/v_e}$), assuming $K_{trans} = 1\ min^{-1}$ and $v_e = 0.5$. The signal intensity was calculated from the shortened T_1 value due to the contrast agent, assuming R_{1o} = 1/900 ms and a Gd-DTPA-BMA (Omniscan) relaxivity of 0.0036 $(ms\ mM)^{-1}$. The phase of the enhancement was calculated using our measured conversion factor and the input AIF curve. Figure C.1 shows the phantom with this enhancement.

Projection data is attained by rotating the Cartesian image by the desired an-

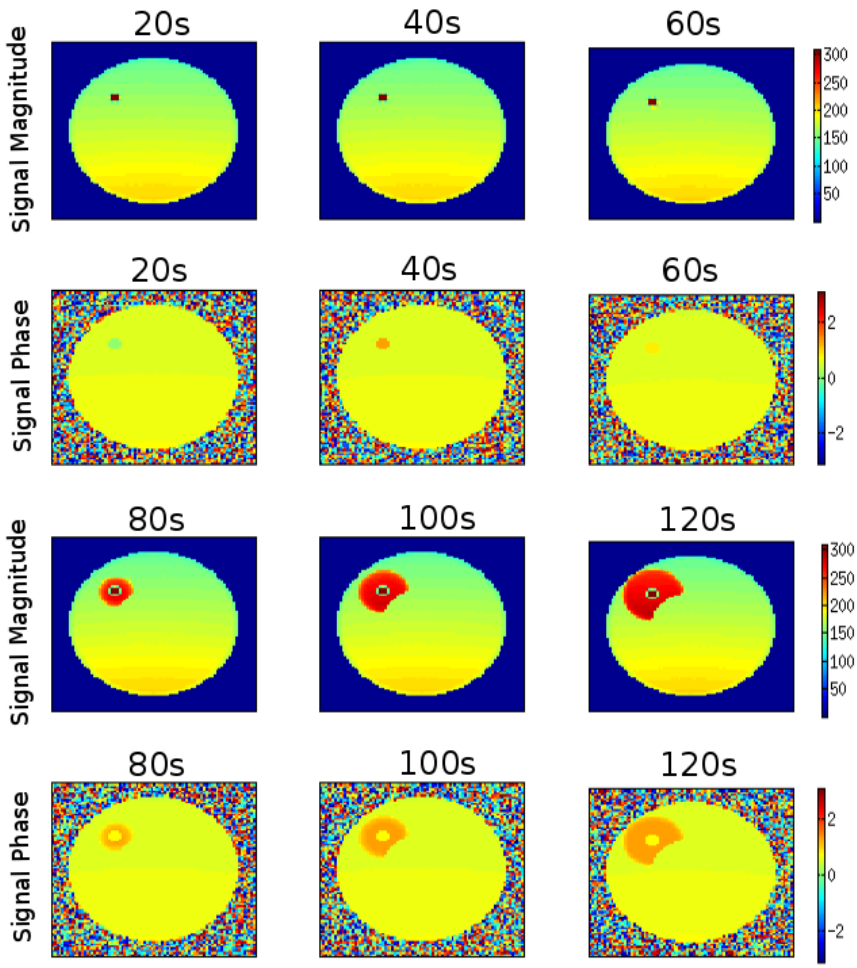

Figure C.1: The simulated tail phantom with a single vessel in the top left hand corner. The tail is approximated as a cyclindrical tube of radius 32 voxels (magnitude calculated by the steady state FLASH equation with $T_1 = 900$ ms and flip angle 30°, and zero phase for simplicity). The vessel has a radius of 1.5 voxels, magnitude of 500 and phase following the mathematical fit to our projection-based AIF presented in chapter 4. Local tissue enhancement was seeded from the vessel and allowed to grow outward. The magnitude and phase was determined from the concentration of contrast agent in the pixel at the given time. The injection took place at 25.6 s.

gle, and projecting the rotated image along the second dimension. Golden angle sampling is used to best fill k-space with recently acquired data, while providing flexibility in reconstructing images with various numbers of projections. The 1-D FFT is applied to get the simulated k-space projection data. Zeroth-order phase shifts are corrected for by multiplying each projection by the phase of the central point (pixel 129 for a vector of length 256).

A mask of the vessel was drawn out and rotated for each of the 233 unique angles. This rotated mask is used in calculating the background profile for the different angles and to determine which sampling angles have overlapping vessels for further studies. The mask was extended by one pixel in all spatial directions to remove partial volume voxels along the outer edges of the vessel.

NFFT images were constructed for each angle from 233 pre-injection samples. The reference angle for each image was updated to match the angle of interest. As a result, the background signal could easily be determined through a projection of the image, after applying the vessel mask to block out the vessel signal.

The signal from the vessel was determined through a subtraction of the background signal from the simulated projection data as shown in Figure C.2. The phase data was unwrapped within the projection before taking the average. This constitutes the raw, uncorrected AIF. Phase wrapping was also corrected between samples, by looking for phase jumps greater than π.

We propose to correct for local tissue enhancement from projections of post-injection images. Theoretically, comparing images before and after will provide a projection profile of the expected difference between the two time points. After subtracting this profile from the acquired data, the local tissue enhancement bias will be replaced with the expected signal from the contrast agent-free tissue. NFFT images were constructed with a Fibonacci number of projections along the entire time series of the experiment. The chosen projections were all consecutive, and shifted by a random number between images. A total of 200 images were constructed, which provides a good balance between computation time and sufficient temporal resolution for the correction. This number can be increased for longer experiments or cases with faster perfusion. The correction technique is outlined in Figure C.3. Similar to the previous measurement, the phase within the projection is unwrapped, then averaged.

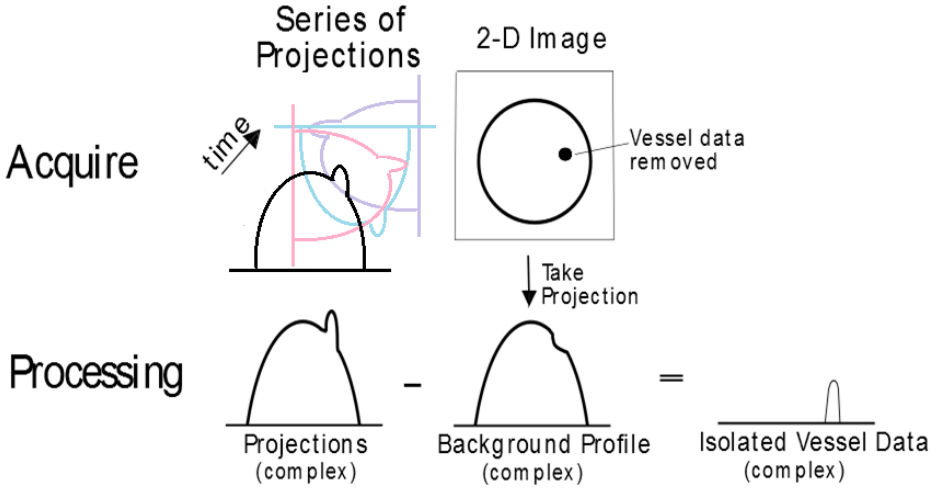

Figure C.2: Schematic of the radial-based AIF measurement. Similar to our original technique, a series of projections are aquired before, during and after contrast injection, but in a radial format. This allows us to reconstruct radial images temporally throughout the scan to identify and correct for local tissue enhancement. From these images, we can once again obtain a background projection for the data at each angle of acquisition.

It is extremely difficult to center the tail at isocenter for each experiment. As such, it is common to have a small spatial offset in image space. The simulation study was repeated for a phantom offset by 16 voxels in the read direction, and again for an offset of 16 voxels in both the read and phase encode directions. The results from this study are compared to the centered case to ensure that the correction technique is robust for objects located anywhere in image space.

Radial data can be prone to gradient mis-timings or slight shifts in the k-space trajectory due to B_o inhomogeneities, eddy currents, etc. Early observations from our acquired radial projections showed that the center of k-space follows an oscillating pattern (repetitive over 180°) with an amplitude of approximately one pixel. Additional simulation studies were performed after shifting the center of k-space by 1.3 or 2.6 voxels in both image dimensions. The centered image will explore the issues resulting from only a mis-centering of k-space, while the shifted image will explore a more realistic situation where the object is likely mis-centered in

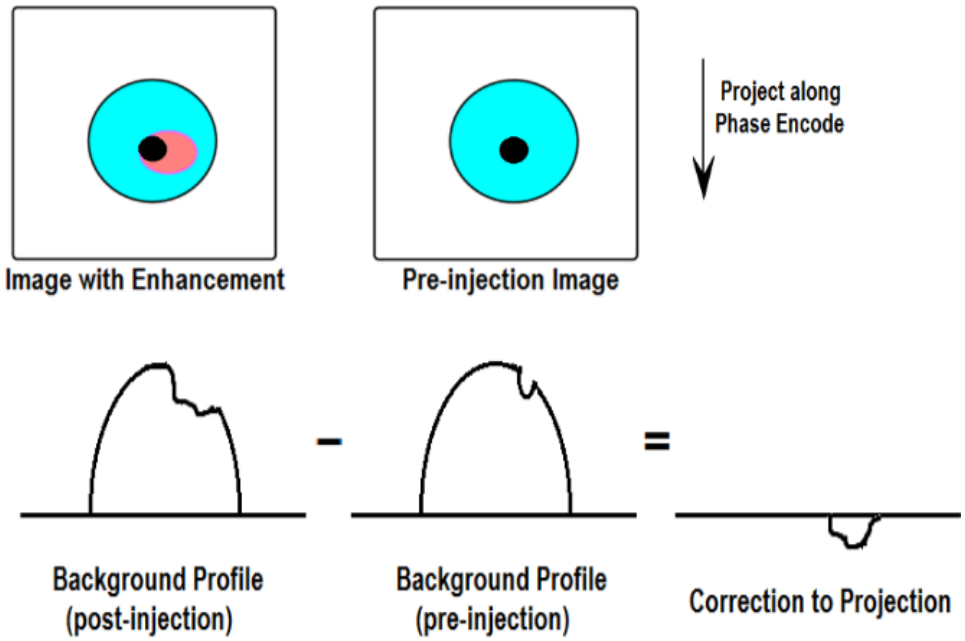

Figure C.3: Schematic for the local tissue enhancement correction. The presence of contrast agent in tissue will alter the T_1 and T_2^* relaxation time constants, and therefore affect the acquired signal. It is expected that the original signal from the tissue can be recovered by comparing projections before and after the contrast injection. To do this, NFFT images are constructed with a Fibonacci number of projections (233, 144, 89, 55, 34, 21), using the same sampling scheme in both. The vessel signal is blocked out with a mask, and the image is projected. Subtracting the post-injection profile from the pre-injection profile will produce a correction profile. This may be subtracted from the acquired projections, post-injection, to remove the tissue enhancemnet bias.

both image and k-space. The results of this study could help identify limitations in our correction when the projection data is slightly distorted.

The mouse tail has four major vessels. When performing a projection-based measurement, there are some angles in which the signal from two or more vessels interferes with one another. To investigate potential issues with multiple vessels, the study was repeated with two and four vessels. The vessels were of similar size, and equally spaced around the perimeter of the phantom. The injection was

initiated in the top-left hand vessel. The same AIF passed through the other vessels, but with a temporal delay of 50 time points. Consequently, the local enhancement was also delayed relative to the top-left hand vessel. In a second study, the phase of the vessel was set to the conjugate phase in alternating vessels to simulate blood flow in the opposite direction. This also provided a more complicated system in which to evaluate the AIF correction.

Another study involving a box-car AIF is investigated as a perfect bolus injection profile. The AIF was simulated as the sum of two step-functions - of concentrations +2 and -2 mM, respectively - and the second shifted 89 or 233 data points from the first. This bolus shape, though unrealistic in-vivo, will set a lower limit on the temporal resolution required for rapid changes in the contrast agent concentration or cases where the temporal resolution must be compromised for spatial coverage.

C.2 Results and Discussion

C.2.1 The Radial AIF: Centered in Image-space

The first study evaluated the tissue correction, when only one vessel is present in the imaging plane. The initial, uncorrected AIF was measured with the radial projection-based method with NFFT images constructed with 233 radial projections (all pre-injection). The resulting curve has the characteristic shape immediately following the peak of enhancement, when local tissue enhancement is minimal. But, as the enhancement grows in size and intensity, the AIF diverges from simulated intra-vascular concentration.

The tissue-enhancement correction involved reconstructing 200 NFFT images along the time coarse of the DCE experiment. The correction images used 233, 144, 89, 55 and 34 projections in the reconstruction, and were shifted by a random amount. The corrected AIF curves are shown in figures C.4, C.5 and C.6, for 144, 55 and 34 projections, respectively. In all figures, the black curve represents the expected input AIF (mathematical fit to a projection-based AIF), the green curve shows the initial, uncorrected AIF, and the pink curve is the tissue enhancement corrected AIF.

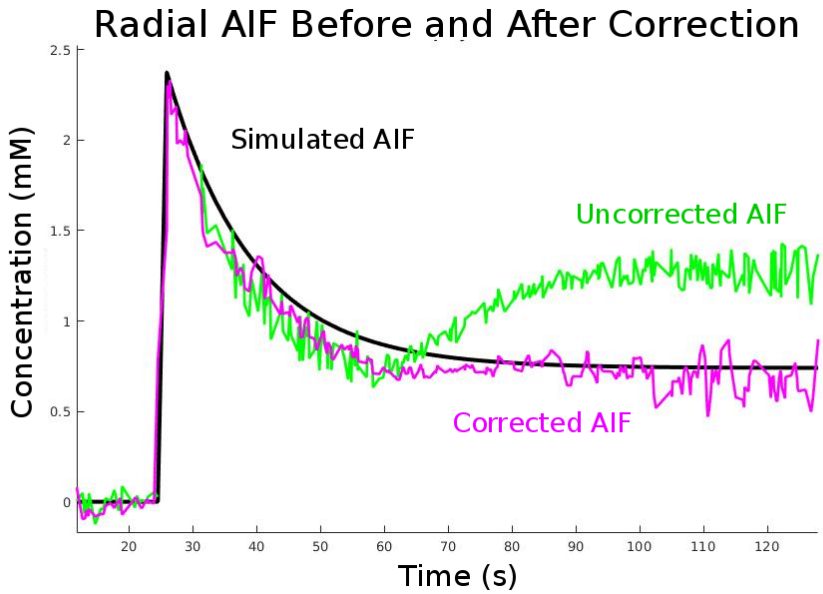

Figure C.4: The radial projection-based AIF before and after applying the local tissue enhancement correction. Tissue enhancement correction involved reconstructing NFFT images with 144 projections acquired with Golden angle sampling. The tissue enhancement correction was effective as the AIF more closely resembles the input curve.

The figures show that the tissue enhancement correction is effective when 55 or more projections are used in the NFFT reconstructions. Further reduction to 34 projections results in an underestimation of the concentration across the entire experiment by $10-20\%$ and $40-60\%$ when 21 projections are used.

Temporal blurring, from reconstructing images with a large number of projections, does not appear to impact the measurement of the AIF. This is assessed at the later wash-out section of the AIF (from 40-60 s), in which the corrected AIF is in good agreement with the tissue-enhancement corrected AIF. This may be a result of having a high temporal resolution for the projection data (100 ms) and a relatively slow contrast agent uptake in the surrounding tissue immediately following the injection.

Closer to the peak of the AIF, the curves with 55 or 34 projections underestimate the concentration. This might be from lower degrading image quality (signal

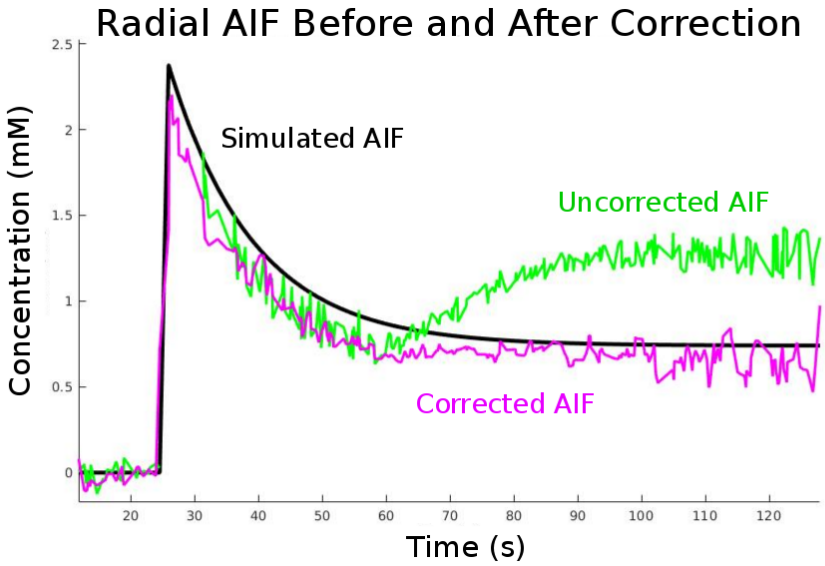

Figure C.5: The radial projection-based AIF before and after applying the local tissue enhancement correction. Tissue enhancement correction involved reconstructing NFFT images with 55 projections acquired with Golden angle sampling. The tissue enhancement correction is again effective throughout the experiment.

blurring, loss of contrast between structures within the image, artifacts, etc.) as fewer projections are used. The corrected curve with 144 projections continues to be in good agreement here, again suggesting that the rates of change in the intravascular concentration are slow enough to be accurately modeled with a temporal resolution of 14.4 s. These results may not be indicative of faster changes within the vessel, but shows that image reconstructions near the peak of the AIF must be carefully considered. It would be beneficial to employ a variable density sliding window for the analysis, in which radial images are reconstructed more densely after local tissue enhancement become problematic.

A more instructive comparison looks at the ratio of the tissue corrected AIF and the simulated AIF (Figure C.7). The results show that the corrected AIF most closely agrees with the input curve when a larger number of projections is used in the NFFT reconstruction. The ratios gradually reduce as fewer projections are used, with significant drops occurring with the data sets using 34 and 21 projec-

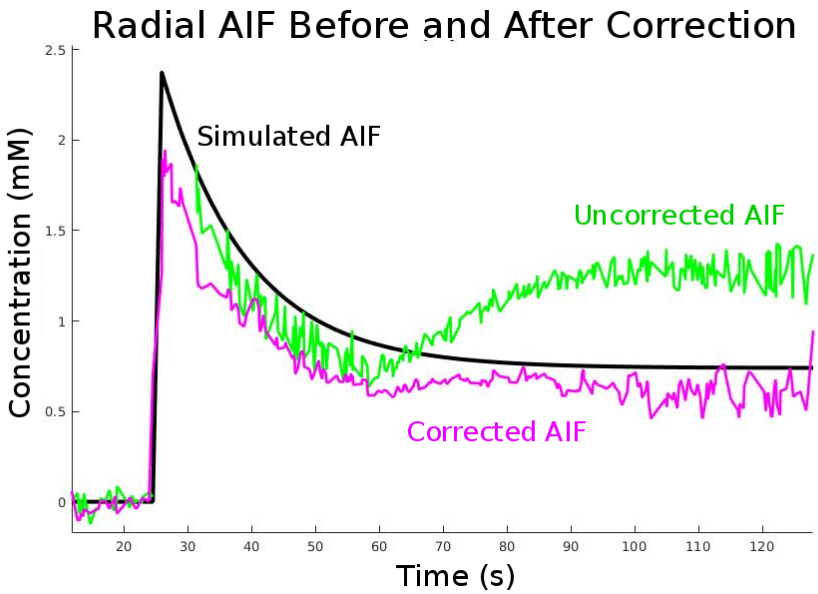

Figure C.6: The radial projection-based AIF before and after applying the local tissue enhancement correction. Tissue enhancement correction involved reconstructing NFFT images with 34 projections acquired with Golden angle sampling. The tissue enhancement correction is somewhat effective at the late stages of the experiment, wheile the peak of the AIF was under-estimated.

tions. For the data sets with 55 or 144 projections, the corrected AIF is in good agreement with the simulated curve at the peak and immediately after. The ratios for the data set with 55 projections has similar trends, but slightly reduced ratios in the proximity of the peak concentration.

Following the peak, until the AIF approaches a steady value, the ratios for all data sets gradually drops, reaches a minimum around 61.7-66.3 s, then increases again until time point 84.6-87.4 s. Beyond this point, the ratios get noisier and starts to drop again. The ratios at the important time points are summarized in Table C.1. The peak is defined from time points 12.7-16.0 s, the wash-out section from 43.7-54.9 s, and the long term stage from 93.9-127.99 s (the end of the experiment). Tissue enhancement affects the AIF measurement at time point 62.5 s.

Setting a threshold value for the ratio can help identify the number of projec-

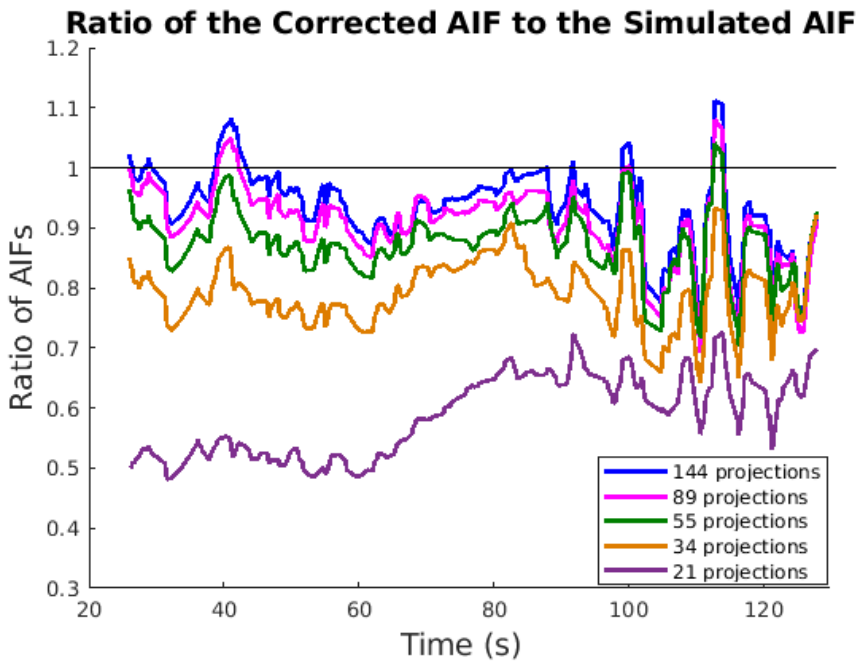

Figure C.7: Ratio of the corrected AIF to the simulated AIF. The results suggest that the correction is most effective when 89 or more projections are used (range 0.95-1.01 near the peak concentration and 0.81-0.98 at the end of the experiment). Reducing this to 34 projections causes severe underestimation throughout (range 0.7-0.83) and would not provide a suitable AIF.

Table C.1: Ratio of Concentrations Between the Corrected AIF and the Simulated AIF

Number Projections	Peak	Wash-out	Long Term
233	1.006 ± 0.045	0.890 ± 0.009	0.88 ± 0.13
144	1.001 ± 0.041	0.924 ± 0.007	0.88 ± 0.13
89	0.977 ± 0.042	0.898 ± 0.007	0.85 ± 0.14
55	0.926 ± 0.045	0.849 ± 0.005	0.84 ± 0.13
34	0.825 ± 0.043	0.751 ± 0.005	0.77 ± 0.12
21	0.520 ± 0.034	0.502 ± 0.003	0.625 ± 0.080

tions required for a local tissue correction. For this analysis, a ratio exceeding 0.900 indicates excellent agreement, those exceeding 0.850 are good and ratios exceeding 0.800 are satisfactory. Looking the average long-term concentration from Table C.1 and focusing on the ratios from time points 62.5 s to the end of the experiment (Figure C.7), the correction requires at least 89 projections for a good corrected AIF and 55 for satisfactory results. The data set with 21 projections is clearly insufficient, as the ratio hovers around 0.50 following the injection and around 0.55-0.70 at the end of the experiment.

C.2.2 AIF Measurement on an Off-Centered Image

The next study looked at the effects of imaging an object off-center within the FOV. The same phantom was used, but centered at positions [112.5 128.5] or [112.5 112.5] on an image grid 256x256 voxels^2 (spatial shifts of 16 and 22.6 voxels from the center). If the tissue-enhancement correction technique is robust, then the results should be similar to the centered study.

Figure C.8 shows the initial projection-based AIF and the corrected AIF for a phantom centered at position [112.5 128.5], and using 55 projections in the NFFT reconstruction. The tissue enhancement correction is effective in removing the bias at later times, but the concentration appears to be slightly under-estimated throughout the entire experiment. The ratios of the corrected AIF and the simulated AIF are similar to the centered case (Figure C.9) and the average ratios at the peak, wash-out and late stage are summarized in Table C.2 (phantom centered at [112.5 128.5]) and Table C.3 (phantom centered at [112.5 112.5]).

Table C.2: Ratio of Concentrations Between the Corrected AIF and the Simulated AIF: Image Centered at [112.5 128.5]

Number Projections	Peak	Wash-out	Long Term
233	0.981 ± 0.044	0.851 ± 0.011	0.939 ± 0.13
144	0.969 ± 0.048	0.886 ± 0.009	0.924 ± 0.14
89	0.948 ± 0.051	0.863 ± 0.008	0.896 ± 0.14
55	0.890 ± 0.055	0.814 ± 0.006	0.879 ± 0.14
34	0.791 ± 0.048	0.723 ± 0.005	0.801 ± 0.12
21	0.511 ± 0.035	0.483 ± 0.002	0.620 ± 0.07

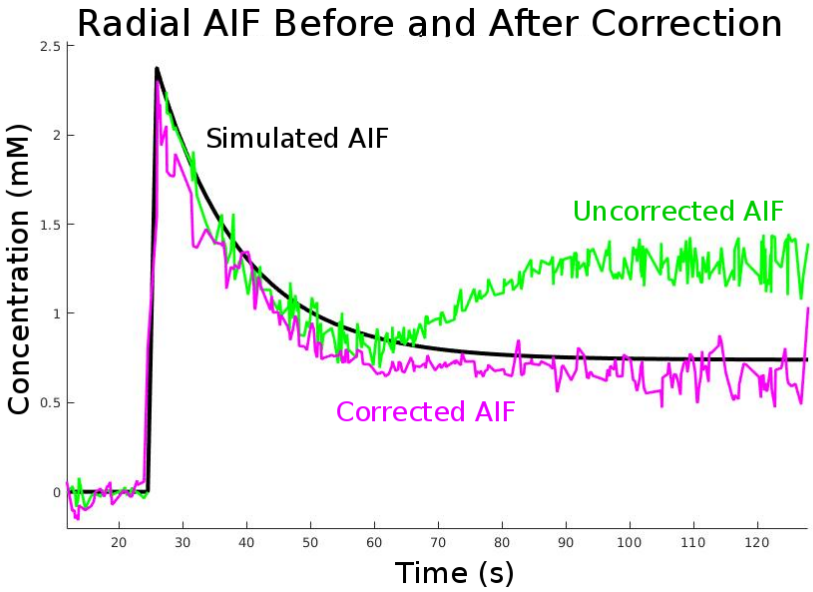

Figure C.8: The radial projection-based AIF measured from a phantom off-center in image space (center at [112.5 128.5] for an image matrix size of 256*x*256). The correction was effective in recovering the input AIF with 55 projections. With 34 projections, there was slight underestimation at the peak, while the curve with 21 projections greatly uderestimated the AIF for all times.

Similar to the ratios from the centered phantom, the ratios for the phantom offset in one dimension reaches a peak around time point 40.2 s, gradually decreases to time point 60.4-60.8 s, then increases again. All curves have a similar shape, regardless of the number of projections used in the reconstruction. However, the ratios show a strong dependence on the number of projections used in the reconstruction, with the data sets using 144 or 233 providing the closest ratios to 1.00. The data set with 55 projection has slightly lower ratios, though this may be considered sufficient if a higher temporal resolution is desired. The results with 34 or 21 projection are clearly inferior, with ratios dropping well below 0.80.

Centering the phantom at [112.5 128.5] in image space produced similar curves to that of the perfectly centered phantom, as displayed in Figure C.10. There were slight differences around the peak and early wash-out. The measured concentra-

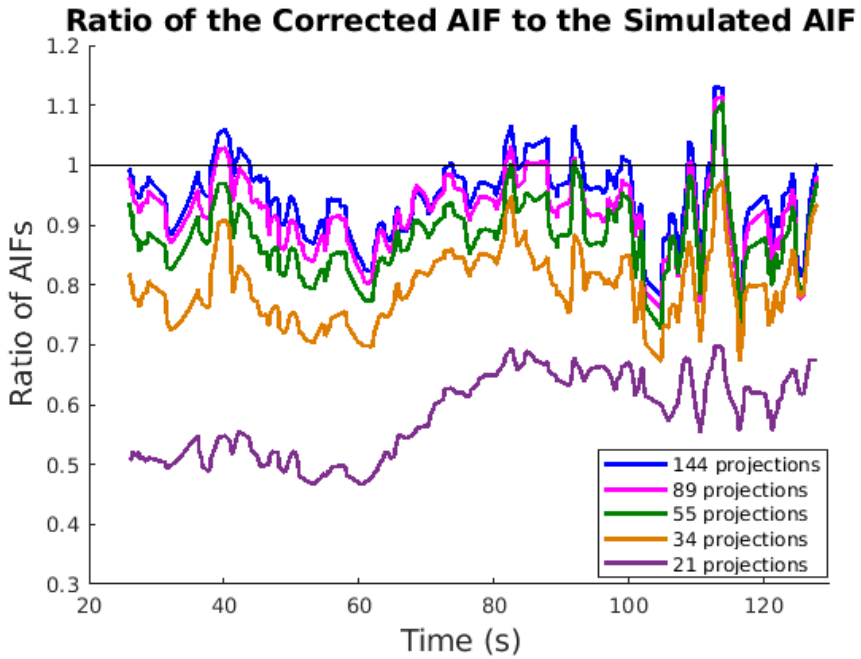

Figure C.9: Ratio of the corrected AIF (center of phantom at [112.5 128.5]) to the simulated AIF. The ratios were averaged over ten post-injection images to reduce noise. The results suggest that the correction is most effective when 89 or more projections are used. Reducing this to 34 projections causes severe underestimation throughout and would not provide a suitable AIF.

tion are lower with the off-centered object, but are generally within 3.6% of that of the centered object. The measurements with 89-233 projections estimated the peak concentration within 5.2% of the actual concentration, which constitutes an excellent AIF curve. Reducing the number of projections showed a dramatic drop in the measured peak concentration. In general, the tissue enhancement correction appeared to be effective at the later time stages when at least 89 projections were used in the image reconstructions. However, the errors still approached $6.1 - 10.4\%$ in these data sets. Moving towards the early wash-out stage, the ratios are all greatly under-estimated, with values of 0.851-0.886 with 89 or more projections. At this stage, local tissue enhancement may not be problematic. Therefore, the uncorrected AIF should be used here.

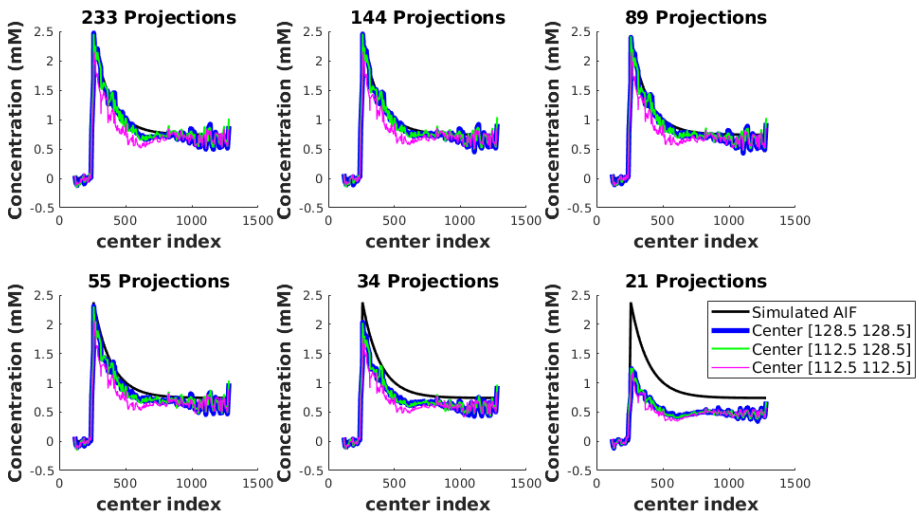

Figure C.10: Tissue enhancement corrected AIFs for a phantom centered at [128.5 128.5] (blue), [112.5 128.5] (green) or [112.5 112.5] (pink) in imagespace. The results show that a correction using at least 89 projection produces a reasonable estimate of the actual AIF. Reducing the number of projections to 55, 34 or 21 will under-estimate the concentration throughout. All curves under-estimate the concentration at the peak.

Table C.3: Ratio of Concentrations Between the Corrected AIF and the Simulated AIF: Image Centered at [112.5 128.5]

Number Projections	Peak	Wash-out	Long Term
233	0.861 ± 0.040	0.682 ± 0.010	0.919 ± 0.12
144	0.855 ± 0.044	0.725 ± 0.008	0.912 ± 0.12
89	0.843 ± 0.048	0.708 ± 0.008	0.882 ± 0.12
55	0.806 ± 0.050	0.670 ± 0.007	0.869 ± 0.12
34	0.705 ± 0.042	0.601 ± 0.006	0.802 ± 0.11
21	0.468 ± 0.037	0.420 ± 0.004	0.643 ± 0.06

Moving the center of the phantom to [112.5 112.5] caused further underestimation of the concentration at the peak and early wash-out region. This is illustrated in the figure, where the magenta curve shows lower concentrations than the blue and green curves. The ratios at the peak and early wash-out phase are much lower

than observed when the object is centered or offset in one direction. The ratios are all lower than 0.900 at the peak and below 0.75 at the wash-out stage, which is 8.4-12.0% and 12.1-16.9% lower than the data set offset in one dimension.

These results suggest that shifting the phantom along one spatial dimension has minimal effect on the measurement of the radial projection-based AIF, but shifting it in both dimensions leads to an under-estimation at and following the peak. The shift from the center of image space increased by a factor of 1.414, or from 16 voxels to 22.6 voxels. The radon transform upsamples the matrix by a factor of $\sqrt{2}$, then rotates the image by a specified angle using bi-linear data interpolation. The increased under-estimation could be related to how the data was interpolated and then input into the reconstruction. If the positions are off-set by a sub-pixel amount, and interpolated with the linear or nearest neighbour approach, then the echo may have a different shape from expected. Translations cause a global phase shift in k-space.

The results from this section suggest that the corrected projection-based AIF should use at least 89 or 144 projections in the correction image, though 55 projections would be considered reasonable if a higher temporal resolution is desired. The greatest gains from the tissue enhancement correction are at the late stage. All corrected AIF bring the AIF closer to the expected concentrations, but generally under-estimate the concentration.

C.2.3 AIF Measurement with Distortions in k-Space

Radial data is known to be prone to issues with mis-centering of the echo due to a gradient timing error or deviations of the trajectory due to magnetic field inhomogeneities. As such, the next study evaluated potential issues with acquiring mis-centered k-space data. Small shifts in k-space (1.3 or 2.6 voxels) were applied prior to taking the projection data.

Figure C.11 shows the uncorrected and corrected AIF measurements when the center of k-space is shifted by 1.3 voxels in both image dimensions, and using 144 projections in the correction. The corrected AIF more closely approximates the concentration long after the injection, but the signal is noisier. In general, the shape of the AIF is preserved in the correction, but the SNR has degraded.

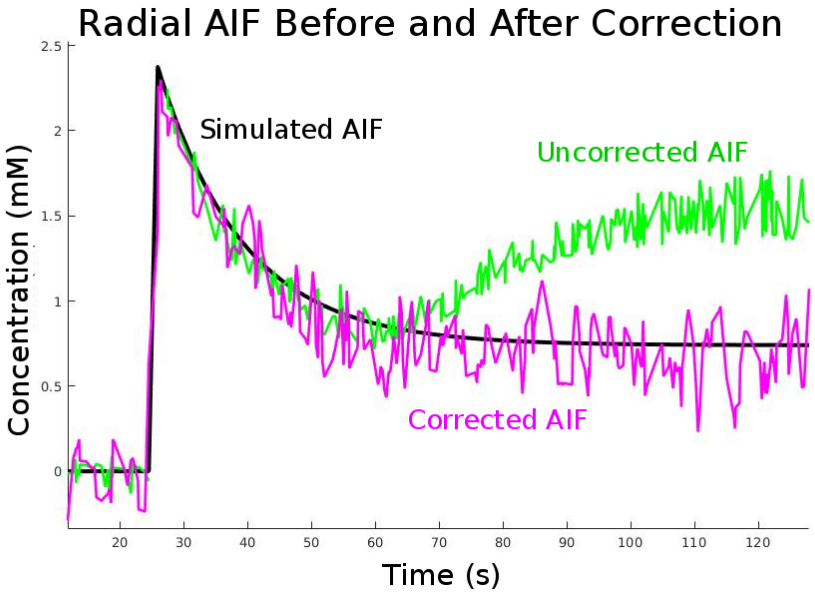

Figure C.11: The radial projection-based AIF measured for a shift in k-space center (shifted by [1.3 1.3] voxels from centre). The correction was accomplished with 89 projections, and was effective at removing the bias from tissue enhancement at the later times. The concentration at the peak is reasonably close to the expected result (97 $\pm$ 3%), but the wash-out region following the peak was under-estimated.

The corrected curves with 89 and 233 projections look similar to the curve at 144 projections. This suggested that the additional data did not significantly affect the quality of the correction. As a results, with our temporal resolution and simulated contrast kinetics, 89 projections will be sufficient. Reducing the number of projections to 55 or 34 revealed a slight underestimation of the concentration throughout. The underestimation is most severe at the peak and wash-out regions of the curve, however, and may not be an issue if the uncorrected AIF is unaffected by local tissue enhancement here. When using only 21 projections, the AIF was significantly underestimated across all times. Based on these results, it is suggested to use at least 55 projections in the correction, though 89 or more is preferred.

The ratio of concentrations between the corrected AIF and the simulated AIF are summarized in Table C.4.

Table C.4: Ratio of Concentrations Between the Corrected AIF and the Simulated AIF: k-Space shifted by $[-1.3 - 1.3]$ voxels

Number Projections	Peak	Wash-out	Long Term
233	0.985 ± 0.039	0.85 ± 0.19	0.89 ± 0.25
144	0.975 ± 0.036	0.86 ± 0.19	0.88 ± 0.24
89	0.960 ± 0.035	0.85 ± 0.19	0.86 ± 0.25
55	0.922 ± 0.038	0.81 ± 0.18	0.87 ± 0.25
34	0.836 ± 0.055	0.74 ± 0.17	0.80 ± 0.23
21	0.602 ± 0.043	0.54 ± 0.15	0.66 ± 0.20

The ratios are greatest with 233 projections and steadily decreases as fewer projections are used. Though the ratios are close to 1.0 near the peak of the AIF with 89-233 projections, the concentrations in the wash-out and long term regions are under-estimated by more than 10%. Further, the signal is noisy, which contributes to the larger standard deviations in these regions. At the late stage, the intra-vascular concentration is approaching a steady value. Averaging of signals in this region could increase our confidence of the concentration without losing important image features.

There does not appear to be much difference in the effectiveness of the tissue enhancement correction between the data sets with 89-233 projections, which again suggests that 89 projections is a good compromise between temporal resolution and image quality. Reducing the projections to 55 shows a slight drop in the ratio in the wash-out region, though this may not be sufficient to argue against it. Further reduction of the number of projections to 34 or 21 shows dramatic drops in the ratios. Neither would be recommended for a tissue enhancement correction when the k-space data is slightly off-center. For accurate model fitting, it is recommended to use least 89 projections in the correction images for our input AIF and temporal resolution (100 ms).

Shifting the center of k-space by 2.6 voxels in both image dimensions, showed more dramatic effects on the corrected AIFs. The results for a correction with 89 projections is shown in Figure C.12 and the ratios between the corrected and simulated AIF are summarized in Table C.5. Similar to the results of the k-space shift by [1.3 1.3], the ratios are best near the peak of the AIF and show a significant under-

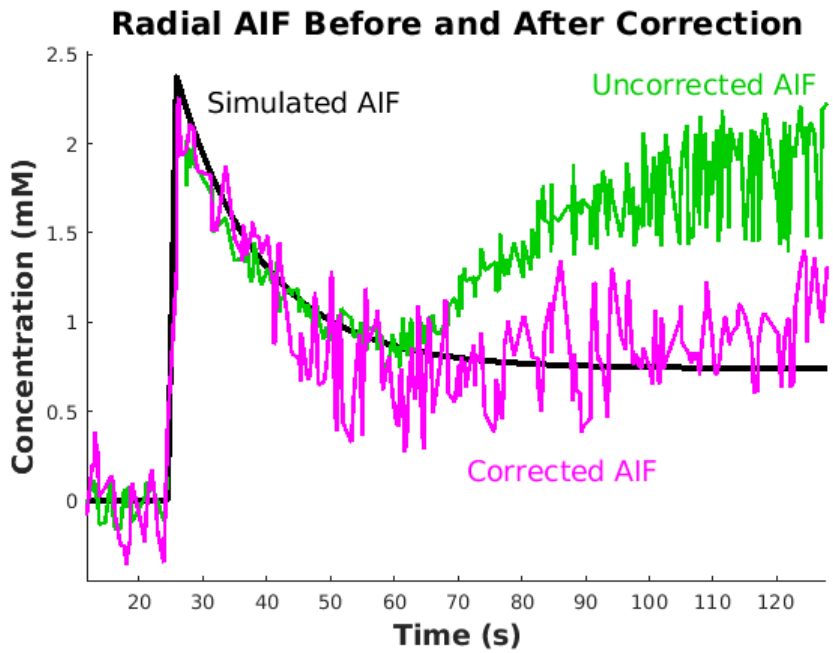

Figure C.12: The radial projection-based AIF measured for a shift in k-space center (shifted by [2.6 2.6] voxels from centre). For a fair comparison with the smaller k-space shift, this AIF used 89 projections in the correction. The correction was not effective as the concentration at the end of the experiment was over-estimated, and the curve still has an upward trend and is very noisy beyond time point 48.1 s. The uncorrected AIF should be used until tissue enhancement is observed.

Table C.5: Ratio of Concentrations Between the Corrected AIF and the Simulated AIF: k-Space shifted by $[-2.6 - 2.6]$ voxels

Number Projections	Peak	Wash-out	Long Term
233	0.945 ± 0.051	0.79 ± 0.28	1.27 ± 0.25
144	0.940 ± 0.050	0.83 ± 0.28	1.25 ± 0.25
89	0.929 ± 0.051	0.81 ± 0.27	1.23 ± 0.25
55	0.895 ± 0.058	0.80 ± 0.27	1.25 ± 0.24
34	0.853 ± 0.066	0.77 ± 0.26	1.24 ± 0.23
21	0.75 ± 0.14	0.75 ± 0.20	1.46 ± 0.17

estimation in the wash-out region. However, the tissue enhancement correction is not effective as all ratios are greater than 1.0 and the figure clearly shows that the corrected projection-based AIF over-estimates the concentration and continues to have an upward trend at the end of the experiment.

The concentration near the peak is measured closest with the data set with 233 projections, and gradually gets worse as fewer projections are used in the correction image. The peak concentration is within 10% of the expected value with at least 89 projections, and very close with 55 projections. In the wash-out region the ratios all drop to 0.75-0.83. Unlike the peak, there seems to be no correlation between the ratio and the number of projections used as the values are all close together and the standard deviations are all large due to a noisy signal. Based on the appearance of the tissue enhancement corrected AIF, It would be advisable to use the values from the uncorrected curve here, as it more closely approximates the expected concentration. Use of the corrected curve would affect the affect the model parameter estimates.

The study was repeated after shifting the center of the phantom to position $[112.5\ 128.5]$ within a $256x256$ matrix. The ratios of the corrected to simulated AIFs are summarized in Table C.6.

Table C.6: Ratio of Concentrations Between the Corrected AIF and the Simulated AIF: k-Space shifted by $[-1.3\ -1.3]$ voxels, and phantom centered at $[112.5\ 128.5]$

Number Projections	Peak	Wash-out	Long Term
233	0.870 ± 0.034	0.71 ± 0.20	0.94 ± 0.21
144	0.860 ± 0.035	0.74 ± 0.19	0.91 ± 0.21
89	0.851 ± 0.039	0.73 ± 0.19	0.89 ± 0.21
55	0.833 ± 0.033	0.70 ± 0.19	0.88 ± 0.21
34	0.746 ± 0.051	0.64 ± 0.18	0.81 ± 0.20
21	0.518 ± 0.063	0.47 ± 0.16	0.66 ± 0.17

Comparing the results with the phantom centered at $[128.5\ 128.5]$, the concentration at the peak and wash out region are lower while the later times are comparable. In all instances, the concentration was under-estimated with this data set. Similar to the previous cases studied, the ratios are greatest with 233 projections

and gradually decreases as fewer projections are used. The data sets with 89, 144 and 233 projection have similar values throughout, while the curve with 55 projections is slightly lower. Data sets using 34 or 21 projections greatly under-estimate the concentrations at all three stages and should not be used in PK modeling.

The ratios at the peak of the AIF range are 0.83-0.87 with 55-233 projections. These ratios are $8.9-11.5\%$ lower than the values reported for the image in which the phantom was centered in image-space (but offset in k-space). Since the standard deviation is on the order of 0.033-0.039 for these ratios, this is a significant drop. The under-estimation of concentration at the peak of the AIF is compounded, as the concentration of the uncorrected AIF was already under-estimated by $10-15\%$. This result alone shows the importance of getting a good shim prior to scanning and attempting to reduce gradient delay or trajectory issues if present.

The ratios in the wash-out region experience a similar drop of $10-0.14\%$ in the data sets with 34-233 projections, with ratios ranging from 0.64-0.74. These under-estimates are too large for modeling. If tissue enhancement is low at this stage, it is highly recommended to use the uncorrected curve until it causes a noticeable deviation. The corrected curve can be smoothed, and compared to the uncorrected curve to identify where the shape changes most dramatically.

The ratios at the long term time-points are much closer between the two cases. There is no statistically significant change between the two, with the largest difference in the ratio being 0.05 with standard deviations of 0.21 and 0.25 for the two cases (t-value 0.15 or p-value 0.9, stating that the shift is not statistically significant). The corrected AIFs from the two data sets are both noisy here, and would require signal smoothing to improve our confidence in the concentration.

The results from this analysis highlight the importance of acquiring the echo of each projection correctly. Even with a gradient mis-timing error, corresponding to a 1.3 pixel shift in k-space, the measured AIF is grossly under-estimated at the peak and washout regions when the phantom is not centered in the image. Gradient mis-timing effects can be pre-compensated for following the methods of Peters et al. [178], and deviations in the k-space trajectory can be determined through trajectory measurements [193, 194]. The effects are compounded when the phantom is also off-center in image-space.

C.2.4 Multiple Vessels within the Phantom

The mouse tail contains multiple vessels, which could complicate the AIF measurement if the signal from two vessels overlap in the projection. In this study, four vessels are added to the phantom image (see Figure C.13). To make the simulation more realistic, the contrast agent was allowed to flow through all four vessels, but shifted temporally by 50 projections (5 *s*) relative to the vessel in which the injection takes place (top, left hand vessel). The phase shift was in the same direction within all vessels for this analysis.

Figure C.14 shows the initial radial projection-based AIF measurement for the multi-vessel experiment. The data points with overlapping vessels are indicated with the open circles. There are several blips along the curve, although most of these can be attributed to interference from another vessel. This curve was measured in vessel 1, in which the injection took place (top-left).

The tissue enhancement correction removed the signal blips in the curve and brought the later time points closer to their expected values. The results from all four vessels, and all acceleration rates tested, are summarized in Figure C.15. The corrected curves with 89, 144 and 233 projections all have similar shapes, and accurately capture the shape of the input curve. The corrected AIF with 55 projections provides a reasonable estimate, but still under-estimates the concentration at the peak and wash-out phases. Reducing the number of projections to 34 or 21 results in a significant concentration under-estimation at the peak and wash-out regions. Neither of these curves would be appropriate for modeling.

The same bolus flows through the remaining three vessels. As such, the shape of the measured AIF should be similar. In our simple phantom, the vessels are equally spaced around the perimeter. The main difference is the signal intensity of the vessel signal, due to the coil's sensitivity gradient. For instance, vessels 1 and 2 are located further from the coil and have a lower signal intensity than vessels 3 and 4. The contribution of vessels 1 and 2 to the projection signal will therefore be less. Though the AIF is similar in all the vessels, their positions within the phantom may impact the measurement. It is expected that the quality of the measured AIF in vessels 1 and 2 will be similar, as well as the AIF in vessels 3 and 4.

Figure C.15 shows all the corrected AIFs from all four vessels. As expected,

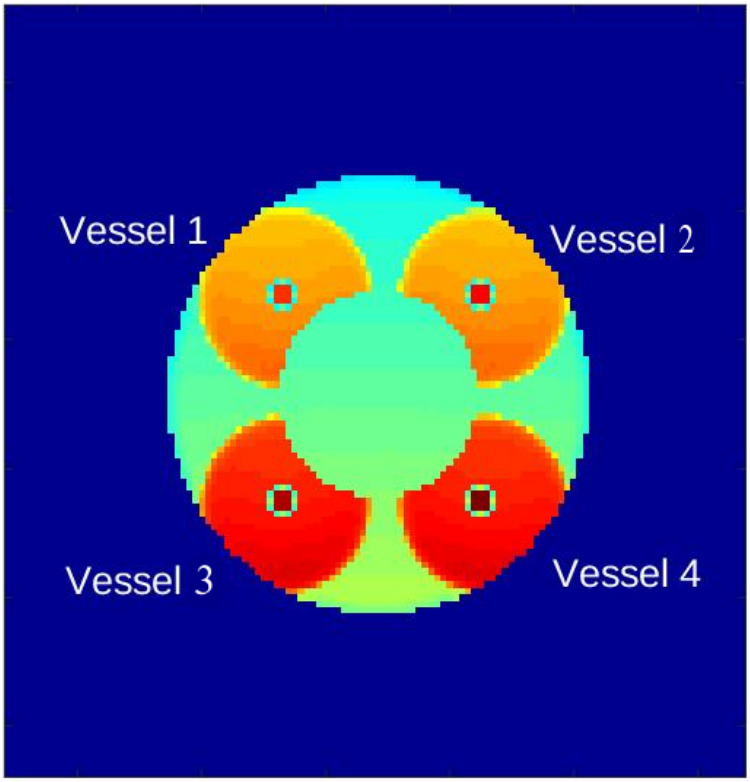

Figure C.13: Digital phantom with 4 vessels. Vessels 1 and 2 are located farther away from the surface coil, and have a lower signal intensity than vessels 3 and 4.

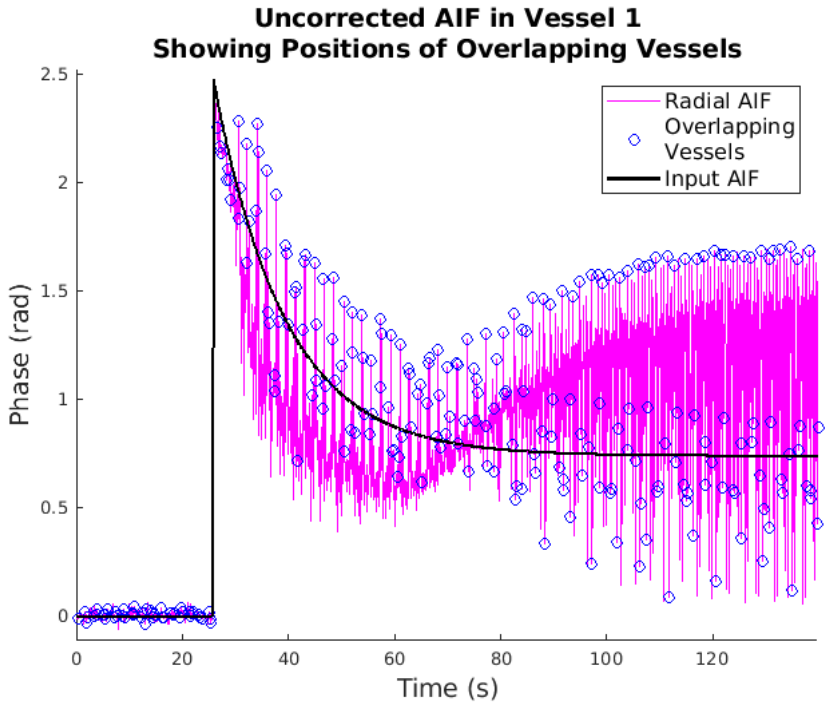

Figure C.14: Initial AIF measurement in vessel 1 (top-left hand). The later stages of the AIF deviate to larger concentrations due to local tissue enhancement in the surrounding vessels. Since there are four vessels in the phantom, the signal from two may overlap and bias the AIF measurement. These data points are indicated with the open circles.

the shape of the AIF from vessels 1 and 2 are similar, with the exception that the curves are shifted relative to one another. Likewise, the AIF from vessels 3 and 4 are comparable. All of the corrected AIFs under-estimate the concentration at the peak. The concentration is more accurately estimated in the wash-out region when at least 89 projections are used in the correction. 55 or fewer projections results in a significant underestimation of the concentration, making these curves unusable for analysis. The concentration at the peak is lower for vessels 2, 3 and 4; though this is an artifact of the random data sampling in time; shifting these curves to match the uptake from vessel 1 confirms this, so a lower peak concentration is expected.

The correction effectively reduces the concentration bias at the later times, but

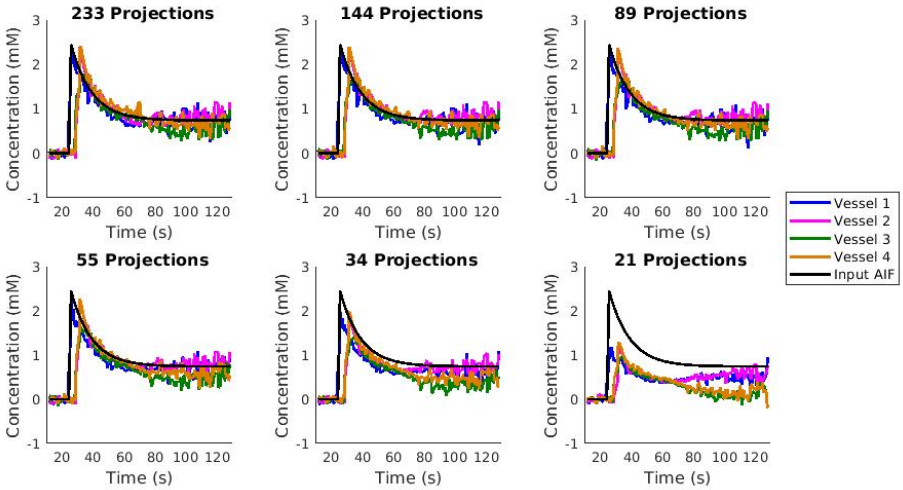

Figure C.15: Corrected AIF measurement using the radial projection-based measurement. In this example, the injection takes place in vessel 1 (top-left). The phase shift in the remaining three vessels is in the same diretion, but delayed by 50 time-points (5 s). The corrected AIF measurements are in better agreement with the expected curve, and the shape is presered in all vessels.

it is not ideal. The AIF from vessel 2 has a slight positive slope at the later stages of the experiment. This slope is also observed in the curve from vessel 1, but it is less obvious. The curves from vessels 3 and 4 both have a concave shape here.

The ratios at all three time-points have a similar shape, regardless of the number of projections used in the correction. However, they become noisier at later times, likely an artifact of the tissue enhancement correction. The intra-vascular concentration would have approached a steady-state value by this point, so the growing tissue enhancement region is more likely the cause. As the concentration of Gd increases in the tissue, the phase of the signal is also affected. For the expected maximum concentration, the change in phase is 0.75-0.80 rad ($43-46^o$). This would impact the resultant phase and magnitude of the background projection.

The results from this analysis suggest that differences in the coil sensitivity in space can affect the AIF measurement. The simple phantom would represent an ideal situation. The addition of susceptibility effects, or using a surface coil with

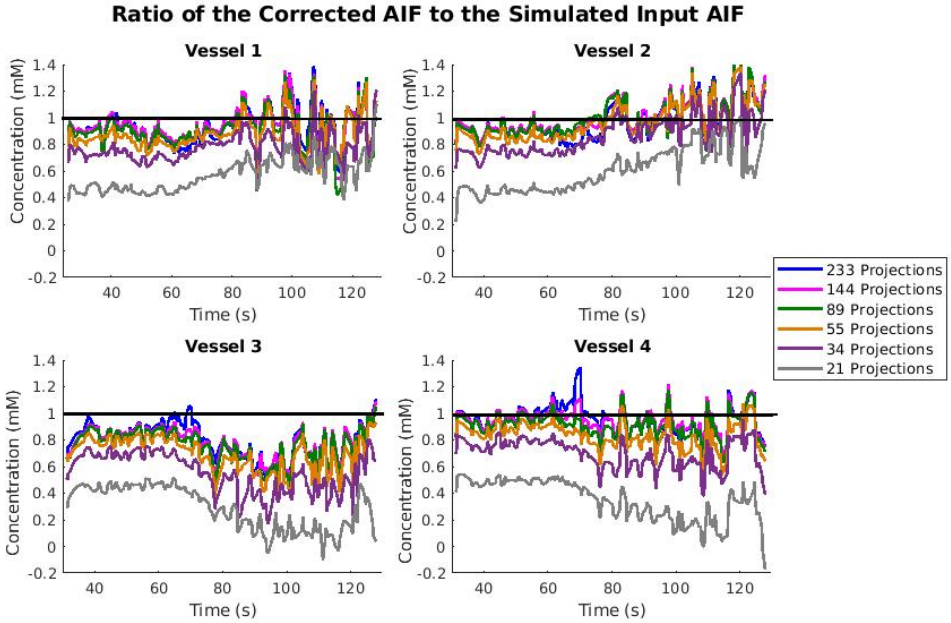

Figure C.16: Concentration ratios of the corrected AIF to the simulated AIF. The ratios are greatest when 89, 144 or 233 projections are used in the correction, slightly lower with 55 projections and significantly lower with 34 or 21 projections. The AIF measurements appear to be closer the simulated curve in vessels 1, 2 and 4 (ratios near 1.00), and under-estimate the concentrations in vessel 3.

a stronger sensitivity gradient could further distort the shape of the AIF of vessels located in the less sensitive regions due to low SNR. Based on our analysis thus far, a reasonable estimate of the true AIF is possible if 89 or more projections are used in the correction. Since the signal is noisy post correction, signal smoothing may be required. This will not affect the validity of the AIF measurement as the correction provides a rough estimate of how much the concentration has been over/under-estimated across the experiment.

The ratios of the measured concentration to the expected value are summarized in Figure C.16 for all four vessels, with the average values at the peak summarized in Table C.7, within the wash-out region in Table C.8 and at the late stage of the experiment in Table C.9. The average ratio from the uncorrected AIF are listed in the titles as a comparison. The shape of the ratio is consistent for all acceleration

rates within a vessel, suggesting that the results are vessel dependent, and the number of projections in the image reconstruction only degrades the effectiveness of the tissue enhancement correction.

The corrected AIFs with 89, 144 and 233 all have similar ratios at the three points of interest. The AIF with 55 projections retained the shape of the AIF, but under-estimated the concentration slightly. Though the error in concentration is less than 5%, it could impact the accuracy of the model parameters. Therefore, at least 89 projections should be used to correct the AIF for this experiment. Reducing the number of projections to 34 or 21 caused a significant drop in the ratio.

Table C.7: Ratio of the Corrected AIF and the Simulated AIF at the Peak
Uncorrected AIF ratio: 0.954 ± 0.014

# projections	233	144	89	55	34	21
vessel 1	0.963	0.970	0.943	0.884	0.796	0.480
(std dev)	0.041	0.044	0.056	0.068	0.043	0.035
vessel 2	0.986	0.992	0.970	0.933	0.776	0.44
(std dev)	0.041	0.035	0.038	0.040	0.032	0.10
vessel 3	0.815	0.764	0.74	0.737	0.611	0.480
(std dev)	0.073	0.095	0.10	0.071	0.090	0.074
vessel 4	1.033	1.029	1.005	0.956	0.845	0.541
(std dev)	0.031	0.028	0.034	0.038	0.035	0.032

The ratios at the peak concentration were greatest in vessels 1, 2 and 4, and comparable with the uncorrected AIF when at least 89 projections were used in the correction images. Vessel 3 had ratios ranging from 0.737-0.815 with 55-233 projections, which is 15-26% lower than the ratios in the other three. Both vessels 3 and 4 have similar signal intensities, so the AIFs should be similar. Since vessels 1 and 3 are on opposite corners, it is possible that the early tissue enhancement affects more projections used in estimating the peak concentration in vessel 3. The ratios from the other three vessels were greatest when at least 89 projections were used in the correction (range 0.943-1.033). The ratios dropped $1-8\%$ when 55 projections were used, $13-21\%$ when using 34 projections and by $26-55\%$ for 21 projections.

Table C.8: Ratio of the Corrected AIF and the Simulated AIF in the Washout Region
Uncorrected AIF ratio: 0.783 ± 0.025

# *projections*	233	144	89	55	34	21
vessel 1	0.839	0.875	0.851	0.802	0.699	0.453
(std dev)	0.079	0.060	0.054	0.040	0.034	0.026
vessel 2	0.825	0.911	0.918	0.872	0.762	0.477
(std dev)	0.051	0.035	0.037	0.036	0.038	0.030
vessel 3	0.954	0.862	0.824	0.772	0.661	0.444
(std dev)	0.061	0.045	0.044	0.048	0.047	0.040
vessel 4	1.09	0.996	0.931	0.864	0.745	0.476
(std dev)	0.11	0.057	0.048	0.045	0.046	0.042

Table C.9: Ratio of the Corrected AIF and the Simulated AIF at Late Stage
Uncorrected AIF ratio: 1.50 ± 0.27

# *projections*	233	144	89	55	34	21
vessel 1	0.95	0.92	0.93	0.92	0.81	0.65
(std dev)	0.24	0.24	0.25	0.23	0.21	0.16
vessel 2	1.10	1.10	1.11	1.08	0.97	0.73
(std dev)	0.21	0.20	0.20	0.18	0.18	0.15
vessel 3	0.74	0.73	0.722	0.65	0.49	0.19
(std dev)	0.22	0.23	0.22	0.20	0.18	0.15
vessel 4	0.96	0.96	0.93	0.86	0.72	0.28
(std dev)	0.17	0.17	0.17	0.17	0.17	0.18

The ratios in the washout region were lower than at the peak of the AIF, but greater than the uncorrected AIF when 55 or more projections were used in the corrections images. The under-estimation in concentration could be related to a combination of the projections containing a wide range of concentration (form the time of acquisition) and partial volume effects along the edges. Similar to the peak, the ratios are lower as fewer projections are used in the correction images.

At the end of the study, all vessels ratio improved compared to the uncorrected

AIF, which had a ratio of 1.50 ± 0.27. Vessels 1 and 4 seemed to benefit the most, with ratios ranging between 0.92-0.96 with 89-233 projections. The correction in vessel 2 was effective in reducing the bias from local tissue enhancement, but still produced ratios on the order of 1.08-1.11 with 55 or more projections. This vessel is in a less sensitive region of the surface coil, so the signal measured from it is more sensitive to changes within the phantom. Vessel 3 had by far the lowest ratios, with values around 0.72-0.74. The standard deviation of all vessels were large, relative to the other two time stages. This could be a result of taking the difference between two noisy signals. It would be worthwhile smoothing the signal at the later stages to reduce noise and get a better measure of the corrected concentration.

In the next study, the phase of the vessel signal alternates between positive and negative values. The motivation was to investigate if the direction of flow had an impact on the AIF measurement, such as the case with arteries and veins. The corrected AIFs for this study are shown in Figure C.17.

In general, 144 projections are required for an accurate description of the AIF. The corrected AIF with 144 projections provides a good representation of the expected result. As we reduce the number of projections to 89 or 55, there is a slight underestimation of the concentration at the peak and wash-out areas. This underestimation becomes more prominent when 34 or 21 projections are used in the correction. Similar to the above study, the tissue enhancement correction removes the bias at the later stages of the experiment, though the signal is noisy.

Due to the alternating phase, the AIF in vessels 2 and 4 appear inverted relative to the simulated curve. This is a direct result of the phase difference being negative and not accounting for this in the conversion from phase to concentration. The shape of the AIF, however, is consistent between all vessels around the peak and wash-out regions. At the later stages of the experiment, there is a slight deviation between the curves; vessels 2 and 4 suggest that the concentration of the contrast agent continues to decrease, while the curve in vessel 3 suggests that the concentration increases slowly. The concentration at the peak is under-estimated in all cases, though this may be an artifact of the chosen image reconstruction points.

The ratios of concentrations, between the corrected AIFs to the simulated AIF, showed variable results between the four vessels (Figure C.18). Visually, the ratios are closest to 1.00 when 144 or 233 projections are used in the correction, with

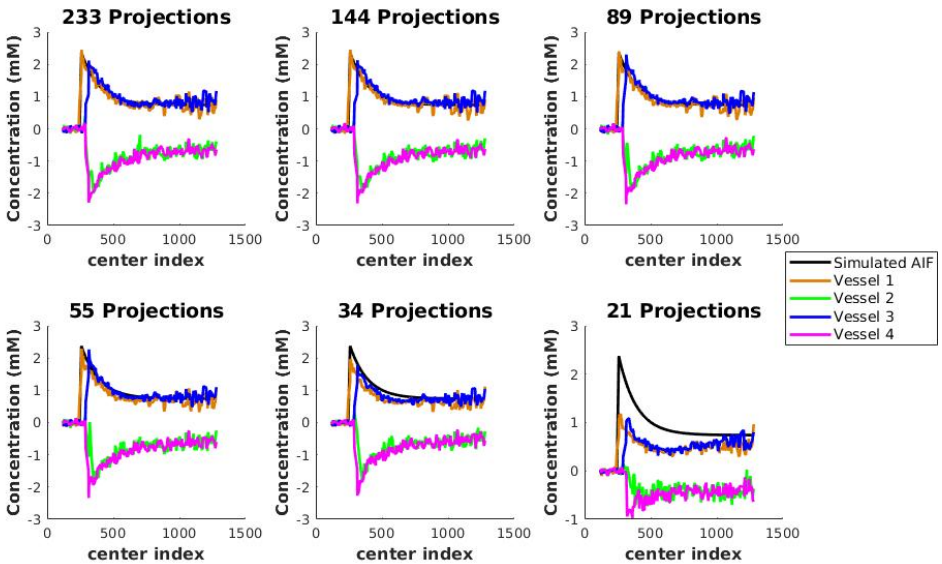

Figure C.17: Corrected AIF using the radial projection-based measurement. In this example, the injection takes place in vessel 1. The phase shift in the remaining three vessles is delayed by 50 data points (5 s), and alternates directions (i.e. phase changes in opposite directions). The shape of the AIF is presered in all vessels and the tissue enhancement correction brings the concentration back to a steady value.

89 and 55 projections falling just short. The ratios have an upward trend towards the later stages of the experiment in vessel 3. This vessel has the same phase shift as injection, so early tissue enhancement around vessel 1 may contribute to the distortion. Both vessels 3 and 4 are in the more sensitive regions of the simulated coil, and should theoretically have comparable results. Since the ratios are just above -1.00 in vessels 2 and 4 at the end of the measurement, the correction appears to be insensitive to the direction of phase evolution in the vessel.

At the peak, the corrections with 144 or 233 projections produced the best results. However, reducing the number of projections to 89 or 55 resulted in a percentage drop of $1-3\%$ and $5-10\%$, respectively. The results with 34 projections were $15-21\%$ lower in vessels 1, 2 and 4, and up to 47-49% in vessels 1, 3 and 4 with 21 projections. Figure C.18 shows that the ratios from data sets with 34-233 projections are similar, though the ratios decrease as fewer projections are used.

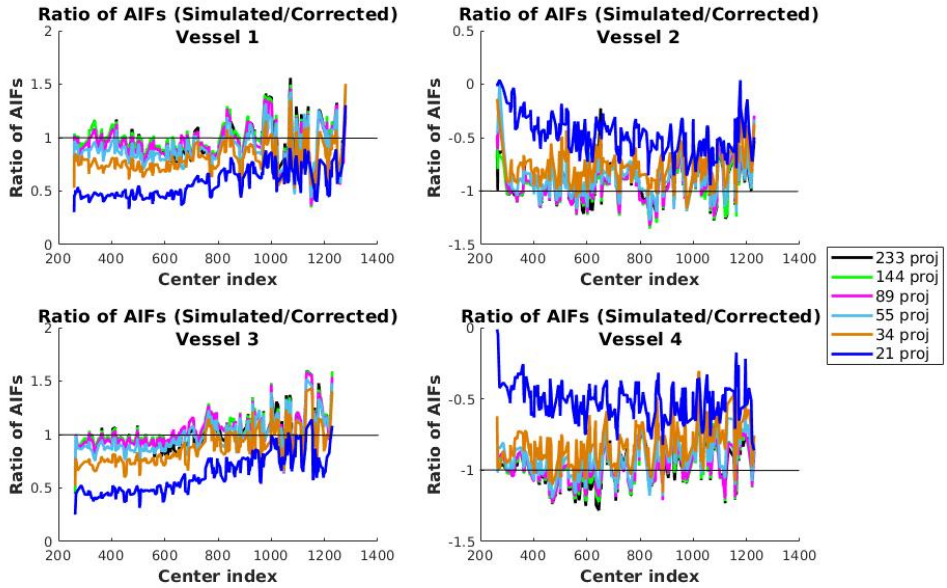

Figure C.18: Concentration ratios of the corrected AIF to the simulated AIF for a multi-vessel experiment where the phase direction alternates between vessels (positive for vessels 1 and 3, negative for vessels 2 and 4). Consistent with prevoius observatios, the ratios are greatest when 89, 144 or 233 projections are used in the correction, slightly lower with 55 projections and significantly lower with 34 or 21 projections. The tissue correction appears to be most effective in vessels 1 and 4 as the ratios are steady and closest to 1.00 at the end of the measurement.

In the washout area, the ratios fall into the range of 0.88-1.05 with 89-233 projections (Table C.10). This is closer to the expectations from the previous study in which all vessels phase changed in the same manner. It is possible that the signal changes between neighbouring vessels cancels on another out if the phase within the vessel is in opposite directions, and therefore essentially self corrects the AIF. The ratios fall slightly with 55 projection, and more dramatically as fewer projections are used. Based on this analysis, it is suggested to use 89 projections in the tissue enhancement correction if local tissue enhancement presents early.

The ratios at the later stages of the experiment are summarized in Table C.11. Leading into the later stages of the AIF, the ratios approach values closer to 1.0,

Table C.10: Ratio of Concentrations Between the Corrected AIF and the Simulated AIF at washout phase

# *projections*	233	144	89	55	34	21
vessel 1	0.879	0.911	0.879	0.835	0.721	0.455
(std dev)	0.061	0.056	0.054	0.059	0.046	0.029
vessel 2	−0.95	−0.96	−0.94	−0.88	−0.79	−0.50
(std dev)	0.23	0.14	0.14	0.15	0.45	0.44
vessel 3	0.880	0.950	0.954	0.903	0.788	0.498
(std dev)	0.059	0.036	0.042	0.040	0.039	0.050
vessel 4	−1.05	−1.02	−0.99	−0.94	−0.84	−0.537
(std dev)	0.14	0.12	0.12	0.11	0.11	0.082

but still under-estimate the concentration in vessels 1, 2 and 4, and over-estimate in vessel 3. In general, the ratios decrease as fewer projections are used in the correction image. We must be careful in interpreting these results, as the larger standard deviation in the ratio could result from a noisy signal (vessel 1) or from data with a clear linear trend (vessels 2 and 3). With the noisy signal, it would be beneficial to compare the final concentration with a value determined directly from the image to improve our confidence in the correction. Having phase shifts in opposite directions improved the quality of the tissue enhancement correction. For this study, the correction image should use at least 55 projections.

C.2.5 AIF Measurment with a Box Car Injection

The final simulation evaluated the temporal limits of the radial projection-based AIF. An ideal rectangular bolus injection, was created with two step functions separated by 89 time-points. The bolus had a concentration of 2 mM during the injection and 0 mM before and after. The purpose of this study was to evaluate the response of the projection-based measurement to a sharp injection profile. As such, no re-circulation peak or local tissue enhancement were considered. The background profiles used for the AIF measurement came from radially reconstructed images. Similar to the previous study, the phantom had four vessels. The injection was performed through vessel 1, and passed through the remaining three vessels

Table C.11: Ratio of Concentrations Between the Corrected AIF and the Simulated AIF at Late Stages

# *projections*	233	144	89	55	34	21
vessel 1	0.96	0.93	0.91	0.93	0.84	0.67
(std dev)	0.24	0.24	0.24	0.23	0.20	0.16
vessel 2	−0.88	−0.87	−0.83	−0.80	−0.69	−0.50
(std dev)	0.21	0.22	0.21	0.21	0.21	0.19
vessel 3	1.12	1.12	1.11	1.09	1.00	0.78
(std dev)	0.22	0.21	0.20	0.18	0.18	0.15
vessel 4	−0.93	−0.91	−0.90	−0.82	−0.70	−0.50
(std dev)	0.16	0.16	0.16	0.14	0.14	0.15

50 time-points (5.0 s) later. The AIFs in the analysis are determined from the corrected projection-based measurement. This provides insights into temporal limitations in the correction procedure. The radial projection-based AIFs are shown in Figure C.19, and the summary statistics of the measured AIFs in Table C.12.

Table C.12: Box Car Injection Summary Statistics

# *projections*	233	144	89	55	34	21
vessel 1	1.93	1.93	1.88	1.76	1.52	0.939
(std dev)	0.12	0.12	0.13	0.15	0.10	0.073
% Injection	96.3	96.6	94.0	88.2	76.2	47.0
vessel 2	1.83	1.79	1.74	1.65	1.40	0.89
(std dev)	0.20	0.20	0.21	0.17	0.21	0.10
% Injection	91.5	89.5	87.2	82.3	70.2	44.3
vessel 3	1.90	1.931	1.893	1.796	1.518	0.920
(std dev)	0.12	0.098	0.094	0.096	0.063	0.086
% Injection	95.1	96.6	94.6	89.8	75.9	46.0
vessel 4	1.99	1.974	1.946	1.836	1.601	1.010
(std dev)	0.10	0.089	0.089	0.097	0.083	0.094
% Injection	99.5	98.7	97.3	91.8	80.0	50.5

The curves from vessel 1 (a)) show that the concentration is at a maximum

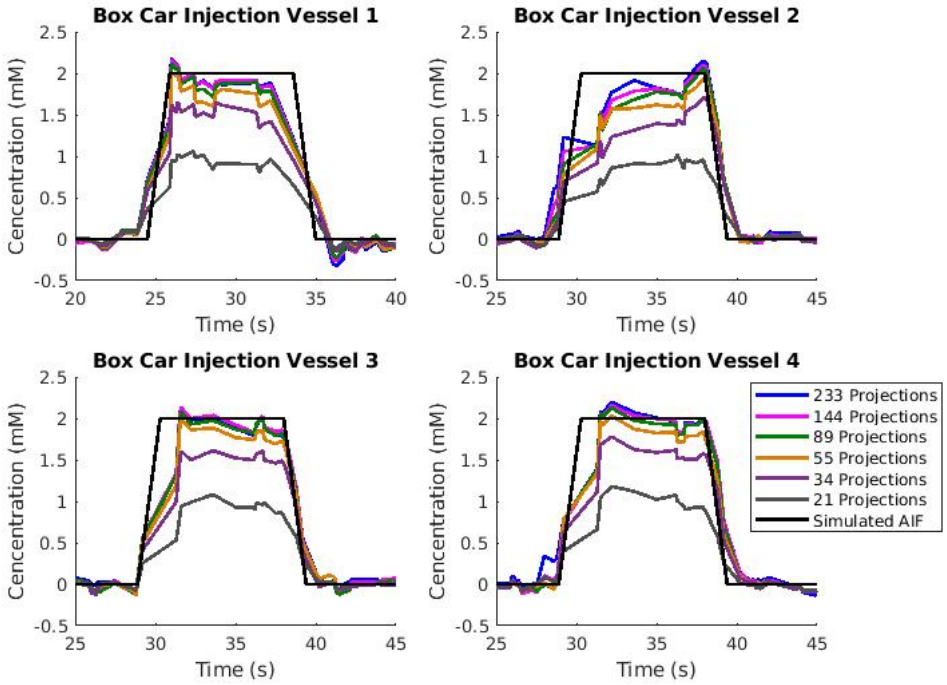

Figure C.19: Radial projetion-based AIFs of an ideal rectangular injection bolus. The injection covers 89 time-points and was performed in vessel 1. The remaining vessels experineced the same bolus, but delayed by 5 s. The beginning and end of the AIFs all appear rounded, likely due to temporal blurring.

at the onset of the bolus, levels out, then gradually decreases near the end of the injection. The curve shape is similar among all acceleration rates, with the main difference being the average concentration. Setting the threshold for an excellent measurement to requiring an average concentration exceeding 1.9 mM (within 5% of expected), the technique would require at least 144 projections in the reconstruction. The data set with 89 would constitute a good measurement with an average concentration within 10% of the input, while the data set is reasonable with an average concentration within 20% of expected.

The AIFs in vessel 2 (b)) increase monotonically until reaching a maximum concentration at the end of the bolus injection. This vessel is located further from

the coil (that is in a less sensitive region of the coil), so any signal change within the vessel will have a lesser impact to the projection profile than a closer vessel. The slow rise could be a result of temporal blurring with the pre-injection profiles. The average concentration in this vessel is much lower than with the other three vessels. Only the reconstruction with 233 projections is an good measurement of the AIF (within 10%), while those with 55, 89 or 144 are reasonable (within 20%). Of the four vessel AIFs, this one had the worst result.

The AIFs in vessel 3 (c)) approximates the concentration of the bolus more precisely, but has a slight downward slope from time position 32.2 s (the maximum). Despite this, the average concentration is within 5% of 2 mM with 144 or 233 projections, and within 10% with 89 projections. The data set with 55 projections, while considered a reasonable measurement, is not far off from the threshold of being within 10%, and could be considered a good estimate. As with vessel 2, the curve takes a couple samples to rise from 0 mM to its maximum value, and the concentration also drops off rapidly at the end of the bolus.

The AIFs in vessel 4 (d)) closely approximate the concentration at the plateau precisely when 89-233 projections are used in the background estimate, providing average concentration between 1.946-1.99 mM (within 2.7% of expected). Similar to the AIFs in vessel 3, the concentration reaches a peak concentration early, then gradually approaches a steady value as the bolus is injected. The initial up-slope covers a couple samples rather than being instantaneous.

The ratio of concentrations of the projection-based AIFs to the box car AIF are summarized in Figure C.20. The results show that the concentration is initially over-estimated in vessel 1 before reaching a steady concentration between time positions 27.5-32.2 s. The ratios are greatest when more projections are use in the image reconstruction, and gradually decreases as fewer projections are used. Data sets with 89 or more projections closely resemble the input curve.

Vessels 3 and 4 have a similar shape in the ratio curve. The ratios reach a maximum immediately following the injection, then approach a steady value between time points 32.2-37.5 s. Again data sets with 89-233 projections reproduce the input curve with high accuracy, while the data set with 55 projections slightly under-estimates the concentration. Vessel 2 shows the opposite effect, where the initial concentration is under-estimated, and gradually increases as the bolus is in-

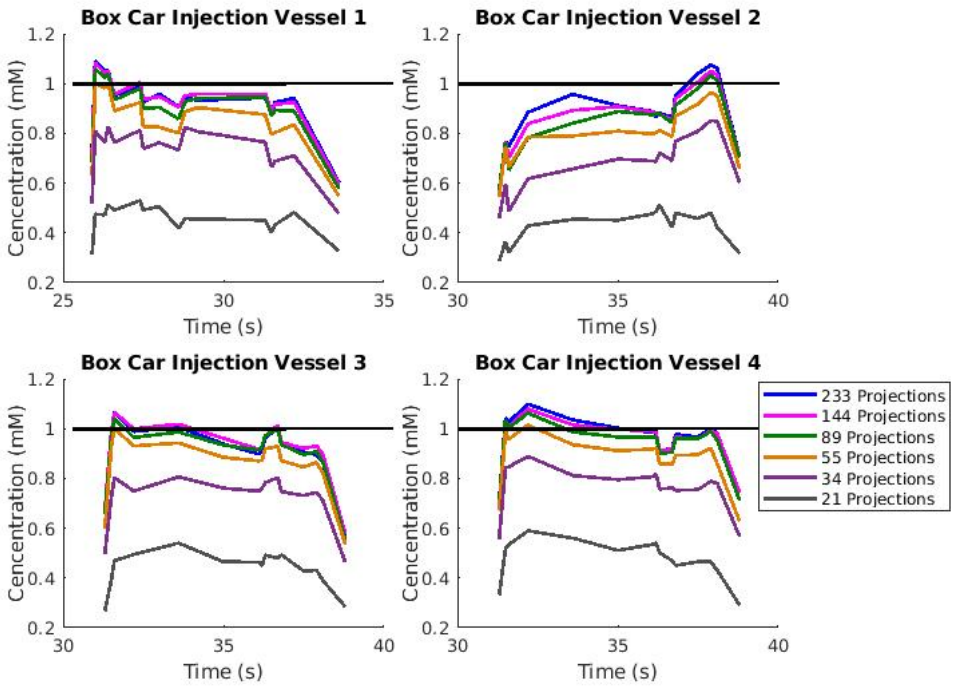

Figure C.20: Concentration ratios of the radial projection-based AIF to the box car AIF for a multi-vessel experiment. The box car injection has a concentration of 2 *mM* and covers 89 samples. In general, the curves with 89, 144 or 233 projections reproduce the input curve with excellent accuracy, while the data set with 55 is good. Data sets wtih 34 or 21 projections greatly underestimate the concentration.

jected. This may be an effect of the lower relative signal of this vessel compared to the other two.

Based on the results of this analysis, at least 89 projections should be used in the reconstruction for an excellent estimate of the AIF, while 55 projections may be used for a good estimate if a higher temporal resolution is desired. In addition, the vessels closer to the coil provide a more accurate estimate of the bolus shape and peak concentration. These vessels should be used if available.